THE UNIVERSITY *of* EDINBURGH

Spatial and Temporal Statistics of SAR and InSAR Observations for Providing Indicators of Tropical Forest Structural Changes due to Forest Disturbance

Elsa Carla De Grandi

DOCTOR OF PHILOSOPHY

The University of Edinburgh

School of GeoSciences

2017

Declaration

I confirm that this work is my own, except where otherwise state. No part of this thesis has been submitted for any other degree or qualification.

Signed: ..Elsa Carla De Grandi.....

Elsa Carla De Grandi

Date: .....11/08/2017.....

Abstract

Tropical forests are extremely important ecosystems which play a substantial role in the global carbon budget and are increasingly dominated by anthropogenic disturbance through deforestation and forest degradation, contributing to emissions of greenhouse gases to the atmosphere.

There is an urgent need for forest monitoring over extensive and inaccessible tropical forest which can be best accomplished using spaceborne satellite data. Currently, two key processes are extremely challenging to monitor: forest degradation and post-disturbance re-growth.

The thesis work focuses on these key processes by considering change indicators derived from radar remote sensing signal that arise from changes in forest structure. The problem is tackled by exploiting spaceborne Synthetic Aperture Radar (SAR) and Interferometric SAR (InSAR) observations, which can provide forest structural information while simultaneously being able to collect data independently of cloud cover, haze and daylight conditions which is a great advantage over the tropics.

The main principle of the work is that a connection can be established between the forest structure distribution in space and signal variation (spatial statistics) within backscatter and Digital Surface Models (DSMs) provided by SAR. In turn, forest structure spatial characteristics and changes are used to map forest condition (intact or degraded) or disturbance.

The innovative approach focuses on looking for textural patterns (and their changes) in radar observations, then connecting these patterns to the forest state through supporting evidence from expert knowledge and auxiliary remote sensing observations (e.g. high resolution optical, aerial photography or LiDAR). These patterns are descriptors of the forest structural characteristics in a statistical sense, but are not estimates of physical properties, such as above-ground biomass or canopy height. The thesis tests and develops methods using novel remote sensing technology (e.g. single-pass spaceborne InSAR) and modern image statistical analysis methods (wavelet-based space-scale analysis).

The work is developed on an experimental basis and articulated in three test cases, each addressing a particular observational setting, analytical method and thematic context.

The first paper deals with textural backscatter patterns (C-band ENVISAT ASAR and L-band ALOS PALSAR) in semi-deciduous closed forest in Cameroon. Analysis concludes that intact forest and degraded forest (arising from selective logging) are significantly different based on canopy structural properties when measured by wavelet based space-scale analysis. In this case, C-band data are more effective than longer wavelength L-band data. Such a result could be explained by the lower wave penetration into the forest volume at shorter wavelength, with the mechanism driving the differences between the two forest states arising from upper canopy heterogeneity.

In the second paper, wavelet based space-scale analysis is also used to provide information on upper canopy structure. A DSM derived from TanDEM-X acquired in 2014 was used to discriminate primary lowland Dipterocarp forest, secondary forest, mixed-scrub and grassland in the Sungai Wain Protection Forest (East Kalimantan, Indonesian Borneo) which was affected by the 1997/1998 El Niño Southern Oscillation (ENSO). The Jeffries- Matusita separability of wavelet spectral measures of InSAR DSMs between primary and secondary forest was in some cases comparable to results achieved by high resolution LiDAR data.

The third test case introduces a temporal component, with change detection aimed at detecting forest structure changes provided by differencing TanDEM-X DSMs acquired at two dates separated by one year (2012-2013) in the Republic of Congo. The method enables cancelling out the component due to terrain elevation which is constant between the two dates, and therefore the signal related to the forest structure change is provided. Object-based change detection successfully mapped a gradient of forest volume loss (deforestation/forest degradation) and forest volume gain (post-disturbance re-growth).

Results indicate that the combination of InSAR observations and wavelet based space-scale analysis is the most promising way to measure differences in forest

structure arising from forest fires. Equally, the process of forest degradation due to shifting cultivation and post-disturbance re-growth can be best detected using multiple InSAR observations.

From the experiments conducted, single-pass InSAR appears to be the most promising remote sensing technology to detect forest structure changes, as it provides three-dimensional information and with no temporal decorrelation. This type of information is not available in optical remote sensing and only partially available (through a 2D mapping) in SAR backscatter. It is advised that future research or operational endeavours aimed at mapping and monitoring forest degradation/re-growth should take advantage of the only currently available high resolution spaceborne single-pass InSAR mission (TanDEM-X).

Moreover, the results contribute to increase knowledge related to the role of SAR and InSAR for monitoring degraded forest and tracking the process of forest degradation which is a priority but still highly challenging to detect. In the future the techniques developed in the thesis work could be used to some extent to support REDD+ initiatives.

Lay Summary

Tropical forests are the largest forest biome on the planet, and play a key role for regulating the climate system and supporting hundreds of millions of people. Anthropogenic disturbance severely affects tropical forests through deforestation and forest degradation (the removal of some trees in an area that remains classified as forest). The Congo Basin and South-East Asian tropical forests are considered hotspots of forest disturbance. The former is characterised by vast areas of forest under commercial logging concessions and widespread small-scale disturbance from small-holders. The latter has long been prone to damaging forest fires exacerbated by the El Niño Southern Oscillation, as well as high intensity commercial logging, and clearing of land for palm oil plantations. Large scale conversion of forests into different land uses (deforestation) is routinely mapped from satellites and the contribution to greenhouse gas emissions is reasonably well quantified. Detecting degraded and regenerating forest and the associated release (or uptake) of carbon is more challenging to perform by observations from space. These processes are usually limited in size, with low magnitude leading to almost imperceptible changes, (often restricted to understorey vegetation) which makes them hard to detect by the most commonly employed optical satellites, since these are not sensitive to vertical vegetation structure. Importantly, forest degradation practices have severe consequences on forest properties (e.g. change in structure, biodiversity and carbon stocks), but using current technologies these may all be undetectable. The thesis explored new ways based on radar observations to detect changes in forest structure (patterns arising from canopy development in width and height) caused by forest disturbance in three test sites: Cameroon, Indonesian Borneo and the Republic of Congo. Each case included different forest degradation drivers and each presenting particular challenges. The main challenges faced in detecting degraded and re-growing forest in tropical countries are: a) possibility of all-weather, cloud and haze independent image acquisitions; b) snapshots repeated in time to capture dynamic events; c) high resolution to track small changes; d) three-dimensional (3D) datasets. The work follows a stepwise approach by leveraging on limitations identified by the previous results and by testing ways of extracting information on forest structure from: a) images of the returned radar echo; b) 3D images of canopy vertical patterns and c) multiple 3D images taken at different times. The use of multiple high resolution 3D datasets proved to be the most suitable way to track forest degradation and forest re-growth. The thesis demonstrated the potential of radar remote sensing coupled with pattern recognition methods for detecting disturbed and re-growing forest. Results might support projects under an upcoming scheme under the UN Framework Convention on Climate Change.

Acknowledgements

First of all I would like to express my gratitude to my supervisor Edward Mitchard for the support and patience throughout the PhD. A special thank you goes to Prof Iain Woodhouse for providing his knowledge and valuable experience in SAR remote sensing. I have valued the contribution of my advisor Prof John Grace who ensured the smooth progress of my PhD.

I would also like to thank those who contributed to improve my work and knowledge. In particular Dr Dirk Hoekman for letting me work on his study site, for providing extensive LiDAR and aerial photography datasets and for his SAR expertise. Special thanks go to Dr Astrid Verhegghen for providing valuable information on tropical forest disturbance in the Congo Basin and on optical remote sensing.

Special thanks go to researchers who have provided expert knowledge and data related to the study sites: Dr Fiona Maisels and Derek Bruggeman for their contribution related to the site in Cameroon. Dr Lan Qie and Dr Ishak Yassir who provided insight related to the site in Borneo.

I would like to acknowledge the data providers: DLR, ESA and Astrium. In particular, the team at DLR (Dr Thomas Busche and Prof Irena Hajnsek) for providing TanDEM-X data (TanDEM-X AO VEGE6702). The research would have never been possible without this data. Thank you to Dr Kostas Papathanassiou and Dr Matteo Pardini for the interesting exchange of ideas during the TerraSAR-X/TanDEM-X Meeting.

My gratitude goes to Sarmap who provided SARScape software to process all the SAR and InSAR data. In particular, thank you to Dr Francesco Holecz and Paolo Riccardi who taught me about SAR processing and for sharing their knowledge during my internship at Sarmap without which my PhD would have been much more challenging.

A thank you goes to the funding bodies and sponsors. First of all, the Principal's Development Career Scholarship and the University of Edinburgh (School of

GeoSciences) for funding the PhD. I acknowledge the support from the Elizabeth Sinclair Irvine Bequest Fund during the last couple of months of my PhD. I would also like to thank the Institute of Electrical and Electronics Engineers (IEEE) and the Remote Sensing and Photogrammetry Society for providing contribution to attend IGARSS 2014 and the 2016 TanDEM-X/TerraSAR-X Meeting.

A huge thank you goes to Rose Pritchard who has been supporting me throughout the good and bad times during the PhD (despite being miles away for a long time!). I am very grateful for all the valuable times shared whilst climbing Scottish mountains. A big thank you goes to Nicola Rigonat who has always been able to cheer me up and supported me with lots of coffee. Thank you to Yaqing Gou for always making me smile and Neha Joshi for sharing conference times in Quebec and Milan.

I am also grateful to my family for supporting me throughout these years. Last but not least, I would like to thank two special friends: Olivia Cooke and Sophie Shorey for their friendship despite living far away.

Table of Contents

1. Introduction

1.1. Thesis Overview..... 1
1.2. Tropical Forests..... 4
1.3. Monitoring Forest Degradation in the Tropics Using Remote Sensing: Overview and Challenges..... 11
1.4. Aims and Objectives..... 24
1.5. Thesis Highlights and Novel Aspects..... 25
1.6. References..... 26

2. Technical Background: Synthetic Aperture Radar (SAR) and Interferometric SAR (InSAR): Key Concepts, Sensors and Data Analysis Methods

2.1. Synthetic Aperture Radar (SAR) Key Concepts and Sensors..... 39
2.2. Interferometric Synthetic Aperture Radar (InSAR) 47
2.3. InSAR Overview and Key Concepts..... 49
2.4. Wavelets 60
2.5. Link between Forest Structure and SAR Signal Structure..... 68
2.6. References..... 70

3. Spatial Wavelet Statistics of SAR Backscatter for Characterising Degraded Forest: A Case Study from Cameroon

3.1. Introduction 76
3.2. Background and Context..... 78
3.3. Study Site..... 80
3.4. Methods..... 82
3.5. ENVISAT ASAR Results and Interpretation..... 94
3.6. ALOS PALSAR Results and Interpretation..... 105
3.7. Conclusion..... 110
3.8. Acknowledgments..... 112
3.9. References……... 113

4. Wavelet Based Analysis of TanDEM-X and LiDAR DEMs across a Tropical Vegetation Heterogeneity Gradient Driven by Fire Disturbance in Indonesia

4.1. Introduction..... 120
4.2. Forest Structural Heterogeneity Derived from Remote Sensing..... 123
4.3. Study Site..... 129
4.4. Methods..... 130
4.5. Results and Interpretation..... 139
4.6. Discussion..... 160
4.7. Conclusion..... 163
4.8. Acknowledgements 165
4.9. Reference..... 165

5. Object-Based Structural Change Detection from TanDEM-X Digital Surface Models to Map Tropical Forest Disturbance and Re-Growth: A Case Study in the Republic of Congo

5.1. Introduction 174
5.2. Study Site..... 180
5.3. Datasets..... 183
5.4. Methods..... 185
5.5. Results..... 202
5.6. Validation 218
5.7. Discussion and Interpretation..... 219
5.8. Conclusion and Future Work..... 230
5.9. Acknowledgements..... 232
5.10. References..... 232

6. Summary and Implications

6.1. Summary..... 241
6.2. Implications..... 250
6.3. Future Research and Improvements..... 260
6.4. References..... 262

Appendix I: Published version of Chapter 3..... 267

Appendix II: Published version of Chapter 4..... 280

List of Figures

Chapter 1

Figure 1. Thesis overview and interaction between the 3 results chapters (Chapter 3, 4 and 5) illustrating (a) study site; (b) disturbance drivers; (c) sensors used and (d) methods tested. Chapter 3 and 4 are linked by the used wavelet space-scale analysis method, while Chapter 4 and 5 both made use of InSAR observations. All results chapters are based on statistical analysis: spatial statistics (Chapter 3 and 4) and temporal statistics (Chapter 5). 3

Figure 2. (a) Central Africa and (b) South-East Asia Global Land Cover Map (GlobCover 2009) (Bontemps, et al., 2011) illustrating the main landcover types and the Intact Forest Landscape 2013 (IFL) dataset (red outline) (Potapov, et al., 2017). The figure illustrates areas of remaining IFL in 2013 located around the tropics in Africa (99 million ha) and in South East Asia (60 million ha) (Potapov, et al., 2017). Note that IFLs are not the same as 'primary forest' but these are included in the IFL dataset. IFLs are defined as: 'a seamless mosaic of forests and associated natural treeless ecosystems that exhibit no remotely detected signs of human activity or habitat fragmentation and are large enough to maintain all native biological diversity, including viable populations of wide-ranging species') (Potapov, et al., 2017). 8

Chapter 2

Figure 1. Side-looking Synthetic Aperture Radar (SAR) system imaging geometry (Bamler, 2000). The side-looking radar acquires images of the ground reflectivity at microwave frequency by measuring distances in the range direction by time of flight. This is performed by sending pulses of electromagnetic energy, while the satellite moves in the azimuth (cross-range or along-track) direction, that cover a portion of the ground called the swath. The ground range is the distance from the nadir position of the satellite to the first pulse return in the slant range geometry. Conversion from slant range to the ground geometry must be performed for mapping applications. 40

Figure 2. Example of SAR imagery acquired at different wavelength and polarisation over the city of Bertoua (Lom-et-Djerem, Cameroon) surrounded by agricultural fields, savanna and semi-deciduous forest. SAR image acquired by: (a) ENVISAT ASAR (C-band, VV polarisation, 15 m resolution) and (b) L-band ALOS PALSAR (L-band, HV, 15 m resolution). 43

Figure 3. Interferometric Synthetic Aperture Radar (InSAR) viewing geometry illustrating the acquisition from two satellites S_1 and S_2 acquiring radar signals separated by a baseline B and located at a height H and at range distances R_1 and R_2 respectively from a target P which is situated at height h_0 (Cloude, 2010). 50

Figure 4. SAR interferogram derived from TanDEM-X StripMap bistatic mode acquisitions over tropical forest in the Republic of Congo (processed using 52

SARscape 5.0) (Sarmap, 2016). In bistatic mode one satellite (master) transmits and receives pulses, while the second satellite (slave) only receives (at a different incidence angle) pulses transmitted by the first satellite. In the interferogram image the phase difference (in radians) received by the two antennas at slightly different position is colour coded. Each colour circle (from black to red) represent a 2π cycle. The regular pattern of fringes correspond to the variation of phase per unit range distance over flat terrain. When this high frequency component is removed by a suitable processing step (flat earth removal) the phase will carry information on the terrain elevation. The absence of fringes are due to scattering from moving water with very low signal to noise ratio. TanDEM-X data acquisition parameters: baseline: 52 m, incidence angle: 47°, polarisation: HH. Data: TanDEM-X AO: VEGE6702 (DLR).

Figure 5. TanDEM-X coherence over the Republic of Congo. Areas with low coherence (green) represent lowland tropical forest dominating the scene, while higher coherence illustrates areas where there is less volume decorrelation from lack of vegetation (e.g. bare soil and agricultural fields) (orange) as well as swamp forest (right). Lowest coherence (black and blue) is observed in water and roads due to the low signal to noise ratio. TanDEM-X data acquisition parameters: baseline: 52 m, incidence angle: 47°, polarisation: HH. Data: TanDEM-X AO VEGE6702 (DLR). 55

Figure 6. Phase centre (PC) dependence on the instrument frequency of acquisition (X-band in red; C-band in green; L-band in blue and P-band in yellow) and volume height (m) calculated using model with a uniform layer and an exponential profile (Cloude, 2010). Notice that at X-band the PC is located > 90% of the height for height > 20 m and at P-band the PC is still located > 50% of the height. 58

Figure 7. TanDEM-X height estimates standard deviation image derived from phase noise $SD(h_\varphi)$ generated by SARScape 5.0 (Sarmap, 2016) in Central Kalimantan, Indonesian Borneo. Higher $SD(h_\varphi)$ values (m) indicate lower measurement precision. Areas of dense forest (red and green) in the top-centre of the image and water to the left of the image (red) present higher $SD(h_\varphi)$ values (lower precision) while, areas of agriculture and bare fields (black and dark blue) have a higher precision. This is related to the degree of decorrelation; in areas where there is less volume scattering the precision is higher.areas where there is less volume scattering the precision is higher. 60

Figure 8. Typical shape of a wavelet. 62

Figure 9. Mallat's wavelet frame chosen to undertake the textural analysis in the thesis. It consists of just 2 points when sampled at integer values (+0.5 and -0.5) and therefore acts as a differential operator. 65

Chapter 3

Figure 1. (a) Study area within the extent of ENVISAT ASAR acquisitions (WGS84, UTM zone 33 N). (b) Location of all landcover samples (N = 80) selected based on VHR RapidEye imagery (27/12/2010) and Landsat 7 (18/01/2011 and 17/12/2010) used in the analysis overlaid on ENVISAT ASAR VV (WGS84, UTM projection-zone 82

33N). The green shape outlines Deng Deng National Park. The red shape outlines a logging concession. Red squares mark samples of degraded forest (DF) within the concession (n= 20), green squares mark intact forest (IF) samples inside the National Park (n= 20), yellow squares mark samples within forest-savanna (FS) (n= 20) and blue squares mark samples within forest-agriculture mosaic (FAM) (n= 20) (see also Table). Data source: World Resources Institute and European Space Agency.

Figure 2. Mother wavelet (red line) and the dilated by $2^{0.25}$ version (first and second voice) (green line). 92

Figure 3. Wavelet variance scaling signatures computed on single date ENVISAT ASAR VV backscatter (2010) for 4 classes of interest: forest-agriculture mosaic (FAM) (blue), degraded forest (DF) (red), intact forest (IF) (green) and forest-savanna (FS) (black). The error bars correspond to the standard error of the wavelet variance estimator. Two parameters need to be considered for the interpretation of the figure. The correlation length (signature maxima) given in terms of scale (m) (x-axis) indicates the point (scale) where the autocorrelation (two-point statistic) between the pixels belonging to a certain class within the window of choice decays to zero. The variance of the wavelet coefficients (y-axis) is a proxy of the process variance within a neighborhood of a given scale (one-point statistic) and thus indicates the "roughness" of the process at a given scale 95

Figure 4. (a) Wavelet scaling signature for two classes: intact forest (green cross) and degraded forest (red cross) and the fitted 3rd degree polynomial function (green and red solid lines for intact forest and degraded forest respectively); (b) first derivative of the intact forest (green) and degraded forest (red) fitted wavelet scaling signatures; (c) second derivative (inflection) of the intact forest (green) and degraded forest (red) fitted wavelet scaling signatures. The wavelet signature at 4 dyadic scales was fitted using a 3rd degree polynomial to obtain a functional description of the signature. The first zero crossing of the first derivative corresponds to the signature maximum (correlation length of the process); the zero crossing of the second derivative indicates the onset of an inflection point in the signature; both indicators occur at different scales for intact and degraded forest and thus can be considered as a potential way to discriminate between the two forest classes. 98

Figure 5. Wavelet spectrum for a transect in (a) Forest-savanna (FS) (in the northing direction) and (b) Forest-agriculture mosaic (FAM) (easting direction) showing the different textural properties of each class in the space-scale domain. The spectrum is estimated in a 43 × 43 pixels window (equivalent to 645 × 645 m in the ENVISAT ASAR geocoded dataset). SAR backscatter within the corresponding windows (rendered in false color) is shown to the right of the spectra. These test cases highlight the capability of the wavelet space-scale representation to characterize radiometrically heterogeneous targets, such as a forest ribbon in (a) and the margin between bare soil and forest in (b). 102

Figure 6. Wavelet normalized covariance between ENVISAT ASAR scenes acquired in 2006 and 2010 for four landcover classes: degraded forest (red), forest-savanna (FS) (green), intact forest (IF) (blue), and forest-agriculture mosaic (FAM) (black). Wavelet normalized covariance values range from 0 to 1 with higher values 104

indicating greater textural correlation between the two dates. There is a decreasing trend in wavelet covariance with increasing scale for all landcover classes but in particular for forest-agriculture mosaic, which can be linked to changes due to agricultural practices between the two dates. Decreasing wavelet covariance for IF, DF and FS classes could be due to phenological or moisture differences between the two dates.

Figure 7. (a) ALOS PALSAR HH and (b) ALOS PALSAR HV wavelet variance scaling signatures (4 dyadic scales) for four classes of interest: forest-agriculture mosaic (FAM) (blue), degraded forest (DF) (red), intact forest (IF) (green) and forest-savanna (FS) (black) with corresponding error bars (black). See Figure 3 for details on the interpretation of the signatures. 106

Figure 8. (a) Wavelet scaling signature for two classes: IF (green cross) and DF (red cross) and the fitted third-degree polynomial functions (green and red solid lines); (b) First derivative of the fitted polynomial and (c) Second derivative of the fitted polynomial. See Figure 4 for the interpretation of the functional representation of the signatures. 108

Chapter 4

Figure 1. (a) Study site location and data extent overlaid on a land cover map provided by the Indonesian Ministry of Forestry (Indonesian Ministry of Forestry, 2015). TanDEM-X data extent (black box, only partially covered in this image), LiDAR site A and B (red) and 315 sample plots (35 x 35 m^2) (blue squares). LiDAR Site A is primarily covered by primary forest (PF) (undisturbed) while; Site B is dominated by secondary forest (SF) (disturbed), mixed scrub (MS) and grassland (GR); (b) Range of vegetation structures observed from high resolution aerial photography (0.5 m) (blue square: 35 x 35 m^2 plot). 130

Figure 2. (a) TanDEM-X coherence modulus; (b) Aerial photo (0.5 m resolution); (c) Canopy Height Model (CHM) derived from airborne LiDAR (1 m resolution); (d) TanDEM-X DSM; and (e) TanDEM-X DSM subset. Boundary between primary forest (PF) and secondary forest (SF) (red line) according to the land cover map provided by the Indonesian Ministry of Forestry (Indonesian Ministry of Forestry, 2015) is shown on the aerial photo (b); LiDAR CHM (c) and TanDEM-X DSM (e). 132

Figure 3. Sample classes derived from a LiDAR Canopy Height Model (CHM) (m) within 35 x 35 m^2 plots illustrating vertical structure arrangement (height) in: primary forest (intact) (PF), secondary forest (disturbed) (SF), mixed scrub (MS) and grassland (GR). 135

Figure 4. Flowchart illustrating the application of 2D wavelet spectra to 3D datasets for the analysis of landscape heterogeneity across a disturbance gradient: (a) 3D input dataset; (b) generation of 2D wavelet spectra image with 16 fractional scales with $2^{1/4}$ spacing between scales at four dyadic scales (S_1, S_2 … S_n); (c) feature reduction to four wavelet polynomial coefficients (P_0, P_1, P_2 and P_3) by fitting a 3rd order polynomial to the wavelet signature; (d) wavelet signature (wavelet variance as a function of scale); and (**e**) interpretation of the wavelet signature based on target structural characteristics. 137

Figure 5. (a) Wavelet variance as a function of 10 dyadic scales (2 m to 1000 m) computed over a 6.95 km transect in intact (PF) and disturbed secondary forest (SF). TanDEM-X DSM (green) and LiDAR derived datasets (DSM: black, CHM: blue and DTM: red). The figure indicates how the information related to canopy structure provided by the LiDAR CHM (apparent with higher wavelet variance at short scale ≅ 10 m) is reflected onto the TanDEM-X DSM within the same scale range. Whereas, structure due to topography as provided by the LiDAR DTM are captured in the region around the wavelet variance maximum at longer scales (≅ 200 m), and are reflected onto the TanDEM-X DSM within the same scale range. Therefore, the TanDEM-X DSM contains both textural components due to forest canopy structure and elevation variation, these however appearing at largely different scale domains. (b) Wavelet co-variance providing information on pairwise textural correlation between datasets: LiDAR DTM, DSM and CHM versus TanDEM-X DSM. LiDAR DTM/LiDAR CHM (green); LiDAR DTM/LiDAR DSM (red) and LiDAR DTM/TDX DSM (black). The textural correlation between two datasets can be appreciated as being low at short scales and higher at long scales. Abbreviations: Canopy Height Model (CHM); Digital Surface Model (DSM) and Digital Terrain Model (DTM). 141

Figure 6. Wavelet signatures based on: (a) LiDAR CHM; and (b) TanDEM-X DSM based on one pixel taken in: primary forest (PF) (red), mixed-scrub (MS) (black), secondary forest (SF) (green) and grassland (GR) (blue). Colored squares within the LiDAR CHM or TanDEM-X DSM subsets indicate the pixel selected for the analysis: 1 pixel (1 x 1 m^2 in LiDAR CHM and 4.6 x 4.6 m^2 in TanDEM-X DSM. Interpretation of the signature should take into account the location of the maxima (sill) or correlation length which indicates the point in terms of scale where the process autocorrelation decays to zero. The process "roughness" when considering the process smoothed at a given scale is indicated by the wavelet variance values at that scale, with higher wavelet variance indicating greater process roughness. Wavelet signature that do not present a correlation length (flat signature) is typical of a white noise processes which means that the process is self-similar at all scales indicating homogeneity. Similarities and differences between wavelet signatures must be considered in terms of correlation properties (correlation length), which are indicated by functional relations such as maxima and slope, and process variance as a function of scale, which is indicated by the wavelet variance magnitude. 143

Figure 7. Probability distribution (PD) of the first coefficient P_0 in the polynomial approximation of the wavelet signature by class (grassland- GR, mixed-scrub- MS, primary forest- PF and secondary forest- SF): (a) LiDAR CHM P_0 PD; and (b) TanDEM-X DSM P_0 PD. Greater information was observed using one-point statistic of P_0 compared to using one point-statistic of each P_1, P_2 and P_3. P_0 is the intercept with the y-axis in the log-log wavelet variance-scale plot, therefore it is a good approximation of the wavelet variance at short scale. 147

Figure 8. Logarithmic relationship between: (a) LiDAR CHM standard deviation (m) and LiDAR CHM P_0 (red cross) (R^2 = 0.78, N = 315), and LiDAR CHM standard deviation (m) and TanDEM-X DSM P_0 (black circle) (R^2 = 0.34, N = 315). (b) TanDEM-X DSM standard deviation (m) and TanDEM-X P_0 (R^2 = 0.72, N = 315). 149

Figure 9. LiDAR CHM, TanDEM-X DSM and corresponding P_0 frequency distributions (FD) for primary forest (intact) (PF) (black line) and secondary forest (SF) (red line): (a) LiDAR CHM FD (23 x 23 pixels); (b) LiDAR CHM P_0 FD (23 x 23 pixels); (c) LiDAR CHM FD (351 x 351 pixels); (d) LiDAR CHM P_0 FD (351 x 351 pixels); (e) TanDEM-X DSM (m) FD (351 x 351 pixels); and (f) TanDEM-X DSM P_0 FD (351 x 351 pixels). 151

Figure 10. (a) LiDAR CHM; (b) LiDAR CHM wavelet spectrum image (P_0); (c) TanDEM-X DSM; and (d) TanDEM-X DSM wavelet spectrum image (P_0). The red line marks the boundary between secondary forest (SF) and primary forest (PF) according to data supplied by the Indonesian Ministry of Forestry (Indonesian Ministry of Forestry, 2015). The onset of homogeneous (in terms of height distribution) forest patches, characteristics of the burnt secondary forest, is clearly visible in the LIDAR CHM (a) to the North of the boundary line, and it is well detected by areas of lower LiDAR CHM P_0 (brown) in (b) and lower TanDEM-X P_0 (brown) corresponding to secondary forest. Sample plots used in the FD analysis reported in Figure 9: 23 x 23 pixel plots (black squares) and 351 x 351 pixel plots (yellow squares). 154

Figure 11. Scale by scale pairwise Jeffries Matusita (JM) distance trend for primary forest (PF), secondary forest (SF), mixed scrub (MS) and GR (grassland) at four dyadic scales: (a) $\text{LiDAR}_{\text{CHM}}$WS; (b) TDX_{DSM}WS ($n_{\text{GR/MS}}$ = 44; $n_{GR/SF}$ = 44; $n_{GR/PF}$ = 44, $n_{MS/SF}$ = 49, $n_{MS/PF}$ = 49 and $n_{SF/PF}$ = 96); (c) $\text{LiDAR}_{\text{CHM}}$WS average JM; and (d) TDX_{DSM}WS average JM with associated error bounds (P_e lower and P_e upper). 156

Figure 12. Average wavelet signatures for four classes: primary forest (PF) (red), secondary forest (SF (green), grassland (GR) (blue) and mixed-scrub (MS) (black) (n = 16, N = 64): (a) $\overline{\text{X}}\text{LiDAR}_{\text{CHM}}$WS (scale: 2^0 = 1 m; 2^1 = 2 m; 2^2 = 4 m; 2^3 = 8 m; 2^4 = 16 m); and (b) $\overline{\text{X}}\text{TDX}_{\text{DSM}}$WS (scale: 2^0 = 4.6 m; 2^1 = 9.2 m; 2^2 = 18.4 m; 2^3 = 36.8 m; 2^4 = 73.6 m). 159

Chapter 5

Figure 1. (a) Study area covered by TanDEM-X (approximately 1000 km^2) situated around the Sangha Department capital of Ouesso in the Republic of Congo (RoC) (UL: 15° 56′ 54.55″ E, 1° 44′ 30.50″ N) overlaid on a landcover classification map (FACET Atlas: Forêts d'Afrique Centrale Évaluées par Télédétection) at 60 m resolution (OSFAC, 2012) showing the main landcover classes and forest cover loss between 2000-2010 (Potapov, et al., 2012). (b) The study site is divided into community areas (0.6% of the study area), protection areas (3.4% of the study area) and production areas (10.8% of the study area). The study area hosts two logging concession (black outline) with logging activities within the Pokola and Ngombé concessions taking place between the 1980s until 2008 (World Resources Institute, 2013). Control areas located within the protection area classified as lowland primary forest (black) and swamp forest (blue) were selected to provide no-change areas for the analysis. (c) TanDEM-X Digital Surface Model acquired on 05/12/2012 (t_1). 182

Figure 2. Methodology flowchart including DSM difference processing; DSM difference calibration; morphological algorithm implementation; post-processing 186

and refinement; error propagation estimates and object-based validation relying on VHR Pléiades imagery.

Figure 3. Original trend profile (black), fitted trend line (red) (Equation 4) and corrected (de-trended) range profile (green) (Equation 5). The peak between 2000 and 3000 pixels arises because of an area of very low precision in the DSM (river). This singularity does not influence the estimation of the trend. 188

Figure 4. TanDEM-X standard deviation of height estimates derived from phase noise ($SD(h_\varphi)$) for two dates provided by SARScape 5.0 (Sarmap, 2016): (a) $TDXt_1$: 05/12/2012 and (b) $TDXt_2$: 25/12/2013. Higher $SD(h_\varphi)$ values (m) indicate lower measurement precision. Notice that areas of lowland forest present higher $SD(h_\varphi)$ values (lower precision) while, areas of swamp forest, agriculture and bare fields (dark blue) have a higher precision. This is related to the sensitivity of the interferometer in areas where there is less volume decorrelation. The river presents the lowest precision in the scene (highest $SD(h_\varphi)$) (red). Overall higher precision was achievable at $TDXt_1$ ($B_\perp$= 95.3 m) compared to $TDXt_2$ ($B_\perp$=52 m). 193

Figure 5. Probability of Type I error as a function of effect size. 196

Figure 6. Pléiades data (22/02/2013) with overlaid deforestation/degradation validation objects (DEF/DEG) (red outline) delineated from visual interpretation and expert knowledge captured between two Pléiades scenes (date 1: 22/02/2013 and date 2: 17/12/2013). 200

Figure 7. (a) Three-dimensional TanDEM-X ΔDSM representation showing changes along a 950 m transect across (1) stable lowland forest, (2) forest volume loss, (3) forest volume gain and (4) forest volume loss. (b) Corresponding transect showing the magnitude of changes and (c) ΔDSM image illustrating the transect location. 202

Figure 8. (i) $\Delta DSM_{negative}$ object (red) and (ii) $\Delta DSM_{positive}$ object (green) overlaid on the image and on two Pléiades scenes taken at t_1 (22/02/2013) and t_2 (17/12/2013). 203

Figure 9. (a) Mean $\Delta DSM_{negative}$ objects boxplots (red) (n= 4168) and mean $\Delta DSM_{positive}$ objects boxplots (green) (n= 772). (b) Mean $\Delta DSM_{negative}$ objects by 10 area categories and (c) mean $\Delta DSM_{positive}$ objects (green) by 10 area categories. 206

Figure 10. (a) Mean $\Delta DSM_{negative}$ objects magnitude (red) and associated confidence intervals (CI) ± 68% (blue) and ± 95% (black). (b) Mean $\Delta DSM_{positive}$ objects magnitude (green) and associated confidence intervals (CI) ± 68% (blue) and ± 95% (black). 208

Figure 11. Effect size of $\Delta DSM_{negative}$ objects (red shades) and $\Delta DSM_{positive}$ objects (green shades) with respect to two control plots: lowland primary forest (PF_c) and swamp forest (SW_c). 210

Figure 12. Mean effect size (red) ± 95% confidence interval (black) for $\Delta DSM_{negative}$ objects compared to (a) lowland primary forest control plot (PF_C) and (b) swamp forest control plot (SW_C). Mean effect size (red) ± 95% confidence interval (black) for 211

$\Delta DSM_{positive}$ objects compared to (c) lowland primary forest control plot (PF_C) and (d) swamp forest control plot (SW_C).

Figure 13. DSM height difference (m) between two observations as a function of extinction (dB) for a volume height of 30 m (green) and 50 m (red). 212

Figure 14. DSM height difference as a function of the surface to volume scattering ratio and parameterised by extinction: 0.05 dB (red) and 0.3 dB (green). 213

Figure 15. $\Delta DSM_{negative}$ subset A (n= 2030) (white) and $\Delta DSM_{negative}$ subset B (n= 2137) (grey) boxplots illustrating (a) $\Delta DSM_{negative}$ magnitude (m); (b) $\Delta DSM_{negative}$ subset A binned into 10 area categories and (c) $\Delta DSM_{negative}$ subset B binned into 10 area categories. 215

Figure 16. Minimum distance (m) between $\Delta DSM_{positive}$ objects and $\Delta DSM_{negative}$ objects multi-modal distribution (blue) (estimated by a smoothed histogram) (dataset A+B). A normal distribution (red) is fitted around the first mode at 300 m. Objects with a distance within the 3rd quartile of the normal distribution (d< 500 m) are considered further as post-disturbance re-growth while objects with d≥ 500 m are discarded. 217

Figure 17. Change map showing TanDEM-X $\Delta DSM_{negative}$ objects (deforestation/forest degradation) (red) (subset B) and $\Delta DSM_{positive}$ objects (post-disturbance re-growth) (subset B) (green). 218

Figure 18. Sample of manually delineated deforestation/forest degradation objects (DEF/DEG) (red) detected by both TanDEM-X change detection and Pléiades overlaid on (a) ΔDSM image (extracted changes outlined in black); (b) Pléiades at t_1 (22/02/2012) and (c) Pléiades at t_2 (17/12/2013). 219

List of Tables

Chapter 2

Table 1. Most commonly used SAR systems frequency bands and related frequency (GHz) and wavelength (cm) at which they operate (Moreira, et al., 2013). 42

Table 2. List of spaceborne satellites launched since 1990 including current, future and proposed missions (World Meteorological Organization, 2017; European Space Agency, 2017). 44

Table 3. Space-scale (time-frequency) analysis. 62

Table 4. Spatial random field measures. 67

Chapter 3

Table 1. Four landcover samples used in the analysis (WGS84, UTM projection - Zone 33 N). 85

Table 2. Wavelet resolution for the first four voices. 91

Table 3. Flatness factor statistics for 20 samples of each of the four classes of interest. For Gaussian white noise the flatness factor would be equal to 3. Higher flatness factors indicate the onset of intermittency or non-stationarity. 101

Chapter 4

Table 1. TanDEM-X acquisition configuration parameters. 131

Table 2. JM distance separability between four classes considering full WS: TDX_{DSM}WS; and $LiDAR_{CHM}$WS. Range between 0 and $\sqrt{2}$ ($n_{GR/MS}$ = 44; $n_{GR/SF}$ = 44; $n_{GR/PF}$44, $n_{MS/SF}$ = 49, $n_{MS/PF}$ = 49 and $n_{SF/PF}$ = 96). 157

Table 3. Class separability statistical evaluation based on pairwise JM distance: P_e lower bound; P_e upper bound (%) (N = 176, n = 44). 158

Chapter 5

Table 1. TanDEM-X StripMap mode configuration for 2 dates acquired at HH polarisation, descending orbit direction and right look direction. Tropical Rainfall Measuring Mission (TRMM) precipitation data for a period of 48 h before the acquisition date (GIOVANNI, 2016). 184

Table 2. Ancillary VHR optical Pléiades data used for validation of the TanDEM-X change map (Astrium, 2012; Google Earth , 2016). 185

Table 3. $\Delta DSM_{negative}$ objects (n= 4168), $\Delta DSM_{positive}$ objects (n= 772), lowland primary forest (PF_C) (n= 510) and swamp forest (SW_C) (n= 1161) magnitude and area 206

statistics (mean ± standard deviation: $\mu \pm \sigma$; median: $\tilde{x}$; kurtosis: k; minimum: Min; maximum: Max; lower quartile: Q_1 and upper quartile: Q_3.

Table 4. Standard error of the mean (SEOM ($SD(\hat{h})$) statistics (mean ± standard deviation: $\mu \pm \sigma$ (m); median: $\tilde{x}$ (m); lower quartile: Q_1; upper quartile: Q_3 and kurtosis: k for $\Delta DSM_{negative}$ objects (N= 4168) and $\Delta DSM_{positive}$ objects (N= 772). 208

Table 5. Effect size (E_{size}) statistics for $\Delta DSM_{negative}$ objects (N= 4168) against control plots and for $\Delta DSM_{positive}$ objects (N= 772) against control plots (PF_C and SW_C). 210

Table 6. Statistics of the ± 95% confidence interval (CI) for $\Delta DSM_{negative}$ objects (N= 4168) and control plots and for $\Delta DSM_{positive}$ objects (N= 772) and two control plots (PF_C and SW_C). 211

Table 7. $\Delta DSM_{negative}$ subset A (n= 2030) and B (n= 2137) magnitude (m) and area (ha) statistics (mean ± standard deviation: $\mu \pm \sigma$; median: $\tilde{x}$; minimum: Min; maximum: Max; upper quartile: Q_1; lower quartile: Q_3 and kurtosis: k. 215

Table 8. Minimum distance (m) statistics between $\Delta DSM_{positive}$ objects centroids (N= 755) and $\Delta DSM_{negative}$ objects centroids (N= 2137) for subset A (n= 428) and subset B (n= 327). 217

Abbreviations

ACF	Autocorrelation Function
ASAR	Advanced Synthetic Aperture Radar
ATI	Along Track Interferometry
CHM	Canopy Height Model
CWT	Continuous Wavelet Transform
DEM	Digital Elevation Model
DF	Degraded Forest
DFT	Discrete Fourier Transform
DInSAR	Differential SAR Interferometry
DSM	Digital Surface Model
DTM	Digital Terrain Model
DWT	Discrete Wavelet Transform
ENSO	El Niño Southern Oscillation
ESA	European Space Agency
ETM+	Enhanced Thematic Mapper
FAM	Forest-agriculture mosaic
FAO	Forest and Agriculture Organization
FBD	Fine Beam Dual
FOTO	Fourier Transform Textural Ordination
FS	Forest- savanna
GBFM	Global Boreal Forest Mapping
GLCM	Gray-Level Co-occurrence Matrix
GR	Grassland
GRFM	Global Rain Forest Mapping
H0	Null-hypothesis
HH	Horizontal Send Horizontal Receive
HoA	Height of Ambiguity
HV	Horizontal Send Vertical Receive
IF	Intact Forest
IM	Imaging Mode
InSAR	Interferometric Synthetic Aperture Radar
JM	Jeffries–Matusita
LiDAR	Light Detection and Ranging
MS	Mixed scrub
PALSAR	Phased Array L-band Synthetic Aperture Radar
PC	Phase Centre
PCH	Phase Centre Height
PD	Probability Density
PF	Primary Forest
PolInSAR	Polarimetric Interferometric Synthetic Aperture Radar
RCS	Radar Cross Section
REDD+	Reducing Emissions from Deforestation and Forest Degradation
SAR	Synthetic Aperture Radar

SF	Secondary forest
SRF	Spatial Random Fields
SRTM	Shuttle Radar Topographic Mission
SWPF	Sungai Wain Protected Forest
TDX	TanDEM-X
UFA	Forest management Units
UNFCCC	United Nations Framework on Climate Change
UTM	Universal Transverse Mercator
VV	Vertical Send Vertical Receive
WASS	Wavelet Scaling Signature
WS	Wavelet Spectra

1. Introduction

1.1. Thesis Overview

The thesis focuses on the use of Synthetic Aperture Radar (SAR) and Interferometric Synthetic Aperture Radar (InSAR) data for detecting the difference between undisturbed and disturbed tropical forests in three sites: Cameroon, the Republic of Congo and Indonesian Borneo. The research develops and uses a variety of techniques, and applies them to a number of datasets from different SAR sensors, in order to compare the utility of different approaches.

In terms of methods the thesis focuses on the use of wavelet analysis (**Chapter 3** and **4**) applied to radar backscatter (**Chapter 3**) or Digital Surface Models (DSMs) (**Chapter 4**); and object-based change detection applied to differences in DSMs (**Chapter 5**). The different study sites are chosen in order to investigate different mechanisms of forest disturbance, featuring selective logging in Cameroon (**Chapter 3**), fire disturbance in Indonesian Borneo (**Chapter 4**), and shifting-cultivation in the Republic of Congo (**Chapter 5**). The analysis was undertaken by complementing the SAR and InSAR data with expert knowledge, ancillary datasets (optical satellite data, aerial photography and airborne LiDAR data), and novel methods, to understand canopy spatial structure variations.

Three chapters in the thesis (3-5, herewith referred to as "results chapters") report on research results, two of which are almost unchanged versions of published peer-reviewed articles. The three results chapters were developed independently, but taking into account, and building on, the challenges and limitations of previously achieved results. The first results chapter concerns SAR backscatter analysis, this being sensitive to upper canopy properties but less efficient at probing the forest vertical structure. The second results chapter calls into play interferometric phase and derived DSMs, and progresses to consider changes in the three-dimensional forest structure caused by forest disturbance. Finally, the third results chapter introduces a

temporal dimension, tackling change in time of the three-dimensional DSM information as a mechanism for detecting and characterising disturbance.

The three results chapters mentioned above are framed by two introductory chapters and a final chapter. **Chapter 1** presents the context of this research, **Chapter 2** provides a technical introduction to SAR and InSAR concepts and background related to wavelet analysis. **Chapter 6** provides a synthesis of the findings, reports the implications of the PhD research and suggests improvements and future work.

The thesis fits into the context required to improve understanding of the capabilities of SAR and InSAR to detect disturbed forests with potential implications for international initiatives that aim to reduce and eventually reverse deforestation and forest degradation in the attempt to curb greenhouse gas emissions (UNFCCC, 2015).

A synoptic view of the overall work development, including instruments, datasets and methods, and how it is reflected in the thesis structure is given in Figure 1.

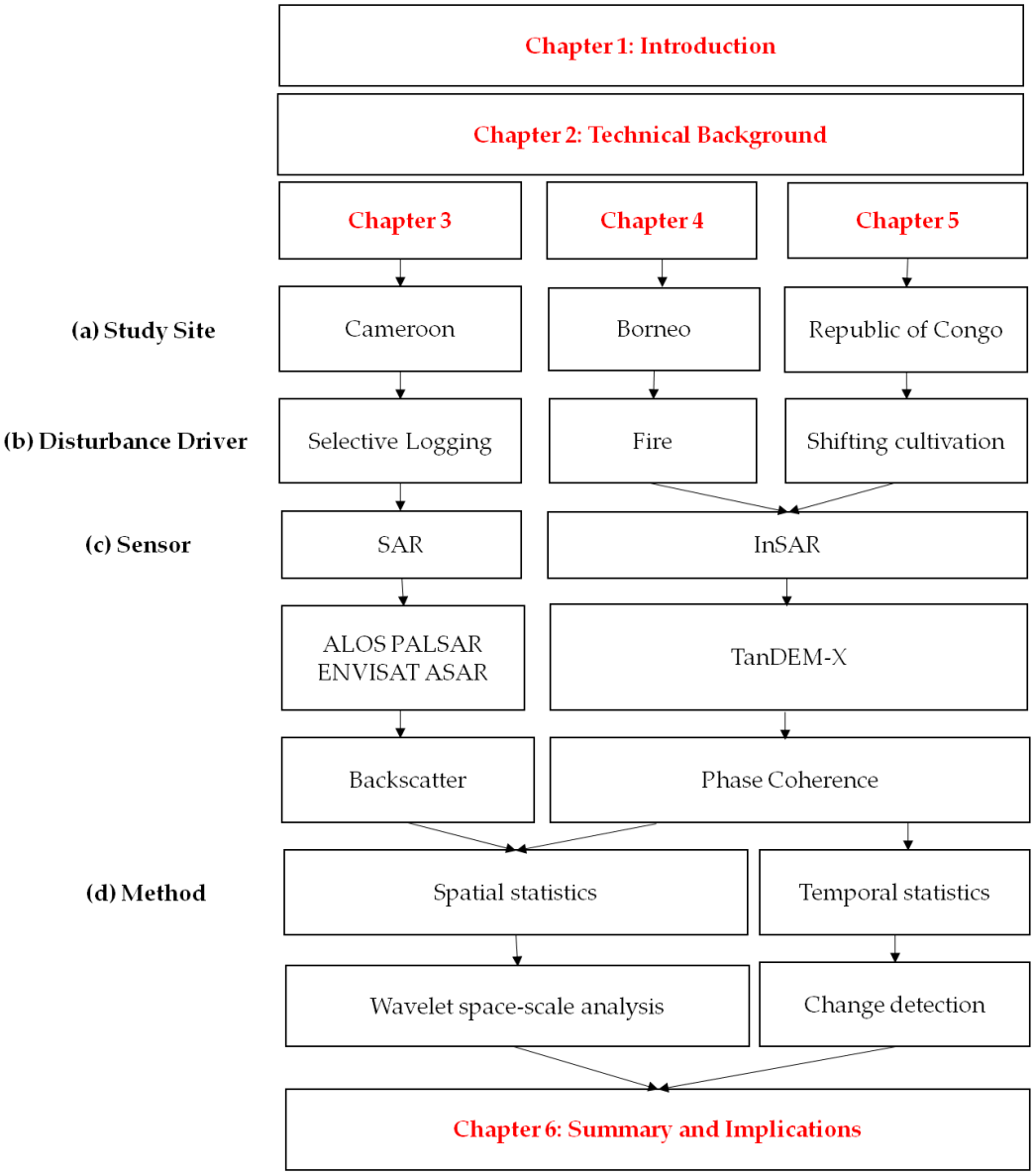

Figure 1. Thesis overview and interaction between the 3 results chapters (**Chapter 3**, **4** and **5**) illustrating (**a**) study site; (**b**) disturbance drivers; (**c**) sensors used and (**d**) methods tested. **Chapter 3** and **4** are linked by the used wavelet space-scale analysis method, while **Chapter 4** and **5** both made use of InSAR observations. All results chapters are based on statistical analysis: spatial statistics (**Chapter 3** and **4**) and temporal statistics (**Chapter 5**).

1.2. Tropical Forests

1.2.1. Tropical Forests Carbon Storage and Carbon Cycle

Tropical forests are defined as: 'land with a tree canopy cover > 10%, 5 m (metres) tall, covering an area of more than 0.5 ha' (FAO, 2015) and situated between the tropics of Cancer and Capricorn (23.44° North and South). The tropics cover approximately 4.4 billion ha (30% of the global land surface) of which 1. 78 billion ha are covered by forests (FAO, 2011), this constitutes approximately 40% of the tropics land surface and 12% of the global land surface, making it the largest forest biome on the planet. Tropical forests can be broadly divided into: the Amazon Rainforest Basin (800 million ha); the Congo Basin (300 million ha) and South-East Asian forest (240 million ha) (FAO, 2011). Note that estimates reported in the literature by different sources are affected by a wide degree of variation) (Grace, et al., 2014).

They store the greatest amount of above-ground carbon (a total of 180 - 210 Pg C) (Baccini, et al., 2012; Saatchi, et al., 2011), and are highly productive (Lewis, et al., 2009) having the highest rate of gross primary production (GPP) of any ecosystem (Malhi, 2012) (~40 Pg C/year) (Beer, et al., 2010) as well as high net primary production (NPP) (21.9 Pg C/year) (Saugier, et al., 2001; Mahli, et al., 2004); host a high diversity of plants and animals (Montagnini & Jordan, 2005) (at least two-thirds of the world's organisms and 3 million species) (Raven, 1988) and provide goods and services (Lewis, et al., 2015; Montagnini & Jordan, 2005) (including food, timber and medicines) supporting approximately between 1.2-1.5 billion people globally (including the supply of local to global markets for commodities) (Lewis, et al., 2015).

Tropical forests are critical for climate system regulation (Maynard & Royer, 2004) and play a substantial role in the global carbon budget as a carbon source, through deforestation, forest degradation practices, harvesting and peat fires (2.01 ± 1.1 Pg/annum) (Grace, et al., 2014) and contribute to about 6-17% of global anthropogenic emissions (van der Werf, et al., 2009).

They are also the largest terrestrial carbon sink (Gibbs, et al., 2007) with an estimated carbon sequestration, through forest regeneration and afforestation, equivalent to 1.8 ± 0.9 Pg C/annum (Grace, et al., 2014).

As well as anthropogenic disturbance, future climatic changes pose a threat to tropical forests. This will lead to changes in rainfall patterns and predicted temperature increase (a 3-6°C increase in land surface temperature within this century) (Zelazowski, et al., 2011) are forecasted to affect Africa significantly given its high exposure and low capability to adapt (Niang, et al., 2014).

Understanding the sensitivity of tropical forests to climate change has been mainly focused on the impacts in Amazonia (Malhi, et al., 2009) and is even less understood and researched in African rainforests (Malhi, et al., 2013; James, et al., 2013). According to several models potential forest expansion will occur in the Congo Basin (Zelazowski, et al., 2011). Increased CO_2 concentration in the atmosphere is set to undoubtedly affect forest productivity as this enhances photosynthesis (Cernusak, et al., 2013) and several model simulations indicated that CO_2 is projected to enhance tropical forest biomass (Huntingford, et al., 2013).

1.2.2. Deforestation and Forest Degradation

Anthropogenic disturbance of forests can be divided into two types: deforestation and forest degradation. Deforestation is the complete loss of forest encompassing the conversion of forest to a different land cover for the purpose of, for instance, agriculture expansion. Forest degradation leads to the partial and persistent loss of forest properties such as carbon stocks (Herold, et al., 2011) and structure (Grainger, 1993), while still remaining 'forest', defined based on canopy cover above a set threshold, it does not constitute a land use conversion (Herold, et al., 2011).

Deforestation drivers range from large scale clearing for cattle ranching (Garcia, et al., 2017) and agriculture (e.g. soybean production) in the Amazon (Barona, et al., 2010), to clearing for palm oil and paper pulp plantation in South East Asia (Koh, et al., 2011), to forest degradation from widespread industrial scale selective logging of valuable tree species for global commodities in the Congo Basin (Laporte, et al., 2007),

fuel-wood collection (Specht, et al., 2015) and shifting cultivation (Molinario, et al., 2015) spreading from urban settlements and road networks in Central Africa (LaPorte, et al., 2004) and South East Asia (Mukul & Herbohn, 2016). Anthropogenic forest fires are also commonly employed after initial clearing, in order to prepare land for shifting or commercial cultivation (Goldammer, 2015; Mukul & Herbohn, 2016), and can result in complete loss of forest or less severe damage that can be considered forest degradation.

There is high uncertainty in measuring and monitoring carbon emissions from forest degradation (Mertz, et al., 2012). A recent study found that the contribution of forest degradation has been largely underestimated and has reported that, in the period 2005-2010, 2.1 billion tons of CO_2 were emitted from forest degradation practices alone (consisting of selective timber harvest, woodfuel harvest and fire) which represents about 25% of the total emissions from deforestation and forest degradation, but there is high uncertainty on this estimate (Pearson, et al., 2017). In several, possibly many, countries forest degradation emissions even exceeded emissions from deforestation (Pearson, et al., 2017).

Estimates related to the extent, rates and the associated carbon emissions from forest degradation are currently challenging to provide given the multitude of definitions, indicators reported in the literature (e.g. reduction in carbon stocks, provision of goods and services, canopy cover and forest structure alterations), drivers (e.g. selective logging or forest fires for instance) (Simula, 2009; Ghazoul, et al., 2015), and limited capability to estimate any of these using optical remote sensing (due to lack of sensitivity to forest three-dimensional structure) (Lucas, et al., 2014) which means that there are no updated statistics related to the area affected by forest degradation derived from remote sensing, and only recent research has provided estimates of the contribution of forest degradation to GHG emissions between 2005-2010 in 74 developing countries in the tropics and sub-tropics based on available field measurements, remote sensing products and various models (Pearson, et al., 2017). These findings have further highlighted the significant contribution of emissions due to forest degradation which, in some cases (28/74 countries), have even exceeded

emissions from deforestation. Furthermore, post-disturbance forest re-growth extent and the associated rates of carbon uptake are even more problematic to measure (Mitchard & Flintrop, 2013) thus, there are still significant challenges to overcome.

Estimates from the World Resources Institute (WRI) suggest that 781 million ha of tropical forest have been degraded (30% of the total current tropical forest area), while 24% are still intact and 46% are considered fragmented (Mercer, 2015) (these are only approximations to give an idea of the scale of degradation in the tropics). Since then, widespread and dynamic forest degradation has taken place for instance from the 2015/2016 El Niño droughts in the Amazon (Jiménez-Muñoz, et al., 2016), forest fires in South-East Asia (Chisholm, et al., 2016) or through continued and pervasive selective logging in Central Africa (Potapov, et al., 2017) so the extent of degraded forests will have increased significantly.

The most up to date estimates on 'intact forest' are provided by the Intact Forest Landscape (IFL), these include true 'primary forest' as well as ecosystems which have no sign of human activity (based on remote sensing observations) (Potapov, et al., 2017). The total area covered by Intact Forest Landscape (IFL) stands at 1.19 billion ha (approximately 20.6% of the total forest zone area considering a tree canopy cover threshold equal to 25%, Figure 2) (Potapov, et al., 2017), and evidence suggests a reduction of IFL between 2000-2013 (Potapov, et al., 2017). This is exemplified by the 2013 IFL area estimates in Africa which covered 99 million and 62 million ha in South East Asia, a 10.1% and 13.9% reduction compared to 2000 estimates respectively (Potapov, et al., 2017).

The IFL decline has been driven by wildfire, timber harvesting, agriculture and pasture expansion and mining. Timber harvesting being the main cause of IFL reduction in Africa (7.75 million ha) and in South East Asia (7.56 million ha) (Potapov, et al., 2017). The intense pressure that has led to the reduction in primary forest as the decline reported for IFL (and the associated impacts on forest structure, AGB, carbon stocks and biodiversity) provide a key motivation for testing novel methods to improve forest disturbance monitoring especially in the tropics with particular attention directed towards degraded forest.

All this uncertainty means that numbers related to the total flux exchanged to and from the atmosphere is still considerable, such that we do not know if tropical forests are overall a net source or sink. A better understanding is a priority. This is especially true to enable better prediction of whether the current carbon sink in undisturbed and secondary forests could reverse to a significant source under climate change (Cox, et al., 2004). Recent evidence based on ground-based monitoring of mature Amazon forests suggests that these have acted as a very significant carbon sink thus mitigating climate change (Phillips & Brienen, 2017), and it has been reported that the carbon sink in African tropical forests is similar in magnitude to the emissions from deforestation in tropical Africa (0.1-0.3 Pg C/year over 1980-2000) (Lewis, et al., 2009).

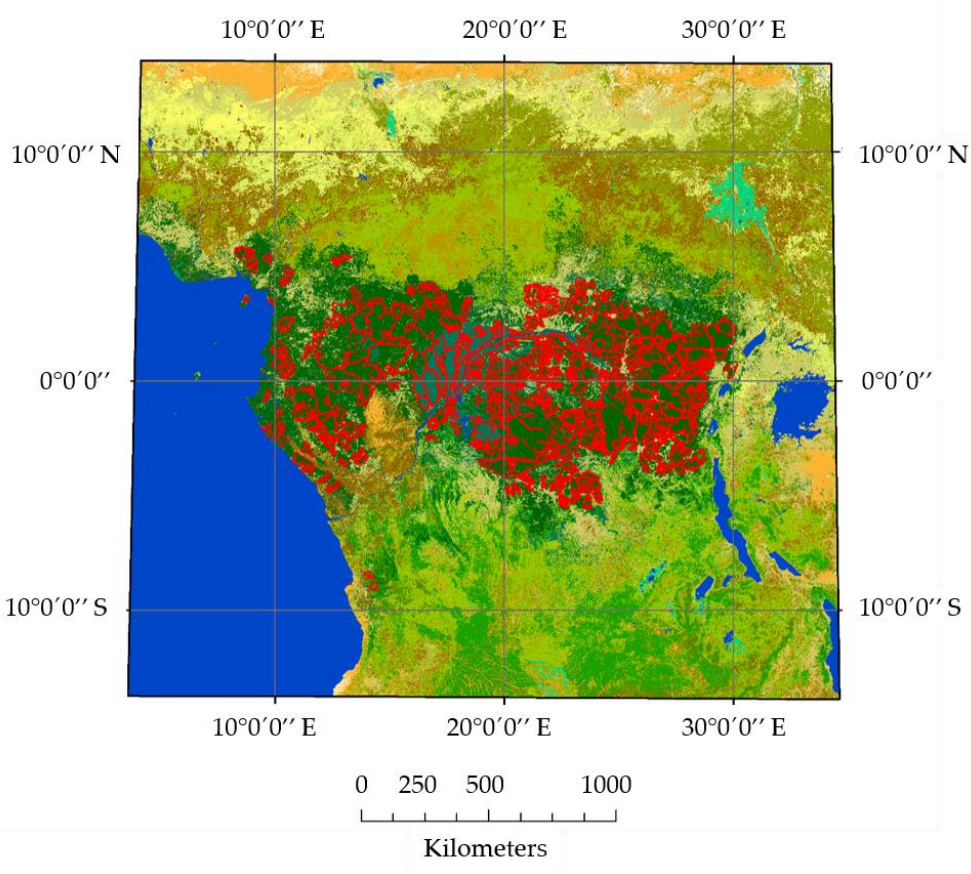

(**a**)

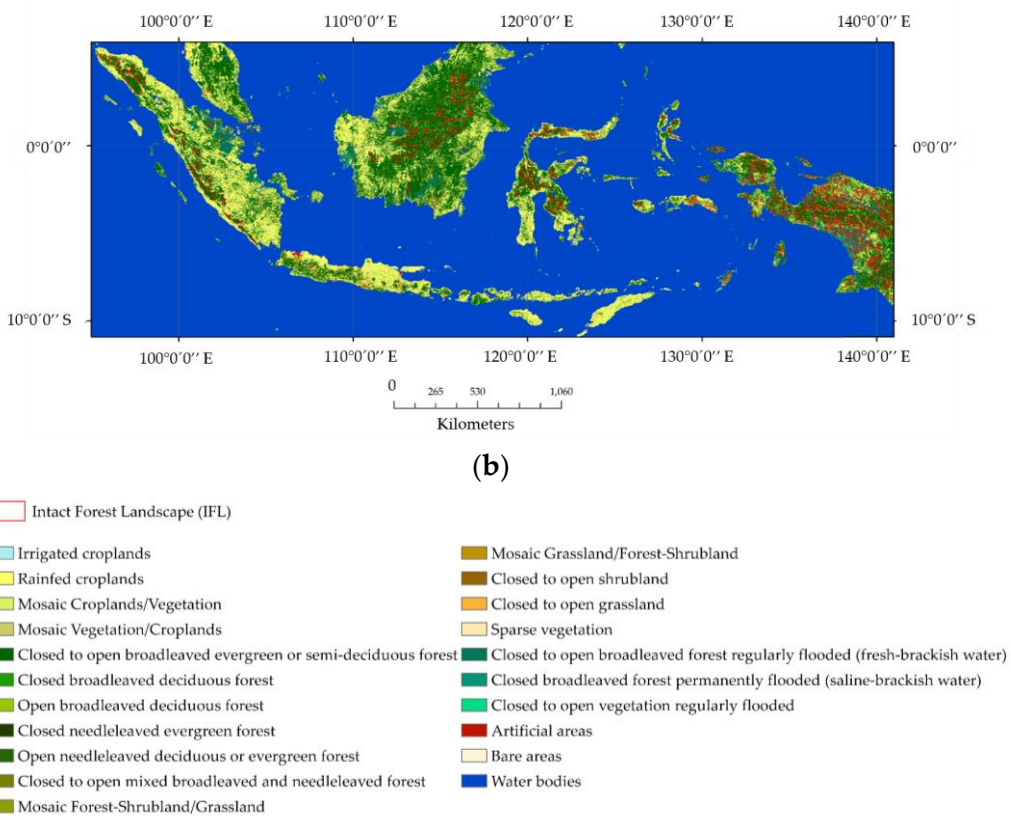

Figure 2. (**a**) Central Africa and (**b**) South-East Asia Global Land Cover Map (GlobCover 2009) (Bontemps, et al., 2011) illustrating the main landcover types and the Intact Forest Landscape 2013 (IFL) dataset (red outline) (Potapov, et al., 2017). The figure illustrates areas of remaining IFL in 2013 located around the tropics in Africa (99 million ha) and in South East Asia (62 million ha) (Potapov, et al., 2017). Note that IFLs are not the same as 'primary forest' but these are included in the IFL dataset. IFLs are defined as: 'a seamless mosaic of forests and associated natural treeless ecosystems that exhibit no remotely detected signs of human activity or habitat fragmentation and are large enough to maintain all native biological diversity, including viable populations of wide-ranging species') (Potapov, et al., 2017).

1.2.3. REDD+

REDD+ (a term which stands for 'reducing emissions from deforestation and forest degradation and the role of conservation, sustainable management of forests

and enhancement of forest carbon stocks in developing countries') (UNFCCC, 2008) is a climate mitigation strategy that aims to reduce or reverse deforestation and forest degradation in order to provide about 20% of the reduction in GHG (van der Werf, et al., 2009) needed to keep warming well below 2 °C in the coming century in accordance with the Paris Agreement (UNFCCC, 2015; Rogelj, et al., 2016).

Estimates of forest area change (loss and gain) and the change in carbon stocks are the two fundamental variables (Penman, et al., 2003; Gibbs, et al., 2007; Herold, et al., 2011) required to fulfil international initiatives aimed at curbing GHG emissions advocated by REDD+. The mechanism is centred around payments towards developing countries for their effort towards the conservation of forest and the reduction of forest related emission (Tegegne, et al., 2016), in response to meeting audited targets through Monitoring, Reporting and Verification (MRV) systems. Such MRV systems will be based on the IPCC Good Practice Guidelines (GPG) (Herold & Skutsch, 2011; Penman, et al., 2003), where satellite remote sensing is going to provide the consistent approach needed for national estimates.

The capacity of countries to perform such MRV varies markedly between countries, with African countries in general having particularly low capacity (Romijn, et al., 2012). Bilateral deals, such as that between Norway and Indonesia involving the transfer of $1 billion to Indonesia in return for implementing a deforestation moratorium in some landcover classes, have by contrast seemed to lead to increased MRV capacity (Government of Norway, 2010), if questionable overall success in reducing the rate of deforestation.

Overall, it is very clear that the technological development to map and quantify degradation for MRV systems is far behind that for deforestation (Global Forest Observations Initiative, 2016). The next section will cover the main problems, current developments, and potential solutions for using satellite methods to map forest degradation, and this thesis will explore and test new methods that could be used in the future.

1.3. Monitoring Forest Degradation in the Tropics Using Remote Sensing: Overview and Challenges

Forest degradation drivers, scale, magnitude and frequency partly determines the ability to which remote sensing can detect these processes. Forest degradation is determined by a multitude of drivers which can be either restricted to a limited area (e.g. selective logging of trees) or have widespread impacts (e.g. forest fires) (Global Forest Observations Initiative, 2016). In turn, different processes are characterised by different frequency (e.g. selective logging is a planned one-time event, while forest fires can affect a large area, and recur through time). It is therefore, difficult to agree on a standard procedure to map the multitude of facets of forest degradation and its effects on forest properties, even if consistent definitions are agreed (Ghazoul, et al., 2015).

Direct and indirect approaches are employed to detect forest degradation using remote sensing observations (Herold, et al., 2011). Direct methods involve the detection of canopy gaps (Deutscher, et al., 2013; Verhegghen, et al., 2015), canopy cover changes (Wang, et al., 2005), small clearings (e.g. Asner et al., 2005; Souza et al., 2005), and forest structure changes (Hirschmugl, et al., 2014). In contrast, indirect methods are aimed at extracting proxy indicators that cause collateral damage (e.g. logging roads, skid trails, log landings and other infrastructural damage) (Matricardi, et al., 2007). These are only clearly detectable in the case of planned logging and are less visible in the case of illegal logging practices (Franke, et al., 2012).

The majority of research has so far has been focused on the detection of proxy damage indicators of forest degradation (i.e. the most evident damage such as new logging roads), as directly mapping the process from an intact forest to a degraded forest condition has been more challenging since most of the drivers are restricted spatially and temporally affecting only a limited number of trees (e.g. removal of tree components such as branches for fuelwood, selective logging, and fire affecting the understory) with almost imperceptible effects on canopy cover and consequently on spectral reflectance from optical remote sensing (DeFries, et al., 2007). It is hard to

improve on current methods using optical remote sensing, as the data is severely limited due to cloud cover and the inability to penetrate into the forest canopy to detect the three-dimensional distribution of vegetation material (Lucas, et al., 2014).

In order to test novel methods using radar data, two significant forest degradation hotspots with different drivers of forest degradation are considered in the thesis: 1) Congo Basin (section 1.3.1) and 2) South East Asia (section 1.3.2), with the drivers described in turn below. A review of forest degradation drivers and their importance in selected tropical countries was collated by Hosonuma et al. (2012) and the contribution to carbon emissions is reported for selected drivers (selective timber harvest, woodfuel harvest and fire) in 74 tropical and sub-tropical countries in Pearson et al. (2017).

The following section gives an overview of selected forest degradation drivers, demonstrating their variety and different challenges related to their detection using remote sensing. Further details related to the challenges in detecting these processes using remote sensing are reported in **Chapter 3**, **4** and **5**.

1.3.1. Congo Basin Forests: Overview

The tropical forest of Central Africa are the second largest contiguous block of tropical forests in the world after the Amazon (Fayolle, et al., 2014) covering approximately 170 million ha (Mayaux, et al., 1999). Rich biodiversity is characteristic of the Guineo-Congolian rainforest with an estimated 8000 plant species (more than 80% being endemic) (White, 1983). Forest type is significantly influenced by rainfall (Fayolle, et al., 2014), geological substrates (Fayolle, et al., 2012), temperature, topography and fire regime (Bond, et al., 2005).

As well as highly diverse, the tropical forests of Central Africa have extremely high above-ground-biomass (AGB) and act as a significant carbon sink and source through deforestation and forest degradation (Grace, et al., 2014). Mean AGB in Africa is estimated to be much higher than Amazonian forests, with particularly high AGB values (429 Mg/ha) found in the Congo Basin intact forest (similar to Bornean forest) (Lewis, et al., 2013).

However, in general the Congo Basin forests are to some degree degraded, and average carbon stocks in the Congo Basin is 188 Mg/ha, lower than the Amazon Basin (220.5 Mg/ha), but higher than South East Asia (157.8 Mg/ha) (2010 estimates) (FAO, 2011). However, in turn, these estimates are affected by large uncertainties and it remains challenging to map and quantify these accurately and consistently (Mitchard, et al., 2014) as indicated by the marked divergence in AGB values from the available pan-tropical maps (Mitchard, et al., 2013). Further evidence of the uncertainty in the location and extent of AGB and carbon storage is provided by a recent discovery and mapping of the largest tropical peatland complex in the Congo Basin which stores up to 30.6 Pg/C belowground (Dargie, et al., 2017), similar in magnitude to the aboveground carbon storage of the whole Congo Basin forests, but covering only about 2% of their area.

Population density in Central Africa Congo Basin is generally low (24 inhabitants/ km^2) (FAO, 2011), with non-city dwellers concentrated in small rural communities and settlements which drive deforestation and forest degradation by wood-fuel, charcoal extraction and small scale slash-burn agriculture (Joiris, 1997). Future population increase is projected for all the countries of the Congo Basin (e.g. 3% annual increase in population forecasted for the Democratic Republic of Congo between 2015-2025) (World Bank, 2017) will greatly augment pressure on forest to accommodate the demand for forest resources at the local scale (e.g. agricultural products).

Current estimates report that among the countries located in the Congo Basin, the Democratic Republic of Congo (DRC) ranks as the 5^{th} country in the world in terms of forest cover loss and has undergone the highest forest cover loss among the Congo Basin countries between 2001-2014 (7.98 Mha) followed by Cameroon (657.06 Kha) and the Central African Republic (CAR) (546.92 Kha) (Hansen, et al., 2013). However, the DRC has also been reported to have had highest forest cover gain among the Congo Basin countries (1.39 Mha) between 2001-2012 followed by the Republic of Congo (46.65 Kha) and the CAR (39.31 Kha) (Hansen, et al., 2013), probably representing recovery of previously cleared forest.

Securing biodiversity conservation through the creation of protected areas is a key priority (Convention on Biological Diversity, 2011; Doumenge, et al., 2015). Protected areas (PAs) cover approximately 45 million ha, this is less than the area granted for forest concessions, with the majority of PAs located in the Democratic Republic of Congo (51 out of a total of 143) (Marquant, et al., 2015). The remaining forest area located outside PAs that have not been allocated for industrial logging face extensive pressure (for instance due demand for woodfuel and charcoal by local population) and are not likely to remain intact in the next decade (Fayolle, et al., 2014). Encroachment into PAs has been long observed with consequences on biomass loss (e.g. for instance between 2000-2012 biomass loss was equivalent to approximately 19,500 Mg/C year in the Odzala Kokoua National Park, Republic of Congo) (Collins & Mitchard, 2017).

1.3.1.1. Forest Degradation in the Congo Basin

The main forest degradation drivers which will be covered in the following section are: a) commercial selective logging; b) shifting cultivation; c) fuel-wood and charcoal extraction and d) forest fires.

a) Commercial Selective logging

Large scale commercial logging has been taking place in Central Africa since the end of WWII (Nasi, et al., 2012) with private logging companies being granted logging concession covering extensive areas (Marquant, et al., 2015). In the Congo Basin, a total of 403 forest concessions have been allocated covering over 49 million ha (Marquant, et al., 2015) as a result of the increasing demand for timber export for to national and international markets (Malhi, et al., 2014). A total area of over 8.8 million ha are certified concessions under either the Forest Stewardship Council (FSC) certification, the Origin and Legality of the Woods (OLB), Verification of Legal Compliance (VLC) or Controlled Wood certification (the majority situated in Cameroon followed by the Republic of Congo) (OSFAC, 2016).

Selective logging in the Congo Basin is primarily characterised by the removal of a limited number of commercially valuable tree species (e.g. *Entandrophragma* spp.)

per hectare (e.g. 1-2 trees harvested/ha) with high AGB (Medjibe, et al., 2011). Whilst, in the Amazon this process has been observed to lead to deforestation (Asner, et al., 2006), in the Congo Basin this is not the case (Mayaux, et al., 2013).

Selective logging has significant negative impacts on ecosystem composition, biodiversity (Malcolm & Ray, 2000; Wilkie, et al., 2000) and AGB with the potential of these values to recover to a certain extent at different timescales (e.g. for instance, AGB recovery to similar pre-disturbance conditions occurred after an average of 24 years, but biodiversity may take far longer to recover) (Gourlet-Fleury, et al., 2013).

Reduced Impact Logging (RIL), a more sustainable form of logging to avoid long term forest damage (Durrieu de Madron, et al., 1998) is only sparsely employed in logging concessions (Putz, et al., 2008). RIL implementations have shown to substantially reduce impact on trees in certain cases (Bertault & Sist, 1997; Martin, et al., 2015). In certified logging concession, management plans involve a choice of RIL techniques. The most frequently employed technique is the planning of logging tracks (used in 79% of the 30 concessions considered in one study) (de Blas & Pérez, 2008).

As well as the selective extraction of trees causing canopy openings, other impacts are more severe and long-lasting: for instance, logging roads are considered the most visible form of damage (Gullison & Hardner, 1993), skid trails and log-loading areas persist longer in time compared to canopy openings (Kleinschroth, et al., 2015).

From an optical remote sensing perspective, inactive logging roads are the most evident and persistent form of damage observed (Kleinschroth, et al., 2015) and thus more easily mapped. In some cases, it can take up to 20 years for old re-vegetating logging roads to disappear completely (Kleinschroth, et al., 2015). Instead, canopy damage is usually only detectable from optical sensors for 1-2 years at most (Souza, et al., 2005), as in most cases rapid recovery of canopy gaps has been observed based on optical data to occur within 50 days after disturbance (Verhegghen, et al., 2015). Hence, the majority of research has been focused on the Amazon (characterised by higher intensity logging practices) to detect indirect damage (Matricardi, et al., 2007) and there are currently no comparable studies focusing on the Congo Basin but

research is advancing towards the detection of canopy gaps resulting from selective logging activities using medium to high resolution optical remote sensing (e.g. SPOT4 and Sentinel-2) by adopting spectral unmixing methods developed by INPE (e.g. Shimabukuro et al., 1998) and widely tested in the Amazon (Verhegghen, et al., 2015).

The PhD provides the first step in addressing the detection of selective logging using InSAR derived DSMs (**Chapter 5**).

b) Shifting cultivation

Shifting agriculture is a well-established traditional practice (Ickowitz, 2006) employed by rural communities (Joiris, 1997) for providing food security for millions of people. This is generally undertaken at small scale with clearing that are globally on average ~1 ha (Aweto, 2012) (but clearing size can be as low as 0.25 ha in some areas of the Congo Basin) (Wilkie, et al., 1998) resulting in a so-called rural-complex (10–30% tree cover and more than 50% croplands as defined by Mayaux et al., 2013) which is a patch-work of degraded forest, forest at various successional stages interspersed with agricultural fields developing along the main roads and settlements (LaPorte, et al., 2004; Nasi, et al., 2012; Molinario, et al., 2015). Overall shifting cultivation is estimated to be the third largest land use in the Congo Basin (43.88 million ha) after industrial logging (59.5 million ha) and protected areas (44.5 million ha) (Nasi, et al., 2009).

Shifting cultivation consists of a long term cycle starting from clear felling (partial or complete) of forest for agriculture with fields that are commonly re-used multiple times for a few years (1-3 years) (Zhang, et al., 2002) followed by a phase in which recovery of soil properties occurs (fallow phase) (Ewel, 1986).

The first phase in the shifting cultivation cycle involves the removal of selected trees (degradation) while, a portion is not felled and some are left to decay (Kleinman, et al., 1995; Molinario, et al., 2015). After weeks (or months) the remaining vegetation is burned and therefore, there is a substantial time where the remaining forest exists in a degraded state that will be eventually cleared completely for cultivation. After the fields are cultivated for several years (e.g. up to 15 years) (Wilkie & Finn, 1988),

the fields are left to recover until they achieve suitable properties for re-cultivation based on a number of indicators (e.g. fallow age, vegetation composition, soil fertility, soil structure/hardness and texture) that indicate if the field is ready to be re-used (Norgrove & Hauser, 2016).

Prevalently, fallow forests that are 10-15 years old are cleared as this is easier than clearing primary forest, however, in their absence, primary forest is used (Wilkie, et al., 1998). Fallows will generally not revert to the exact original conditions (e.g. in terms of biomass, forest structure and biodiversity for instance) but in some cases recovery of most botanical conservation parameters considered can be achieved after 50-60 years, though the proportion of endemic species may remain depressed (Van Gemerden, et al., 2003). It was observed that forest structure is slower to recover after shifting cultivation (30-60 years) than after selective logging, elucidating the different recovery mechanisms between the two drivers (Van Gemerden, et al., 2003).

One of the issues associated with shifting agriculture is the long term conversion to fallow fields which are re-used and thus, unable to recover back to similar original conditions leaving these as impoverished in the long term as soil and nutrient properties deteriorate over time (Molinario, et al., 2015), especially as rising population will lead to an increased demand for food which will require an intensification agricultural practices. On the other hand, fallow fields that are re-used for several years can take the pressure off primary forests which would otherwise be cleared (Molinario, et al., 2015).

It is challenging to distinguish and classify each successional stage within the rural-complex using remote sensing. Notably, patches that are at an advanced stage of regeneration cannot be discriminated using optical sensors as these lack the capability to penetrate into the canopy and detect vertical structure (e.g. vegetation height differences). Studies using remote sensing have commonly been able to map the rural-complex (Mayaux, et al., 2000; Verhegghen, et al., 2012) rather than the proportion occupied by each successional stage, which would require a long and dense time-series to track the process since disturbance first occurred (Akkermans, et al., 2013).

InSAR may be suitable for the detection of changes in vegetation height based on time-series of three-dimensional information but this is relatively novel and will be explored in the PhD (**Chapter 5**).

c) Woodfuel and Charcoal

In the Congo Basin most of the total volume of wood harvested from peri-urban forests is used as woodfuel and charcoal which has increased (e.g. demand for charcoal has increased by 20% between 1990-2009 and the future demand is set to increase as population increases) (Megevand, et al., 2013). Per capita consumption of firewood and charcoal is higher in Central Africa (0.99 m^3/inhabitants) compared to other parts of Africa (e.g. lowest in North Africa with 0.25 m^3/inhabitants) (Marien, 2009).

In drier forest ecosystems (e.g. African savannas and woodlands) where the productivity is lower, removal of wood for fuel as local use is a commonplace driver of forest degradation (DeFries, et al., 2007). Often, this process involves selective harvesting of trees with a reduction in woody biomass (forest degradation) to complete clearing (deforestation) (Chidumayo & Gumbo, 2013).

Woodfuel collection causes almost imperceptible damage to the forest canopy, it is extremely spatially restricted, involves changes below canopy, it is not associated with any form of more evident damage such as is the case with commercial selective logging (e.g. logging roads and log landings) and therefore is challenging to capture even using sub-meter resolution optical remote sensing.

The process was not considered in the thesis as it is the most challenging driver to detect supposedly requiring very high resolution (< 1 m) and time-series of radar data to be tested complemented by ground-data (in-situ carbon stock inventories) which were not available for our study sites and given that this process is more widespread in dry tropical forests and woodlands (e.g. in Mozambique) (Ryan, et al., 2012; Ryan, et al., 2014) and is usually studied using biophysical data collected through ground surveys (Woollen, et al., 2016).

d) Fire

Forest fires in Central African moist tropical forests rarely occur due to the wet conditions (Cochrane, 2009) while, they are commonly ignited by humans in savannas to suppress woody cover (Bucini & Hanan, 2007). During El Niño years fire events are exacerbated by dry conditions, whilst these events are well documented in the Amazon (Nepstad, et al., 1999) and in South-East Asia (Siegert, et al., 2001), the impact of fire during El Niño in Central African moist tropical forests is lacking (Verhegghen, et al., 2016) since the impact of these events have only recently (2015-2016) been observed and recorded from remote sensing observations (Verhegghen, et al., 2016).

Synergy between radar and optical (Sentinel-1 and 2) has enabled the mapping of the extent of fire damage, but this required acquisitions before and after the event occurred which will be increasingly possible thanks to the Sentinel missions higher revisit time (European Space Agency, 2013).

Lessons can be drawn from South East Asia where previously logged areas were the most vulnerable to fire disturbance during the 1997/1998 El Niño (Siegert, et al., 2001) and this could potentially pose fatal consequences in the Congo Basin given the vast proportion of forest allocated to logging concessions and the recent finding that much of the central Congo overlies peat (Dargie, et al., 2017).

1.3.2. South-East Asia Forests Overview

South-East Asia tree cover is approximately 210 Mha (maritime SE Asia tree cover considering forest using a 30% threshold) (Hansen, et al., 2013) and is characterised by high AGB (Slik, et al., 2009) but also by a significant rate of annual forest change (0.41%) (2000-2010) (FAO, 2011). Almost half of the total forest area is allocated for the production of wood and non-wood products (111 Mha) (FAO, 2011). A major concern is habitat loss in valuable conservation areas with high species richness and endemism (Sodhi, et al., 2004).

South East Asian peatlands (approximately 56% of all tropical peatland) are also of fundamental importance as they store a huge amount of carbon (68.5 Pg C, 11–14%

of global peat carbon) (Page, et al., 2011) and have been undergoing intensive pressure from deforestation driven by the conversion to industrial oil palm and paper pulp plantations (Stibig, et al., 2014) and degradation practices from peatland draining and fires (Hoekman, 2016) which have contributed to GHG emissions (Siegert, et al., 2001). Whilst there are still considerable uncertainties and limited knowledge on the area, carbon stored and emissions from peatland degradation located in South East Asia are comparatively well studied, compared to African and South American peatlands, but mostly because of the high rate of exposure and destruction they have experienced in the past decades (Lawson, et al., 2015).

Indonesia is a particularly critical country storing the highest amount of tropical peat carbon (57.4 Gt) (Page, et al., 2011) and one of the most affected countries during the recent El Niño fires. Most recent and severe El Niño events occurred 1997/1998 when emissions from peat fires reached 0.95 Pg C in Indonesia alone (Page, et al., 2002) and more recently during the 2015 which resulted in the highest CO_2 emissions since the 1997 El Niño event (11.3 Tg CO_2/day) (Huijnen, et al., 2016) and a total of approximately 1.1 Pg CO_2 (July-November 2015) (Heymann, et al., 2017).

As well as extensive areas of peatland, until the 1960s, South East Asia was dominated by high AGB intact primary lowland *Dipterocarpaceae* forests but the majority of these former old-growth forests are now considered disturbed (Mietten, et al., 2014). The average AGB in South East Asia is substantially higher (approximately 60% higher) than forest in Amazonia because of the dominance by large individuals of the dominant *Dipterocarpaceae* genus (Slik, et al., 2009).

Within South East Asia, Indonesia is the country with the highest reported forest cover loss (18.51 Mha) (2001-2014) (Hansen, et al., 2013) primarily due to logging and for the conversion of forest for large scale oil palm and paper pulp plantations (Abood, et al., 2015). The area of forest with a management plan is 90.1 Mha (95% of the forest area) of which 54.7% is allocated to production (2010 estimates) and the area with Forest Stewardship Council Certificate (FSC) is approximately 1.9 Mha (2014 estimates) (FAO, 2015).

As well as industrial scale disturbance, smallholder farmers play a role in degrading forest areas by practicing shifting agriculture in rural areas, but it is argued that government policies are shifting towards the intensification of agricultural practices (Ahrends, et al., 2015).

Efforts to protect areas from anthropogenic disturbance include the creation of PAs, which cover 22.62 million ha (~11.9% of the total land area) (UNEP-WCMC, 2016). Assigning the status of PAs does not necessarily ensure that these areas remain undisturbed (Collins & Mitchard, 2017) as the expansion of illegal logging within PAs is commonplace (Curran, et al., 2004).

1.3.2.1. Forest Degradation in South-East Asia

The forest degradation drivers prevalent in South East Asia considered here are: a) commercial logging; b) fire and c) shifting cultivation. These often occur in combination and some processes lead to deforestation (commercial logging and in some cases forest fires).

a) Commercial Logging

The scale at which commercial logging occurs is different compared to the Congo Basin. Logging intensity is much higher in South East Asia where approximately 10-20 tree/ha are harvested compared to 1-2 trees/ha in the Congo Basin (Malhi, et al., 2013). This process often causes near-complete deforestation as opposed to forest degradation. Forests are rarely left to recover after logging, but then converted into other land use: estimates indicate that extensive areas of forest were converted into oil palm plantations (2.1 Mha) and paper pulp plantation (*Acacia*, 0.85 Mha) in 2010 alone, following previous logging (Mietten, et al., 2012).

Within South East Asia, Indonesia is a critical country given that approximately 33% of the total area of its territory is allocated to industrial concessions (57 Mha in total) subdivided into logging sector (24 Mha), followed by palm oil (12 Mha), fiber (10 Mha), mixed concession (5.8 Mha) and mining (4 Mha) (Abood, et al., 2015).

Given the above-mentioned considerations, commercial logging in South-East Asia is not considered in the thesis, as this is primarily a driver of deforestation,

contrary to the degradation driver that is selective logging in the Congo Basin. Much research using remote sensing has been directed towards mapping large scale commercial logging and the expansion of palm oil and paper pulp plantations in South-East Asia (Koh, et al., 2011; Gaveau, et al., 2014; Cheng, et al., 2016).

b) Fire

Naturally occurring fires in humid tropical forests are rare thanks to the prevalently moist conditions and the availability of low-fuel loads which reduce the probability of fire spreading to neighbouring areas; indeed, most species are intolerant to fire, suggesting it has not been regularly present for millions of years (Cochrane, 2003). Instead, anthropogenic fire used in slash-burn practices is commonly used to clear fields before conversion into agriculture as this is the easiest and most efficient method to clear land (Goldammer, 2015). Fires that result in the conversion of forest into a different land cover type (e.g. grassland) lead to deforestation while, fires which only reduce canopy cover without complete clearance are considered drivers of forest degradation.

Forest fires affect structure and species composition (Gerwin, 2002) and areas that are repeatedly disturbed can ultimately be converted into impoverished grassland (e.g. *Imperata* sp.) (Goldammer, 2015).

Forest fires are often exacerbated by dry conditions during El Niño Southern Oscillation (ENSO) years and often expand uncontrollably due to increased forest flammability (Goldammer, 2015) to neighbouring areas (e.g. Frederiksson, et al., 2006). Moreover, fires can be exacerbated by previous anthropogenic disturbance (e.g. selective logging) (Siegert, et al., 2001; Gerwin, 2002; Cochrane, 2003) and draining of peatlands (Hooijer, et al., 2010).

It is evident how forest degradation drivers are often interlinked and occur in combination with one another (Mietten, et al., 2014). Especially concerning, is the increase in frequency and magnitude of climatic anomalies such as ENSO which will increasingly threaten both lowland and peatland forest (Cai, et al., 2014).

It was estimated that the 1997/1998 fires burned a total of over 5 million ha of land (Siegert, et al., 2001). Release of CO_2 in the atmosphere is of great concern in particular after the greatest ENSO fires since the 1997/1998 event which took place in 2015-2016 (Huijnen, et al., 2016). It was estimated that during September and October 2015 the mean emission rate was 11.3 Tg CO_2 per day (Huijnen, et al., 2016) (higher than the emission rate of the European Union countries: 8.9 Tg CO_2 per day) (Huijnen, et al., 2016).

The impact of fire leading to complete forest loss is comparatively easier to detect using remote sensing than detecting partial damage (forest degradation) and the subsequent recovery. This is especially true if the fire is a sub-canopy fire. Several researchers have mapped large scale forest damaged area from remote sensing (Siegert, et al., 2001; Mietten & Liew, 2009). However, partial forest structure changes and subsequent forest recovery remains challenging to detect. The PhD has contributed to address this challenge using InSAR data in **Chapter 4**.

c) Shifting cultivation

The cycle of shifting cultivation in South East Asia is similar to practices employed in the Congo Basin. This is practiced by broadly 14-34 million people (Mertz, et al., 2009) and has relatively lower impact compared to other more intensive types of land use (e.g. industrial scale monoculture) (Dressler, et al., 2015) and potential for vegetation recovery during the fallow phase.

With time, its impact has however, become more damaging as the size of forest cleared has been increasing and the fallow periods have been reduced (Goldammer, 2015) leading to environmental degradation (e.g. deterioration of soil fertility) (Bruun Beech, et al., 2009).

Traditional shifting cultivation has been undergoing changes in terms of crops that are cultivated (Li, et al., 2014) and in terms of extent and intensity (van Vliet, et al., 2013). It has been observed that to some extent there has been a decline of shifting agriculture in mainland South-East Asia, with replacement by permanent, more intensive agriculture (Padoch, et al., 2007). However, the demise of shifting

cultivation is not agreed unequivocally and a study concludes that it will still persist for some time in the 21st century (van Vliet, et al., 2013).

As with shifting agriculture in the Congo Basin this can be mapped from optical remote sensing broadly as "rural-complex", or has been mapped using low to medium resolution time-series tracking spatio-temporal dynamics which would otherwise not be possible to detect with a single image (Hurni, et al., 2013). SAR has not been used for this purpose (Li, et al., 2014) since the rural-complex is composed of vegetation at various stages as well as cropland and it is not a "radiometrically homogeneous class" because it includes variable backscatter values, these depending on different scattering mechanisms. Therefore, the class cannot be mapped based on a unique backscatter value.

1.4. Aims and Objectives

The thesis has a core of three chapters reporting results of experiments that explore how to detect several forest degradation processes using different approaches.

The overall thesis aim is to establish the relative capabilities and limits of SAR and InSAR spatial statistics and change detection to generate indicators of forest disturbance.

The main objective is partitioned for each chapter according to different thematic contexts: study site, disturbance driver, SAR observations (backscatter and interferometric phase) and methodology. These objectives are not disjoined, but threaded together by a common approach consisting of looking for textural patterns and their changes in radar observations, then connecting the patterns to forest condition through supporting evidence from expert knowledge and auxiliary remote sensing observations (e.g. high resolution optical or LiDAR). It is to be noted that these patterns are descriptors of the forest structural characteristics and their changes in a statistical sense, but are not direct estimates of physical properties, such as AGB or canopy height.

Chapter 3: Assesses the capability of retrieving information about landcover discrimination, in particular intact and degraded forest in a closed semi-deciduous forest in Cameroon by analysis based on the spatial statistic of SAR backscatter provided by wavelet frames. The chapter compares the relative capabilities of two spaceborne missions at different wavelengths (C-band ENVISAT ASAR and L-Band ALOS PALSAR).

Chapter 4: Investigates statistical measures of three-dimensional information in TanDEM-X InSAR and LiDAR Digital Elevation Models (DEMs), testing their capability of detecting differences in vegetation heterogeneity through a disturbance gradient in Indonesia.

Chapter 5: Exploits differences of InSAR Digital Surface Models acquired at two dates to detect independently from topography forest volume loss and gain that can be linked to deforestation/forest degradation and post-disturbance re-growth.

1.5. Thesis Highlights and Novel Aspects

The work presented in this thesis rests on the unifying principle that a connection can be established between the forest structure distribution in space and signal variation (spatial statistics) within backscatter and Digital Surface Models (DSMs) provided by SAR. In turn, forest structure spatial characteristics and changes are considered as mapping of forest state or disturbance. The main novel aspect consists therefore of looking at patterns (and changes thereof) within the SAR signal, these being considered as measures of forest structure, as opposed of considering absolute reflectivity or phase coherence values, these being considered as measures of some physical property of the natural target.

Instrumental to the implementation of this line of research is the use of advanced statistical signal processing techniques (wavelet frames) and the most advanced observational instruments (e.g. single-pass interferometry). These assets are called into play to address challenges identified by the international community (e.g.

REDD+) to detect degraded forests, the process of forest degradation and post-disturbance re-growth in tropical forests.

Two main partitions can be defined along the overall methodological line are summarised below:

1. **Spatial statistics of SAR backscatter and InSAR Digital Surface Models:** Testing advanced statistical methods based on wavelet space-scale analysis to detect difference in forest structure as a consequence of forest degradation.

2. **InSAR Digital Surface Model Temporal change detection:** Exploiting differences between InSAR derived DSMs to detect a gradient of forest volume loss or gain.

1.6.References

- Abood, S. A. et al., 2015. Relative Contributions of the Logging, Fiber, Oil Palm, and Mining Industries to Forest Loss in Indonesia. *Conservation Letters,* 8(1), pp. 58-67.
- Ahrends, A. et al., 2015. Current trends of rubber plantation expansion may threaten biodiversity and livelihoods. *Global Environmental Change,* Volume 34, pp. 48-58.
- Akkermans, T. et al., 2013. Quantifying successional land cover after clearing of tropical rainforest along forest frontiers in the Congo Basin. *Physical Geography* , 34(6), pp. 417-440.
- Asner, G. P. et al., 2006. Condition and fate of logged forests in the Brazilian Amazon. *PNAS,* 103(34), pp. 12947-12950.
- Asner, G. P. et al., 2005. Selective Logging in the Brazilian Amazon. *Science,* 310(5747), pp. 480-482.
- Aweto, A., 2012. *Shifting cultivation and secondary succession in the tropics.* 1st ed. Ibadan, Nigeria: CABI.
- Baccini, A. et al., 2012. Estimated carbon dioxide emissions from tropical deforestation improved by carbon-density maps. *Nature Climate Change,* Volume 2, pp. 182-185.

- Barona, E., Ramankutty, N. H. G. & Coomes, O. T., 2010. The role of pasture and soybean in deforestation of the Brazilian Amazon. *Environmental Research Letters,* 5(2), pp. 1-9.
- Beer, C. et al., 2010. Terrestrial Gross Carbon Dioxide Uptake: Global Distribution and Covariation with Climate. *Science,* 329(5993), pp. 834-838.
- Bertault, J.-G. & Sist, P., 1997. An experimental comparison of different harvesting intensities with reduced-impact and conventional logging in East Kalimantan, Indonesia. *Forest Ecology and Management,* 94(1-3), pp. 209-218.
- Bond, W., KJ, Woodward, F. I. & Midgley, G. F., 2005. The global distribution of ecosystems in a world without fire. *New Phytologist,* 165(2), pp. 525-538.
- Bontemps, S. et al., 2011. *GlobCover.* [Online]. Available at: http://due.esrin.esa.int/page_globcover [Accessed 2 January 2017].
- Bruun Beech, T., de Neergaard, A., Lawrence, D. & Ziegler, A. D., 2009. Environmental Consequences of the Demise in Swidden Cultivation in Southeast Asia: Carbon Storage and Soil Quality. *Human Ecology,* 37(3), pp. 375-388.
- Bucini, G. & Hanan, N. P., 2007. A continental-scale analysis of tree cover. *Global Ecology and Biogeography,* 16(5), p. 593–605.
- Cai, W. B. S. et al., 2014. Increasing frequency of extreme El Niño events due to greenhouse warming. *Nature Climate Change,* Volume 4, pp. 111-116.
- Cernusak, L. A. et al., 2013. Tropical forest responses to increasing atmospheric CO2: current knowledge and opportunities for future research. *Functional Plant Biology,* 40(6), p. 531–551.
- Cheng, Y., Yu, L., Cracknell, A. P. & Gong, P., 2016. Oil palm mapping using Landsat and PALSAR: a case study in Malaysia. *International Journal of Remote Sensing,* 37(22), pp. 5431-5442.
- Chidumayo, E. N. & Gumbo, D. J., 2013. The environmental impacts of charcoal production in tropical ecosystems of the world: A synthesis. *Energy for Sustainable Development,* 17(2), pp. 86-94.
- Chisholm, R. A., Wijedasa, L. S. & Swinfield, T., 2016. The need for long-term remedies for Indonesia's forest fires. *Conservation Biology,* 30(1), pp. 5-6.
- Cochrane, M., 2003. Fire science for rainforests. *Nature,* Volume 421, pp. 913-919.
- Cochrane, M., 2009. *Tropical Fire Ecology: Climate Change, Land Use and Ecosystem Dynamics.* 1st ed. Berlin/Heidelberg, Germany: Springer.

- Collins, M. B. & Mitchard, E. T. A., 2017. A small subset of protected areas are a highly significant source of carbon emissions. *Scienific Reports,* Volume 7, pp. 1-11.

- Convention on Biological Diversity, 2011. *Convention on Biological Diversity X/2: Strategic plan for biodiversity 2011–2020,* Nagoya, Japan: Convention on Biological Diversity.

- Cox, P. M. et al., 2004. Amazonian forest dieback under climate-carbon cycle projections for the 21st century. *Theoretical and Applied Climatology,* 78(1), pp. 137-156.

- Curran, L. M. et al., 2004. Lowland Forest Loss in Protected Areas of Indonesian Borneo. *Science,* 303(5660), pp. 1000-1003.

- Dargie, G. C. et al., 2017. Age, extent and carbon storage of the central Congo Basin peatland complex. *Nature,* Volume 542, pp. 86-90.

- de Blas, D. E. & Pérez, M. R., 2008. Prospects for Reduced Impact Logging in Central African logging concessions. *Forest Ecology and Management,* 256(7), pp. 1509-1516.

- De Grandi, E. C., Mitchard, E. & Hoekman, D., 2016. Wavelet Based Analysis of TanDEM-X and LiDAR DEMs across a Tropical Vegetation Heterogeneity Gradient Driven by Fire Disturbance in Indonesia. *Remote Sensing* , 8(641), pp. 1-27.

- De Grandi, E. C., Mitchard, E., Woodhouse, I. & De Grandi, G. D., 2015. Spatial Wavelet Statistics of SAR Backscatter for Characterizing Degraded Forest: A Case Study From Cameroon. *IEEE Journal of Selected Topics in Applied Earth Observations and Remote Sensing,* 8(7), pp. 3572-3584.

- DeFries, R. et al., 2007. Earth observations for estimating greenhouse gas emissions from deforestation in developing countries. *Environmnetal Science and Policy,* 10(4), pp. 385-394.

- Deutscher, J. P. R., Gutjahr, K. & Hirschmugl, M., 2013. Mapping Tropical Rainforest Canopy Disturbances in 3D by COSMO-SkyMed Spotlight InSAR-Stereo Data to Detect Areas of Forest Degradation. *Remote Sensing,* 5(2), pp. 648-663.

- Doumenge, C. et al., 2015. *Aires protégées d'Afrique centrale. État 2015,* Kinshasa, République Démocratique du Congo: OFAC.

- Dressler, W. et al., 2015. *Examining how long fallow swidden systems impact upon livelihood and ecosystem services outcomes compared with alternative land-uses in the uplands of Southeast Asia.* [Online]. Available at:

http://www.cifor.org/publications/pdf_files/WPapers/WP174Clendenning.pdf [Accessed 13 March 2017].

- Durrieu de Madron, L., Forni, E. & Mekok, M., 1998. *Les techniques d'exploitation à faible impact en forêt dense humide camerounaise,* Montpellier: CIRAD-Forêt.
- European Space Agency, 2013. *Sentinel-1 User Handbook,* s.l.: European Space Agency.
- Ewel, J. J., 1986. Designing Agricultural Ecosystmes for the humid tropics. *Annual Review of Ecology and Systematics,* 17(1), pp. 245-271.
- FAO, 2011. *State of the World's Forests 2011,* Rome, Italy: Food and Agriculture Organization of the United Nations.
- FAO, 2011. *The State of Forests in the Amazon Basin, Congo Basin and Southeast Asia,* Brazaville, Republic of Congo: Food and Agriculture Organization of the United Nations.
- FAO, 2015. *The Global Forest Resources Assessment (FRA) 2015. Terms and Definitions,* Rome, Italy: Food and Agriculture Organization of the United Nations.
- Fayolle, A. et al., 2012. Geological Substrates Shape Tree Species and Trait Distributions in African Moist Forests. *PLoS ONE,* 7(8), pp. 1-10.
- Fayolle, A. et al., 2014. A new insight in the structure, composition and functioning of central African moist forests. *Forest Ecology and Management,* 3(29), p. 195–205.
- Franke, J. et al., 2012. Monitoring fire and selective logging activities in tropical peat swamp forests. *IEEE Journal of Selected Topics in Applied Earth Observations and Remote Sensing,* 5(6), pp. 1811-1820.
- Frederiksson, G., Danielsen, L. & Swenson, J., 2006. Impacts of El Niño related drought and forest fires on sun bear fruit resources in lowland dipterocarp forest of East Borneo. *Biodiversity Conservation,* Volume 6, pp. 249-264.
- Garcia, E., Vianna Ramos Filho, F. S., Mallmann, G. M. & Fonseca, F., 2017. Costs, Benefits and Challenges of Sustainable Livestock Intensification in a Major Deforestation Frontier in the Brazilian Amazon. *Sustainability,* 9(158), pp. 1-17.
- Gaveau, D. L. et al., 2014. Four Decades of Forest Persistence, Clearance and and Logging on Borneo. *PLoS ONE,* 9(7), p. e101654.
- Gerwin, J., 2002. Degradation of forests through logging and fire in the easter Brazilian Amazon. *Forest Ecology and Management,* Volume 157, pp. 131-141.

- Ghazoul, J., Burivalova, Z., Garcia-Ulloa, J. & King, L. A., 2015. Conceptualizing Forest Degradation. *Trends in Ecology and Evolution,* 30(10), pp. 622-632.
- Gibbs, H. K., Sandra Brown, S., Niles, J. O. & Foley, J. 0., 2007. Monitoring and estimating tropical forest carbon stocks: making REDD a reality. *Environmental Research Letters,* 2(4), pp. 1-13.
- Global Forest Observations Initiative, 2016. *Integration of remote-sensing and ground-based observations for estimation of emissions and removals of greenhouse gases in forests: Methods and Guidance from the Global Forest Observations Initiative,* Rome: Food and Agriculture Organization of the United Nations.
- Goldammer, H. G., 2015. Fire Management in Tropical Forests. In: L. Pancel & M. Köhl, eds. *Tropical Forestry Handbook.* Berlin: Springer-Verlag, pp. 1-42.
- Gourlet-Fleury, S. et al., 2013. Tropical forest recovery from logging: a 24 year silvicultural experiment from Central Africa. *Philosophical Transactions of the Royal Society B,* 368(1625), p. 20120302.
- Government of Norway, 2010. *Norway and Indonesia in Partnership to Reduce Emissions from Deforestation.* [Online]. Available at: https://www.regjeringen.no/en/aktuelt/norway-and-indonesia-in-partnership-to-r/id605709/ [Accessed 5 March 2017].
- Grace, J., Mitchard, E. & Gloor, E., 2014. Perturbations in the carbon budget of the tropics. *Global Change Biology,* 20(10), p. 3238–3255.
- Grainger, A., 1993. *Controlling tropical deforestation.* 1st ed. London.: Earthscan Publications Ltd.
- Gullison, R. E. & Hardner, J. J., 1993. The effects of road design and harvest intensity on forest damage cause by selective logging: empirical results and a simulation model from the Bosque Chimanes, Bolivia. *Forest Ecology and Management,* 59(1-2), pp. 1-14.
- Hansen, M. et al., 2013. High-Resolution Global Maps of 21st Century Forest Cover Change. *Science,* 342(6160), pp. 850-853.
- Herold, M. et al., 2011. A review of methods to measure and monitor historical carbon emissions from forest degradation. *Unasylva,* 62(238), pp. 16-24.
- Herold, M. & Skutsch, M., 2011. Monitoring, reporting and verification for national REDD+ programmes: two proposals. *Environmental Research Letters,* 6(1), p. 014002.
- Heymann, J. et al., 2017. CO2 emission of Indonesian fires in 2015 estimated from satellite-derived atmospheric CO2 concentrations. *Geophysical Research Letters,* 44(1), pp. 1-8.

- Hirschmugl, M., Steinegger, M., Gallaun, H. & Schardt, M., 2014. Mapping Forest Degradation due to Selective Logging by Means of Time Series Analysis: Case Studies in Central Africa. *Remote Sensing,* 6(1), pp. 756-775.
- Hoekman, D., 2016. Remote Sensing of Wetland Types: Peat Swamp. In: C. M. Finlayson, et al. eds. *The Wetland Book.* s.l.:Springer Netherlands, pp. 1-10.
- Hooijer, A. et al., 2010. Current and future CO2 emissions from drained peatlands in Southeast Asia. *Biogeosciences,* Volume 7, pp. 1505-1514.
- Hosonuma, N. et al., 2012. An assessment of deforestation and forest degradation drivers in developing countries. *Environmental Research Letters,* Volume 7, pp. 1-12.
- Huijnen, V. et al., 2016. Fire carbon emissions over maritime southeast Asia in 2015 largest since 1997. *Nature Scientific Reports,* Volume 6, pp. 1-8.
- Huntingford, C. et al., 2013. Simulated resilience of tropical rainforests to CO2-induced climate change. *Nature Geoscience,* Volume 6, pp. 268-273.
- Hurni, K. et al., 2013. Dynamics of Shifting Cultivation Landscapes in Northern Lao PDR Between 2000 and 2009 Based on an Analysis of MODIS Time Series and Landsat Images. *Human Ecology,* 41(1), pp. 21-36.
- Ickowitz, A., 2006. Shifting Cultivation and Deforestation in Tropical Africa: Critical Reflections. *Development and Change,* 37(3), p. 599–626.
- James, R., Washington, R. & Rowell, D. P., 2013. Implications of global warming for the climate of African rainforests. *Philosophical Transactions of the Royal Society B,* 368(1625), pp. 1-8.
- Jiménez-Muñoz, J. C. et al., 2016. Record-breaking warming and extreme drought in the Amazon rainforest during the course of El Niño 2015–2016. *Scientific Reports,* Volume 6, p. 33130.
- Joiris, D. V., 1997. Afrique Equatoriale: Introduction régionale. In: *Les peuples des forêts tropicales. Civilisations*, pp. 38-43.
- Kleinman, P. J. A., Pimentel, D. & B, B. R., 1995. The ecological sustainability of slash-and burn agriculture. *Agriculture, Ecosystems and Environment,* Volume 52, pp. 235-249.
- Kleinschroth, F. et al., 2015. Legacy of logging roads in the Congo Basin: How persistent are the scars in forest cover?. *Ecosphere,* pp. 1-17.
- Koh, L. P., Miettinen, J., Liew, S. C. & Ghazoul, J., 2011. Remotely sensed evidence of tropical peatland conversion to oil palm. *PNAS,* 108(12), p. 5127–5132.

- LaPorte, N. T. et al., 2004. Towards an operational forest monitoring system for Central Africa. In: G. Gutman, et al. eds. *Land Change Science: Observing, Monitoring and Understanding Trajectories of Change on the Earth's Surface.* The Netherlands: Kluwer Academic Publishers, pp. 97-110.

- Laporte, N. T. et al., 2007. Expansion of Industrial Logging in Central Africa. *Science,* Volume 316, p. 1451.

- Lawson, I. T. et al., 2015. Improving estimates of tropical peatland area, carbon storage, and greenhouse gas fluxes. *Wetland Ecology and Management,* Volume 23, pp. 327-346.

- Lewis, S. L., Edwards, D. P. & Galbraith, D., 2015. Increasing human dominance of tropical forests. *Science,* 349(6250), pp. 827-832.

- Lewis, S. L. et al., 2009. Increasing carbon storage in intact African tropical forests. *Nature Letters,* Volume 457, pp. 1003-1007.

- Lewis, S. L. et al., 2013. Above-ground biomass and structure of 260 African tropical forests. *Philosophical Transactions of the Royal Society B,* Volume 368, pp. 1-14.

- Li, P. et al., 2014. A Review of Swidden Agriculture in Southeast Asia. *Remote Sensing,* Volume 6, pp. 1654-1683.

- Lucas, R. M. et al., 2014. Mapping forest growth and degradation stage in the Brigalow Belt Bioregion of Australia through integration of ALOS PALSAR and Landsat-derived foliage projective cover data. *Remote Sensing of Environment,* Volume 155, pp. 42-57.

- Mahli, Y. et al., 2004. The above-ground coarse wood productivity of 104 Neotropical forest plots. *Global Change Biology,* Volume 10, pp. 563-591.

- Malcolm, J. R. & Ray, J. C., 2000. Influence of Timber Extraction Routes on Central African Small-Mammal Communities, Forest Structure and Tree Diversity. *Conservation Biology,,* 14(6), pp. 1623-1638.

- Malhi, Y., 2012. The productivity, metabolism and carbon cycle of tropical forest vegetation. *Journal of Ecology,* Volume 100, pp. 65-75.

- Malhi, Y. et al., 2013. African rainforests: past, present and future. *Philosophical Transactions of the Royal Society B,* pp. 1-10.

- Malhi, Y. et al., 2009. Exploring the likelihood and mechanism of a xploring the likelihood and mechanism of the Amazon rainforest. *PNAS,* 106 (49), p. 20610–20615.

- Malhi, Y. et al., 2014. Tropical Forests in the Anthropocene. *Annual Review of Environment and Resources,* Volume 39, pp. 11.1-11.35.

- Marien, J. N., 2009. Chapter 13: Peri-Urban Forests and Wood Energy: What are the perspectives for Central Africa?. In: C. de Wasseige, et al. eds. *The Forests of the Congo Basin: State of the Forest 2008.* Luxembourg: Publication Office of the European Union, p. 411.

- Marquant, B. et al., 2015. Chapter 1: The Importance of Central Africa's Forests. In: C. de Wasseige, M. Tadoum, R. Eba'a Atyi & C. Doumenge, eds. *The Forests of the Congo Basin: Forest and Climate Change.* Neufchâteau: Weyrich, Belgium, p. 128.

- Martin, P. A. et al., 2015. Impacts of tropical selective logging on carbon storage and tree species richness: A meta-analysis. *Forest Ecology and Management* , Volume 356, pp. 224-233.

- Matricardi, E. A. T. et al., 2007. Multi-temporal assessment of selective logging in the Brazilian Amazon using Landsat data. *International Journal of Remote Sensing,* 28(1), pp. 63-82.

- Mayaux, P., Gianfranco, D. G. & Paul, M. J., 2000. Central African Forest Cover Revisited: A Multisatellite Analysis. *Remote Sensing of Environment,* Volume 71, pp. 183-196.

- Mayaux, P. et al., 2013. State and evolution of the African rainforests between 1990 and 2010. *Philosophical Transactions of the Royal Society B,* 368(1625), pp. 1-7.

- Mayaux, P., Richards, T. & Janodet, E., 1999. A vegetation map of Central Africa derived from satellite imagery. *Journal of Biogeography,* Volume 25, pp. 353-366.

- Maynard, K. & Royer, J. F., 2004. Effects of ''realistic'' land-cover change on a greenhouse-warmed African climate. *CLimate Dynamics,* Volume 22, p. 343–358.

- Medjibe, V. P. et al., 2011. Impacts of selective logging on above-ground forest biomass in the Monts de Cristal in Gabon. *Forest Ecology and Management,* Volume 262, p. 1799–1806.

- Megevand, C. et al., 2013. *Deforestation Trends in the Congo Basin,* Washington, D.C.: The World Bank.

- Mercer, B., 2015. *Tropical Forests: A Review,* London: Interantional Sustainability Unit.

- Mertz, O. et al., 2009. Who Counts? Demography of Swidden Cultivators in Southeast Asia. *Human Ecology,* Volume 37, p. 281–289.

- Mertz, O. et al., 2012. The forgotten D: challenges of addressing forest degradation in complex mosaic landscapes under REDD+. *Geografisk Tidsskrift-Danish Journal of Geography,* 112(1), pp. 63-76.

- Mietten, J. et al., 2012. Extent of industrial plantations on Southeast Asian peatlands in 2010 with analysis of historical expansion and future projections. *Bioenergy,* Volume 4, pp. 908-918.

- Mietten, J. & Liew, S. C., 2009. Burn-scar patterns and their effect on regional burnt-area mapping in insular South-East Asia. *International Journal of Wildland Fire,* Volume 18, pp. 837-847.

- Mietten, J., Stibig, H.-J. & Achard, F., 2014. Remote sensing of forest degradation in Southeast Asia—Aiming for a regional view through 5–30 m satellite data. *Global Ecology and Conservation,* Volume 2, pp. 24-36.

- Mitchard, E. T. A. et al., 2014. Markedly divergent estimates of Amazon forest carbon density from ground plots and satellites. *Global Ecology and Biogeography,* 23(8), pp. 935-946.

- Mitchard, E. T. A. & Flintrop, C. M., 2013. Woody enchroachment and forest degradation in sub-saharan Africa's woodlands and savannas 1982-2006. *Philosophical Transactions of the Royal Society B*, pp. 1-7.

- Mitchard, E. T. A. et al., 2013. Uncertainty in the spatial distribution of tropical forest biomass: a comparison of pan-tropical maps. *Carbon Balance and Management,* 8(10), pp. 1-13.

- Molinario, G., Hansen, M. & Potapov, P., 2015. Forest cover dynamics of shifting cultivation in the Democratic Republic of Congo: a remote sensing-based assessment for 2000-2010. *Environmental Research Letters,* Volume 10, pp. 1-15.

- Montagnini, F. & Jordan, C. F., 2005. *Tropical Forest Ecology. The Basis for Conservation and Management.* 1st ed. Berlin: Springer.

- Mukul, S. A. & Herbohn, J., 2016. The impacts of shifting cultivation on secondary forests dynamics in tropics: A synthesis of the key findings and spatio temporal distribution of research. *Environmental Science and Policy,* Volume 55, p. 167–177.

- Nasi, R., Billand, A. & Vanvliet, N., 2012. Managing for timber and biodiversity in the Congo Basin. *Forest Ecology and Management,* Volume 268, pp. 103-111.

- Nasi, R. et al., 2009. Chapter 12: a first look at carbon stocks and their variations in Congo Basin Forests. In: C. D. D. d. M. P. de Wasseige & R. N. R. M. P. Eba'a Atyi, eds. *State of the Forests 2008.* Luxembourg: Publicaons Office of the European Union, p. 191–208.

- Nepstad, D. C. et al., 1999. Large-scale impoverishment of Amazonian forests by logging and fire. *Nature,* Volume 398, pp. 505-508.

- Niang, I. R. O. C. et al., 2014. Africa. In: V. R. Barros, et al. eds. *Climate Change 2014: Impacts, Adaptation, and Vulnerability. Part B: Regional Aspects. Contribution of*

Working Group II to the Fifth Assessment Report of the Intergovernmental Panel on Climate Change . Cambridge: Cambridge University Press, pp. 1199-1265.

- Norgrove, L. & Hauser, S., 2016. Biophysical criteria used by farmers for fallow selection in West and Central Africa. *Ecological Indicators* , Volume 16, pp. 141-147.
- OSFAC, 2016. *Forest management and certification in the Congo Basin,* Kinshasa: OFAC.
- Padoch, C. et al., 2007. The Demise of Swidden in Southeast Asia? Local Realities and Regional Ambiguities. *Geografisk Tidsskrift, Danish Journal of Geography,* 107(1), pp. 29-41.
- Page, S. E., Rieley, J. O. & Banks, C. J., 2011. Global and regional importance of the tropical peatland carbon pool. *Global Change Biology,* Volume 17, pp. 798-818.
- Page, S. E. et al., 2002. The amount of carbon released from peat and forest fires in Indonesia during 1997. *Nature,* Volume 420, pp. 61-65.
- Pearson, T. R. H., Brown, S., Murray, L. & Sidman, G., 2017. Greenhouse gas emissions from tropical forest degradation: an underestimated source. *Carbon Balance and Management,* 12(3), pp. 1-11.
- Penman, J. et al., 2003. *Good Practice for Land Use, Land-Use Change and Forestry.* Kanagawa, Japan: IPCC National Greenhouse Gas Inventories Programme and.
- Phillips, O. L. & Brienen, R. J. W., 2017. Carbon uptake by mature Amazon forests has mitigated Amazon nations' carbon emissions. *Carbon Balance and Management,* 12(1), pp. 1-9.
- Potapov, P. et al., 2017. The last frontiers of wilderness: Tracking loss of intact forest landscapes from 2000 to 2013. *Science Advances,* Volume 3, pp. 1-13.
- Putz, F. E., Sist, P., Fredericksen, T. & Dykstra, D., 2008. Reduced-impact logging: Challenges and opportunities. *Forest Ecology and Management,* Volume 256, p. 1427–1433.
- Raven, P. H., 1988. Our Diminishing Tropical Forests. In: E. O. Wilson & F. M. Peter, eds. *Biodiversity.* Washnigton, D.C.: National Academy Press, pp. 119-122.
- Rogelj, J. et al., 2016. Paris Agreement climate proposals need a boost to keep warming well below 2 °C. *Nature,* Volume 534, pp. 631-639.
- Romijn, E. et al., 2012. Assessing capacities of non-Annex I countries for national forest monitoring in the context of REDD+. *Environmental Science and Policy,* Volume 19-20, pp. 33-48.

- Ryan, C., Berry, N. J. & Joshi, N., 2014. Quantifying the causes of deforestation and degradation and creating transparent REDDþ baselines: A method and case study from central Mozambique. *Applied Geography,* Volume 53, pp. 45-54.

- Ryan, C. et al., 2012. Quantifying small-scale deforestation and forest degradation in African woodlands using radar imagery. *Global Change Biology* , 18(1), p. 243–257.

- Saatchi, S. S. et al., 2011. Benchmark map of forest carbon stocks in tropical regions across three continents. *PNAS,* 108(24), p. 9899–9904.

- Saugier, B., Roy, J. & Mooney, H. A., 2001. Estimations of global terrestrial productivity: converging toward a single number?. In: J. Roy, H. Mooney & S. Saugier, eds. *Terrestrial Global Productivity.* San Diego: Academic Press, p. 543–557.

- Shimabukuro, Y. E. et al., 1998. Using shade fraction image segmentation to evaluate deforestation in Landsat Thematic Maepper Images of the Amazon Region. *International Journal of Remote Sensing* , 19(3), pp. 535-541.

- Siegert, F., Ruecker, G., Hinrichs, A. & Hoffmann, A., 2001. Increased damage from fires in logged forests during droughts caused by El Nino. *Letters to Nature,* Volume 414, pp. 437-440.

- Simula, M., 2009. *Towards Defining Forest Degradation: Comparative Analysis of Existing Definitions,* Rome: FAO.

- Slik, J. W. F. et al., 2009. Environmental correlates of tree biomass, basal area, wood specific Borneo's tropical forests. *Global Ecology and Biogeography,* Volume 19, pp. 50-60.

- Sodhi, N. S., Koh, L. P., Brook, B. W. & Ng, P. K. L., 2004. Southeast Asian biodiversity: an impending disaster. *Trends in Ecology and Evolution,* 19(12), pp. 654-660.

- Souza, C. M. J., Roberts, D. A. & Cochrane, M. A., 2005. Combining spectral and spatial information to map canopy damage from selective logging and forest fires. *Remote Sensing of Environment,* Volume 98, pp. 329-343.

- Souza, C. M. J., Roberts, D. A. & Monteiro, A. L., 2005. Multitemporal Analysis of Degraded Forests in the Southern Brazilian Amazon. *Earth Intercations* , Volume 9, pp. 1-24.

- Specht, M. J. et al., 2015. Burning biodiversity: Fuelwood harvesting causes forest degradation in human-dominated tropical landscapes. *Global Ecology and Conservation,* Volume 3, pp. 200-209.

- Stibig, H. A. et al., 2014. Change in tropical forest cover of Southeast Asia from 1990 to 2010. *Biogeosciences,* Volume 11, pp. 247-258.

- Tegegne, Y., Lindnera, M., Fobissie, K. & KanninenbaEuropean, M., 2016. Evolution of drivers of deforestation and forest degradation in the theCongo Basin forests: Exploring possible policy options to address forest loss. *Land Use Policy,* Volume 51, pp. 312-324.

- UNEP-WCMC, 2016. *Global statistics from the World Database on Protected Areas (WDPA),* Cambridge, UK: UNEP- WCMC.

- UNFCCC, 2008. *Report of the conference of the parties on its thirteenth session, held in Bali from 3 to 15 December 2007,* Bali: UNFCCC.

- UNFCCC, 2015. *Conference of the Parties (COP): Adoption of the Paris Agreement. Proposal by the President,* Geneva, Switzerland: United Nations Office.

- van der Werf, G. R. et al., 2009. CO2 emissions from forest loss. *Nature Geoscience,* Volume 2, pp. 737-738.

- Van Gemerden, B., Shu, G. N. & Han, O., 2003. Recovery of conservation values in Central African rain forest after logging and shifting cultivation. *Biodiversity and Conservation,* Volume 12, pp. 1553-1570.

- van Vliet, N., Mertz, O., Birch-Thomsen, T. & Schmook, B., 2013. Is There a Continuing Rationale for Swidden Cultivation in the 21st Century?. *Human Ecology,* 40(1), pp. 1-5.

- Verhegghen, A., Eva, H. & Achard, F., 2015. *Assessing forest degradation from selective logging using time series of fine spatial resolution imagery in Republic of Congo.* Milan, Italy, IEEE, pp. 2044-2047.

- Verhegghen, A. et al., 2016. The Potential of Sentinel Satellites for Burnt Area Mapping and Monitoring in the Congo Basin Forests. *Remote Sensing* , 8(986), pp. 1-22.

- Verhegghen, A., Mayaux, P., de Wasseige, C. & Defourny, P., 2012. Mapping Congo Basin vegetation types from 300 m and 1 km multi-sensor time series for carbon stocks and forest areas estimation. *Biogeosciences,* Volume 9, pp. 5061-5079.

- Wang, C., Qi, J. & Cochrane, M., 2005. Assessment of Tropical Forest Degradation with Canopy Fractional Cover from Landsat ETM+ and IKONOS Imagery. *Earth Interactions,* 9(22), pp. 1-18.

- White, F., 1983. *The vegetation of Africa: a descriptive memoir to accompany the Unesco/AETFAT/UNSO vegetation map of Africa,* Paris, France: Unesco.

- Wilkie, D., Curran, B., Tshombe, R. & Morelli, G. A., 1998. Modelling the Sustainability of Subsistence Farming and Hunting in the Ituri Forest of Zaire. *Conservation Biology* , 12(1), pp. 137-147.

- Wilkie, D. S. & Finn, J. T., 1988. A spatial model of land use and forest regeneration in the Ituri Forest of Northeastern Zaire. *Ecological Modelling,* Volume 41, pp. 307-323.

- Wilkie, D. et al., 2000. Road Development, amd Conservation in the Congo Basin. *Conservation Biology,* 14(6), pp. 1614-1622.

- Woollen, E., Ryan, C. M., Baumert, S. & Vollmer, F., 2016. Charcoal production in the Mopane woodlands of Mozambique: what are the trade-offs with other ecosystem services?. *Philosophical Transactions of the Royal Society B,* 371(1703), p. 20150315.

- World Bank, 2017. *World Development Indicators: Population dynamics.* [Online]. Available at: http://wdi.worldbank.org/table/2.1 [Accessed 10 March 2017].

- Zelazowski, P. et al., 2011. Changes in the potential distribution of humid tropical forests on a warmer planet. *Philosophical Transactions of the Royal Society A,* Volume 369, p. 137–160.

- Zhang, Q., Justice, C. O. & Desanker, P. V., 2002. Impacts of simulated shifting cultivation on deforestation and the carbon stocks of the forests of central Africa. *Agriculture, Ecosystems and Environment,* 90(2), pp. 203-209.

2. Technical Background: Synthetic Aperture Radar (SAR) and Interferometric SAR (InSAR): Key Concepts, Sensors and Data Analysis Methods

The chapter provides an overview of Synthetic Aperture Radar (SAR) and Interferometric SAR (InSAR) sensors and key concepts related to their remote sensing capabilities. It also outlines the methodological approaches that enable the link between forest properties and the SAR and InSAR signal. Detailed explanation of the methodological approaches related to the use of wavelet-based statistics is found in **Chapter 3** and developed further in **Chapter 4** while, the use of morphological algorithms and object-based change detection method is explained in **Chapter 5**.

2.1. Synthetic Aperture Radar (SAR) Key Concepts and Sensors

Synthetic Aperture Radar (SAR) are active sensors that operate in the microwave portion of the electromagnetic spectrum (cm to dm wavelength) (Bamler & Hartl, 1998) (Figure 1). As active sensors, they transmit their own signal, and thus are independent of solar illumination and are unaffected by most meteorological conditions, with longer wavelengths having the ability to fully penetrate cloud and haze (Oliver & Quegan, 2004; Woodhouse, 2005). This characteristic makes them highly suitable for use in the tropics, where almost constant cloud cover in places greatly hinders the acquisition of optical remote sensing data. Operational monitoring of tropical forests can, therefore, only be accomplished using SAR systems. One more advantage of spaceborne SAR systems is that they are able to view extensive areas.

SAR systems send microwave pulses towards the Earth's surface looking sideways at an angle from the normal to the ground (incidence angle) (Figure 1). It is a ranging device, measuring the distance to an object by time of flight. Spatial resolution in range is dictated by the duration of the pulse. Each pulse illuminates in

the range direction a portion of the ground called the swath, while the satellite moves in a direction called cross-range or azimuth. For each pulse, a portion of the radiation is scattered back to the sensor where it is detected. In the cross-range direction the pulse footprint covers a portion of the ground, whose width is dictated by the geometric characteristics if the real antenna. As the satellite moves along its orbit, several pulses are returned while covering the same slice of the illuminated ground. These pulses are combined to construct the equivalent of an observation provided by a virtual antenna much longer than the real antenna. It is through this process, called synthetic aperture formation that much higher resolution in the azimuth direction can be obtained with respect to the resolution afforded by a single physical antenna.

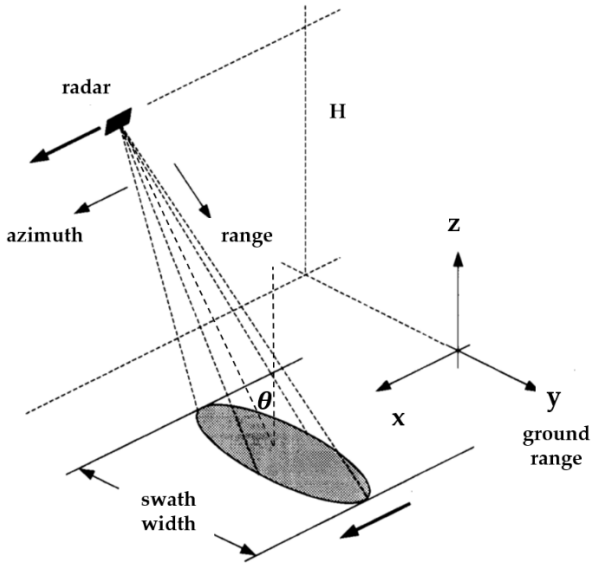

Figure 1. Side-looking Synthetic Aperture Radar (SAR) system imaging geometry (Bamler, 2000). The side-looking radar acquires images of the ground reflectivity at microwave frequency by measuring distances in the range direction by time of flight. This is performed by sending pulses of electromagnetic energy, while the satellite moves in the azimuth (cross-range or along-track) direction, that cover a portion of the ground called the swath. The ground range is the distance from the nadir position of the satellite to the first pulse return in the slant range geometry. Conversion from slant range to the ground geometry must be performed for mapping applications.

The SAR sensor in imaging mode measures the normalised radar cross section for each resolution element (backscattering coefficient usually expressed in dB). The backscattering coefficient can be higher if the energy is backscattered towards the radar (e.g. urban areas which appear white) while, it can be lower if the energy is directed away from the sensor (e.g. in the case of smooth surfaces like water which appears black) (Moreira, et al., 2013) (Figure 2).

The amount of scatter depends on the physical and electrical properties of the target on the ground, as well as the wavelength and polarisation at which the SAR system is operating (Moreira, et al., 2013).

SAR wavelengths have letter designations that herald from their military heritage (Moreira, et al., 2013). The range of wavelengths used spans from short wavelength X-band (λ = 2.5-4 cm) to the longest wavelength available for spaceborne SAR systems P-band (λ = 60-120 cm) (Table 1).

Microwave polarisation is defined as the direction in which the electric field vector oscillates in space. SAR systems emit, most commonly, polarised microwaves either in the vertical direction (V) or horizontal direction (H) (Lee & Pottier, 2009; Cloude, 2010). The returned signal is also a polarised microwave, but its properties are changed by the interaction with the target, and it can be, for instance, rotated and be neither purely in the linear horizontal or vertical configuration.

The satellite receiver with the two antennae measures the returned wave in the H and V direction, thus producing a representation in an orthogonal basis (Lee & Pottier, 2009). To make this representation complete, that is, to allow for the reconstruction of any polarisation configuration, the amplitude and phases of all the combinations of the measurements in the two bases must be performed, and combined in a matrix called the scattering matrix.

Complete measurement of the scattering matrix (called SAR fully polarimetric mode) affords the distinctive capability of polarimetric SAR to be sensitive to object shapes, symmetries and orientations (Lee & Pottier, 2009). When the information richness, and cost, of the full scattering matrix are dispensable, the returned power

in selected polarisation combinations is commonly used (e.g. HH, VV and HV) (Lee & Pottier, 2009).

Interaction with vegetation components is similar to the SAR system wavelength thus, long wavelength P-band will interact with the largest vegetation components (e.g. trunk and large branches), while the shorter wavelength X-band will interact will the smallest vegetation components (e.g. twigs and small branches) and the orientation of the vegetation elements that are of similar orientation in comparison to the incoming signal polarisation (Fung, 1994). Details related to underlying theory, principles and concepts of SAR systems are outside the scope of this chapter and can be found in Woodhouse (2005) and Bamler (2000).

Table 1. Most commonly used SAR systems frequency bands and related frequency (GHz) and wavelength (cm) at which they operate (Moreira, et al., 2013).

Frequency Band	**X**	**C**	**S**	**L**	**P**
Frequency (GHz)	12–7.5	7.5–3.75	3.75–2	2–1	0.5–0.25
Wavelength (cm)	2.5–4	4–8	8–15	15–30	60–120

Figure 2a and Figure 2b illustrate the different information that can be retrieved from SAR systems operating at different wavelengths (C-band ENVISAT ASAR and L-band ALOS PALSAR) and polarisation (VV and HV polarisation for ENVISAT ASAR and ALOS PALSAR respectively). Better discrimination can be noted between forest (grey) and bare soil/agriculture (black) using ALOS PALSAR (longer wavelength). This is because L-band penetrates deeper into the forest canopy and is more sensitive to taller vegetation through the interaction with the larger tree components (e.g. large branches), while smaller tree components, such as leaves, tend to become in the limit transparent to the radiation. Instead, at C-band backscatter saturates at lower biomass, which results in low contrast between forest and agriculture; while, hard point targets, as in the urban area (white), give higher return with respect to L-band.

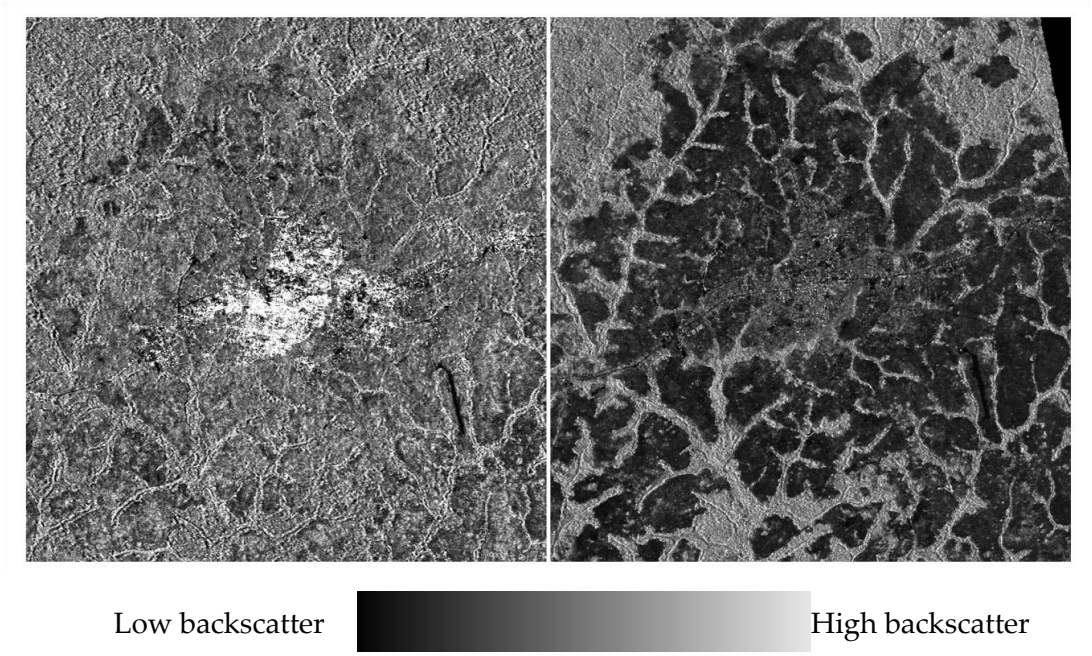

(**a**) C-band ENVISAT ASAR (VV polarisation)

(**b**) L-band ALOS PALSAR (HV polarisation)

Figure 2. Example of SAR imagery acquired at different wavelength and polarisation over the city of Bertoua (Lom-et-Djerem, Cameroon) surrounded by agricultural fields, savanna and semi-deciduous forest. SAR image acquired by: (**a**) ENVISAT ASAR (C-band, VV polarisation, 15 m resolution) and (**b**) L-band ALOS PALSAR (L-band, HV, 15 m resolution).

Table 2 summarises spaceborne SAR systems launched since the 1990s with wavelengths from X-band (λ≅ 3 cm) upwards. These instruments have provided a plethora of data through time, though it should be noted that most data is available at C-band, followed by the shorter wavelength X-band; the longer L-band has been collected least frequently, and the longer still P-band not yet launched in space (though a satellite is planned).

Table 2. List of spaceborne satellites launched since 1990 including current, future and proposed missions (World Meteorological Organization, 2017; European Space Agency, 2017).

Satellite (Agency)	Life Span	Spatial resolution (m)	Polarisation	Repeat cycle (days)
Past missions				
X-band				
SRTM (X-SAR) (NASA/DLR/ASI)	2000	30	VV	N/A
C-Band				
ERS-1 (ESA)	1991-2000	30	VV	35
ERS-2 (ESA)	1995-2011	30	VV	35
ENVISAT/ASAR (ESA)	2002-2012	30-1 km	Single, Dual	35
SIR-C (NASA)	1994-	10-40	HH, VV, HV (quad)	1
RADARSAT-1 (CSA)	1995-2013	10-100	HH	24
RADARSAT-2 (CSA)	2007-present	3-100	Single, Dual, Quad	24
SRTM (C-SAR) (NASA JPL)	2000	30	HH, VV	N/A
L-Band				
Seasat (NASA)	1978- 1978	25	HH	17
JERS-1 (JAXA)	1992-1998	18	HH	44
ALOS PALSAR 1 (JAXA)	2002-2011	7-100	Single, Dual, Quad pol	46
Current missions				
X-Band				
CosmoSkyMed 1 (ASI) CosmoSkyMed 2 (ASI) CosmoSkyMed 3 (ASI) CosmoSkyMed 4 (ASI)	2007- ≥2017 2007- ≥2017 2008- ≥2017 2010 -≥2017	1-100	Single or Dual pol	16
RISAT- 2 (ISRO)	2009-2017	1-8	HH or VV or HV or VH	14
TerraSAR-X (DLR) **TanDEM-X (DLR)**	2007-2017 2010-2017	1-16	Single, Dual HH or VV or HV or VH	11
C-Band				
Sentinel 1A/B (ESA)	2014-2021 2016-2023	4-80	Single, Dual, Quad	12
RISAT-1 (ISRO)	2012-present	1-50	HH or VV or HH/HV or VV/VH	25
L-Band				
ALOS PALSAR-2 (JAXA)	2014-2019	1-100	Single, Dual	14
Future and proposed missions				
X-band				
PAZ (CDTI/INTA)	≥2017	1-15	HH or VV or HV or VH	11

C-Band				
RADARSAT 3 (CSA)	2018	1-100		
RISAT-1A (ISRO)	2019-2023	1-50	HH or VV or HH/HV or VV/VH	12
L-Band				
TanDEM-L (DLR)	(proposed mission)			
SAOCOM-1A (CONAE) SAOCOM-2A(CONAE) SAOCOM -1B (CONAE) SAOCOM -2B (CONAE)	≥2017-≥2022 ≥2019-≥2024 ≥2018-≥2023 ≥2020-≥2025	10-100	Single (HH or VV), Dual (VV/HH, HH/HV, VV/VH)	16 days (one satellite) 8 days with constellation
NISAR (L-S-band) (NASA and ISRO)	2020-	10 m (depends on polarisation mode)	HH or VV (single pol); HH/HV or VV/VH (dual pol); RH/R (compact pol); HH/HV/VH/VV (quad pol)	12
P-Band				
BIOMASS (ESA)	2021	50-60	Fully polarimetric	17

* highlighted in **bold** the sensors used in the thesis.
Acronyms: European Space Agency (ESA), National Aeronautics and Space Administration (NASA), Agenzia Spaziale Italiana (ASI), Japanese Aerospace Exploration Agency (JAXA), German Aerospace Agency (DLR), Canadian Space Agency (CSA), Indian Space Research Organisation (ISRO), Argentine Space Agency (CONAE), Centro para el Desarrollo Tecnológico Industrial - Spain's Center for Development of Industrial Technology) (CDTI) and Instituto National de Técnica Aeroespacial (INTA).

Notable recent technological advancements are provided by the C-Band Sentinel-1 mission developed by the European Space Agency (ESA). Sentinel-1 (A and B) satellites launched in 2014 and 2016 respectively (European Space Agency, 2013) which are set to enhance the role of SAR in aid of tropical forest monitoring. Particular improvements, compared to ESA's previous missions, include the open data policy, and data quality in terms of temporal (up to 6 days revisit time) and spatial resolution (5 x 5 m spatial resolution in StripMap mode) (European Space Agency, 2013). These assets afford the ability to monitor natural processes frequently and at finer detail compared to its predecessor (ENVISAT ASAR) (30 m spatial resolution in StripMap mode) (World Meteorological Organization, 2017).

Notable, future missions include the BIOMASS mission (Table 2) which is directed towards monitoring and quantifying changes in terrestrial forest above-ground biomass globally and annually. BIOMASS is scheduled to be launched in

2021 and will be the first and longest wavelength spaceborne satellite operating at P-band (λ = 70 cm; frequency = 435 MHz) (Le Toan, et al., 2011).

TanDEM-L is also a highly innovative mission concept proposed by DLR consisting of two satellites operating in formation for monitoring dynamic processes on the Earth's Surface with the aim to provide interferometric information once a week over the land mass (Moreira, et al., 2015). The mission is set to provide tomographic measures required to capture vegetation three-dimensional structure as well as other applications (e.g., glaciology and ground deformation) (Moreira, et al., 2015).

The following sections describe in detail the satellite sensors used in the thesis.

2.1.1. ALOS PALSAR

The Advanced Land Observing Satellite (ALOS) was a satellite launched in 2006 by the Japanese Space Exploration Agency (JAXA) and carried the Phased-Array L-band Synthetic Aperture Radar (PALSAR). PALSAR, a successor of JERS-1 SAR, acquired data at L-Band (λ = 23.6 cm) (Rosenqvist, et al., 2007). Compared to its predecessor, ALOS PALSAR could acquire data at higher resolution in all modes, better signal-to-noise ratios, and better polarimetric characteristics (it collected most data over land in the Fine Beam Dual polarisation mode, with HH and HV polarisations, whereas JERS-1 data provided HH polarisation only) (Table 2).

JERS-1, had shown the value of SAR data for characterising forests and ALOS PALSAR was developed with the aim of providing a systematic acquisition plan in continuation with the JERS-1 strategy. In this context, data were acquired consistently over tropical regions and boreal zones in the framework of the Global Rain Forest Mapping (GRFM) (De Grandi, et al., 2000) and Global Boreal Forest Mapping (GBFM) (Rosenqvist, et al., 2004) initiatives.

The dataset used in this thesis consists of twelve ALOS PALSAR Fine Beam Dual (FBD) scenes acquired between 2007 and 2010 at HH and HV polarizations in work described in **Chapter 3**.

2.1.2. ENVISAT ASAR

The Advanced Synthetic Aperture Radar (ASAR) onboard ENVISAT was launched by the European Space Agency (ESA) in 2002 to acquire data at C-band (λ = 5.6 cm) until its failure in April 2012 (Miranda, et al., 2013). The ENVISAT ASAR mission follows the ERS-1/2 mission that was operating between 1991-2000 and 1995-2011.

One of the acquisitions modes, the Imaging Mode (IM) is a conventional StripMap mode whereby changes in the elevation beam permit the acquisition of data with decreased swath width. IM mode permitted the acquisition of single polarisation data (either HH or VV polarisation) as opposed to the dual-polarisation acquisition capability in Alternating Polarisation mode (HH/VV, HH/HV or VV/VH) (Miranda, et al., 2013).

The focus of the mission was on ocean, land (including global vegetation monitoring), natural disasters and snow and ice applications. The ENVISAT ASAR mission was followed by the Sentinel-1 (A and B) constellation which aims to provide multi-temporal data at high revisit time (ESA, 2016).

Nine ENVISAT ASAR IM scenes used in **Chapter 3** were acquired between 2003 and 2010 at 23° incidence angle and VV polarization.

2.2. Interferometric Synthetic Aperture Radar (InSAR)

The use of SAR interferometry took off later compared to SAR imaging systems. The first applications of InSAR to terrestrial monitoring were published in the 1980s (Bamler & Hartl, 1998) (e.g. Zebker & Goldstein, 1986).

The field of SAR interferometry took longer to mature because it required sophisticated signal processing algorithms (time-frequency analysis, phase unwrapping), precision orbital mechanics for accurate baseline estimation, and novel understanding of the physics of wave propagation in the layer between the satellite and the Earth.

Notably, the evolution of the interferometric SAR field has widened to explore entirely new possibilities beyond the generation of digital surface models. Among

these the capability of measuring target velocity provided by Along Track Interferometry (ATI) and the capability of measuring displacements of permanent targets of the order of magnitude of the wavelength by differential SAR interferometry (DInSAR).

Nowadays, the methodology for processing InSAR data, at least for the generation of DEMs is highly advanced, with excellent software packages available such as SARscape (Sarmap, 2016) and GAMMA (GAMMA, 2006).

The most significant advance in data availability occurred in 2011 with the launch of the TanDEM-X satellite system. TanDEM-X flies in formation with its twin satellite TerraSAR-X, in a helical orbit that keeps the satellite 10s to 100s of meters apart (Krieger, et al., 2007). Prior to this, all spaceborne InSAR data was acquired in repeat-pass mode, involving images captured at different times (usually several days) by the same satellite sensor from a slightly different position; the TanDEM-X system allows a single-pass whereby two images are captured simultaneously.

2.2.1. TanDEM-X

TanDEM-X (with its twin satellite TerraSAR-X flying in formation) is the first single-pass spaceborne interferometer that acquires data at X-Band (λ = 0.031 m, 9.65 GHz) with a high spatial resolution (1 m in SpotLight mode). Its main goal is to provide a consistent Digital Elevation Model (DEM) with global coverage (WorldDEM™) (Airbus Defence and Space, 2014) and at high accuracy (HRTI-3 specifications) (10 m absolute vertical accuracy, 10 m horizontal accuracy and 12 m spatial resolution) (Krieger, et al., 2007). A single bistatic scene usually covers 30 x 50 km (range and azimuth respectively) (Martone, et al., 2016). How InSAR works and data acquired can be used to generate DEMs is detailed in the next section.

TanDEM-X acquires data using an innovative technique called bistatic interferometry (bistatic mode), which involves the illumination of a common footprint simultaneously measured using two receivers, thus eliminating temporal decorrelation (Krieger, et al., 2007) (which is inherent in repeat-pass systems) (Martone, et al., 2016).

Single-pass interferometry has provided excellent potential for scientific research for the study of forest structure. TanDEM-X Single Look Complex (SLCs) data was provided on-demand to the scientific community, as part of announcements of opportunity. From this data, it is possible to generate a DEM, corresponding to approximately the 'top of the canopy', with a variance dependent on the forest type (e.g. density) and environmental conditions (Treuhaft, et al., 2015).

TanDEM-X data acquired in StripMap bistatic mode are used in **Chapter 4** and **5** of this thesis. In **Chapter 4** data acquired in 2014, at HH polarisation, ascending mode at 41° incidence angle with an effective baseline equal to 223 m. In **Chapter 5** data were acquired at HH polarisation at 2 dates (2012 and 2013) at 47° incidence angle in descending mode with effective baselines equal to 52 m and 95.3 m. Data were processed from co-registered Single Look Complex (CoSSC) provided by DLR using ENVI/SARScape 5.0, as described in **Chapter 4** and **Chapter 5**.

2.3. InSAR Overview and Key Concepts

SAR instruments acquire data by sending a number of electromagnetic pulses while the satellite moves along its orbit, and reconstructing a high resolution two-dimensional map (image) of the energy backscattered from the terrain. In this acquisition mode, also called StripMap SAR, the instrument is restricted to two-dimensional measurements (Rosen, et al., 2000).

Instead, Interferometric Synthetic Aperture Radar (InSAR) involves the acquisition of two radar signals from two positions S_1 and S_2 with slightly different look angles, separated by a baseline B. The antennas are located at distance R_1 and R_2 from a target located on the surface P which is situated at height h_0 compared to the ground surface (Cloude, 2010) (Figure 3.

The InSAR configuration affords the ability to derive a third dimension, the height of the target h_0, through measuring the phase difference of the returning waves (Gens & Van Genderen, 1996; Bamler & Hartl, 1998; Rosen, et al., 2000; Richards, 2006) (Figure 3).

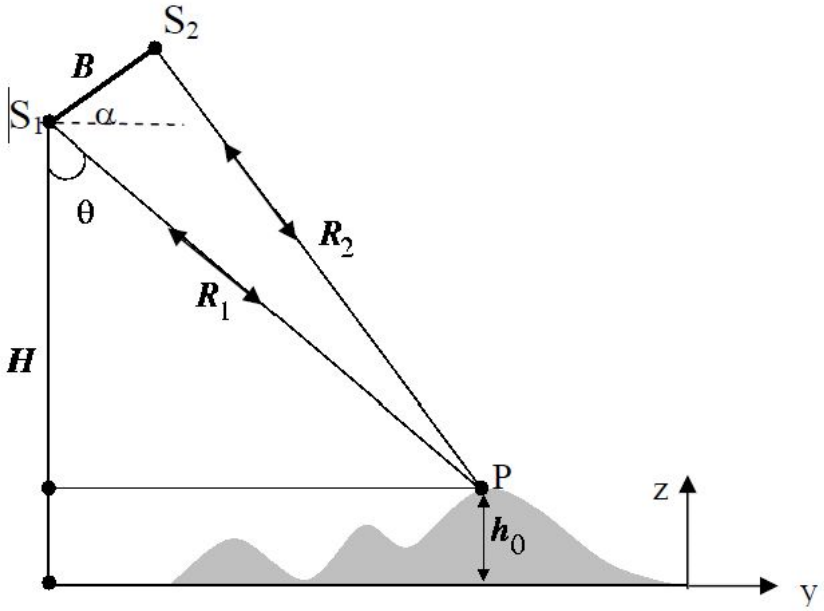

Figure 3. Interferometric Synthetic Aperture Radar (InSAR) viewing geometry illustrating the acquisition from two satellites S_1 and S_2 acquiring radar signals separated by a baseline B and located at a height H and at range distances R_1 and R_2 respectively from a target P which is situated at height h_0 (Cloude, 2010).

A peculiar characteristic of radar systems (in particular interferometric and polarimetric SAR) is that they process radiation coherently, that is, both the amplitude and the phase of the transmitted and received waves are measured using a unique reference clock. It is this property that allows an interferometer to measure terrain height, and a polarimeter to detect object's shapes and symmetries (Lee & Pottier, 2009).

Regarding InSAR the key variable is the complex conjugate product of the two coherent signals, also called the interferogram. The interferogram can be generated from two images that are acquired in two different ways: repeat-pass interferometry (the acquisition using one antenna over the same area at two different times) (e.g. acquisitions by ERS-1/2 or ENVISAT ASAR 1/2) or single-pass interferometry (acquisition using two antennas) (e.g. acquisitions from TanDEM-X) (Balzter, 2001). An important step to consider when generating an interferogram (Figure 4) involves

the accurate co-registration of the Single Look Complex (SLC) image pairs acquired by S_1 and S_2.

Considering a single pulse and a single scatterer for a point P centered at the origin of the x, y coordinate system the interferogram is:

$$s_1 s_2^* = A_1 A_2 e^{i(\phi_1 - \phi_2)} = A e^{i\frac{4\pi\Delta R}{\lambda}} \cong A e^{i\frac{4\pi\Delta\theta}{\lambda} z sin\theta} \qquad \text{Equation 1}$$

Where A_1 and A_2 are amplitudes, θ is the incidence angle, $\Delta\theta$ is the difference in look angle due to the antennae position, λ is the wavelenght, z is the vertical coordinate of point P. Notice that in this formula and in the next derivations the dual-transmitter (or ping-pong mode is assumed).

The simplified equation derived for a single point P at height z indicates how the phase of the interferogram bears information on the vertical position of a scatter, apart a scaling factor $\frac{4\pi\Delta R\theta}{\lambda}$, which is called the interferometric wavenumber. Importantly, the phase of the interferogram (ϕ), the key radar observable, is 2π ambiguous (Cloude, 2010):

$$\phi = arg\{s_1 s_2^*\} = -\frac{4\pi}{\lambda}\Delta R + 2\pi N \qquad \text{Equation 2}$$

where s_1 is the radar signal from satellite S_1; s_2^* is the complex conjugate of the radar signal derived from satellite S_2; λ is the wavelength and $\Delta R = R_1 - R_2$ gives the distance between the range distances.

Because the range to terrain R can be many times the radar wavelength the phase will be a large number of radians. This points to the problem that to convert the phase to terrain height the ambiguity of the values must be resolved by a process called phase unwrapping (Richards, 2006).

The interferogram (Figure 4) contains fringes due to the rate of change of phase across a flat surface (height variation $\Delta z = 0$). This high frequency phase term is removed by further processing called 'interferogram flattening', which means that a constant phase is generated for flat terrain, thus emphasising phase changes due to

topography (Cloude, 2010). This process requires the use of an external DEM to take into account of the topographic phase. Further details related to the complete processing workflow can be found in Sarmap (2016).

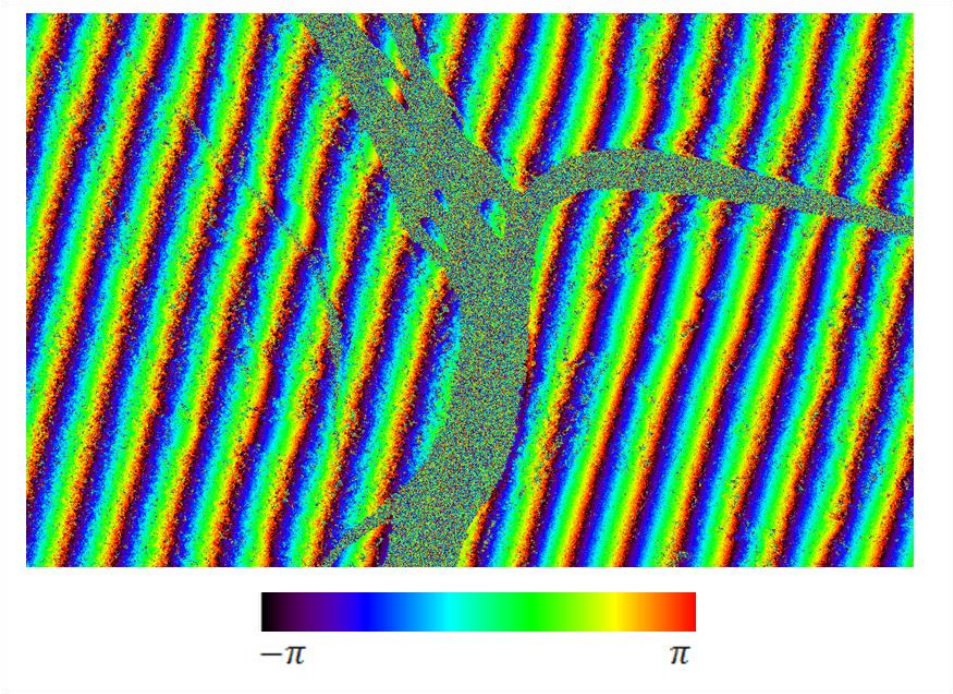

Figure 4. SAR interferogram derived from TanDEM-X StripMap bistatic mode acquisitions over tropical forest in the Republic of Congo (processed using SARscape 5.0) (Sarmap, 2016). In bistatic mode one satellite (master) transmits and receives pulses, while the second satellite (slave) only receives (at a different incidence angle) pulses transmitted by the first satellite. In the interferogram image the phase difference (in radians) received by the two antennas at slightly different position is colour coded. Each colour circle (from black to red) represent a 2π cycle. The regular pattern of fringes correspond to the variation of phase per unit range distance over flat terrain. When this high frequency component is removed by a suitable processing step (flat earth removal) the phase will carry information on the terrain elevation. The absence of fringes are due to scattering from moving water with very low signal to noise ratio. TanDEM-X data acquisition parameters: baseline: 52 m, incidence angle: 47°, polarisation: HH. Data: TanDEM-X AO: VEGE6702 (DLR).

2.3.1. Interferometric Coherence

Interferometric coherence is a statistical measure of the correlation between the two signals that form the interferogram, and has an important impact on the quality of the interferogram. The complex coherence (γ) (Figure 5) is the normalised complex correlation coefficient of S_1 and S_2 (master and slave signals) (Cloude, 2010):

$$\gamma = \frac{\langle S_1 S_2^* \rangle}{\sqrt{\langle S_1^2 \rangle \langle S_2^2 \rangle}} \qquad 0 \leq |\gamma| \leq 1 \qquad \text{Equation 3}$$

Where γ is the complex coherence; $\langle \dots \rangle$ indicates ensemble average and S_1, S_2 are the complex slant range signals acquired by the two instruments.

The modulus of the coherence $|\gamma|$ ranges between 0 (not coherent) and 1 (completely coherent) (Woodhouse, 2005). Several phenomena affect the coherence magnitude in repeat-pass InSAR acquisitions such as temporal decorrelation (γ_{Temp}) (Hanssen, 2001), for instance in the case of the ERS-1/2, ENVISAT ASAR and ALOS PALSAR 1/2 missions. Further details related to repeat-pass InSAR can be found in (Bamler & Hartl, 1998).

In the most general case, sources of coherence loss that need to be taken into account for repeat-pass InSAR are highlighted in Equation 4 (Martone, et al., 2012):

$$\gamma = \gamma_{SNR}\gamma_{Vol}\gamma_{Quant}\gamma_{Amb}\gamma_{Range}\gamma_{Azimuth}\gamma_{Temp} \qquad \text{Equation 4}$$

where γ_{SNR} is the signal-to-noise ratio; γ_{Vol} is the volume decorrelation; γ_{Quant} is the quantization errors; γ_{Range} is the baseline decorrelation and γ_{Amb} is the noise from ambiguities.

The thesis only deals with single-pass interferometry acquisitions. For single-pass interferometers, such as TanDEM-X, temporal decorrelation (changes in the scatterer structure over two acquisition times) can be considered negligible (i.e., γ_{Temp}= 1) (Equation 4) (Martone, et al., 2016). Signal decorrelation is primarily due to volume decorrelation (γ_{Vol}) from the vegetation layer, due to interference of the coherent sums of the returns from all the scattering centres (e.g. leaves and twigs)

distributed vertically across the vegetation layer (Treuhaft & Siqueira, 2000; Cloude, 2010) (Equation 4).

Another important source of decorrelation is geometric (or baseline) decorrelation (γ_{Range}). This mechanism is similar to volume decorrelation, but now it is due to surface scattering and to the coherent sum of scatterers along the y coordinate in space, as opposed to the vertical z coordinate. Since the surface is seen by two different antennae positions, the coherent sums will be slightly different in the two signals, and therefore decorrelation is generated. Contrary to volume decorrelation, baseline decorrelation can be corrected by suitable processing (called spectral shift) but up to a maximum separation of the baseline (Gatelli, et al., 1994).

Figure 5 shows TanDEM-X coherence over tropical forest in the Republic of Congo. Coherence is low in lowland tropical forest (green), due to high volume decorrelation given by the heterogeneous density and vertical distribution of scatterers within the resolution cell while, high coherence is noticeable for areas such as bare soil and agricultural fields (orange), but also in swamp forest (orange), due to homogeneous and dense canopy structure, which pushes the effective vegetation volume towards the canopy top.

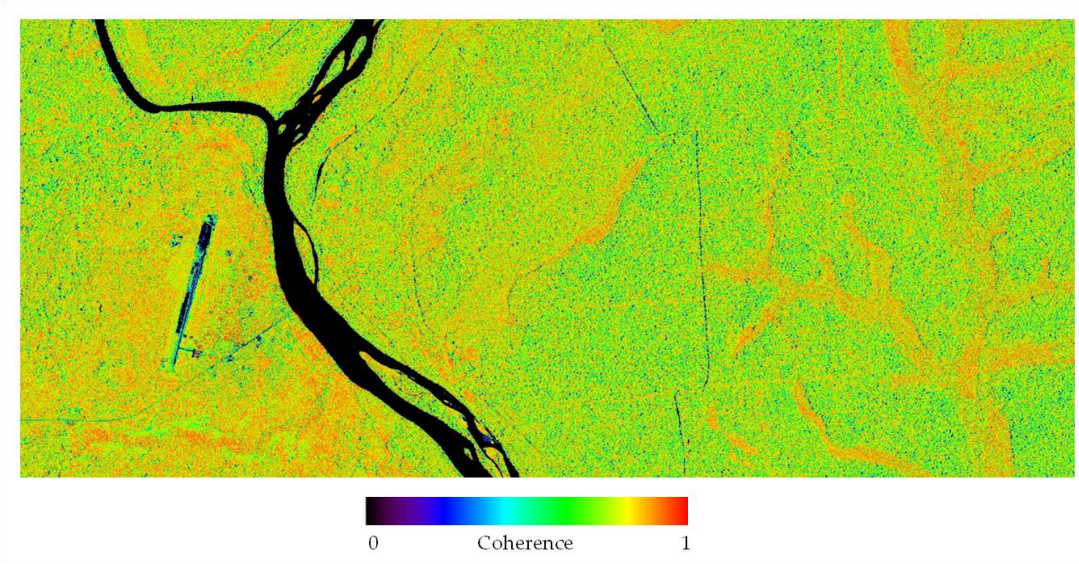

Figure 5. TanDEM-X coherence over the Republic of Congo. Areas with low coherence (green) represent lowland tropical forest dominating the scene, while higher coherence illustrates areas where there is less volume decorrelation from lack of vegetation (e.g. bare soil and agricultural fields) (orange) as well as swamp forest (right). Lowest coherence (black and blue) is observed in water and roads due to the low signal to noise ratio. TanDEM-X data acquisition parameters: baseline: 52 m, incidence angle: 47°, polarisation: HH. Data: TanDEM-X AO VEGE6702 (DLR).

2.3.2. Height of Ambiguity

The height of ambiguity (HoA) is the elevation difference corresponding to a complete 2π cycle of the interferometric phase (Martone, et al., 2016). HoA gives an indication of the phase-to-height sensitivity of the interferogram and is defined in Equation 5 (Martone, et al., 2012):

$$HoA = \frac{\lambda r \sin(\theta_i)}{B_\perp} \qquad \text{Equation 5}$$

Where λ is the radar wavelength, r is the slant range, θ_i is the incidence angle and $B_\perp$ is the baseline perpendicular to the line of sight.

2.3.3. Phase-to-Height Conversion

Conversion from phase to height of a point P can be performed from the unwrapped and flattened phase of the coherence and the vertical wavenumber (rad/m):

$$h_0 = \frac{\phi}{\beta_z} \quad \text{Equation 6}$$

For terrain mapping, the difference of interferometric phase from one pixel to the next is used to estimate a height change between two pixels. A height map is then formed using a reference point with known height h_{ref}, supplied by an auxiliary lower resolution DEM (e.g. SRTM):

$$h\,(x,y) = h_{ref} + \frac{1}{\beta_z}\Big(\phi(x,y) - \phi_{ref}\big(x_{ref}, y_{ref}\big)\Big) \quad \text{Equation 7}$$

where h_{ref} is the reference height from the auxiliary DEM; ϕ_{ref} is the phase from the auxiliary DEM and x_{ref}, y_{ref} are the coordinates for the auxiliary DEM.

If the point lies on a vegetated terrain, the height h will be the sum of the topographic height and the position of the phase centre within the vegetation volume. The fractional phase centre height (PC), i.e. the position of the phase centre with respect to the vegetation volume height, is dictated by the amount of volume decorrelation, and is defined as (Equation 8) (Cloude, 2010):

$$PC = \frac{\phi}{h_v \beta_z} \quad \text{Equation 8}$$

Where is ϕ the interferometric phase; h_v is the height of the volume and β_z is the vertical wavenumber.

Therefore, PC is the ratio of the coherence phase (radians) resulting from decorrelation induced by volume scattering to the volume height measured in unit of the vertical wavenumber.

Location of PC depends on the sensor's parameters (e.g. wavelength, incidence angle and baseline), the forest properties (e.g. density and presence of canopy gaps) (Treuhaft, et al., 2015) and attenuation from the canopy volume (Cloude, 2010).

At X-band, the PC is located close to the 'top of the canopy' (Izzawati, et al., 2006), while with longer wavelength (e.g. L-band and P-band) this moves downwards (Figure 6). This means that X-band is able to provide an approximation of a Digitals Surface Model (DSM) over vegetated areas.

Penetration depth also depends on environmental conditions (e.g. seasonality and recent rainfall), with dry and sparser forests characterised by the presence of canopy gaps (e.g. boreal forests or temperate or seasonal forests in the winter/dry season) allowing a greater penetration into the canopy volume compared to dense forest (Garestier, et al., 2008). Accordingly, the PC at X-band is located deeper within the canopy volume for sparser boreal forest (e.g. PC was found to be located at 75% of the canopy height in boreal forest) (Praks, et al., 2012).

Currently, there is no spaceborne sensor which provides both the 'top of the canopy' (DSM) and ground topography (Digital Terrain Model). The Shuttle Radar Topographic Mission (SRTM, a C-band single-pass InSAR mission flown on the Space Shuttle in 2000) is the only mission that has so far provided a global DEM which approximates to ground topography, especially in areas with the absence of vegetation cover. However, its resolution is lower than that produced by TanDEM-X (30 m compared to 12 m) (Farr, et al., 2007).

To illustrate the location of the PC a model with a uniform layer and an exponential profile for the scattered power along the vertical coordinate can be used (Cloude, 2010):

$$\gamma = f(h, \sigma_e, \beta_z) = \frac{p\left(e^{(p+i\beta)h} - 1\right)}{(p + i\beta)(e^{ph} - 1)} \quad p = 2\sigma sec\vartheta \qquad \text{Equation 9}$$

where γ is the complex coherence, h is the volume height, σ is the extinction coefficient, ϑ is the incidence angle, $\beta_z = \frac{4\pi B_\perp}{\lambda R \sin\vartheta}$ is the vertical wavenumber, a parameter that summarises the interferometric sensitivity.

Figure 6 reports an example where the PC was computed as a function of the volume height (h) and parameterised by increasing wavelength.

At X-band and C-band (high extinction) the PC will be moved up near the top of the canopy. At L-band and P-band (lower extinction) the PC will tend to settle at half the volume height. Volume decorrelation will always move up the PC even at P-band. Therefore, vegetation height estimation at P- or L-band will always be biased because PC is halfway up into the canopy. Only multi-frequency acquisitions will provide a better approximation of vegetation height (e.g. TanDEM-X and TanDEM-L).

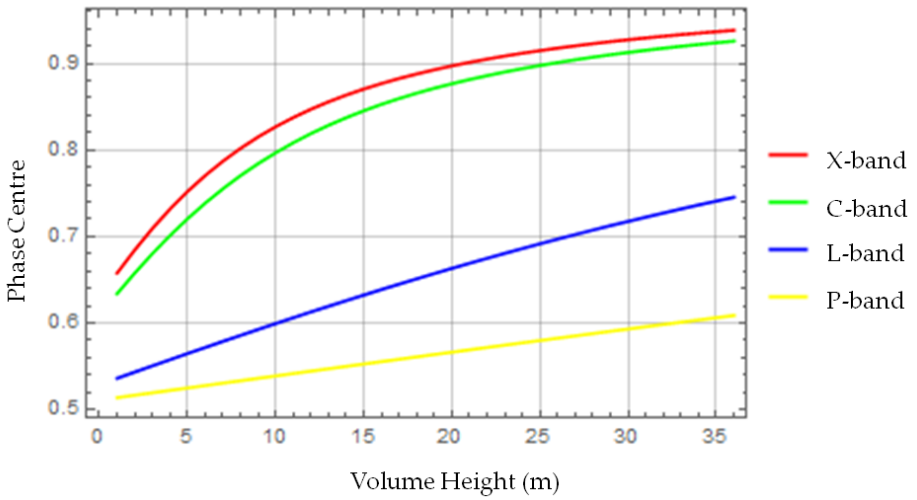

Figure 6. Phase centre (PC) dependence on the instrument frequency of acquisition (X-band in red; C-band in green; L-band in blue and P-band in yellow) and volume height (m) calculated using model with a uniform layer and an exponential profile (Cloude, 2010). Notice that at X-band the PC is located > 90% of the height for height > 20 m and at P-band the PC is still located > 50% of the height.

2.3.4. Phase Error

Each sample in the TanDEM-X DSM (height estimate) is affected by an error induced by phase noise whose standard deviation ($SD\phi$) can be related to the coherence by a Cramer-Rao bound (Figure 7) (Cloude, 2010).

$$SD\phi = \sqrt{\frac{1 - |\gamma|^2}{2|\gamma|^2}} \qquad \text{Equation 10}$$

Where ϕ is the phase and γ is the interferometric coherence.

The standard deviation of the height estimate $SD(h_\phi)$ is computed by SARscape for each pixel in the DSM dataset (Sarmap, 2016). Lower coherence values result in a lower measurement precision and vice versa (Sarmap, 2016).

The phase error propagates to the height estimate error and it is dependent on the sensor's acquisition parameters, including the wavelength λ, the slant range distance R, the local incidence angle ϑ and the effective baseline $B_\perp$. For instance, TanDEM-X acquisitions will have a higher precision with long baselines.

$$SD(h_\phi) = SD\phi \frac{\lambda R \sin\vartheta}{4\pi B_\perp} \qquad \text{Equation 11}$$

Where λ is the wavelength, R is the slant range distance, ϑ is the local incidence angle and $B_\perp$ is the effective baseline.

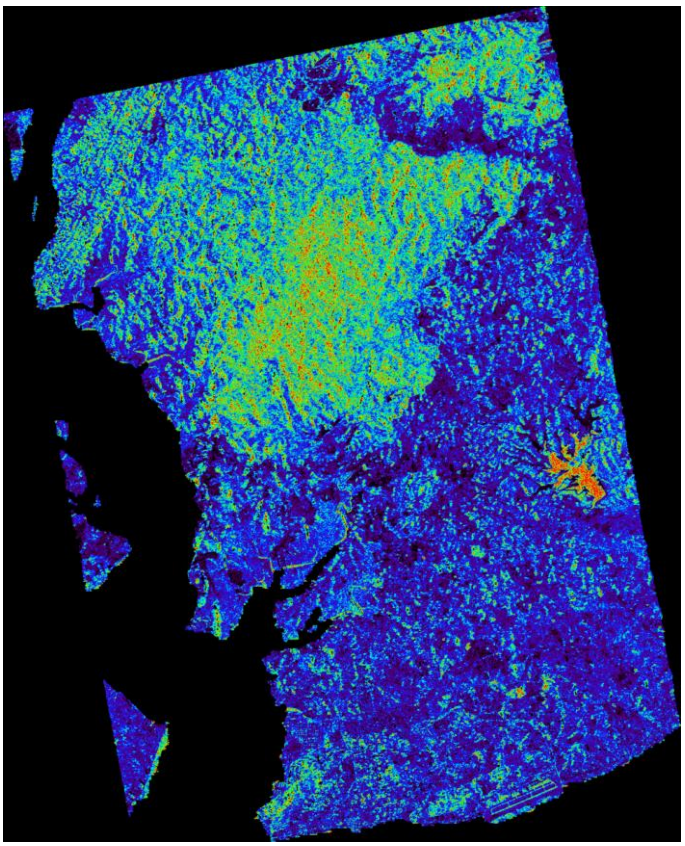

High precision  Low precision

Figure 7. TanDEM-X height estimates standard deviation image derived from phase noise $SD(h_\phi)$ generated by SARScape 5.0 (Sarmap, 2016) in Central Kalimantan, Indonesian Borneo. Higher $SD(h_\phi)$ values (m) indicate lower measurement precision. Areas of dense forest (red and green) in the top-centre of the image and water to the left of the image (red) present higher $SD(h_\phi)$ values (lower precision) while, areas of agriculture and bare fields (black and dark blue) have a higher precision. This is related to the degree of decorrelation; in areas where there is less volume scattering the precision is higher.

2.4. Wavelets

Much of the potential gain for improving our ability to use SAR data (both backscatter and InSAR coherence) to map forest characteristics can be made by calling into play texture. By considering the relationships between neighbouring pixels much more information about the surface structure and its scattering

mechanisms can be elucidated, enhancing the ability to detect differences between vegetation types in time and space.

Wavelets emerged in the field of applied mathematics in the 1980s and rapidly gained interest and underwent great theoretical development is various application areas, such as geoscience. They are nowadays a well established tool both from the theoretical and the computational standpoint. In both **Chapters 3** and **4** wavelets are used to analyse radar texture, building on earlier work (Simard, et al., 1998; De Grandi, et al., 2009) showing their potential for considerable utility in the analysis of SAR images.

Given that wavelets are not a standard tool, an introduction is provided here to assist the reader in understanding the results presented in these chapters.

Their merits with respect to other methods used in the past in the framework of statistical analysis in the combined space-scale domain are discussed in detail in **Chapter 3**; an overview is also given here.

Wavelets are functions that oscillate and decay rapidly (Figure 8). They can be used to decompose a signal (field) in a complete way (without losing information) into more elementary building blocks (or oscillatory waveforms) (Mallat, 2008). A 'mother' wavelet is the main function which is used to generate by dilation and translation a series of basis functions (Mallat, 2008).

There are many other ways of building a basis aside from wavelets. For example, sine waves (functions which oscillate at a specific frequency) are widely used, for example in the well-known Fourier transform, but these are only suitable for stationary signals (Mallat, 2008) (signals whose statistical properties do not change with time) (Peebles, 1980). Wavelets are considered to have many advantaged over these for instance, the ability to keep optimal time and frequency resolution and to detect abrupt changes (Mallat & Zhong, 1992).

Wavelets are able to adapt the space-frequency resolutions in such a way that their product is constant (Mallat, 2008). Frequency and space resolution cannot be made independently and arbitrarily better. For instance, the basic function of the Fourier transform (sine wave) presents zero spread in frequency (pure tone) while

infinite spread in space (it oscillates everywhere) (Mallat, 2008). What would be desirable is to have more resolution in time when dealing with smaller scale (higher frequency) analysis, and lower resolution in time when dealing with processes that are evolving slowly. Wavelets do exactly that, by adapting the space-frequency resolution. The capability is of importance when considerations that analyse the dynamics of the signal at specific points in time (or in space) through time-frequency analysis (space-scale analysis) are of interest (Davis, et al., 1994). It was also the main reason for using wavelets for textural analysis rather than Fourier based techniques in the thesis work.

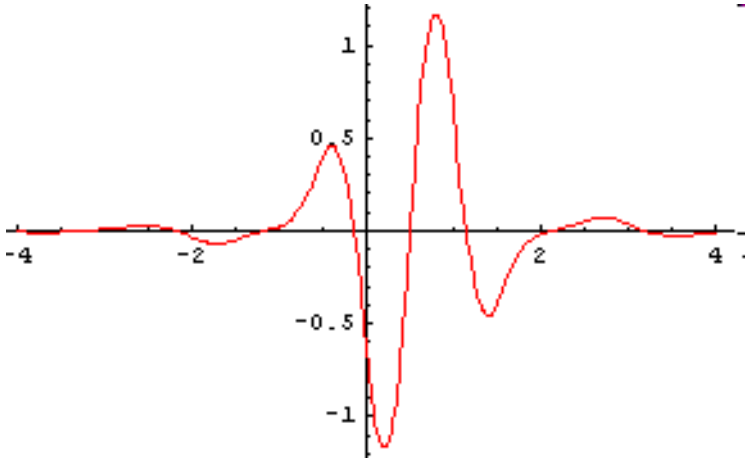

Figure 8. Typical shape of a wavelet.

Table 3. Space-scale (time-frequency) analysis.

Atoms	**Time spread**	**Frequency spread**	**Time-frequency resolution**
Fourier	Infinite	Zero	Undetermined
Windowed Fourier	σ_t	σ_ω	$\sigma_t\sigma_\omega$= constant
Wavelet	$s\sigma_t$ (adaptive)	$\frac{\sigma_\omega}{s}$ (adaptive)	$\sigma_t\sigma_\omega$= constant

Advantages of using as building blocks in a time-frequency transform wavelets compared to Fourier waveforms are summarised in Table 3. The waveforms in the linear time-frequency transform are called atoms. The Fourier atom is a sine wave oscillating at frequencyω. The windowed Fourier atom is obtained by limiting a sine wave oscillating at frequency ω in time by means of translations of a window function centered at time t. The wavelet atom, as explained above, is obtained by

translations and dilations of a unique primitive function, the mother wavelet. The relative merits of these decompositions are measured in terms of the capabilities of achieving combined resolution both in time and in the frequency domain. As explained in more detail in 3.4.2, resolution is measured by the atom spread in time or frequency (a measure similar to the variance in statistics:

$$\sigma_t^2 = \int_{-\infty}^{+\infty} t^2 \psi^2 dt \qquad \text{Equation 12}$$

$$\sigma_\omega^2 = \int_{-\infty}^{+\infty} (\omega - \eta)^2 \hat{\psi}^2 d\omega \qquad \text{Equation 13}$$

Table 3 indicates that better performance is achieved in going from the pure Fourier atom (o resolution in time) to wavelets with adaptive resolution. Adaptive resolution means that in time the spread is proportional to scale and in frequency it is inversely proportional to scale. Therefore, when dealing with fast signals characterized by short scales the frequency support is widened, this assuring the correct representation of higher frequencies. Whilst, for slow signals (large scales) the frequency support is reduced, since the signal frequency content is smaller.

The wavelet representation (Continuous Wavelet Transform, CTW) in the realm of continuous real functions can be defined as (Daubechies, 1992):

$$c(b,s) = \frac{1}{\sqrt{s}} \int f(x) \psi\left(\frac{x-b}{s}\right) dx \qquad \text{Equation 14}$$

where $c(b,s)$ are the wavelet coefficients at point b in space and scale s, and are the fingerprints of the signal in the new representation.

The representation can be inverted to reconstruct the signal (Daubechies, 1992):

$$f(x) = \frac{1}{C_\psi} \iint \frac{1}{\sqrt{s}} c(b,s)\, \psi\left(\frac{x-b}{s}\right) \frac{dsdb}{s^2} \qquad \text{Equation 15}$$

Where C_ψ is a normalization factor that constrains the wavelet definition and assures the existence of the transform.

The representation in the wavelet basis is obtained by applying translations and dilations of the wavelet to the signal to be decomposed (Mallat, 2008). Considering a wavelet with dilation $s = 1$ we move the function along the signal of interest. At each point in space (e.g. at xn), the wavelet is multiplied with the signal. Given that the wavelet has short support (i.e. decays fast in space) it will capture the similarities (correlation) with the signal in a small neighbourhood of xn (Kumar & Foufoula-Georgiou, 1994).

Since the wavelet at dilation $s = 1$ oscillates fast around this point, it will even capture details of the signal that are also changing rapidly. The first wavelet coefficient will therefore capture information of rapidly changing features at each point in space. Using a dilated version of the wavelet ($s = 2$) slower evolving features will be captured given that these will resemble more the dilated wavelet. The wavelet coefficients will provide indication of where (in space) the signal presents dynamical features and how 'fast' they are (in term of frequency).

The new representation will enable to detect features of the signal by their dynamical properties (oscillations, impulses) that would otherwise not be detected within overlapping unwanted features (e.g. noise) (Katul & Parlange, 1994). Wavelets are also commonly used in filtering techniques by modifying the wavelet coefficients that belong to unwanted features and by reconstructing an approximation of the signal (Argenti & Alparone, 2002). Filtering techniques are not the objective of the thesis work and will therefore not be considered further.

The purpose of the research is to exploit the wavelet representation in the domain of space-frequency analysis, particularly to derive space-variant statistical measures of the signal from the statistics of the wavelet coefficients.

Remote sensing imagery (signal) is composed of discrete variables and not continuous functions (Vetterli, et al., 2014). As a consequence, the Discrete Wavelet Transform (DWT) was used in the thesis. The DWT is derived by discretising the translation and scale parameters Equation 14 as follows (Daubechies, 1992):

$$W(m,n) = \frac{1}{\sqrt{a_0^m}} \sum_k f_k \left(\frac{k - nb_0 a_0^m}{a_0^m} \right) \qquad \text{Equation 16}$$

where a_0 is the scale parameter, m is an integer number and b_0 is the translation parameter.

The scale parameter a_0 is usually set to $a_0 = 2$ (dyadic scales) and the translation parameter $b_0 a_0^m$ with b_0 =1 (implementation used in **Chapter 3** and **Chapter 4**) (Daubechies, 1992).

Another important point needs to be taken into account when going from a Continuous Wavelet Transform (CWT) to a Discrete Wavelet Transform (DWT) to assure a complete and stable basis, special conditions must be verified (Daubechies, 1992). A particular basis, the frame, is an optimal choice to ensure this. The frame used in this thesis work was designed by Mallat (2008) and can be obtained by discretizing a box spline function of order 3. The wavelet consists of only two points (Figure 9).

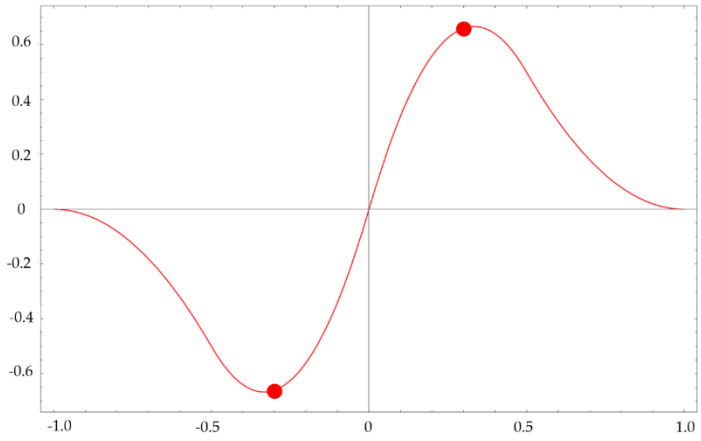

Figure 9. Mallat's wavelet frame chosen to undertake the textural analysis in the thesis. It consists of just 2 points when sampled at integer values (+0.5 and -0.5) and therefore acts as a differential operator.

2.4.1. Statistical Characterisation of Random Signals

Given the aims of this thesis, the main application of wavelet analysis was targeted at a statistical characterisation of the signal. This is achieved by considering the variance of the wavelet coefficients. When the non-dilated wavelet frame (Figure

9) is applied to the signal as in Equation 15, successive shifts of the wavelet will detect differences of the signal spaced by one pixel. The detected samples are squared (W^2), and a local average in the neighbourhood of a point j is taken:

$$\langle W^2(j)\rangle = \langle (s(j+1) - s(j)^2\rangle = 2\langle s^2\rangle - 2\langle s(j+1)s(j)\rangle \qquad \text{Equation 17}$$

Where s is the scale and j is a point in the image.

Equation 17 shows that the variance of the wavelet coefficients at scale 1 captures the signal second moment (first term) and the auto-correlation of the signal at lag 1 pixel (second term), when estimated in the neighbourhood of a point j.

When the wavelet is dilated by 2^m the resulting variance of the wavelet coefficients will be:

$$\langle {W^2}_{2^m}(j)\rangle = \langle (s(j+2^m) - s(j)^2\rangle = 2\langle s^2\rangle - 2\langle s(j+2^m)s(j)\rangle \qquad \text{Equation 18}$$

In this case, the wavelet variance will capture the auto-correlation of the signal at lag 2^m pixels when estimated in the neighbourhood of a point j.

The wavelet variance will provide the auto-correlation function of the process for a stationary process. In the case of non-stationary processes, processes whose mean changes over time, the wavelet variance will give point-estimates of the process second moment $2\langle s^2\rangle$ and of the process correlations $2\langle s(j+1)s(j)\rangle$ at each position within the signal. From this ability, the derivation of the wavelet spectrum ($Wspectr$) (Equation 19) is enabled, this being a statistical tool with the ability to map (in space) the structural properties of the natural target.

$$Wspectr\ (m,n) = \sum_t W^2(m,t) \times b(n-t) \qquad \text{Equation 19}$$

where $W(m,t)$ are the wavelet coefficients at scale 2^m and position index n, $b(n)$ is an averaging low pass filter, and the summation over t is performed over the width of the filter b. The wavelet spectrum provides therefore local estimates of the wavelet variance at scale m and position n.

The algorithm is not part of the developments that are the objective of the thesis. An overview was given to enable understanding of the motivation for its use and to enable interpretation of experimental results, these being the main objective of the thesis. The application of this method to SAR and InSAR signals and experimental results related to the detection of degraded forest are reported in **Chapter 3** and **Chapter 4**.

A comparison of the method based on wavelet statistics with alternative methods for spatial random fields (SF) analysis is reported in Table 4. Among the methods, we consider the auto-correlation function (ACF), co-occurrence matrix, and the wavelet variance. Non-stationarity qualifiers refers to the capability of characterising scale invariant fields (fractals) and estimate the power law with respect to the scale parameter. Intermittency measures refers to the ability of quantifying the ratio of the presence of coherent structures in a field (e.g. spikes, clusters). Anisotropy refers to the capability of measuring directional effects in the field statistics. Two-point-statistic refers to the fact that the measure is based on a relationship between elements in the field. Speckle sensitivity refers to the capability of the method to produce correct estimation of the underlying signal statistic (e.g. texture) in presence of multiplicative noise (e.g. in the case of SAR backscatter). Underpinning statistical theory refers to the availability of a consolidated theory supporting the method, in such a way that the result's interpretation can be based on a quantitative criteria (e.g. correlation length, process variance etc.).

Table 4. Spatial random field measures.

	ACF	**Co-occurrence matrix**	**Wavelet variance**
Non-stationarity qualifiers	No	No	Yes (structure function)
Intermittency measures	No	No	Yes (singular measures)
Anisotropy	No	Yes	Yes (gradient angle)
Two-point statistics	Yes	No	Yes
Speckle sensitivity	High	High	Low through normalisation
Underpinning statistical theory	Yes	No	Yes

2.5. Link between Forest Structure and SAR Signal Structure

The basic principle underlying the thesis work is that distribution in space of structural forest properties, such as canopy height and density, is reflected onto signal variation (spatial statistic) within backscatter and DSMs provided by SAR. As a consequence, statistical measures of the SAR observation were proposed as means to characterise different forest structure or their dynamics (e.g. primary or degraded forest). Insight related to the link between forest structure and SAR signal structure can be provided by considering scattering physics, and by simple models.

Firstly we consider the link between canopy height profile and the radar cross section fluctuations. A discrete imaging model is suggested by Williams (1997). The model consists in slicing the one-dimensional canopy profile into sections corresponding to the width of the SAR resolution element. In each independent section the radar reflectivity is modelled by a layer of Rayleigh scatterers within two regular surfaces, where the local incidence angle with respect to the top surface is dictated by the slope of the canopy profile. The model provides an estimate of the radar cross section as a function of local (within the slice) geometric parameters and dielectric properties of the medium (Williams, 1997):

$$\sigma^0 = f(\vartheta_i, k_e, h, \epsilon) \qquad \text{Equation 20}$$

Where ϑ_i is the local incidence angle, k_e is the extinction coefficient, h is the vegetation layer height and ϵ is the dielectric constant of the medium.

In particular, at X-band and C-band the wave penetration is short with respect to the canopy height, volume scattering becomes less important, the model predicts that backscatter is dominated by a micro-topography effect, with the upper canopy surface slope being the main driver. Therefore, the coupling between the radar reflectivity and canopy structure is established mainly by the geometry of the canopy height development in space and, to a less extent, by other local forest physical properties affecting extinction, such as canopy density and closure.

For the influence of forest structure on InSAR DSMs a different physics needs to be considered. While for the backscatter case the main effect was due to geometry (local incidence angle) of a surface lying on the top canopy layer, now the volume that is responsible for decorrelation needs to be considered. Within the volume, the main drivers affecting the coherence are the distribution of the scattering elements and the their scattering and extinction coefficients along the vertical coordinate (vertical structure function $f(z)$). Due to the heterogeneous composition of the forest, the structure function will also be a function of the space coordinates. The complex coherence for each resolution element at position x, y will be the result of a coherent sum of all the returns from the volume weighted by the vertical structure function. Considering Equation 21 (Cloude, 2010):

$$\gamma = \frac{\int_0^h f(\acute{z}) e^{i\beta\acute{z}} d\acute{z}}{\int_0^h f(\acute{z}) d\acute{z}} = F(f(z,x,y), h, z_0, \beta)\acute{z} = z - z_0 \qquad \text{Equation 21}$$

Where γ is the complex coherence, β is the vertical wavenumber, h is the volume height, z_0 is the topographic height of the vegetation volume, z is the vertical coordinate and x, y are the space coordinates of the resolution element.

Equation 21 emphasises that the structure function is also a function of position. A model based on these principles, is developed by Varekamp & Hoekman (2002). Variation of the structure function in space, cause by variation of the forest structure, will affect coherence phase, and, as a consequence, the phase centre height within the volume. Therefore, spatial static of the InSAR DSM is expected to reflect forest structural properties (see **Chapter 5**).

The wavelet space-scale analysis method outlined in this chapter sets the basis for deriving the results of the experiment described in the next chapter, where C-band (ENVISAT ASAR) and L-band (ALOS PALSAR) observations were used to discriminate between landcover classes. In particular, the chapter demonstrates the use of wavelet signature and wavelet spectra to detect patterns derived from differences in forest structure due to forest disturbance (e.g. differences between

intact forest and degraded forest) and the presence of edges within forest-savanna and forest-agriculture mosaic landcover classes. The experimental study focuses on semi-deciduous forest in South-East Cameroon.

2.6. References

- Airbus Defence and Space, 2014. *WorldDEM Technical Product Specification 1.0.* [Online]. Available at: http://www.engesat.com.br/wp-content/uploads/455-201404_worlddem_technicalspecs_i1 [Accessed 11 November 2015].
- Argenti, F. & Alparone, L., 2002. Speckle Removal From SAR Images in the Undecimated Wavelet Domain. *IEEE Transactions on Geoscience and Remote Sensing,* 40(11), pp. 2363-2374.
- Balzter, H., 2001. Forest mapping and monitoring with interferometric synthetic aperture radar (InSAR). *Progress in Physical Geography,* 25(2), pp. 159-177.
- Bamler, R., 2000. Principles of Synthetic Aperture Radar. *Surveys in Geophysics,* 21(2-3), pp. 147-157.
- Bamler, R. & Hartl, P., 1998. Synthetic Aperture Radar Interferometry. *Inverse Problems,* 14(4), pp. 1-54.
- Cloude, S., 2010. *Polarization applications in remote sensing.* 1st ed. Oxford, UK: Oxford University Press.
- Daubechies, I., 1992. *Ten Lectures on Wavelets.* 2nd ed. Philadelphia, PA: Society for Industrial and Applied Mathematics.
- Davis, A., Marshak, A. & Wiscombe, W., 1994. Wavelet-based multifractal analysis of non-stationary and/or intermittent geophisical signals. In: E. Foufoula-Georghiou & P. Kumar, eds. *Wavelets in Geophysics.* New Yor, NY, USA: Academic, p. 249–298.
- De Grandi, D., D, G., Lucas, R. M. & Kropacek, J., 2009. Analysis by wavelet frames of spatial statistics in SAR data for characterizing structural properties of forests. *IEEE Transactions on Geoscience and Remote Sensing,* 47(2), p. 494–507.
- De Grandi, G. et al., 2000. The Global Rain Forest Mapping Project JERS-1 Radar Mosaic of Tropical Africa: Development and Product Characterisation Aspects. *IEEE Transactions on Geoscience and Remote Sensing,* 38(5), pp. 2218-2233.
- ESA, 2016. *Sentinel-1 Product Definition.* [Online]. Available at: https://sentinel.esa.int/documents/247904/1877131/Sentinel-1-Product-Definition [Accessed 25 May 2016].

- European Space Agency, 2013. *Sentinel-1 User Handbook.* [Online]. Available at: https://sentinel.esa.int/web/sentinel/user-guides/sentinel-1-sar/revisit-and-coverage [Accessed 21 June 2016].
- European Space Agency, 2017. *The CEOS Database.* [Online]. Available at: http://database.eohandbook.com [Accessed 8 January 2017].
- Farr, T. et al., 2007. The Shuttle Radar Topography Mission. *Reviews of Geophysics,* 45(2), pp. 1-33.
- Fung, A. K., 1994. *Microwave Scattering and Emission Models and their Applications.* 1st ed. Norwood: Artech House Publishers.
- GAMMA, 2006. *GAMMA SAR and Interferometry Software,* Bern: GAMMA.
- Garestier, F., Dubois-Fernandez, P. C. & Papathanassiou, K. P., 2008. Pine Forest Height Inversion Using Single-Pass X-Band PolInSAR Data. *IEEE Transactions on Geoscience and Remote Sensing,* 46(1), pp. 59-68.
- Gatelli, F. et al., 1994. The Wavenumber Shift in SAR Interferometry. *IEEE Transactions on Geoscience and Remote Sensing,* 32(4), pp. 855-865.
- Gens, R. & Van Genderen, J. L., 1996. SAR interferometry- issues, techniques, applications. *International Journal of Remote Sensing,* 17(10), pp. 1803-1835.
- Hanssen, R. F., 2001. *Radar Interferometry.* 1st ed. Dordrecht, The Netherlands: Kluwer.
- Izzawati, Wallington, E. & Woodhouse, I., 2006. Forest Height Retrieval From Commercial X-Band SAR Products. *IEEE Transactions on Geoscience and Remote Sensing,* 44(4), pp. 863-870.
- Katul, G. G. & Parlange, M. B., 1994. On the Acive Role of Temperature in Surface-Layer Turbulence. *Journal of the Atmospheric Sciences,* 51(15), pp. 2181-2195.
- Krieger, G. et al., 2007. TanDEM-X: A Satellite Formation for High-Resolution SAR Interferometry. *IEEE Transactions on Geoscience and Remote Sensing,* 45(11), pp. 3317-3341.
- Kumar, P. & Foufoula-Georgiou, E. F., 1994. Wavelet Analysis in Geophysics: an Introduction. In: P. Kumar & E. F. Foufoula-Georgiou, eds. *Wavelets in Geophysics.* San Diego, California, USA: Academic Press, pp. 1-43.
- Le Toan, T. et al., 2011. The BIOMASS mission: Mapping global forest biomass to better understand the terrestrial carbon cycle. *Remote Sensing of Environment,* 115(11), pp. 2850-2860.

- Lee, J.-S. & Pottier, E., 2009. *Polarimetric Radar Imaging: From Basics to Applications.* 1st ed. Boca Raton(Florida): CRC Press.
- Mallat, S., 2008. *A Wavelet Tour of Signal Processing.* 3rd Edition ed. New York, NY: Academic Press.
- Mallat, S. & Zhong, S., 1992. Characterization of Signals from Multiscale Edges. *IEEE Transactions on Pattern Analysis and Machine Intelligence,* 14(7), pp. 710-732.
- Martone, M. et al., 2012. Coherence evaluation opf TanDEM-X interferometric data. *ISPRS Journal of Photogrammetry and Remote Sensing,* Volume 73, pp. 21-29.
- Martone, M., Rizzoli, P., Krieger & Gerhard, 2016. Volume Decorrelation Effect in TanDEM-X Interferometric SAR Data. *IEEE Geoscience and Remote Sensing Letters,* 13(12), pp. 1812-1816.
- Miranda, N. et al., 2013. *The ENVISAT ASAR Mission: A Look Back at 10 Years of Operation.* Edinburgh, UK, ESA.
- Moreira, A. et al., 2015. Tandem-L: A Highly Innovative Bistatic SAR Mission for Global Observation of Dynamic Processes on the Earth's Surface. *IEEE Geoscience and Remote Sensing Magazine,* 3(2), pp. 8-23.
- Moreira, A. et al., 2013. A Tutorial on Synthetic Aperture Radar. *IEEE Geoscience and Remote Sensing Magazine,* 1(1), pp. 6-43.
- Oliver, C. & Quegan, S., 2004. *Understanding Synthetic Aperture Radar Images.* 2nd ed. Herndon, VA: SciTech Publishing.
- Peebles, P., 1980. *Probability, Random Variables, and Random Signal Principles.* 2nd ed. New York: McGraw-Hill Science.
- Praks, J., Antropov, O. & Hallikainen, M., 2012. LIDAR-Aided SAR Interferometry Studies in Boreal Forest: Scattering Phase Center and Extinction Coefficient at X- and L-Band. *IEEE Transactions on Geoscience and Remote Sensing* , 50(10), pp. 3831-3843.
- Richards, M. A., 2006. A Beginner's Guide to Interferometric SAR Concepts and Signal Processing. *IEEE Aerospace and Electronic Systems Magazine,* 21(6), pp. 5-29.
- Rosen, P. et al., 2000. Synthetic Aperture Radar Interferometry. *Proceedings of the IEEE,* 88(3), pp. 333-382.
- Rosenqvist, A. et al., 2004. *An overview of the JERS-1 SAR Global Boreal Forest Mapping (GBFM) project.* Anchorage, Alaska, USA, Proceedings of the IEEE International Geoscience and Remote Sensing Symposium.

- Rosenqvist, A., Shimada, M., Norimasa, I. & Watanabe, M., 2007. ALOS PALSAR: A Pathfinder Mission forGlobal-Scale Monitoring of the Environment. *IEEE Transactions on Geoscience and Remote Sensing,* 45(11), pp. 3307-3316.

- Sarmap, 2016. *SARscape Guide.* [Online]. Available at: https://www.harrisgeospatial.com/docs/pdf/sarscape_help.pdf [Accessed 20 May 2016].

- Simard, M., De Grandi, G., Thomson, K. P. B. & Benie, G. B., 1998. Analysis of speckle noise contribution on wavelet decomposition of SAR images. *IEEE Transactions on Geoscience and Remote Sensing,* 36(6), pp. 1953-1962.

- Treuhaft, R. et al., 2015. Tropical-Forest Biomass Estimation at X-Band From the Spaceborne TanDEM-X Interferometer. *IEEE Geoscience and Remote Sensing Letters,* 12(2), pp. 239-243.

- Treuhaft, R. N. & Siqueira, P. R., 2000. Vertical structure of vegetated land surfaces from interferometric and polarimetric radar. *Radio Science,* 35(1), pp. 141-177.

- Varekamp, C. & Hoekman, D. H., 2002. High Resolution InSAR Simulation for Forest Canopies. *IEEE Transactions on Geoscience and Remote Sensing* , 40 (7), pp. 1643-1655.

- Vetterli, M., Kovačević, J. & Goyal, V. K., 2014. *Foundations of Signal Processing.* 3rd ed. Cambridge: Cambridge University Press.

- Williams, M. L., 1997. *Influence of Canopy Shape on SAR Speckle Distributions over Woodland.* Singapore, Proceedings of the IEEE International Geoscience and Remote Sensing Symposium, pp. 755-757.

- Woodhouse, I. H., 2005. *Introduction to Microwave Remote Sensing.* 1st ed. Boca Raton(Florida): CRC Press.

- World Meteorological Organization, 2017. *Observing Systems Capability Analysis and Review Tool.* [Online]. Available at: https://www.wmo-sat.info/ [Accessed 8 January 2017].

- Zebker, H. A. & Goldstein, R. M., 1986. Topographic Mapping From Interferometric Sythetic Aperture Radar Observations. *Journal of Geophysical Research,* 91(B5), pp. 4993-4999.

3. Spatial Wavelet Statistics of SAR Backscatter for Characterising Degraded Forest: A Case Study from Cameroon

Elsa C. De Grandi[a], Edward Mitchard[a], Iain H. Woodhouse[a], and Gianfranco D. De Grandi[b]

[a]School of GeoSciences, University of Edinburgh, Edinburgh EH9 3FF, U.K.
[b]Aberystwyth University, Aberystwyth SY233F, U.K.

Published in *IEEE Journal of Selected Topics in Applied Earth Observations and Remote Sensing*, May 2015[1]

Author contributions: Elsa Carla De Grandi conceived and designed the experiments (assisted by Edward Mitchard, Iain Woodhouse and Gianfranco D. De Grandi). Elsa Carla De Grandi processed the ENVISAT ASAR and ALOS PALSAR data, analyzed the data and wrote the paper. Gianfranco D. De Grandi developed the wavelet method. Edward Mitchard, Iain Woodhouse and Gianfranco D. De Grandi provided comments on the manuscript.

[1]*IEEE Journal of Selected Topics in Applied Earth Observations and Remote Sensing*, vol. 8, no. 7, pp. 3572-3584, doi: 10.1109/JSTARS.2015.2420596. See Appendix I.

Abstract

Forest degradation is an important issue in global environmental studies, albeit not yet well defined in quantitative terms. The present work attempts to address the problem, by starting with the assumption that forest spatial structure can provide an indication of the process of forest degradation, this being reflected in the spatial statistics of synthetic aperture radar (SAR) backscatter observations. The capability of characterizing landcover classes, such as intact and degraded forest (DF), is tested by supervised analysis of ENVISAT ASAR and ALOS PALSAR backscatter spatial statistics, provided by wavelet frames. The test is conducted in a closed semideciduous forest in Cameroon, Central Africa. Results showed that wavelet variance scaling signatures, which are measures of the SAR backscatter two-point statistics in the combined space-scale domain, are able to differentiate landcover classes by capturing their spatial distribution. Discrimination between intact and degraded forest was found to be enabled by functional analysis of the wavelet scaling signatures of C-band ENVISAT ASAR data. Analytic parameters, describing the functional form of the scaling signatures when fitted by a third-degree polynomial, resulted in a statistically significant difference between the signatures of intact and degraded forest ($p < 0.05$, $n = 20$). The results with ALOS PALSAR, on the other hand, were not significant. The technique sets the stage for promising developments for tracking forest disturbance, especially with the future availability of C-band data provided by ESA Sentinel-1.

3.1. Introduction

Forests play a fundamental role in the exchange of gases and energy between the atmosphere and biosphere. In particular, degraded forests (DFs) in tropical forest ecosystems are a large component of the global carbon balance, with the process of degradation representing a large but hard to quantify source of carbon, whereas regrowing degraded forests are also responsible for a significant carbon sink (Grace, et al., 2014). Recognition of the role of deforestation and forest degradation by the U.N. General Assembly has stressed the need for mapping the extent of deforested and degraded forests (Mertz, et al., 2012), in order to enable a successful system for reducing emission from deforestation and forest degradation (REDD+). The International Tropical Timber Organization estimated that there are up to 850 million ha of tropical forest which have already been degraded (Thompson, et al., 2013) due to intensive pressures such as logging, slash and burn agriculture, and shifting cultivation outside of protected areas.

Forest degradation in a remote sensing context can be defined from the ecological standpoint and at a conceptual level as an environmental change process, where a disturbance causes the system to evolve from an initial state toward a final state with loss of valuable properties (e.g., canopy cover or carbon stocks) or capacities (e.g., provision of fuelwood and other ecosystem services). This initial state constituted a spatially contiguous and unmanaged old-growth forest [intact forest (IF)]. If some of its structural and physical properties are affected by a major disturbance (logging, fire, insect infestation, timber harvest, or windthrow), then the system will change to a final state, characterized by a different forest type (i.e., secondary forest or disturbed forest).

A mapping between the ecological process of forest degradation and physical observables is needed to provide measures of its onset and extent. The basic tenet of the work presented in this paper is that the process of forest degradation will result in a change of the forest structure. As a consequence, the mapping was established by considering synthetic aperture radar (SAR) backscatter spatial statistics (texture) as a measure of forest structure, this in turn being one of the ecological variables

that can be assumed to be a fingerprint of the degradation process. Different stages of the degradation process will result in changes of the statistics. For instance, removal of part of an old-growth forest will correspond to the transition from some stationary regime due to backscattering from the irregular top layer of the canopy [e.g., K-distributed with an exponential cosine autocorrelation function (ACF)] (Oliver, 1986) to some nonstationary or intermittent regime. At the final stage of regrowth, when a secondary forest will have taken place, the statistics will revert back to stationary, albeit with different correlation properties due to the different horizontal structure.

This starting assumption is tested by supervised statistical analysis of spatial random fields (SRFs) provided by SAR observations at C- and L-band, i.e., calculating statistics over areas of interest based on expert knowledge and the interpretation of other satellite. The spatial statistics are derived from a signal representation in a wavelet frame basis. The analysis seeks to assess the capability of these textural measures to discriminate between intact and degraded forest.

3.2. Background and Context

Remote sensing plays a primary role for mapping and monitoring deforestation and forest degradation for REDD+ (Global Forest Observations Initiative, 2014). In particular, compared to deforestation, forest degradation is more difficult to detect using remote sensing (Ahrends, et al., 2010; Mon, et al., 2012).

Mapping and monitoring of forest degradation has been the main focus of research efforts by employing optical remote sensing due to the availability of Landsat (Stone & Lefebvre, 1998; Hirschmugl, et al., 2014) and by using spectral mixture analysis methods to enhance canopy damage due to forest degradation (Souza, et al., 2005). Fine resolution optical data has been employed for mapping selective logging proxy indicators (e.g. log landings and logging roads), including IKONOS (Souza & Roberts, 2005) and RapidEye (Franke, et al., 2012); but to our knowledge, such methods have not been used to map actual forest degradation (as opposed to the presence of proxy indicators) in African forests.

Limitations of optical sensors have given impetus to the use of sensors independent of atmospheric conditions, such as SAR, which allows observations regardless of cloud cover and illumination conditions, but most importantly is sensitive to both forest vertical structure (through interferometry) and horizontal structure (through backscatter and coherence).

Five main aspects related to forest degradation have been the focus of research: 1) above-ground biomass and carbon stock changes using SAR backscatter (e.g., Mitchard, et al., (2012); 2) classification of degraded forest and particularly the contribution of texture (focus of the present research); 3) detection of the removal of single trees using very high resolution SAR imagery (e.g., Kuntz, et al., 2011); 4) use of interferometric phase information to determine a change in the canopy structure which can be associated with removal of vegetation (e.g., Deutscher, et al., 2013; Global Forest Observations Initiative, 2014); and 5) use of coherence to provide information on canopy openness (Schlund, et al., 2014).

The future provision of Sentinel-1 (C-band) will enable to study forest degradation at increased revisit time leading to unprecedented levels of SAR data availability (Attema, et al., 2007).

A further topic of interest is the classification of degraded forest, which can be accomplished with the addition of texture that provides complementary knowledge to intensity-only information (Benelcadi, et al., 2012).

The main research that has been employed in the domain of texture analysis for landcover classification includes the use of Haralick parameters based on gray-level co-occurrence matrix (GLCM) (Haralick & Bryant, 1976) and spectral analysis (or ACF, these being techniques in the Fourier transform domain). Notice that the ACF provides a two-point statistics, while GLCM is a second-order one-point one.

The limitations in using these methods for the classification of SAR data are twofold. First, direction constraints on GLCM and insensitivity to short-lived high frequencies in the Fourier transform limit the ability of these methods to quantify the evolution of statistical properties through scale (Sarker, et al., 2013). Second, by their nature, SAR sensors are affected by both multiplicative noise and correlated noise: this means that simple relationships among neighbouring pixels can either bear no information, being themselves just stationary white noise, or even provide false information; for instance, two constant reflectivity areas might be measured as two textured areas because of the presence of speckle. GLCM and ACFs are both highly sensitive to speckle noise. A way out suggested in related work such as in Beauchemin et al. (1996) to apply these statistics after transforming the input signal to the logarithmic domain. This transform makes the multiplicative noise additive. However, introduces side effects such as compressing high dynamics features and boosting low-level noise, such as thermal noise.

Wavelet transforms provide a modern pathway to time frequency (space-scale) analysis with better resolution in the combined domain, and superior computational efficiency on the discrete setting. Moreover, wavelet statistics can be normalized in such a way as to be compatible with multiplicative noise without recurring to the logarithmic transform (see Section 3.4.3).

The field of wavelets developed in the mid-1980s with research by Daubechies (1998) originally, wavelet transform developed in the field of geophysics applied to time-series analysis of one dimensional (1-D) geophysical signals (Kumar & Foufoula-Georgiou, 1997); but since then have been applied in the field of remote sensing including landcover classification using SAR, which is becoming more popular (Cutler, et al., 2012).

Techniques based on the use of wavelet transform with SAR imagery have seldom been used in the thematic context of forest degradation. However, wavelet statistics of SAR backscatter in connection with textural analysis was proposed in a different thematic context in Simard et al. (1998) and De Grandi et al. (2009) and in general, its utility in image processing have been long understood (Unser, 1995).

3.3. Study Site

We center our study in Cameroon, a country of great interest for forest monitoring, since it is the African country with the highest percentage of previously logged forests (Bellassen & Gitz, 2008). Over a third of its territory is covered by moist tropical forest, part of the Congo Basin, and the area covered by active or previously active logging concessions extends over 71 000 km^2, about 40% of total forest area (Mertens, et al., 2012). Cameroon is also a significant hotspot of other forms of forest degradation, including those related to agricultural encroachment, fuelwood extraction, and illegal logging (Bellassen & Gitz, 2008): it is more affected by these than its Congo Basin neighbours as it has a significantly higher population density than neighbouring Gabon, Democratic Republic of the Congo, or the Republic of Congo.

The study site encompasses semi-deciduous closed forest located in Deng Deng National Park and its surroundings in Lom et Djerem, Cameroon (13° 4' E, 5° 28' 39 N). The study site extends for 100 × 100 km^2 and is delimited by the Sanaga River to the west and the forest savanna transition zone to the east (Figure 1). The main urban centre in the area of study is the region's capital Bertoua while, a high number of rural villages are distributed across the landscape contributing to the

highest rate of rural population exploiting forest resources mainly in the form of slash and burn agriculture at small to medium scales (Mertens, 2000). The forest in the area is a semi-deciduous closed forest dominated by *Sterculiaceae* and *Ulmaceae* and extends to the north of the moist evergreen forest (FAO, 1985). Human intervention is widespread in the area giving rise to several stages of degraded forest and areas of regenerating forest developing into secondary formations characterized by *Musanga cecropioides* and *Albizi*a spp. (Tegechouang, 2010).

Another driver of forest degradation is selective logging within the forest management units (UFAs). The logging industry has been present in the area and exploited forest resources through the selective removal of a limited number of high-value trees. Even though the UFA had been exploited long in the past, the presence of old logging roads was still clearly visible in the 2010 Landsat and RapidEye imagery (and less evident in radar imagery).

The climate is classified as equatorial (Guinean type) with one major wet season (September–November) (monthly rainfall over 250 mm) and dry season with rainfall as low as 10 mm (December–February) (World Bank, 2014). Rainfall at the time of ENVISAT ASAR data acquisition (January 15, 2010) and ALOS PALSAR (August 3, 2010) can be considered negligible, since the data was acquired in the dry season. Topography in the study site is hilly to mountainous ranging from 597 to 1060 m with areas of more pronounced topography located to the north of the study site in the forest-savanna mosaic, whereas topography is more gentle in the areas of semi-deciduous forest (ranging between 597 and 700 m a.s.l.).

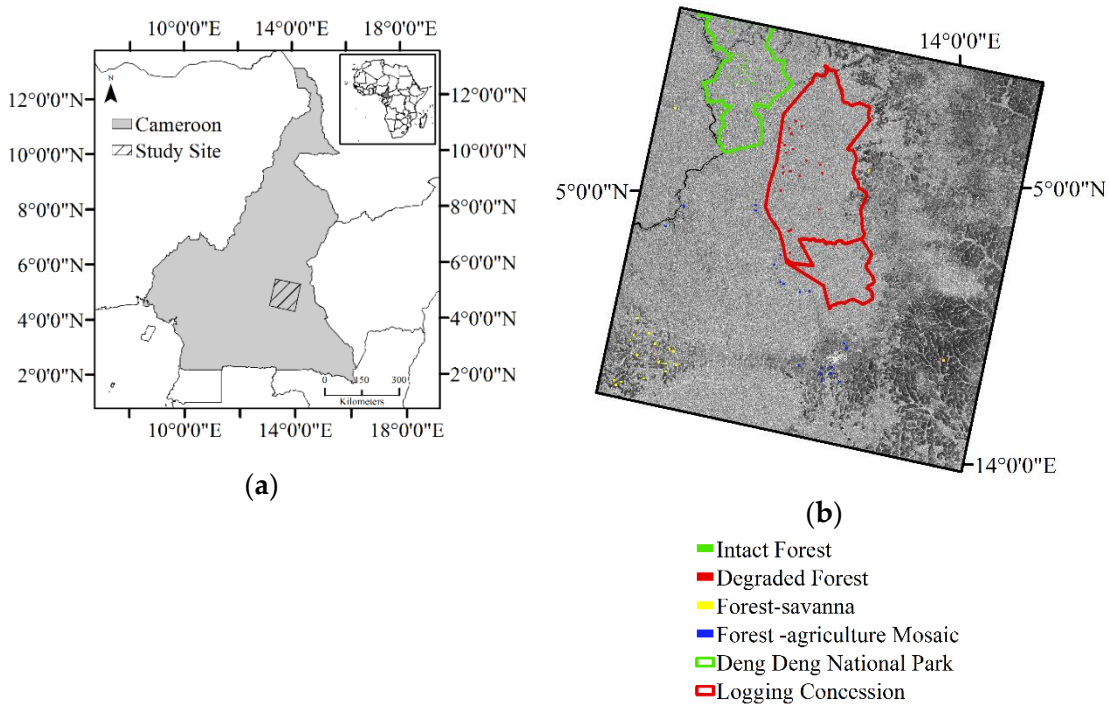

Figure 1. (**a**) Study area within the extent of ENVISAT ASAR acquisitions (WGS84, UTM zone 33 N). (**b**) Location of all landcover samples (N = 80) selected based on VHR RapidEye imagery (27/12/2010) and Landsat 7 (18/01/2011 and 17/12/2010) used in the analysis overlaid on ENVISAT ASAR VV (WGS84, UTM projection-zone 33N). The green shape outlines Deng Deng National Park. The red shape outlines a logging concession. Red squares mark samples of degraded forest (DF) within the concession (*n*= 20), green squares mark intact forest (IF) samples inside the National Park (*n*= 20), yellow squares mark samples within forest-savanna (FS) (*n*= 20) and blue squares mark samples within forest-agriculture mosaic (FAM) (*n*= 20) (see also Table 1). Data source: World Resources Institute and European Space Agency.

3.4. Methods

Methods employed for the analysis of both ENVISAT ASAR (VV) and ALOS PALSAR (HH and HV) scenes comprise the following steps: 1) SAR data processing; 2) thematic class definition and supervised selection of a spatial test set for SAR statistics estimation (43 x 43 pixels windows) for each class; and 3) wavelet

transform of the test set SRFs and wavelet coefficients statistics computation and interpretation.

3.4.1. SAR Data Processing

Nine ENVISAT ASAR IMS scenes were acquired between 2003 and 2010 at VV polarization, IS2 mode (23° incidence angle) over the study area. The datasets were processed using the basic processing module available with SARscape 5.0 software (Sarmap, 2012). The scenes were multi-looked, co-registered, radiometrically calibrated and radiometrically normalized (cosine correction) using a 90 m Shuttle Radar Topography Mission (SRTM) Digital Elevation Model (DEM), geocoded to WGS84, UTM projection (zone 33N) at 15 m pixel spacing. Importantly, the time-series was speckle filtered using "De Grandi multitemporal filter" available in SARscape 5.0 and based on the principles proposed in De Grandi et al. (1997). This step enables the reconstruction of the radar cross-section (RCS) with good preservation of its two-point spatial statistics, whereas abating the strength of the high-frequency noise induced by the fading process to a level inversely proportional to the number of samples in the series. It is therefore fundamental with respect to the capability of retrieving textural properties of the imaged target.

Most of the analysis presented here was then undertaken on a single ENVISAT ASAR scene (January 15, 2010), since it was acquired during the dry season with minimal influence from rainfall events and, correspondent with available ALOS PALSAR and RapidEye data.

Twelve ALOS PALSAR fine beam dual (FBD) scenes were acquired between 2007 and 2010 at HH and HV polarizations and 34° incidence angle. This dataset was processed using the same approach as above.

Supplementary optical data for the interpretation of SAR imagery consisted of Landsat ETM+ (slc-off) at 30-m resolution acquired on January 18, 2011 covering the northernmost part of the study site and Landsat ETM+ (slc-on) data acquired on December 17, 2010 covering the southern part of the study area. The scenes were the only available which were not affected by extensive cloud cover and closest to the

data of the SAR data acquisition. RapidEye at 5-m resolution was also acquired on December 17, 2010 for training purposes covering a selected area of the Unité Forestière d'Aménagement (UFA 10 065) and part of Deng Deng National Park. Contextual data consisting of UFAs, logging roads (digitized with the aid of Landsat), location of protected areas (e.g., Deng Deng National Park) were provided by World Resources Institute (2014). The data were used to help with the selection of classes of interest through a supervised analysis.

3.4.2. Spatial Test Set Preparation by Supervised Analysis

A supervised analysis was chosen due to unavailability of ground truth data for 2010, thus the use of optical imagery and contextual information was used for training purposes. The analysis uses a 43 × 43 pixel window (corresponding to 645 × 645 m^2) on ENVISAT ASAR and ALOS PALSAR geocoded scenes at 15 m pixel spacing. The window size was determined to include a sufficient number of pixels to enable computation of the scaling signature through 4 dyadic scales and also to ensure a significant number of samples within each window for statistical analysis. The classes selected correspond to the following: intact forest (IF), degraded forest (DF), forest-agriculture mosaic (FAM), and forest-savanna (FS). Four samples were used in parts of the analysis but twenty samples were selected for each class of interest to ensure a significant sample size for statistical analysis.

Intact forest samples were selected based on contextual information including the extent of Deng Deng National Park and the absence of logging roads and urban centers in the areas chosen. The chosen areas are all located in the northern section of the Deng Deng National Park, which is known to be intact and has no sign of logging roads in any ancillary dataset.

Degraded forest samples were identified based on the proximity of inactive logging roads (in 2010) inside UFA which were clearly visible in both Landsat and RapidEye data at the time of the analysis and were also noticeable back in the 1980s Landsat imagery, thus indicating the long term pattern of disturbance of forest inside the logging concession. Forest-agriculture mosaic could be clearly identified

in both Landsat and RapidEye scenes as the most complex and heterogeneous class among those selected due to the presence of a mixture of forest, bare soil, and agricultural fields. The pattern of anthropogenic disturbance was also very clear due to the proximity to rural settlements. Forest-savanna was clearly identifiable due to the presence of large patches surrounded by forest ribbons and presented lower and presented lower backscatter values in ENVISAT ASAR VV and ALOS PALSAR HH and HV scenes compared to dense forested areas.

Table 1. Four landcover samples used in the analysis (WGS84, UTM projection - Zone 33 N).

Class	Center Pixel Coordinates
Intact forest (IF)	329220 E, 586850 N
Degraded forest (DF)	344085 E, 556755 N
Forest-agriculture mosaic (FAM)	306510 E, 543045 N
Forest-savanna (FS)	363405 E, 558060 N

3.4.3. Spatial Statistics From a Wavelet Frame Basis Representation

The spatial statistics of interest are derived from a signal (field) representation provided by a nonorthogonal oversampled discrete wavelet transform (DWT). The basis for this representation is generated by a wavelet frame (Daubechies, 1992). The advantage of such an approach in connection with texture (spatial statistic) analysis is proven in Unser (1995). In our case, the mother wavelet in the continuous scale-space domain is the first derivative of a box spline of order 3 (Mallat, 1998) (see Figure 2), with Fourier transform.

$$\widehat{w}(\omega) = -i\frac{\omega}{4}\left(\frac{sin\left(\frac{\omega}{4}\right)}{\frac{\omega}{4}}\right)^4 e^{-i\frac{\omega}{2}} \qquad \text{Equation 1}$$

In the discrete case, the transform is implemented using a variant of the à trous algorithm (Shensa, 1992; Mallat, 1998), with four voices per octave. The design of the multivoice scheme entails the following steps. For each voice in the first octave, a fractionally dilated wavelet is computed in the frequency domain from (Equation 1):

$$\Psi_{\mathrm{dil}}(\omega) = \frac{1}{\sqrt{2^d}} 2^d \Psi\left(2^d \omega\right) e^{-i\omega\left(\frac{1}{2}\left(2^d-1\right)\right)} \qquad \text{Equation 2}$$

where the fractional dilation factor $d = 0.25\, k, k = 0 \cdots 3$. The dilated wavelet is normalized by $\frac{1}{\sqrt{2^d}}$ to preserve the norms, and shifted by $e^{-i\omega\left(\frac{1}{2}\left(2^d-1\right)\right)}$ in such a way so as to match the zero crossings of the original mother wavelet.

Importantly, the multivoice scheme using the à trous algorithm can only be implemented with the $s^{-1/2}$ normalisation to assure equal norms among the mother wavelets which sample the frequency lattice within one octave. In this way, wavelet coefficients corresponding to all voices and octaves carry comparable energy, and can be used in forming measures, e.g., two-point statistics of the signal.

The à trous algorithm (Shensa, 1992; Mallat, 1998), calls for the approximation of the continuous space wavelet by means of an interpolating filter. This condition is expressed in the time and frequency domain by

$$\frac{1}{\sqrt{2}} \psi\left(\frac{t}{2}\right) = \sum_n h[n] \phi(t-n) \qquad \text{Equation 3}$$

$$\frac{2}{\sqrt{2}} \Psi_{\mathrm{dil}}(2\omega) = H_j(\omega) \Phi(\omega) \qquad \text{Equation 4}$$

The high-pass filter coefficients for each fractionally dilated wavelet are computed from Equation 4 by inverse discrete Fourier transform (DFT):

$$h_j[n] = \frac{1}{2\pi} \int_{-\pi}^{+\pi} H_j(\omega)\, e^{i\omega n} d\omega \qquad \text{Equation 5}$$

where j is the voice index.

Each dilated high pass filter h_j for each voice is finally used in a in a recursive à trous decomposition scheme to generate wavelet coefficients at the corresponding dyadic scales $2^{d+j}, j = 1 \ldots n$.

In case of analysis of a two-dimensional (2-D) field, the DWT is implemented by separable (row, columns) convolutions with a low-pass and a high-pass filter (Mallat, 1998)

$$\begin{aligned} f_{s+1}(i,j) &= g_s(j)g_s(i)\otimes_j\otimes_i f_s(i,j) \\ c_{x,s+1}(i,j,v) &= h_s(j,v)\otimes_j f_s(i,j) \\ c_{y,s+1}(i,j,v) &= h_s(i,v)\otimes_i f_s(i,j) \end{aligned} \qquad \text{Equation 6}$$

where $\otimes_j$is the convolution operator over columns, and $\otimes_i$ is the convolution operator over lines, $f_1(i,j)$ is the input signal, h_s is high pass filter at level s and voice v, g_s is low-pass filter (à trous filter) at level s, both filters being upsampled by dilation with s zeros.

In a nutshell, the multivoice scheme for v voices is implemented by applying the à trous algorithm, valid for power of two scales, v times starting from each fractionally dilated mother wavelet.

Importantly, the wavelet coefficients in Equation 6 are normalized by smooth approximations of the input fields $\overline{\overline{f(i,j)_s}}$ at the corresponding scales. The smooth approximations are obtained by convolution with separable smoothing spline filters with unit norm (energy conserving) and dilated by a factor corresponding to the scale s. This position (as pointed out in (Simard, et al., 1998) is necessary to avoid influence on the wavelet statistics of the fading variable when multiplicative noise is developed, and to equalize the dynamic range of the variable of interest (RCS). Theoretical characterization (bias and variance) of estimators of normalized wavelet coefficients is given in De Grandi, et al., (2007).

The mother wavelet (Figure 2) acts as a differential operator. It is this characteristic that establishes the bridge for reaching over to the spatial statistics of interest. Indeed, a wavelet which is a symmetric and odd function of the space coordinate (as the one considered here), when translated performs differences between averages of the signals around points whose distance is proportional to the dilation factor (scale). This leads to consider the following equivalence between

local averages of the wavelet coefficients squared and a two-point statistic known as structure function of order 2

$$\langle {c_{x,s}}^2 \rangle \cong \langle (f(x+\tau) - f(x)^2 \rangle \text{ where } s \xrightarrow{yields} \tau \qquad \text{Equation 7}$$

where ⟨⟩ is a spatial average operator.

In turn, this statistic leads to the characterization of stationary random processes, as well as of nonstationary processes with stationary increments (e.g., fractals) (Davis, et al., 1994). The wavelet variance as a function of scale provides in the log–log variance/scale plane a characteristic signature of the process and measures of the process parameters, such as correlation structures in stationary processes and the scaling exponent in 1/f processes.

Computationally, the wavelet scaling signature (WASS) is estimated from the wavelet coefficients of the 2-D DWT Equation 6 within a 43 × 43 pixels window of the backscatter image centered around points of interest (see Section 3.4.2 for the selection criteria).

$$\begin{aligned} WS_x(s) &= \langle c_{x,s}(i,j)^2 \rangle \\ WS_y(s) &= \langle c_{y,s}(i,j)^2 \rangle \end{aligned} \qquad \text{Equation 8}$$

where the average is taken over the estimation window. The standard error of the wavelet variance estimator S^2 (Equation 8) is $\sigma_{S^2} = S^2 \sqrt{\frac{2}{n-1}}$, where n is the number of samples in the estimation window.

When a second realization of the input random field is available, this being acquired at a different date or with different sensor's configuration (e.g., polarization, incidence angle), a scaling signature can be constructed with the wavelet coefficients cross-correlation

$$\begin{aligned} WCRS_x(s) &= \frac{\langle {c_{x,s}}^1(i,j) {c_{x,s}}^2(i,j) \rangle}{\left(\langle {c_{x,s}}^1(i,j)^2 \rangle \langle {c_{x,s}}^2(i,j)^2 \rangle \right)^{1/2}} \\ WCRS_y(s) &= \frac{\langle {c_y}^1(s,i,j) {c_y}^2(s,i,j) \rangle}{\left(\langle {c_{y,s}}^1(i,j)^2 \rangle \langle {c_{y,s}}^2(i,j)^2 \rangle \right)^{1/2}} \end{aligned} \qquad \text{Equation 9}$$

In the case of spatial statistics, this signature provides an indicator of the textural difference of the observed random fields between acquisitions. For acquisitions at different dates, the wavelet cross-correlation extends the statistics to the time– space–frequency domain.

A second point of view leads us to consider the generation of a scale-dependent gradient field $\in (s,x,y)$ from the wavelet coefficients, which in turn can be used as a random measure in intermittency analysis. Intermittency in our context can be generated in a random field by the presence of singularities such as edges and point targets. The normalized fourth moment of the gradient modulus (called the flatness factor) is taken in this case as an indicator of intermittency within the random field. Indeed, the fourth moment of a probability density function (pdf) (kurtosis) is related to the flatness of the distribution's tails. Since the wavelet frame is a differential operator, thick tails of the distribution indicate the presence of spikes or events with high derivative. The wavelet flatness factor signature (dependence on scale) is computed in a way similar to the wavelet scaling signature (Equation 9):

$$FlS_x(s) = \frac{\langle c_{x,s}(i,j)^4 \rangle}{\langle c_{x,s}(i,j)^2 \rangle^2}$$
$$FlS_y(s) = \frac{\langle c_{y,s}(s,i,j)^4 \rangle}{\langle c_{y,s}(s,i,j)^2 \rangle^2} \qquad \text{Equation 10}$$

Finally, the gradient field modulus squared can be interpreted as the signal energy captured at every point visited by the translated and dilated wavelet in the space-scale lattice and within the resolution cell at that point (Heisenberg box) (Mallat, 1998). Local estimates of the $\in (s,x,y)$ field through the related wavelet coefficients provide a space–frequency analysis of the input random field energy, which is called the wavelet spectrum. The wavelet spectrum is computed by convolution of the wavelet coefficients with a smoothing kernel (a cubic spline β_m, with support m= 25 pixels)

$$Wspctr(s,i,j) = \left(c_{x,s}(i,j)^2 + \langle c_{y,s}(i,j)^2 \rangle\right) \otimes \beta_m(i,j) \qquad \text{Equation 11}$$

Since $W\ spectr\ (s, i, j)$ is a function of three variables, a three-dimensional (3-D) graphic representation is obtained by averaging in one direction (columns or rows). The spectrum is then pictured in a 2-D density plot, with space, scale on the x-, y-axis and a colour palette to represent power density.

In space-scale (time-frequency) analysis, which underpins all the derived spatial statistics considered here, the most important factor is the combined resolution in the two dimensions of the domain. Wavelet provides adaptive resolution with increased frequency support and short-time spread at short scales, and decreased frequency support and wider time spread at long scales. It is important to quantify the combined resolutions and to put these measures in comparison with the order of magnitude of space variations expected in the physical phenomenon of interest (e.g., forest canopy horizontal distribution). The space and frequency spread of the wavelet was computed as follows.

The wavelet $\psi(s, x)$ at each scale s is normalized in such a way that $\|\psi\| = 1$ and shifted to be centered at x = 0. In this way, the spread in space and frequency is

$$\sigma_x^2 = \int_{-\infty}^{+\infty} x^2 \psi^2\, dt \qquad \text{Equation 12}$$

$$\sigma_\omega^2 = \int_{-\infty}^{+\infty} (\omega - \eta)^2 \hat{\psi}^2\, d\omega \qquad \text{Equation 13}$$

where $\hat{\psi}$ is the Fourier Transform of ψ and η is the center frequency.

The spreadσ_x and σ_ω were computed for the first four voices (Table 2). In Table 2, $\sigma_{space}\ (m)$ is the resolution in space related to the reference system of the geocoded SAR imagery with a pixel spacing of 15 m. $\sigma_{period}\ (m)$ is the resolution if frequency given as period $T = \frac{2\pi}{\omega}$, where ω is the frequency given as number of cycles within the estimation window length.

Values in the table can be interpreted as follows. First, notice that resolutions in the space-scale (time–frequency) plane were computed for the continuous wavelet

transform, therefore, space is defined on the real numbers set, and the support of the mother wavelet at scale 1 is in $d = [-1,1]$. Normalized values in the space domain are then converted in metric units with $d\,\Delta\,x\,[m] = [-15,15]$. Values at the next dyadic scales can be computed simply by multiplication (division) by 2.

Table 2. Wavelet resolution for the first four voices.

Scale	$\sigma_{space}[m]$	$\sigma_{period}[m]$	$\sigma_{freq}[cycles/winl]$
2^0	11.34	4.20	1513
$2^{0.25}$	13.48	5.19	1227
$2^{0.5}$	16.03	9.42	675
$2^{0.75}$	19.07	19.76	322
2	22.68	40.61	156

With these figures in mind, let us imagine of considering a backscatter signal portraying intermittent hard targets (e.g., buildings) and periodic features (e.g., a forest canopy or ocean waves). Values σ_{space} (m) tell us that we could distinguish, by the wavelet multiscale representation, the impulsive features if they are spaced apart a distance greater than these values. Values σ_{period} (m) tell us that we could detect the periodic features if their period is greater than those values. Finally, the last column gives us an indication of how many oscillations of the periodic phenomena we could at most observe within an estimation window of 615 m.

In our thematic context, we could conclude regarding space resolution: The first four voices do not provide useful information, being the resolution less than the sensor's one; intermittency patterns with characteristic spacing of $2^j \times 23$ m will be best detected at corresponding resonating scales 2^j. Regarding frequency resolution, the spatial frequency components of an homogeneous forest canopy, this developing with a characteristic period of some $2^j \times 40$ m could be best measured at resonating scales 2^j.

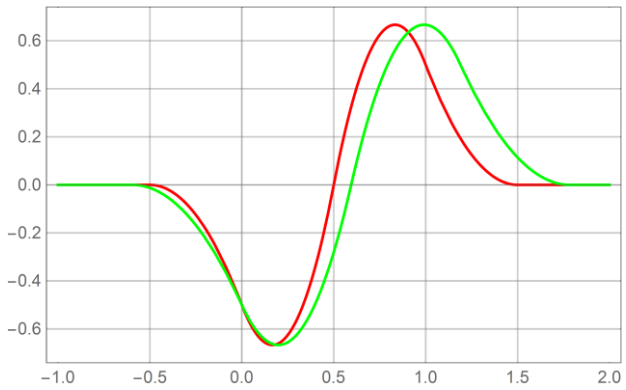

Figure 2. Mother wavelet (red line) and the dilated by $2^{0.25}$ version (first and second voice) (green line).

3.4.4. Connection Between Wavelet Variance Analysis and Fourier Spectral Analysis

Relevance of two-point statistics in connection with SAR imagery textural characterization, in particular of the Fourier spectral analysis and the ACF, was pointed out in a seminal work published in the late 1980s (Ulaby, et al., 1986). This work was targeted to supervised classification, where textural class parameters were estimated from SAR spatial statistics. Analysis was carried out based on stationary Rayleigh statistics for the envelope of the received field, and under the condition of a delta correlated fading component. In this framework, a method was derived for the estimation of the underlying RCS ACF from experimental data, whereas no specific model for the surface fluctuations was proposed. This line of research was extended by a theoretical model for non-Rayleigh SAR scattering statistics, covering the case of correlations between scatterers in the resolution cell (or fluctuating cross-section), and finite illumination window (Oliver, 1984; Oliver, 1988). The surface fluctuations were described by a Gamma distribution and a Lorentzian spectrum (exponential ACF). This model is particularly relevant when imaging forest at the resolution afforded by instruments used in our experiments. These contributions were the springboard over which interest in space–frequency analysis of SAR backscatter took momentum (Sheen & Johnston, 1992; Collins & Huang, 1998; Kurvonen & Hallikainen, 1999; Bujor, et al., 2004).

Wavelet frame spatial statistical measures are rooted in the groundwork established by the classical Fourier ACF analysis adopted in those research works, but extend it in several respects: 1) by enabling space-scale analysis (through good localization in the space–frequency domain); 2) by the capability of dealing with nonstationary processes; and 3) providing statistically better and computationally more efficient estimators. The reader is referred to Percival & Walden (2000) for a discussion on this topic. It appears therefore interesting to establish, for those random processes described by the models mentioned above, the connection between the wavelet space-scale statistics (wavelet variance and covariance) and the ACF based characterization.

For the purpose, analytical and numerical derivations were undertaken to illustrate the response of the wavelet scaling signatures to given correlation properties of the input SRF, including those assumed in the models in Oliver (1984). The gist of the analysis was based on the theory of linear filtering of random signals (Picinbono, 1993), which was exploited to link the spectral properties of the input signal to the statistics (variance) of the output process, this being filtered by the wavelet operator. Detailed analytical derivations and results would be outside the scope of the paper.

Suffice here to mention that for fractal RCS (Stewart, et al., 1993; Wornell, 1993; Franceschetti, et al., 1999), the dependence of the wavelet variance on scale is linear in log-log scale, with the first derivative proportional to the spectral exponent. For a Gamma-distributed RCS with exponential ACF (Oliver, 1984), the wavelet variance increases nonlinearly with the derivative at scale $s = 1$ linear in β (the inverse correlation length). While, the asymptotic value is proportional to the second moment of intensity.

3.5. ENVISAT ASAR Results and Interpretation

3.5.1. Wavelet Variance Signature

The graph in Figure 3 shows the wavelet variance as a function of scale (four dyadic scales and four voices) for four classes of interest with corresponding estimation windows selected on ENVISAT ASAR VV backscatter geocoded data (Table 1). Notice that in this set of classes and with respect to SAR backscatter, there are two radiometrically pure cases (intact and DF) and two mixed cases (FAM and FS). However, in terms of textural analysis, these classes can be handled as pure classes, in the sense that they can be characterized by separable measures.

The following observations can be made. Regarding the general trend with scale, signatures related to IF, DF and FAM all show the fingerprint of a stationary random process with loss of correlation at short scales, a first maximum (sill) in a range of intermediate scales (corresponding to the correlation length concept in Fourier analysis), and a final segment with flattening out (white noise DF, FAM) or the presence of further correlation (or anticorrelation) structures (IF). A striking difference is provided by the FS signature which presents persistent increase with scale, a sign of a nonstationary process. This situation is due to the presence of strong radiometric non homogeneities within the estimation area (mixture), due to the intertwining of grassland and taller vegetation, as it will be documented later by wavelet spectra analysis (see section 3.5.4).

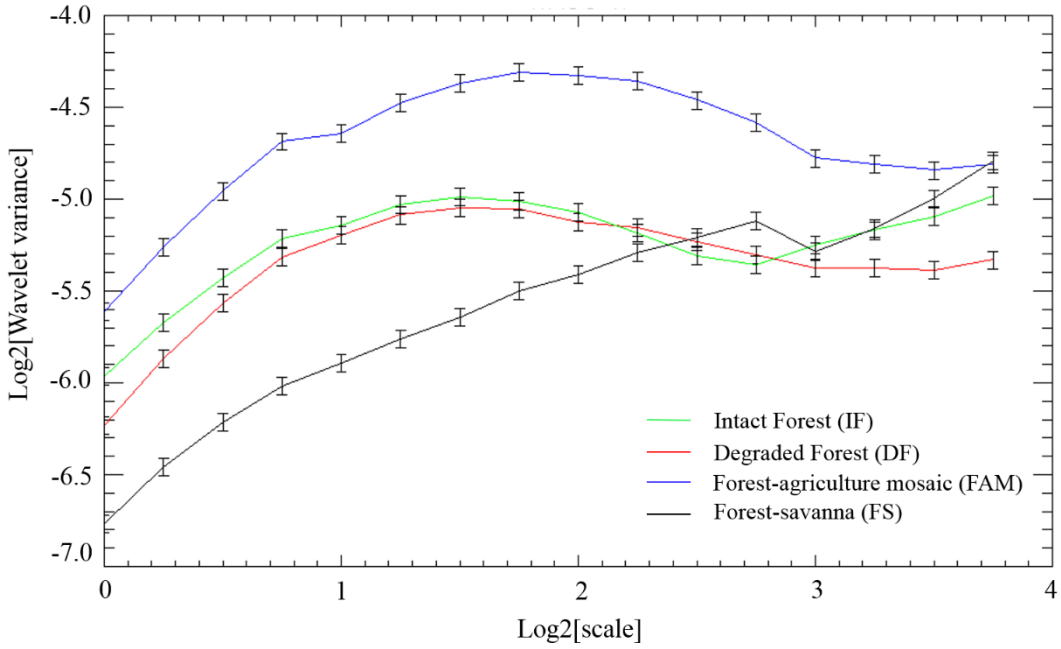

Figure 3. Wavelet variance scaling signatures computed on single date ENVISAT ASAR VV backscatter (2010) for 4 classes of interest: forest-agriculture mosaic (FAM) (blue), degraded forest (DF) (red), intact forest (IF) (green) and forest-savanna (FS) (black). The error bars correspond to the standard error of the wavelet variance estimator. Two parameters need to be considered for the interpretation of the figure. The correlation length (signature maxima) given in terms of scale (m) (x-axis) indicates the point (scale) where the autocorrelation (two-point statistic) between the pixels belonging to a certain class within the window of choice decays to zero. The variance of the wavelet coefficients (y-axis) is a proxy of the process variance within a neighborhood of a given scale (one-point statistic) and thus indicates the "roughness" of the process at a given scale.

Regarding the separation between signatures (in terms of point-wise distance between variance values at each scale with respect to the estimation error), it is clear that between scales 2^0 and 2^2, the two radiometrically mixed classes (forest-agriculture mosaic and forest-savanna) are well separated between themselves and with respect to the union of more homogeneous classes (intact forest and degraded forest). However, separation between intact forest and degraded forest appears problematic, when based only on scale-by-scale differences between signature

values. Statistical analysis on the probability distribution of the signatures' values for 20 samples of each class confirms these results.

The key to the solution of the problem stems from considering the functional dependence on scale of the signatures, as opposed to their point by point differences. For this purpose, the difference between intact forest and degraded forest signatures were analyzed in more detail. The two functions (intact and degraded forest signatures) appear to have a very similar form in the range of scales 2^0-2^2. However, the sill (first maximum) of the intact forest class occurs at shorter scale than the degraded forest one, or, in other words, there is a remarkable and consistent difference in the correlation length for the two classes (Figure 4a). Additionally, the intact forest signature shows persistent correlation/anticorrelation structures at longer scales, whereas the degraded forest signature tends to flatten out.

A link between these two statistical correlation patterns and the underlying structure of the observed target can be conjectured in the following way. The intact forest structure is made up by layers of vegetation and in particular large emergent trees contribute to the signal. Instead, degraded forest has a relatively more homogeneous structure due to the removal of large emergent trees and the vegetation regrowth which has achieved a stage similar to the remnant vegetation from the intact stage. Let us remember that C-band radiation has a short penetration depth into a dense target, like this type of forest. Therefore, the RCS is spatially modulated by height changes and shadowing effects of a thin layer at top of canopy. Therefore, the intact forest return (which is more "rough") will decorrelate at shorter scales than the more homogeneous degraded forest. On the other hand, the intact forest will retain some self-similar structures at longer scales, which will result in long scale memory as far as correlation is concerned. The results concerning the intact forest class are in line with the dense homogeneous forest model in Picinbono (1993), where K-distributed clutter with an exponential cosine ACF is assumed. These considerations suggested a computational approach for the

two-class pattern recognition problem based on signature functional analysis (described in Section 3.5.2).

3.5.2. Wavelet Scaling Signatures Functional Analysis

Functional analysis of the wavelet scaling signatures was undertaken by fitting a polynomial function to the wavelet variance values for two classes of interest: intact forest (green) and degraded forest (red) (Figure 4a). The wavelet scaling signatures points were fitted using a third-degree polynomial function of the form $y = ax^3 + by^2 + cx + d$. Two patterns can be noticed in the graph: the first maximum (sill) of the intact forest signature occurs at shorter scale than the degraded forest one; the presence of persistent correlations (anticorrelations) at long scales in the intact forest signature, whereas the degraded forest signature tends to level off (uncorrelated noise). These two different functional dependences of the wavelet variance on scale can be described by the first and second derivatives of the fitting polynomial, as shown in Figure 4b and Figure 4c. The zero crossing of the first derivative marks the onset of the sill point. The zero crossing of the second derivative marks the inflection point of the signature, this occurring always at longer scales for the degraded forest class.

The combination of these functional parameters provides a consistent condition to discriminate between the two classes. This proposition was proven by a statistical hypothesis test of the difference of the parameters' mean values using 20 samples for each class of interest (H0: $\bar{x}_{DF} - \bar{x}_{IF} = 0$). Concerning the first derivative zero crossings, the test resulted in one-sided p-value equal to 6.477×10^{-7}; thus H0 was rejected indicating that there is a significant difference between the means at a 0.05 significance level. As to the zero crossings of the second derivative, the test gave a one-sided p-value equal to 0.003 with H0 rejected.

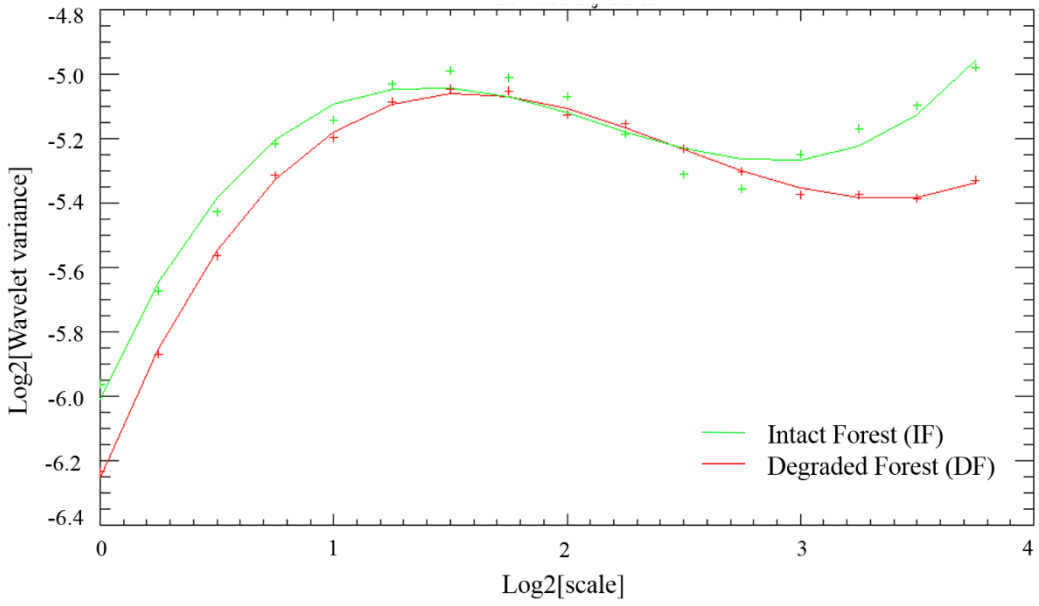

(a) ENVISAT ASAR (VV) Fitted Signature

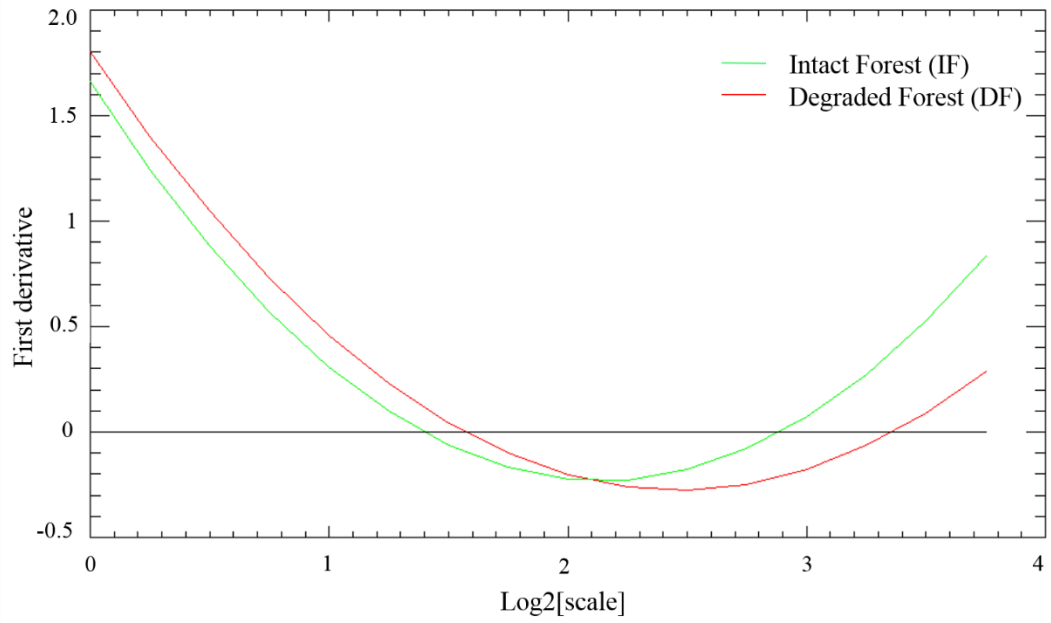

(b) First derivative

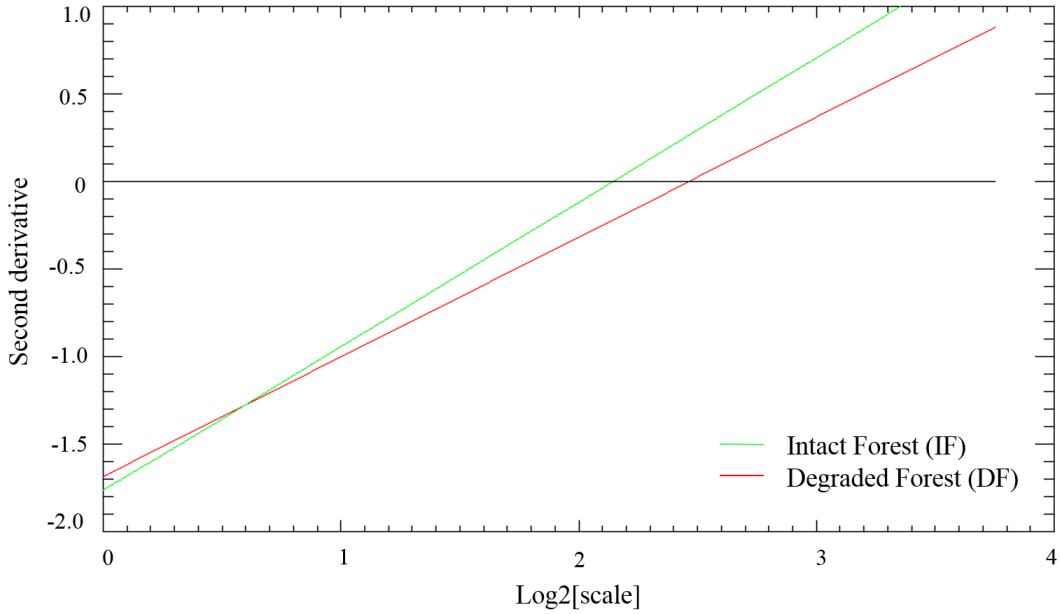

(c) Second derivative

Figure 4. (**a**) Wavelet scaling signature for two classes: intact forest (green cross) and degraded forest (red cross) and the fitted 3rd degree polynomial function (green and red solid lines for intact forest and degraded forest respectively); (**b**) first derivative of the intact forest (green) and degraded forest (red) fitted wavelet scaling signatures; (**c**) second derivative (inflection) of the intact forest (green) and degraded forest (red) fitted wavelet scaling signatures. The wavelet signature at 4 dyadic scales was fitted using a 3rd degree polynomial to obtain a functional description of the signature. The first zero crossing of the first derivative corresponds to the signature maximum (correlation length of the process); the zero crossing of the second derivative indicates the onset of an inflection point in the signature; both indicators occur at different scales for intact and degraded forest and thus can be considered as a potential way to discriminate between the two forest classes.

3.5.3. Flatness Factor

The flatness factor (Equation 10) intuitively gives an indication of the relative variability of the wavelet variance within the data samples, and therefore can

indicate the presence of intermittency in the SAR signal, such as edges and point targets. As a guideline for the interpretation of the experimental data, we remind that for a wavelet frame that acts as a differentiator, and for Gaussian white noise as input, the flatness factor equals 3.

Intact forest is the class which presents the lowest amount of intermittency at all scales, and less spread among samples, with flatness factor values around 3, thus pointing at a nearly Gaussian noise process (Table 3).

Degraded forest reveals some intermittency at short scales, also with large spread among samples (Table III). This result seems to contrast the conclusion derived from the scaling signature, which indicates degraded forest as a more homogeneous process than intact forest. However, closer examination of the degraded forest areas reveals that these high intermittency values are due to topographic effects (shadow, layover) which are present in some of the areas.

The forest-agriculture mosaic and forest-savanna classes both present intermittency of different importance, with the highest values and highest spread among samples for the forest-savanna (Table 3). In both these cases, the intermittency is due to the presence of edges between two homogeneous fields (e.g., soil and forest in forest-agriculture mosaic, and forest clusters in the forest-savanna). These singularities are of different strength, as a function of the related backscatter values, as indicated by higher flatness values with the forest-savanna class. The case of these nonstationary samples will be further analyzed using the wavelet spectrum in section 3.5.4.

Table 3. Flatness factor statistics for 20 samples of each of the four classes of interest. For Gaussian white noise the flatness factor would be equal to 3. Higher flatness factors indicate the onset of intermittency or non-stationarity.

Scale	DF		IF		FAM		FS	
	Mean	Stdev	Mean	Stdev	Mean	Stdev	Mean	Stdev
2^0	6.01	4.58	3.54	0.18	6.20	7.94	5.84	3.29
2^1	4.28	2.29	3.24	0.24	4.21	2.15	5.90	2.55
2^2	3.58	0.86	3.31	0.28	3.77	0.79	6.7	5.26
2^3	3.58	0.44	3.31	0.35	3.54	0.67	5.49	3.69
2^4	4.12	1.41	3.74	0.46	3.56	0.82	4.57	2.85

DF, degraded forest; IF, intact forest; FAM, forest agriculture mosaic; FS, forest-savanna.

3.5.4. Wavelet Space-Scale Signatures (Spectrum)

Analysis by wavelet spectrum of the two heterogeneous classes forest-savanna and forest-agriculture mosaic illustrates well the ability of this technique for localizing features in the combined space–frequency domain. The forest-savanna spectrum is shown in Figure 5a, this being represented in the northing direction. The backscatter in the estimation window (43 × 43 pixels) for forest-savanna and forest-agriculture mosaic is shown in false colour in Figure 5. A singularity (ridge) due to a forest ribbon is present in the image (Figure 5a). This feature is mapped onto the triangular area of higher wavelet variance values spreading in scale and around pixel 30 in space. Changes of the wavelet variance trajectory with scale are due to the intersection of the translated wavelet with the feature. The forest-agriculture mosaic case (Figure 5b) concerns an area with a diagonal edge marking the transition from bare soil to forest. In the spectrum (represented in the easting direction), the first segment (pixels 0–10) reveals a stationary signature (maximum at scale 2) that is due to the bare soil homogeneous region within this range, whereas the following spectrum values indicate a nonstationarity situation (increasing signature at all scale) corresponding to the presence of an edge.

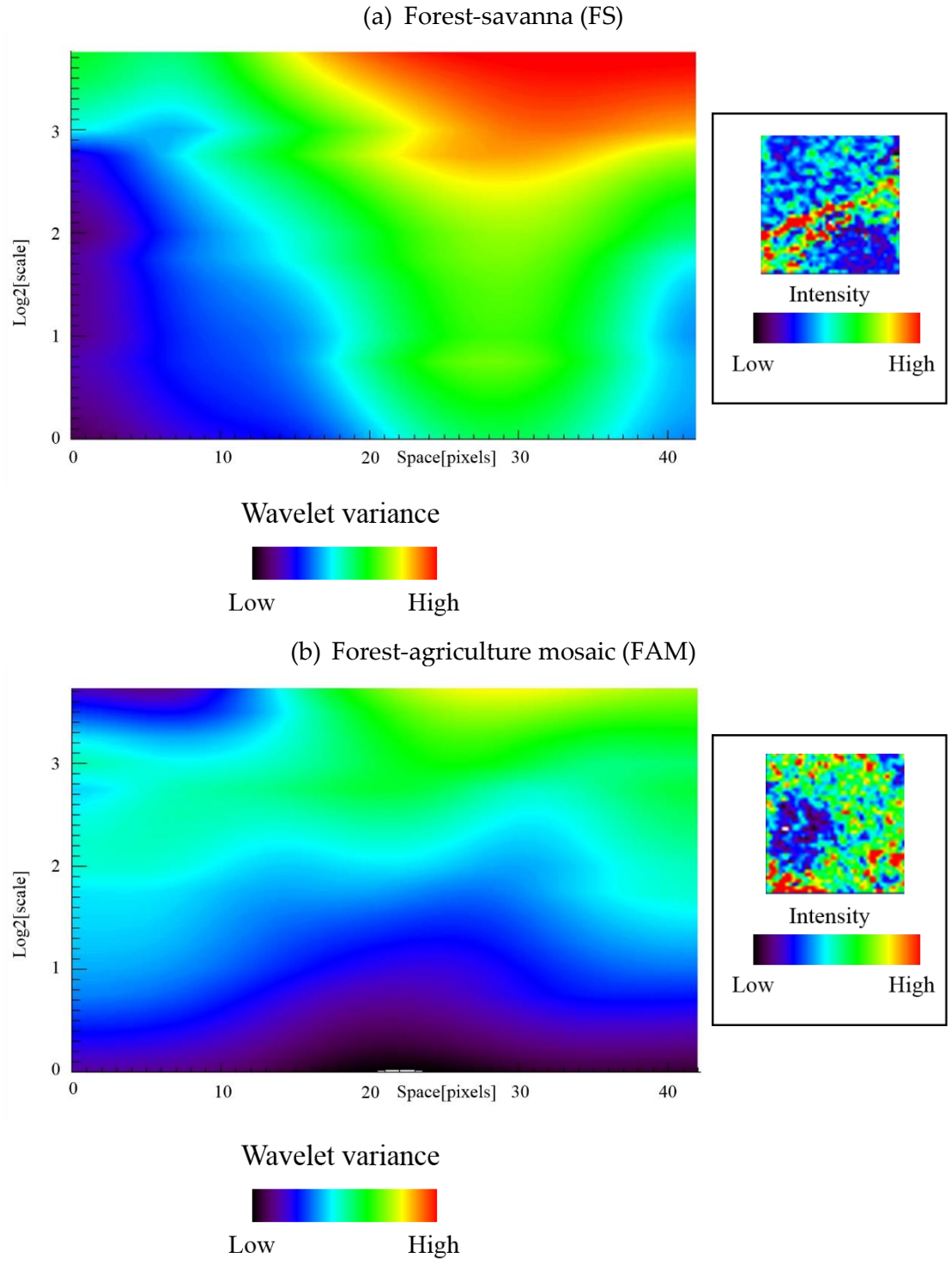

Figure 5. Wavelet spectrum for a transect in (**a**) Forest-savanna (FS) (in the northing direction) and (**b**) Forest-agriculture mosaic (FAM) (easting direction) showing the different textural properties of each class in the space-scale domain. The spectrum is estimated in a 43 × 43 pixels window (equivalent to 645 × 645 m in the ENVISAT

ASAR geocoded dataset). SAR backscatter within the corresponding windows (rendered in false color) is shown to the right of the spectra. These test cases highlight the capability of the wavelet space-scale representation to characterize radiometrically heterogeneous targets, such as a forest ribbon in (**a**) and the margin between bare soil and forest in (**b**).

3.5.5. Wavelet Covariance

The normalized wavelet covariance (correlation) signature (Equation 9) provides a measure of how the SAR backscatter within the estimation window (related to a specific landcover class) changes texturally between two dates and as a function of scale. It is therefore a spatio-temporal fingerprint of the SAR statistics. An example is shown in Figure 6. The signature was computed with the same classes as the wavelet variance signature in Figure 3 and refers to changes between acquisitions in 2006 and 2010. It can be observed that the wavelet variance of all classes loses correlation between the two dates, with lower correlation at longer scales. The changes at short scales may be influenced by residual speckle noise, whereas as scale increases, variation of the RCS spatial distribution comes into play. The forest-agriculture mosaic class (black) shows the highest decorrelation (highest temporal change) at all scales. This pattern depends obviously by temporal changes in the agricultural practices and bare soil extent. At short scales (up to 2^3), the statistics of class forest-savanna (green) shows more decorrelation than the ones of intact forest and degraded forest. Again, this is the other class where changes in the target can be expected. For intact forest (blue), there appears to be more textural change in comparison with degraded forest. This feature must be further investigated to be able to connect it to vegetation changes.

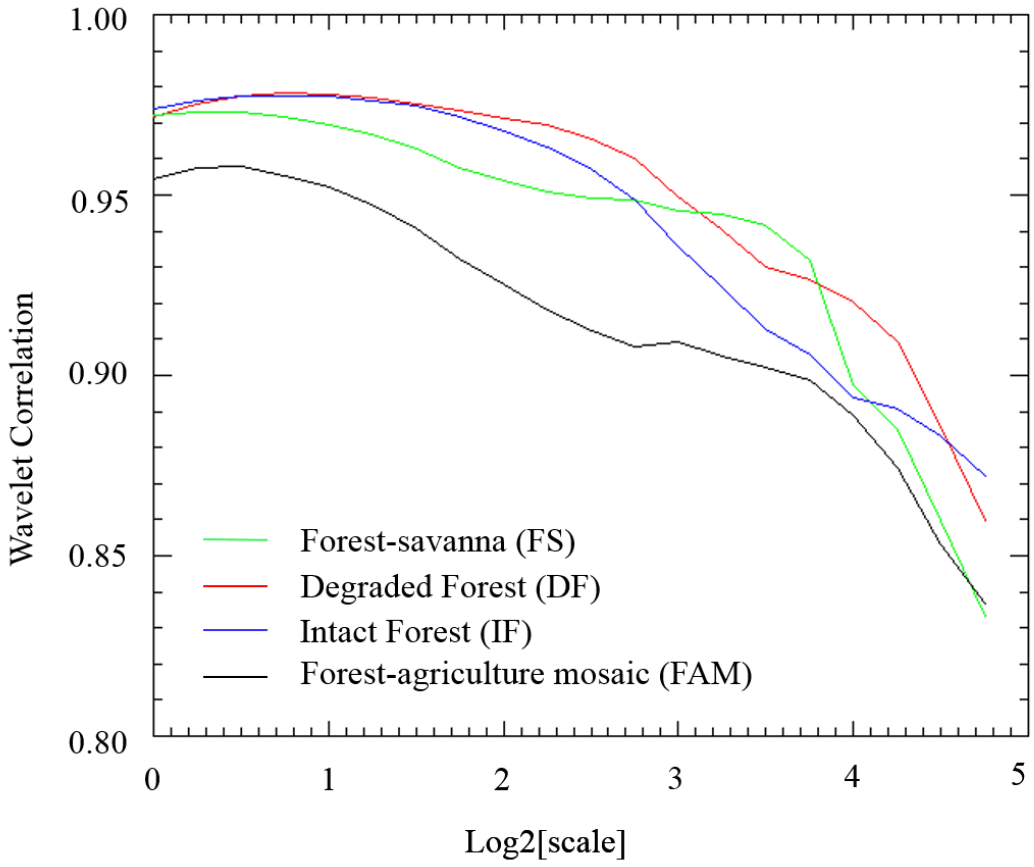

Figure 6. Wavelet normalized covariance between ENVISAT ASAR scenes acquired in 2006 and 2010 for four landcover classes: degraded forest (red), forest-savanna (FS) (green), intact forest (IF) (blue), and forest-agriculture mosaic (FAM) (black). Wavelet normalized covariance values range from 0 to 1 with higher values indicating greater textural correlation between the two dates. There is a decreasing trend in wavelet covariance with increasing scale for all landcover classes but in particular for forest-agriculture mosaic, which can be linked to changes due to agricultural practices between the two dates. Decreasing wavelet covariance for IF, DF and FS classes could be due to phenological or moisture differences between the two dates.

3.6. ALOS PALSAR Results and Interpretation

3.6.1. Wavelet Variance Signatures

The wavelet statistics analysis was also applied to L-band ALOS PALSAR at HH and HV polarizations. The signatures for forest-savanna, intact forest, degraded forest, and forest-agriculture mosaic can be found in Figure 7a and Figure 7b. Differences of the wavelet statistics at HH and HV polarizations (in terms of absolute wavelet variance values and functional form) can be readily seen from the graphs.

At HH polarization, the scaling functional form of the signatures is similar to the one of ENVISAT ASAR VV, with the degraded forest signature flattening out and the intact forest signature keeping memory of its structure (these trends are better highlighted with the fitted wavelet signatures in Figure 8a). While, at HV polarization, the signatures for the two classes reveal the onset of a white noise random process (no texture) and no significant difference between the two. We conclude that the HV return (volume scattering) does not provide spatial information that is useful to discriminate between degraded forest and intact forest. From another standpoint, differences in biomass within and between intact and degraded forest (if any) cannot be detected at this radiometric and spatial resolution by HV backscatter. On the other hand, the HH return is sensitive to the large scattering elements in the top layer of the canopy, and therefore, develops sensitivity to the forest structure in the same way as the C-band VV, although with less strength due to the increased penetration. The signatures of the two heterogeneous classes (forest-agriculture mosaic and forest-savanna), both at HH and HV, bear in a very strong way the tell-tale signs of nonstationarity, and even more so with respect to the ENVISAT ASAR case.

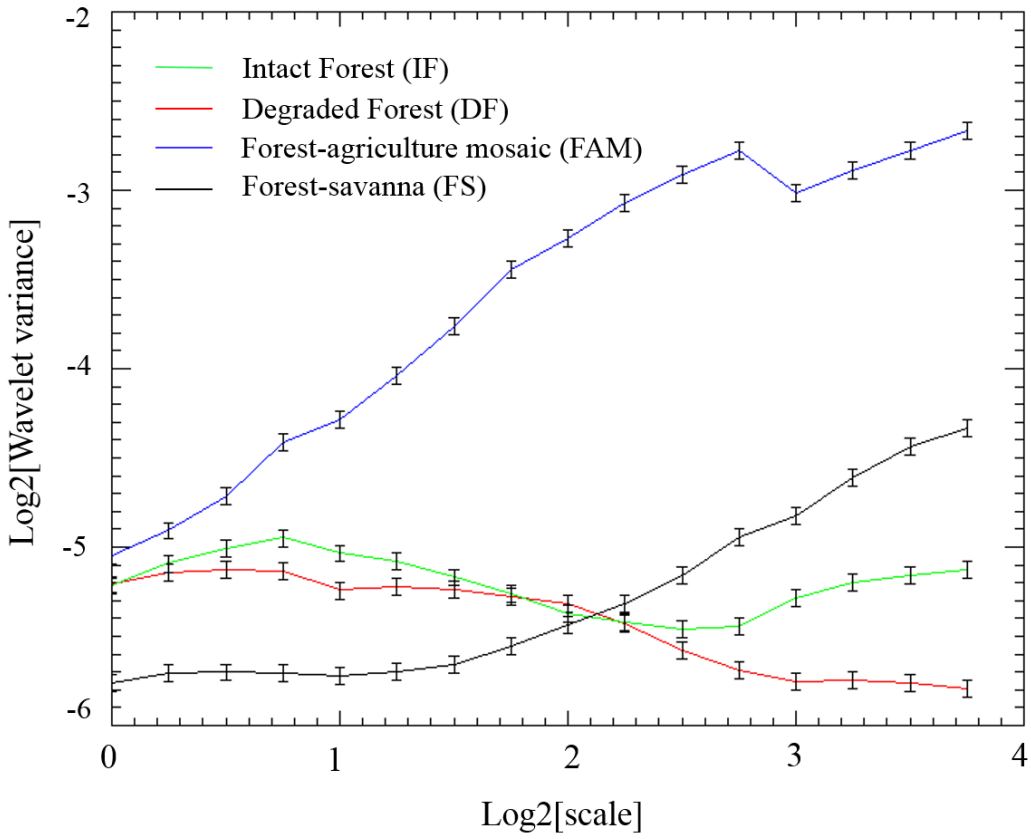

(a) ALOS PALSAR (HH)

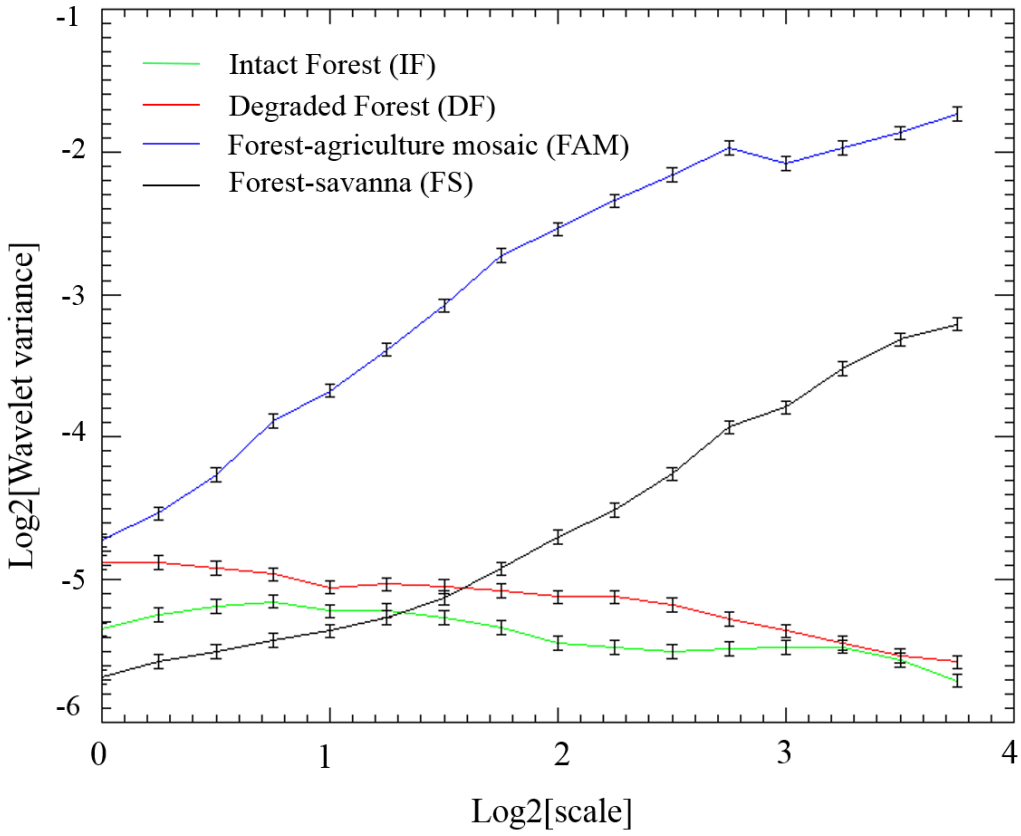

(b) ALOS PALSAR (HV)

Figure 7. (**a**) ALOS PALSAR HH and (**b**) ALOS PALSAR HV wavelet variance scaling signatures (4 dyadic scales) for four classes of interest: forest-agriculture mosaic (FAM) (blue), degraded forest (DF) (red), intact forest (IF) (green) and forest-savanna (FS) (black) with corresponding error bars (black). See Figure 3 for details on the interpretation of the signatures.

3.6.2. Wavelet Scaling Signatures Functional Analysis

This analysis is carried out only for HH polarization in view of intact forest and degraded forest class separation, since the HV does not provide useful spatial information. The fitted wavelet signatures also confirm that the PALSAR HH is similar to the ASAR VV case in terms of functional form. However, the parameters that characterize univocally this dependence are different. Now, the two classes present the same correlation length (Figure 8a). Therefore, the first zero crossing of

the first derivative cannot be used as a marker (Figure 8b). On the other hand, now the second zero crossing is a good candidate, since it occurs at short scales for the intact forest, and at longer scales (if any) for the degraded forest (Figure 8c).

The inflection point (zero of the second derivative) appears to have the same role as in the case of ASAR. The significance of these observations was checked using a hypothesis test at 0.05 significance level of the differences of the mean values of these parameters (second zero crossing of the first derivative and zero crossing of the second derivative) using 20 samples for each class of interest.

The test reports that the H0 cannot be rejected in this case (p = 0.109). Therefore, functional analysis of wavelet signatures does not appear to be a viable solution for the textural discrimination of the two classes using ALOS PALSAR HH.

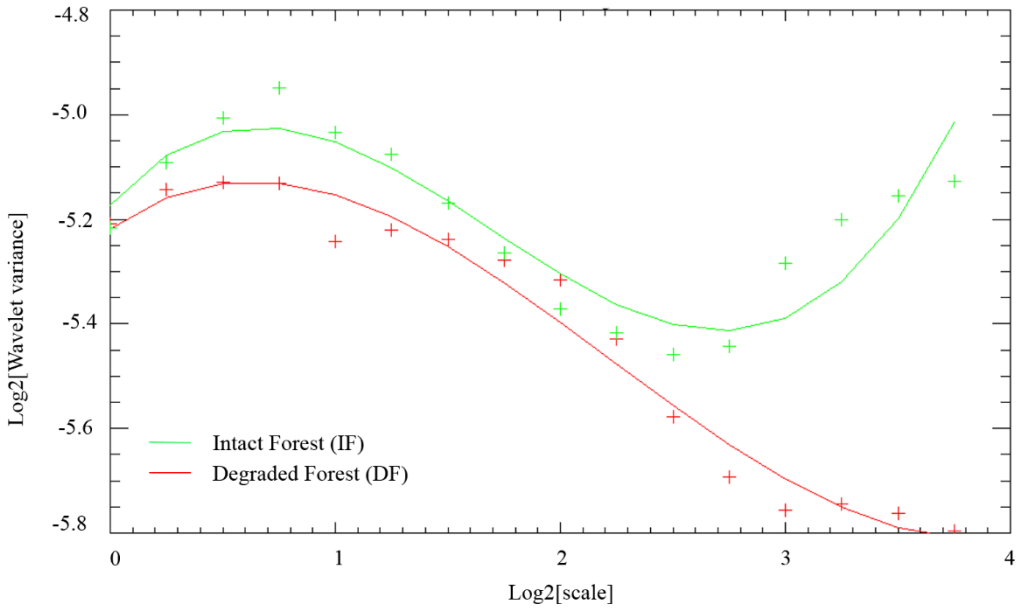

(a) ALOS PALSAR (HH) Fitted Wavelet Signature

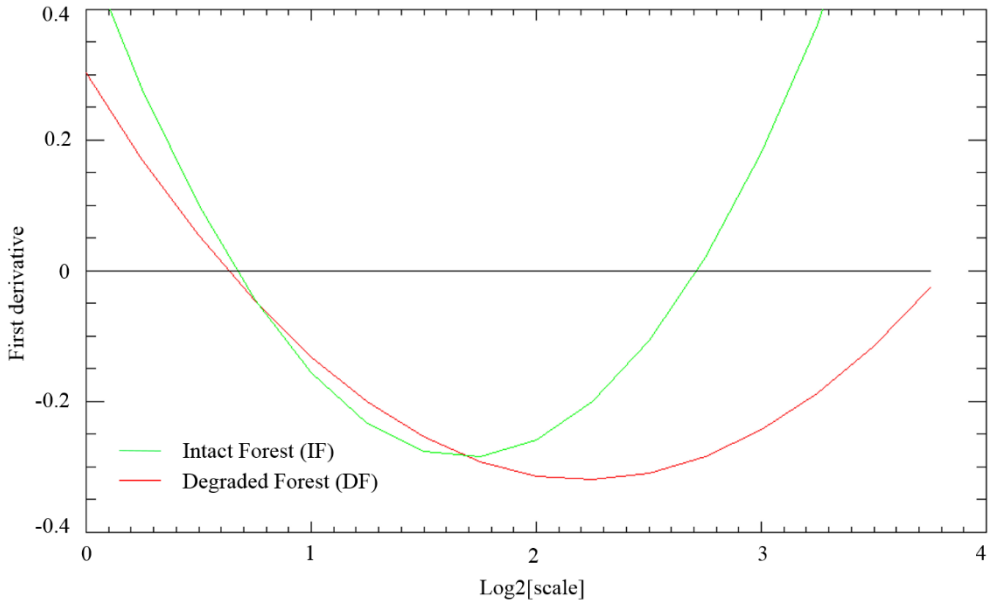

(b) First derivative

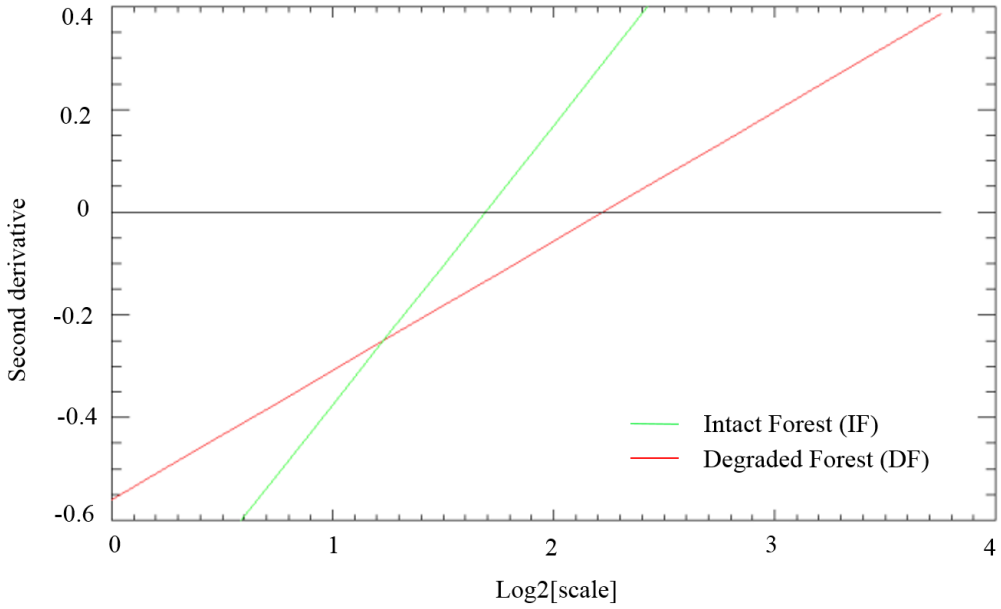

(c) Second derivative

Figure 8. (**a**) Wavelet scaling signature for two classes: IF (green cross) and DF (red cross) and the fitted third-degree polynomial functions (green and red solid lines); (**b**) First derivative of the fitted polynomial and (**c**) Second derivative of the fitted polynomial. See Figure 4 for the interpretation of the functional representation of the signatures.

3.7. Conclusion

Supervised analysis of SAR backscatter spatial statistics, as provided by a wavelet frame representation, was undertaken with the goal of assessing the capability of retrieving information about landcover differentiation, in particular, the ability to differentiate intact and DF in a closed semi deciduous forest context. Test cases were developed using both C-band ENVISAT ASAR and L-band ALOS PALSAR datasets acquired on a site in Cameroon.

Results have shown that wavelet variance scaling signatures, which are measures of the SAR backscatter two-point statistics in the combined space-scale domain, are able to differentiate landcover classes by capturing their spatial distribution. This sensitivity extends the possibility of class discrimination based on intensity values distance, which is effective only for radiometrically pure classes or homogeneous targets, to the case of heterogeneous targets, these giving rise to texturally pure classes. Along this line, wavelet spectra were proven to be effective in characterizing heterogeneous landcover, such as forest-agriculture mosaic, by capturing the onset and the spatial location of singularities, such as edges.

Importantly, discrimination between intact forest and degraded forest which is an important focus for conservation science was found to be enabled by functional analysis of the wavelet scaling signatures of C-band ENVISAT ASAR data. Analytic parameters, describing the functional form of the scaling signatures when fitted by a third-degree polynomial, resulted in a statistically significant difference between the signatures of the two classes. On the other hand, this outcome could not be replicated using the L-band ALOS PALSAR data.

Reasons for the inability to discriminate between intact and degraded forest using ALOS PALSAR could be explained by the fact that L-band penetrates more into the canopy, and therefore, the observed backscatter texture is influenced more by the distribution of large scattering elements, and by the ground return. By contrast, C-band ENVISAT ASAR penetration is lower, and thus, the backscatter return comes primarily from the top of the canopy components, which produce a micro-topography effect on the radar return due to their irregular vertical and

horizontal distribution (e.g., emergent trees, which may be missing in degraded/regenerating forests). Additionally, differences in incidence angle and environmental/seasonal conditions between the C-band and L-band acquisitions could have influenced the differences in observed results.

The study area is characterized by degraded forest that was disturbed by selective logging at least 15 years in the past. It is therefore notable that a SAR sensor at 15 m resolution can still distinguish between this degraded forest stage and intact forest, based on textural features. Additional information could be retrieved from short wavelength and higher resolution sensors (e.g., Sentinel-1 or TanDEM-X).

In this specific environmental setting, the ENVISAT ASAR VV outperforms the ALOS PALSAR at HH and HV polarizations in terms of distinguishing between intact and degraded forest. However, in a different environmental setting with other degradation patterns (e.g., more recent forest degradation patterns or in closed evergreen forest), the results could be different and therefore, testing the method in several areas will need to be undertaken in the future.

The wavelet signatures cannot be generalised to discriminate degraded forest from intact forest when this transition is due to different forest degradation drivers, varying from selective logging to impact of fire, to degradation stage, this depending on the time gap between the scene used in the analysis and the time elapsed since degradation occurred. It would be expected that degraded forest observed just after disturbance would present different upper canopy structure compared to re-growing degraded forest and this would be appreciable in the corresponding signatures.

In terms of location, the approach can be extended to other sites with limitations related to data availability (for instance the availability of a Sentinel-1 StripMap mode mosaic over the whole tropical rainforest would enable a large scale assessment of degraded forest) and availability of supporting ancillary data for supervised training and validation of the analysis. This condition will need to be verified further in different sites.

In terms of SAR center frequency, it was demonstrated from the analysis that short wavelength (C-band) performs better than longer wavelength (X-band); therefore using datasets acquired at short wavelength is advised for this purpose. The performance of C-band ENVISAT ASAR for the purpose of discriminating between intact and degraded forest is a promising result given the increasing availability of C-band data provided by ESA Sentinel-1 mission and the possibility to extend the analysis using multi-temporal signatures which could in principle provide changes in backscatter texture given by the process of forest degradation between multiple dates. However, generalisation of the results to global scale and accounting for different forest degradation drivers or degradation stages has not so far been proved within the reach of this study.

Moreover, the methods tested would not directly enable the estimation of bio-physical parameters, such as above-ground biomass and associated changes in carbon stocks. However, the methods are able to provide a proxy indicator related to whether an area of forest, which has been degraded, is structurally different compared to intact forest based on backscatter texture as opposed to absolute backscatter values, which do not provide ways to distinguish between degraded forest and intact forest.

The following chapter explores how the discrimination between primary forest and secondary forest can be improved using wavelet-based texture analysis by developing further the methodology presented in this chapter and by exploiting TanDEM-X Digital Surface Models, which afford measures of both vertical and horizontal structure.

3.8. Acknowledgments

The authors would like to acknowledge the software providers Sarmap SA (Sarscape 5.0) and the data providers: ESA (ENVISAT ASAR), Sarmap SA, JAXA (ALOS PALSAR), BlackBridge (RapidEye), and USGS (Landsat data).

3.9. References

- Ahrends, A. et al., 2010. Predictable waves of sequential forest degradation and biodiversity loss spreading from an African city. *Proceedings of the National Academy of Sciences,* 107(33), p. 14556–14561.
- Attema, E. et al., 2007. Sentinel-1. The radar mission for GMES operational land and sea services. *ESA Bulletin,* Volume 131, pp. 10-17.
- Beauchemin, M., Thomson, K. P. B. & Edwards, G., 1996. Edge detection and speckle adaptive filtering for SAR images based on a second-order textural measure. *International Journal of Remote Sensing,* 17(9), pp. 1751-1759.
- Bellassen, V. & Gitz, V., 2008. Reducing Emissions from Deforestation and Degradation in Cameroon- Assessing costs and benefits. *Ecological Economics,* 68(1), p. 336–344.
- Benelcadi, H. et al., 2012. *Contribution of TerraSAR-X Radar Images Texture for Forest Monitoring.* Munich, Germany, Proceedings of the IEEE International Geoscience and Remote Sensing Symposium, pp. 6427-6430.
- Bujor, F. et al., 2004. Application of log-cumulants to the detection of spatiotemporal discontinuities in multitemporal SAR images. *IEEE Transactions on Geoscience and Remote Sensing,* 42(10), p. 2073–2084.
- Collins, M. J. & Huang, J., 1998. Uncertainties in the estimation of ACF based texture in synthetic aperture radar image data. *IEEE Transactions on Geoscience and Remote Sensing* , 36(3), p. 940–949.
- Cutler, M. E. J., Boyd, D. S., Foody, G. M. & Vetrivel, A., 2012. Estimating tropical forest biomass with a combination of SAR image texture and Landsat TM data: An assessment of predictions between regions. *ISPRS Journal of Photogrammetry and Remote Sensing,* Volume 70, p. 66–77.
- Daubechies, I., 1988. Orthonormal bases of compactly supported wavelets. *Communications on Pure and Applied Mathematics,* 41(7), p. 909–996.
- Daubechies, I., 1992. Discrete Wavelet Transforms: Frames. In: I. Daubechies, ed. *Ten Lectures on Wavelets.* Philadelphia, PA, USA: Society for Industrial and Applied Mathematics, pp. 53-105.
- Davis, A., Marshak, A. & Wiscombe, W., 1994. Wavelet-based multifractal analysis of non-stationary and/or intermittent geophisical signals. In: E. Foufoula-Georghiou & P. Kumar, eds. *Wavelets in Geophysics.* New Yor, NY, USA: Academic, p. 249–298.

- De Grandi, D., D, G., Lucas, R. M. & Kropoacek, J., 2009. Analysis by wavelet frames of spatial statistics in SAR data for characterizing structural properties of forests. *IEEE Transactions on Geoscience and Remote Sensing,* 47(2), pp. 494-507.

- De Grandi, G. D., Lee, J.-S. & Schuler, D. L., 2007. Target detection and texture segmentation in polarimetric SAR images using a wavelet frame: Theoretical aspects. *IEEE Transactions on Geoscience and Remote Sensing* , 45(11), p. 3437–3453.

- De Grandi, G., Leysen, M., Lee, J. & Schuler, D., 1997. *Radar reflectivity estimation using multiple SAR scenes of the same target: techniques and applications.* Singapore, Proceedings of the IEEE International Geoscience and Remote Sensing Symposium, pp. 1047-1050.

- Deutscher, J., Perko, R., Gutjahr, K. & Hirschmugl, M., 2013. Mapping Tropical Rainforest Canopy Disturbances in 3D by COSMO-SkyMed Spotlight InSAR-Stereo Data to Detect Areas of Forest Degradation. *Remote Sensing,* 5(2), pp. 648-663.

- FAO, 1985. *Forest Genetic Resources. Information -No.14. In Situ Conservation of Forest Genetic Resources in Cameroon.* [Online]. Available at: http://www.fao.org/docrep/006/r4968e/r4968e07.htm [Accessed 14 December 2014].

- Franceschetti, G., Iodice, A., Migliaccio, M. & Riccio, D., 1999. Scattering from natural rough surfaces modeled by fractional Brownian motion two dimensional processes. *IEEE Transactions on Antennas and Propagation,* 47(9), p. 1405–1415.

- Franke, J. et al., 2012. Monitoring fire and selective logging activities in tropical peat swamp forests. *IEEE Journal of Selected Topics in Applied Earth Observations and Remote Sensing,* 5(6), pp. 1811-1820.

- Global Forest Observations Initiative, 2014. *Integrating remote-sensing and ground-based observations for estimation of greenhouse gases in forests.* [Online]. Available at: https://unfccc.int/files/methods/redd/submissions/application/pdf/redd_20140218_mgd_report_gfoi.pdf [Accessed 20 January 2014].

- Grace, J., Mitchard, E. & Gloor, E., 2014. Perturbations in the carbon budget of the tropics. *Global Change Biology,* 20(10), p. 3238–3255.

- Haralick, R. M. & Bryant, W. F., 1976. *Documentation of Procedures fro Textural/ Spatial Pattern Recognition Techniques,* Lawrence, KS, USA: University of Kansas.

- Hirschmugl, M., Steinegger, M., Gallaun, H. & Schardt, M., 2014. Mapping Forest Degradation due to Selective Logging by Means of Time Series Analysis: Case Studies in Central Africa. *Remote Sensing,* 6(1), pp. 756-775.

- Kumar, P. & Foufoula-Georgiou, E., 1997. Wavelet analysis for geophysical applications. *Reviews of Geophysics,* 35(4), p. 385–412.

- Kuntz, S. et al., 2011. *A multi-stage inventory scheme for REDD inventories in tropical countries.* Sydney, Australia, Proceedings of the 34th ISRSE Conference, pp. 1-4.
- Kurvonen, L. & Hallikainen, M. T., 1999. Textural information of multitemporal ERS-1 and JERS-1 SAR images with applications to land and forest type classification in boreal zone. *IEEE Transactions on Geoscience and Remote Sensing,* 37(2), p. 680–689.
- Mallat, S., 1998. Dyadic Wavelet Transform. In: S. Mallat, ed. *A Wavelet Tour of Signal Processing.* New York, NY, USA: Academic, p. 148–156.
- Mallat, S., 1998. Multiscale Edge Detection. In: S. Mallat, ed. *A Wavelet Tour of Signal Processing.* New York, NY, USA: Academic, p. 198–199.
- Mertens, B., Gideon, N. S., Matthew, S. & Bertrand, T., 2012. *Interactive Forestry Atlas of Cameroon. Version 3.0,* Washington, DC: World Resources Institute.
- Mertens, B. L. E. F., 2000. Land-Cover-Change Trajectories in Southern Cameroon. *Annals of the Association of American Geographers,* 90(3), pp. 467-494.
- Mertz, O. et al., 2012. The forgotten D: challenges of addressing forest degradation in complex mosaic landscapes under REDD+. *Geografisk Tidsskrift-Danish Journal of Geography,* 112(1), pp. 63-76.
- Mitchard, E. T. A. et al., 2012. Mapping tropical forest biomass with radar and spaceborne LiDAR in Lopé National Park, Gabon: Overcoming problems of high biomass and persistent cloud. *Biogeosciences,* 9(1), p. 179–191.
- Mon, M. S. et al., 2012. Factors affecting deforestation and forest degradation in selectively logged production forest: A case study in Myanmar. *Forest Ecology and Management,* 267(1), pp. 190-198.
- Oliver, C. J., 1984. A model for non-Rayleigh scattering statistics. *Optica Acta: International Journal of Optics,* 31(6), p. 701–722.
- Oliver, C. J., 1986. The interpretation and simulation of clutter textures in coherent images. *Inverse Problems,* 2(4), pp. 481-518.
- Oliver, C. J., 1988. The representation of correlated clutter textures in coherent images. *Inverse Problems,* 4(3), p. 843–866.
- Percival, D. B. & Walden, A. T., 2000. Wavelet Methods for Time Series Analysis. In: 1st, ed. *Wavelet Methods for Time Series Analysis.* Cambridge: Cambridge University Press, p. 594.
- Picinbono, B., 1993. Linear filtering of random signals. In: *Random Signals and Systems.* Englewood Cliffs, NJ, USA: Prentice Hall, p. 512.

- Sarker, L. R. et al., 2013. Forest biomass estimation using texture measurements of high-resolution dualpolarization C-band SAR data. *IEEE Transactions on Geoscience and Remote Sensing*, 51(6), p. 3371–3384.

- Sarmap, 2012. *SARscape.* [Online]. Available at: http://www.sarmap.ch/pdf/SARscapeTechnical.pdf [Accessed 2 November 2015].

- Schlund, M. et al., 2014. Importance of bistatic SAR features from TanDEM-X for forest mapping and monitoring. *Remote Sensing of Environment,* Volume 151, pp. 16-26.

- Sheen, D. & Johnston, L. P., 1992. Statistical and spatial properties of forest clutter measured with polarimetric synthetic aperture radar (SAR). *IEEE Transactions on Geoscience and Remote Sensing*, 30(3), p. 578–588.

- Shensa, M. J., 1992. The discrete wavelet transform: Wedding the à trous and Mallat algorithms. *IEEE Transactions on Signal Processing*, 40(10), p. 2464–2482.

- Simard, M. et al., 1998. Analysis of speckle noise contribution on wavelet decomposition of SAR images. *IEEE Transactions on Geoscience and Remote Sensing*, 36(6), p. 1953–1962.

- Souza, C. M. J., Roberts, D. A. & Cochrane, M. A., 2005. Combining spectral and spatial information to map canopy damage from selective logging and forest fires. *Remote Sensing of Environment*, 98(2), pp. 329-343.

- Souza, J. C. M. & Roberts, D., 2005. Mapping forest degradation in the Amazon region with Ikonos images. *International Journal of Remote Sensing*, 26(3), pp. 425-429.

- Stewart, C. V., Moghaddam, B., Hintz, K. J. & Novak, L. M., 1993. Fractional Brownian motion models for SAR imagery scene segmentation. *Proceedings of the IEEE*, 81(10), p. 1511–1522.

- Stone, T. A. & Lefebvre, P., 1998. Using multi-temporal satellite data to evaluate selective logging in Para, Brazil. *International Journal of Remote Sensing* , 19(13), pp. 517-2526.

- Tegechouang, Y. Y., 2010. *Contribution a la gestion des relations homme-plantation forestiere dans le sud et l'Est Cameroun: Cas des plantations de Pericopsis elata de bidou ii dans la reserve de la kienke sud et du bloc kebe dans la reserve de Deng-Deng.* [Online]. Available at: ww.itto.int/files/user/cites/cameroon/M%C3%A9moire_gestion%20des%20relations%20homme_Plantations_Yako%2024_05_2010.pdf [Accessed 24 January 2014].

- Thompson, I. D. et al., 2013. An Operational Framework for Defining and Monitoring Forest Degradation. *Ecology and Society,* 18(2), p. 20.

- Ulaby, F. T., Kouyate, F., Brisco, B. & Williams, T. H., 1986. Textural information in SAR images. *IEEE Transactions on Geoscience and Remote Sensing* , 24(2), p. 235–245.

- Unser, M., 1995. Texture Classification and Segmentation Using Wavelet Frames. *IEEE Transactions on Image Processing,* 4(11), pp. 1549-1560.

- World Bank, 2014. *Climate Change Knowledge Portal.* [Online]. Available at: http://sdwebx.worldbank.org/climateportal/index.cfm?page=country_historical_climate&ThisRegion=Africa&ThisCCode=CMR [Accessed 2 December 2014].

- World Resources Institute, 2014. *Congo Basin Forest Atlases.* [Online]. Available at: http://www.wri.org/our-work/project/congo-basin-forests/congo#project-tabs [Accessed 20 January 2016].

- Wornell, G. W., 1993. Wavelet-based representations for the 1/f family of fractal processes. *Proceedings of the IEEE,* 81(10), p. 1428–1450.

4. Wavelet Based Analysis of TanDEM-X and LiDAR DEMs across a Tropical Vegetation Heterogeneity Gradient Driven by Fire Disturbance in Indonesia

Elsa Carla De Grandi[a], Edward Mitchard[a] and Dirk Hoekman[b]

[a] School of GeoSciences, University of Edinburgh, EH8 9XP, UK

[b] Department of Environmental Sciences, Wageningen University, Wageningen 6708 PB, The Netherlands

Published in *Remote Sensing*, August (2016)[2]

Author contributions: Elsa Carla De Grandi conceived and designed the experiments (assisted by Dr Edward Mitchard). Elsa Carla De Grandi processed the TanDEM-X data, analyzed the data and wrote the paper. Dr Edward Mitchard and Prof Dirk Hoekman provided comments on the manuscript. Prof Dirk Hoekman provided LiDAR and aerial photography datasets.

[2] *Remote Sensing*, Vol.8, no. 641; DOI: 10.3390/rs8080641. See Appendix II. Copyright 2016 Remote Sensing.

Abstract

Three-dimensional information provided by TanDEM-X interferometric phase and airborne Light Detection and Ranging (LiDAR) Digital Elevation Models (DEMs) were used to detect differences in vegetation heterogeneity through a disturbance gradient in Indonesia. The range of vegetation types developed as a consequence of fires during the 1997–1998 El Niño. Two-point statistic (wavelet variance and co-variance) was used to assess the dominant spatial frequencies associated with either topographic features or canopy structure. DEMs wavelet spectra were found to be sensitive to canopy structure at short scales (up to 8 m) but increasingly influenced by topographic structures at longer scales. Analysis also indicates that, at short scale, canopy texture is driven by the distribution of heights. Thematic class separation using the Jeffries–Matusita distance (JM) was greater when using the full wavelet signature (LiDAR: $1.29 \leq JM \leq 1.39$; TanDEM-X: $1.18 \leq JM \leq 1.39$) compared to using each decomposition scale individually (LiDAR: $0.1 \leq JM \leq 1.26$; TanDEM-X: $0.1 \leq JM \leq 1.1$). In some cases, separability with TanDEM-X was similar to the higher resolution LiDAR. The study highlights the potential of 3D information from TanDEM-X and LiDAR DEMs to explore vegetation disturbance history when analyzed using two-point statistics.

4.1. Introduction

Tropical forests are the largest and most complex forest biome on the planet covering 16% of the global land surface where pressure exerted by anthropogenic activities is high and their role in the carbon budget is of great significance (Grace, et al., 2014). Forests are a substantial carbon sink sequestering 2.0 ± 0.4 Pg C/year globally (1990–2007 estimates) (Pan, et al., 2011) and simultaneously a large carbon source through deforestation and forest degradation by contributing to approximately 7%–15% of anthropogenic emissions since 2000s (Pan, et al., 2011). The combination of deforestation, degradation, harvesting and peat fires has been estimated as 2.01 ± 1.1 Pg/annum (Grace, et al., 2014). The uncertainty on these numbers, and thus the total flux to/from the atmosphere, is considerable. Indeed, the uncertainty on both these numbers may be underestimated as we struggle to map forest carbon stocks accurately, let alone subtle changes in these stocks (Mitchard, et al., 2014). The disturbance regime, and rate of recovery following disturbance determines their effectiveness in sequestering carbon: therefore, it is important to reduce these uncertainties to allow for global-scale monitoring of the effectiveness of pledges made under the UNFCCC Paris Agreement (2015).

Degraded and secondary forests are a particular concern. They were estimated to make up 60% of the total area classified as forest in tropical regions covering 850 million ha in the year 2000 (International Tropical Timber Organization, 2002), and this number has grown significantly since then. Most studies on changing biomass stocks are focused on intact forest and changes from intact forest to non-forest only (Harris, et al., 2012). These are very dynamic areas, suffering from anthropogenic degradation but also re-growing rapidly (regrowth may represent 1.8 ± 0.9 Pg/annum) (Grace, et al., 2014). We currently lack the tools to map these subtle changes well from satellite data, leading to these large uncertainties.

Secondary forests are now especially dominant in Southeast Asia. Until the 1960s, Southeast Asia was dominated by extensive tracts of high above-ground biomass lowland Dipterocarp forests which acted as a significant carbon sink

(Kartawinata, et al., 1981). Estimates indicate that only 12% of the remaining forests in Southeast Asia remained "intact" in 2000 (Potapov, et al., 2008). The majority of natural old-growth forest areas are now considered disturbed due to different processes such as logging, conversion into degraded savanna and grassland or managed land (Giam, et al., 2011; Mietten, et al., 2014). The increased proportion of secondary forests (or successional communities) at the expenses of old-growth forests requires us to prioritize and re-focus conservation efforts on degraded forest (Lewis, et al., 2015). In fact, after disturbance, forests still retain conservation values (Berenguer, et al., 2014) and maintain appreciable biodiversity. In particular, tropical forests in Southeast Asia are considered some of the most valuable in this respect, since they host endangered species such as orangutans (MacKinnon, et al., 1997).

A major forest degradation driver is fire, which has been extensively and increasingly used in slash and burn practices and to induce clearing for industrial palm oil and paper-pulp plantations as it is the most convenient and efficient conversion method (Mietten, et al., 2014; Goldammer, 2015; Chisholm, et al., 2016). Humid tropical forest flammability is often exacerbated by human intervention (e.g., selective logging) (Siegert, et al., 2001; Gerwin, 2002; Cochrane, 2003). Fire is mainly driven by moisture stress in dry conditions during El Niño Southern Oscillation (ENSO) events (Cochrane, 2003). These have occurred in the past (notably the strong 1997–1998 event) and more recently (2015–2016), causing the alteration and degradation of tropical lowland and peat swamp forest in Southeast Asia (Chisholm, et al., 2016). These climatic anomalies will continue to threaten tropical forests in the future as these events become more frequent and of increased magnitude (Cai, et al., 2014).

Drought conditions during the 1997–1998 ENSO resulted in a total of 2.6 million ha of forest being burned (Siegert, et al., 2001) and the release of 2.97–9.42 Gt CO_2 (Page, et al., 2002), thus acting as a source of CO_2, reducing above-ground biomass and diminishing the potential (at least in the early stages of regeneration) of the newly degraded forest to act as a carbon sink (Jordan & Farnworth, 1982). Most

significantly, the 1997–1998 fires affected more severely those areas which had previously been disturbed by selective logging (Siegert, et al., 2001). This indicates that previously disturbed forests (from logging or previous fires) are more susceptible to further disturbance and thus, it is important to locate these areas (Goldammer, 1999). Fire can result in the alteration of stands in terms of structure and composition (Gerwin, 2002) by converting them from areas that have achieved high diversity to areas dominated by a few pioneer species (Toma, et al., 2005). The resulting vegetation spatial structural alterations (e.g., height, canopy cover and biomass) and composition (e.g., species diversity) after fire are complex to characterize (Kennel, et al., 2013) and there is no "coherent pattern of forest regeneration" (Goldammer, 2015). Recovery to old-growth conditions is not always possible. The majority of degraded forests might not recover and potentially develop into scrubland or grassland dominated by *Imperata cylindrica* (Goldammer, 1999; Goldammer, 2015) (often permanently due to recurring fire management practices).

Given the above, techniques for wide area and spatial measures of vegetation structure and disturbance are evidently necessary. Remote sensing observations afford in principle a vehicle for providing such measures, but methods for doing this are still under development and there is space for considerable improvements to obtain the required information from satellite instruments. We give next a brief summary of the state of the art of remote sensing practices for vegetation spatial structure characterization. Finally, evidence for the potential in this context of wavelet based two-point statistics will be supplied using spatial Interferometric Synthetic Aperture Radar (InSAR) and airborne LiDAR observations of a fire-affected site in Indonesian Borneo.

4.2. Forest Structural Heterogeneity Derived from Remote Sensing

Undisturbed old-growth tropical forests are known to be complex, multi-layered environments where heterogeneity is driven prevalently by species diversity assemblages (Malhi & Román-Cuesta, 2008). Further factors that influence heterogeneity are related to disturbance processes. For example the development of canopy gaps as large trees die and fall over, either naturally or due to extreme events or anthropogenic influence, and compositional alterations caused by changing climate or local conditions (Weishampel, et al., 2007). Spatial patterns in tropical forests are determined by the size, shape and the distribution of the single canopy components (branches and leaves), which have a varying pattern dependent on the scale of observation (Frazer, et al., 2005). Despite its importance in ecological processes, canopy spatial heterogeneity has not yet been fully quantified and lacks a standardized measurement approach given issues on the agreement of a definition (Frazer, et al., 2005). Approaches that are best suited for this include those that are able to take into account the scale-dependence of the processes and are consequently best observed using space-scale analysis derived from two-point statistical measures (wavelet space-scale analysis) of 3D datasets (Bradshaw & Spies, 1992). 3D datasets suitable for such analysis, including Light Detection and Ranging (LiDAR) and Interferometric Synthetic Aperture Radar (InSAR) are now widely available from a range of airborne and spaceborne sources (e.g., the TanDEM-X satellite formation).

Moreover, the nature of the ecological processes (derived from environmental conditions, composition and disturbance processes) results in many cases in statistical non-stationarity of the random fields associated with the instrumental observations. In essence, statistical stationarity (or homogeneity when the independent variable is space) means that the statistical measures are invariant under translation. Non-stationarity in nature includes intermittency and scale invariance (fractal process) (Davis, et al., 1994; Mallat, 2008).

Canopy structure is significantly affected by the scale of observation (Bongers, 2001). At fine-scales, within a forest patch heterogeneity is visible while, at coarser scales, the clumping of canopies results in homogeneous patches with similar structure. In this case, heterogeneity between patches due to differences in structure can be appreciated (Lertzman & Fall, 1998).

Increased availability of fine resolution data provided by commercial satellites (in particular optical sensors such as those publicized through the Google Earth platform (e.g.,QuickBird, WorldView and IKONOS) (Barbier, et al., 2010) have provided the increasing opportunity to explore canopy spatial arrangement and to resolve an unprecedented level of detail and the development of image processing algorithms that can extract single tree crowns (Palace, et al., 2008) as well as manual delineation of tree crowns (Asner, et al., 2002) but this has been more commonly done in the past using aerial photography (Wulder & Franklin, 2003).

Compositional changes (e.g., species succession) and structural changes (e.g., small canopy openings) due to disturbance (e.g., fire or selective logging) can be measured using ground data with point estimates (e.g., gap fraction and canopy openness) at recurring intervals after the occurrence of the disturbance event (Slik, et al., 2002; van Nieuwstadt, 2002; Yeager, et al., 2003; Brearley, et al., 2004; Eichhorn, 2006; Slik, et al., 2008; Delang & Li, 2013). Accessibility limits the retrieval of such information in tropical forest and the ability to gather datasets spanning large areas (Barbier, et al., 2010). Remote sensing observations offer a valuable, complementary tool to explore canopy structure variations due to degradation processes at larger scales in extensive, complex, heterogeneous and multi-layered tracts of tropical forests (Roughgarden, et al., 1991; Bongers, 2001).

Optical sensors are most commonly employed due to their widespread availability (e.g., LANDSAT), but these observations are severely limited in the tropics due to frequent cloud cover and haze, which precludes the acquisition of data (van der Sanden, 1999). Moreover, these observations provide only two-dimensional information (projection of the structure from a volume onto a plane),

lacking sensitivity to vertical structure, which is an important parameters in multi-layered tropical forests. Spectral properties provide limited sensitivity to differentiate successional stages given the rapid recovery of canopy cover after disturbance, which is reflected on the spectral signature of regenerating forest (De Sy, et al., 2012).

Improved understanding and characterization of forest structural arrangement arising from different forest types and forest patches at different successional stages can be improved using geometrical and textural properties of spectral signal from high resolution optical data (Gallardo-Cruz, et al., 2012). Resolution <4 m has also been suggested as optimal for retrieving meaningful information related to canopy structure (Proisy, et al., 2007). While datasets with resolution lower than 4 m are readily available from optical and airborne LiDAR sensors, they have limited spatial coverage (Kaasalainen, et al., 2015). Canopy texture derived from high resolution optical imagery has been employed successfully for discrimination of forest types due to the ability to exploit the variation in illumination between crowns, this resulting in tonal variation between the sunlit and shadow canopy components using Fourier Transform Textural Ordination (FOTO) (Barbier, et al., 2010), (Couteron, et al., 2005; Proisy, et al., 2007). Lacunarity has also been explored for the analysis of spatial patterns derived from canopy arrangements in simulated LiDAR datasets (Frazer, et al., 2005) and in high resolution multi-spectral optical data (Malhi & Román-Cuesta, 2008).

Requirements to capture the complex three-dimensional structure can be best matched by airborne Light Detection and Ranging (LiDAR) (Lim, et al., 2003) and Interferometric Synthetic Aperture Radar (InSAR) (Balzter, 2001). Forest spatial structure from LiDAR datasets has been extensively studied with the aim of characterizing forest types using texture metrics (Kennel, et al., 2013). Also forest disturbance has been addressed using these techniques (e.g., selective logging: (Kent, et al., 2015; Wedeux & Coomes, 2015). Canopy grain analysis from FOTO applied to LiDAR derived Canopy Height Model (CHM) and Digital Surface Model

(DSM) was also used to generate metrics related to structure and to ultimately improve above-ground biomass prediction (Barbier, et al., 2010; Véga, et al., 2015). The extraction of single crowns from LiDAR has also been explored (Garrity, et al., 2012).

InSAR is also sensitive to three-dimensional vegetation structure, with capability of mapping the vegetation spatial distribution by the coherence modulus and the vertical distribution by the interferogram phase. TanDEM-X (and the twin satellite is a single-pass interferometer acquiring data at X-band (λ = 0.031 m, 9.65 GHz) and at high spatial resolution (approximately 5 m pixel spacing). Its unique configuration results in no temporal decorrelation (Krieger, et al., 2007), as this is typically high in multi-pass interferometers where acquisitions are normally at least days, if not longer apart.

The availability of TanDEM-X data has spurred much research on forestry applications and in particular related to vegetation vertical structure (height) through interferometric phase and forest horizontal structure (canopy density) through backscatter and coherence. In this paper we concentrate on the first of these, as a Digital Surface Model (DSM) (WorldDEM™) (Bräutigam, et al., 2015) is provided globally so it is the easiest TanDEM-X data product to access and use. Indeed, TanDEM-X provides the first DSM with global coverage, at high resolution (<5 m), which could provide information on canopy heterogeneity. The DSM potential to characterize structural heterogeneity through texture based methods in tropical forests has however, seldom been explored as far as we are aware.

DSMs are produced from TanDEM-X data using the coherence phase information, which incorporates three-dimensional spatial information on vegetation height superimposed on topography (Balzter, 2001; Solberg, et al., 2015). Sensitivity to sensor's parameters (e.g., polarization) and environmental conditions (e.g., rainfall events and seasonality) have also been noticed to influence the phase center height (PCH) but research has been predominantly focused on boreal or temperate forests. For instance, ground scattering is lower at VV polarization

compared to HH (Kugler & Hajnsek, 2011). Seasonality can also play a part in determining X-band penetration depth with deeper penetration occurring during leaf-off conditions (Praks, et al., 2012). Penetration depth decreases with increasing frequency, so at X-band penetration depth is lower compared to L-band (Balzter, 2001). In tropical forest, phase height was found to be higher for shorter forest (early succession) compared to taller forest stands (Treuhaft, et al., 2015).

Developing methods for the extraction of texture is a key priority to retrieve information on canopy conditions from forest structure (Barbier, et al., 2010). However, texture derived from 3D InSAR datasets has not yet been explored to obtain information related to canopy heterogeneity and in particular for the analysis of differences in structure between landscapes, which are characterized by a gradient of heterogeneity derived from anthropogenic disturbance.

Spatial patterns, which from a cognitive point of view we can associate with forest heterogeneity, such as canopy clusters canopy closure and voids, canopy roughness, vegetation density, and emergent trees, appear in statistical measures of the 3D observations (vegetation height as a function of northing and easting) in, for instance, signal energy which is highly variable both in space and frequency. Their characterization requires therefore a signal representation, which affords local energy estimation. Wavelet frames, which feature an optimal time-frequency (space-scale) resolution, are the ideal representation choice for the purpose (Mallat, 2008).

4.2.1. Rationale

The full LiDAR waveform provide same measure of the forest vertical structure function, obtained by sampling in range time the returns from layers of elementary scattering elements which are distributed in height along the vegetation volume. When the full waveform is processed into a Canopy Height Model (CHM), the vertical structure measure is condensed in one value, namely the distance at each resolution point in space from the ground return to the top canopy return. It carries therefore a three-dimensional geometric characterization of the forest structure, one

dimension being the vegetation height, and the other two dimensions being the spatial distribution of the heights (the horizontal structure).

The phase of the coherence can be exploited to derive a surface model (DSM), which incorporates spatial information on topography and vegetation height. This happens because on a vegetated surface the phase center height (PCH) moves up from the value corresponding to the ground, because of the contribution of the scattering elements in the vegetation volume (Praks, et al., 2012). When the DSM is located near the canopy surface, it carries information on those higher spatial frequencies that are generated by the forest horizontal structure, similarly to the LiDAR CHM and therefore can give an indication of canopy structure.

An intuitive view of the phenomenon in case of the non-stationary and intermittent random field provided by the primary forest canopy height, can be obtained in this way. Moving from one resolution element to the next, the radar beam will intercept different structural patterns of the heterogeneous canopy. As a consequence, the scattering volume dimension will change, because the local incidence angle and the extinction will change (different number density of scattering elements). Reasoning in terms of a piecewise random volume model, the net result of all changing factors will be a corresponding spatial change of the complex coherence and of the phase center height, and in turn on the phase to height conversion (DSM).

The aim of the work presented in this paper is to compare the information content of the spatial statistic (texture) of DEMs provided by two observational sensors, LiDAR and InSAR, these featuring complementary spatial resolution and mapping extent characteristics. The aim is pursued by providing a quantitative characterization of the mapping between observations (LiDAR and InSAR) and target spatial structure using two-point statistical measures. The approach is two-fold: first, LiDAR and InSAR textural correlation is used to assess coupling of topographic and canopy structures. Subsequently, space frequency analysis (2D wavelet spectra) is applied to structure measures provided by LiDAR CHM and

TanDEM-X DSM to test congruency of the measures carried out by the two sensors. Finally, thematic class separability based on the wavelet statistical measures is performed.

4.3. Study Site

Sungai Wain Protection Forest (SWPF) is located to the North of Balikpapan (116°46'14.08"E, 0°59'57.91"S), East Kalimantan (Indonesia) (Figure 1). The study site encompassed intact lowland Dipterocarp forest within the core of the SWPF surrounded by disturbed forest dominated by *Macaranga sp*. which developed after the 1997–1998 fires (Hajnsek, et al., 2009). Cultivated areas are located to the North and to the East of the SWPF with mainly abandoned mixed rice fields, grassland which is dominated by the invasive *Imperata cylindrica* and scrub composed of a mix of vegetation at various stages of development. Intact lowland Dipterocarp forest in the SWPF reaches above-ground biomass up to 400 Mg/ha and heights up to 60 m (Kugler, et al., 2015) and on a large scale appears as homogeneous (Hajnsek, et al., 2009).

Elevation ranges between 30 and 140 m above sea level with an elevation gradient decreasing from North to South and terrain slope ranging from 0° to 30°. The soil type is classified as Alisols (van Nieuwstadt, 2002). The climate is categorized as Tropical Wet (Walsh, 1996), and is wet all year but has infrequent marked dry periods as a consequence of ENSO conditions. Its wet season, December to May, has peak rainfall in March (272 mm), with average annual precipitation equal to 2250 mm (Yassir, et al., 2010), and a rainfall minimum in July (147 mm during the dry season) (MacKinnon, et al., 1997). The 1997–1998 ENSO, which affected the study area, was characterized by a lack of precipitation for several months, leading to fire which caused damage to two thirds of the SWPF (van Nieuwstadt, 2002). As well as altering the species composition of the forest, there were noticeable changes in forest structure such as an increase in canopy openness (van Nieuwstadt, 2002).

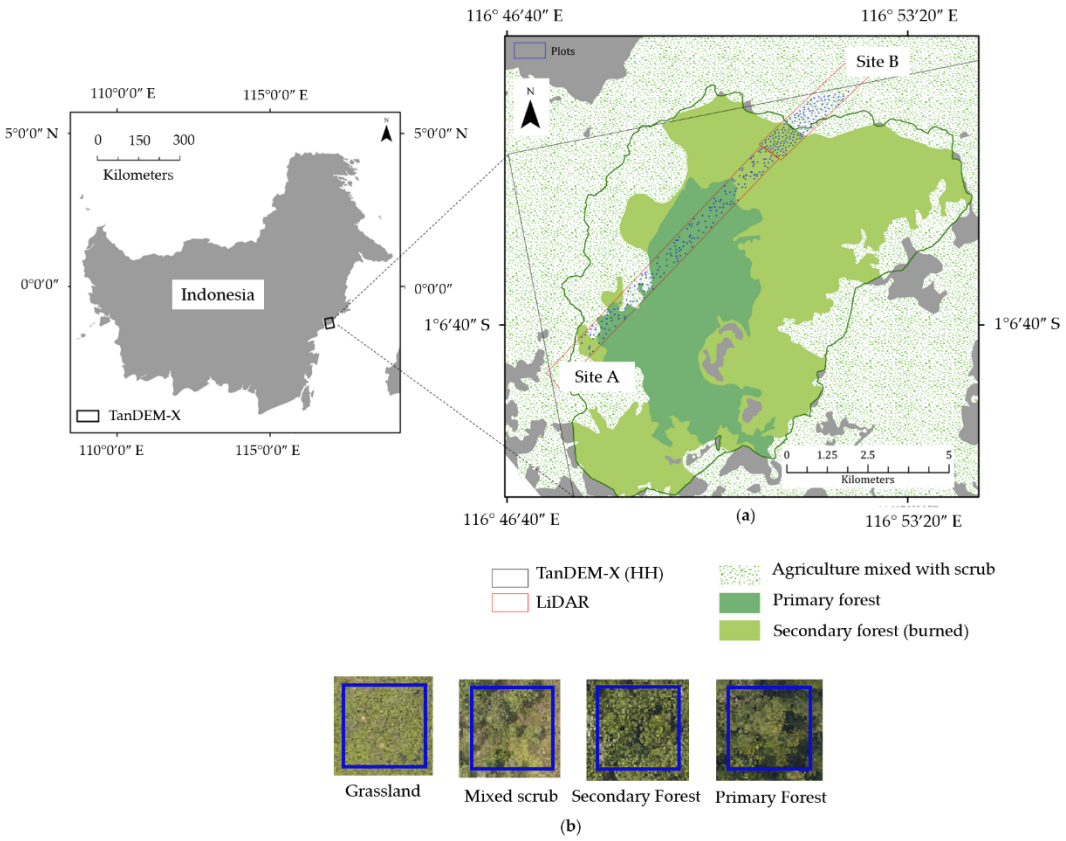

Figure 1. (**a**) Study site location and data extent overlaid on a land cover map provided by the Indonesian Ministry of Forestry (Indonesian Ministry of Forestry, 2015). TanDEM-X data extent (black box, only partially covered in this image), LiDAR site A and B (red) and 315 sample plots (35 x 35 m²) (blue squares). LiDAR Site A is primarily covered by primary forest (PF) (undisturbed) while; Site B is dominated by secondary forest (SF) (disturbed), mixed scrub (MS) and grassland (GR); (**b**) Range of vegetation structures observed from high resolution aerial photography (0.5 m) (blue square: 35 x 35 m² plot).

4.4. Methods

4.4.1. TanDEM-X Data

TanDEM-X data was acquired on 11 December 2014 in StripMap bistatic mode (single polarization HH) at 41° incidence angle supplied through AO VEGE6702 by DLR (Figure 2). The scene covers 32 km W-E x 25 km N-S (UL Geo: 116° 46' 14.08″ E, 0° 59'57.91″ S). A summary of the TanDEM-X acquisition configuration is found in

Table 1. The data was processed using ENVI/SARScape 5.0 Interferometric module to generate coherence modulus and a Digital Surface Model (DSM) (Sarmap, 2012) and consists of the following steps: (a) interferogram generation (2 looks in azimuth and 2 looks in range); (b) retrieval of a subset of the SRTM-4 version DEM which covers the extent of the TanDEM-X acquisition; (c) interferogram flattening; (d) filtering using a Goldstein filter (Goldstein & Werner, 1998) and coherence generation; (e) phase unwrapping using the minimum cost flow algorithm; and (f) geocoding at 4.6 m resolution to WGS84 datum, Zone 50 South. A DSM was generated using the phase to height conversion by setting relaxed interpolation since the low coherence values meant that the phase was difficult to unwrap (Figure 2). The derived DSM was also geocoded at 4.6 m pixel spacing to WGS84 datum, UTM Zone 50 South. The DSM derived from TanDEM-X corresponds to the superimposition of the bare earth (Digital Terrain Model- DTM) plus the vegetation and corresponds to the phase center height (PCH) which is located within the vertical structure of the target (Balzter, 2001). The location of the PCH depends on target parameters (e.g., vegetation spatial configuration such as volume density) and the sensor's parameters (e.g., frequency and polarization) (Balzter, et al., 2007).

Table 1. TanDEM-X acquisition configuration parameters.

Parameter	Value
Mode	StripMap bistatic
Acquisition Date	11/12/2014
Polarization	HH
Incidence Angle (°)	41
Resolution (azimuth, range) (m)	3.3 × 1.8
Ground resolution (m) at 41°	3.3 × 2.74
Effective Baseline (m)	223
HoA (m)	30.2
Orbit direction	Ascending
Look direction	Right

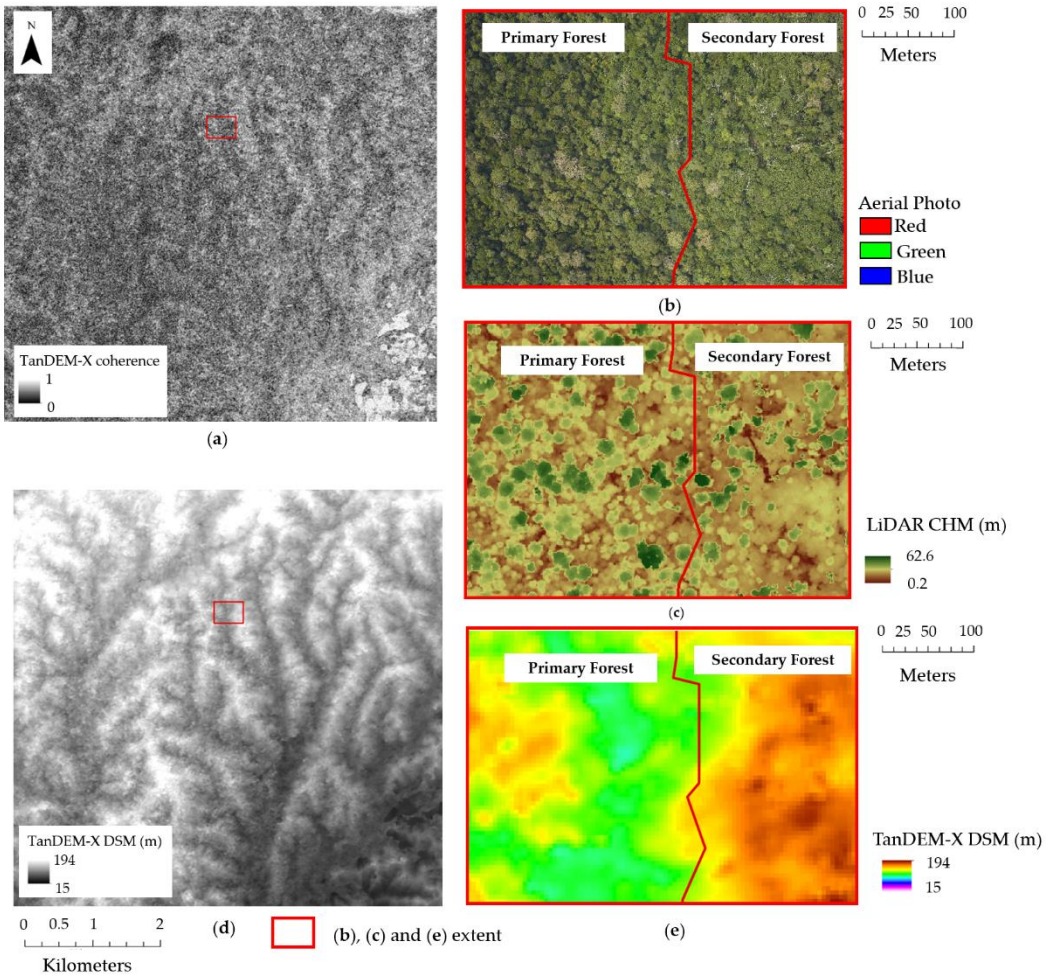

Figure 2.(**a**) TanDEM-X coherence modulus; (**b**) Aerial photo (0.5 m resolution); (**c**) Canopy Height Model (CHM) derived from airborne LiDAR (1 m resolution); (**d**) TanDEM-X DSM; and (**e**) TanDEM-X DSM subset. Boundary between primary forest (PF) and secondary forest (SF) (red line) according to the land cover map provided by the Indonesian Ministry of Forestry (Indonesian Ministry of Forestry, 2015) is shown on the aerial photo (**b**); LiDAR CHM (**c**) and TanDEM-X DSM (**e**).

4.4.2. Reference Data

LiDAR data was acquired on 14 November 2014 using the Optech ORION M300 system (frequency: 55 Hz). The airborne LiDAR instrument was flown at an altitude of 700 m above ground level, scan angle of ~18°, swath width of 455 m with

an overlap of 227 m. The resulting point density was 5.75 points per m^2 (excluding overlap). The vertical accuracy for all LiDAR returns on clear ground was 0.08 m (standard error at 1 sigma). The data covers 9.7 x 0.7 km^2 (Site A) and 4.5 x 0.8 km^2 (Site B). The LiDAR products were geocoded to WGS84 datum, Zone 50 South. Lidar2dems open source software developed by Applied GeoSolutions was used to process the LiDAR data to provide the following: a Canopy Height Model (CHM) at 1 m resolution was generated by subtracting a Digital Terrain Model (DTM) from a Digital Surface Model (DSM) (Figure 2). The general term Digital Elevation Model (DEM) is used to refer to DSM, DTM or CHM.

A land cover map developed by the Indonesian Ministry of Forestry (Indonesian Ministry of Forestry, 2015) was also used to distinguish between broad vegetation classes with additional visual inspection of aerial photography (Figure 1).

Aerial photos (AP) (0.5 m resolution) were acquired at the same time as the LiDAR overpass using a Trimble 80 megapixel medium format digital aerial camera. The APs were used as reference data to aid in the supervised analysis for the selection of classes of interest, since ground truth data was not available. The APs were deemed suitable to aid the selection of structural classes since they were able to capture illumination variability giving rise to textural differences derived from the spatial arrangement of canopy components (combination of sunlit or shadow areas), and so could be used to locate areas with different structural properties through visual inspection.

4.4.3. Vegetation Structural Class Selection

Analysis was performed in 315 virtual plots (35 x 35 m^2 = 0.12 ha) located in primary lowland *Dipterocarpaceae* forest (intact) (PF), secondary forest (disturbed) (SF), mixed scrub (MS) and grassland (GR). Figure 3 shows a representative sample of virtual plots for each class visualized on a LiDAR CHM. A random sampling approach was devised within the extent covered by LiDAR, TanDEM-X and aerial photos datasets so that the number of non-overlapping plots of size 35 x 35 m^2 could

be maximized without user interference. The choice of window size was determined from knowledge of the landscape taking into account the spatial arrangement and size of canopies so that the variability was appropriately captured. The choice was conditioned by the following criteria: a) it could not be smaller as the largest crown dimensions were in the range of 10–20 m in the intact primary forest (PF); and b) in connection with the random sampling approach, the size ensured that the plots were not selected by the user so that the window was not centered on a single emergent crown; c) any larger plots might have contained a mixture of forest types, and the resolution of any eventual product using windows of this size would be reduced.

The random sampling was performed within landcover classes defined in a landcover map derived from Landsat developed by the Indonesian Ministry of Forestry (Indonesian Ministry of Forestry, 2015) and further verified by visual interpretation of high resolution aerial photography (0.5 m resolution). The virtual plots extracted were then checked by visual interpretation of aerial photos acquired at the same time as the LiDAR and TanDEM-X data acquisition to ensure that they effectively belonged to an appropriate landcover class.

From visual interpretation it was evident that the class defined as "mixed agriculture and scrub" in the Indonesian Ministry of Forestry land cover map was broad and not representative of the condition in 2014 (as observed from aerial photography). Thus, it was deemed appropriate to partition the class into two separate classes: grassland (GR) and mixed scrub (MS) based on visual inspection. The MS class is composed of a combination of *Imperata cylindrica* and presents taller re-growing vegetation, such as shrubs and young trees which are not present in the grassland class (GR), this being prevalently colonized by *Imperata cylindrica*.

The final training dataset consisted of a total of 315 virtual plots belonging to primary forest (n= 96), secondary forest (n= 126), mixed scrub (n= 44) and grassland (n= 49).

Landscape heterogeneity from 2D wavelet spectra was assessed based on randomly selected pixels which are representative of the chosen classes (PF, SF, MS and GR) to give insight into the target structure at four scales of decomposition based on a LiDAR CHM and TanDEM-X DSM (the figure in Section 4.5.2). The set of cases considered are as follows: (a) Emergent trees in a multi-layered heterogeneous (in terms of heights) matrix characteristic of old-growth forest (PF); (b) Relatively homogenous secondary forest patches composed by a carpet of crowns with high clumpiness. Absence of tall emergent trees but has reached full canopy cover (SF); (c) Early stage re-growth presenting smaller tree crowns (2–3 m) closely packed but discernible from LiDAR (MS); (d) Homogeneous grassland (*Imperata cylindrica*) presenting low height with scattered small shrubs (GR).

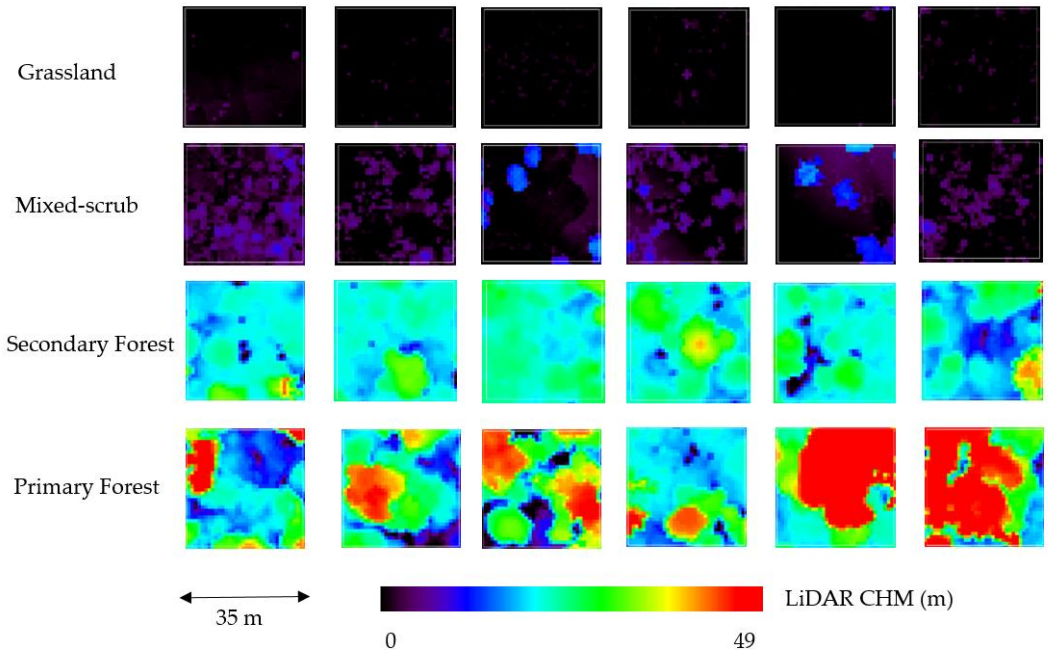

Figure 3. Sample classes derived from a LiDAR Canopy Height Model (CHM) (m) within 35 x 35 m^2 plots illustrating vertical structure arrangement (height) in: primary forest (intact) (PF), secondary forest (disturbed) (SF), mixed scrub (MS) and grassland (GR).

4.4.4. LiDAR and TanDEM-X Texture Correlation Analysis to Assess Impact of Topographic and Canopy Structures

Scaling (spectral) analysis of LiDAR and TanDEM-X datasets was performed in the wavelet domain along a profile covering 6.95 km in a north-south direction dominated by PF and SF. The aim of the analysis was to identify scales where textural patterns associated with topographic or canopy features develop within the different Digital Elevation Models (DEMs). The following two-point spatial statistics were computed in the wavelet domain (**Chapter 3**): (a) wavelet variance; and (b) wavelet co-variance (between LiDAR DTM/DSM, LiDAR DTM/CHM, and LiDAR DTM/TDX DSM). A wavelet representation is used instead of a Fourier one because the processes are multi-scale and non-stationary. The analysis provided an assessment of the relative influence on the signal texture of topographic structures and canopy structures, which is the main concern of the current study.

4.4.5. 2D Wavelet Spectra

Information on canopy structure is carried by datasets where vegetation height (or proxy) is mapped as a function of space (e.g., LiDAR CHM or TanDEM-X DSM) (Figure 4). This mapping provides a two-dimensional random field, whose spatial (two-point) statistics condenses measures of the horizontal and vertical distribution of the forest. These random fields are analyzed using two-point statistics provided by the variance of a wavelet frame that acts as a differential operator Equation 1). This statistics, analogous to the structure function lends to the characterization of stationary random processes, as well as of non-stationary processes with stationary increments (e.g., fractals) (Davis, et al., 1994).

$$\langle WS(s,x)^2 \rangle \cong \langle (f(x+s) - f(x)^2) \rangle \qquad \text{Equation 1}$$

In particular, we consider exploiting the well known properties of optimal space-frequency resolution of wavelets, and local (in space) estimates of the wavelet variance as a function of scale.

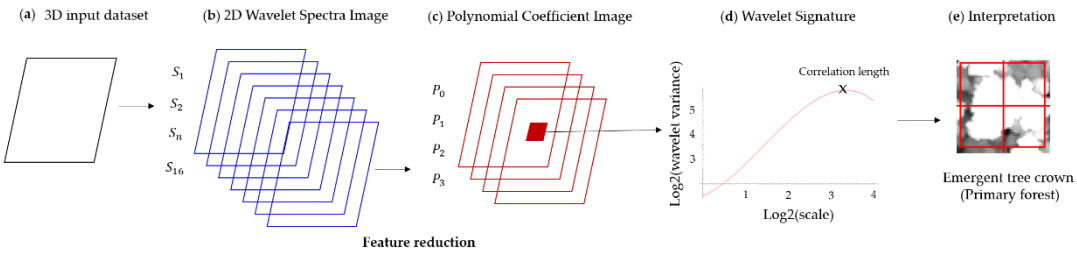

Figure 4. Flowchart illustrating the application of 2D wavelet spectra to 3D datasets for the analysis of landscape heterogeneity across a disturbance gradient: (**a**) 3D input dataset; (**b**) generation of 2D wavelet spectra image with 16 fractional scales with $2^{1/4}$ spacing between scales at four dyadic scales (S_1, S_2 …S_n); (**c**) feature reduction to four wavelet polynomial coefficients (P_0, P_1, P_2 and P_3) by fitting a 3rd order polynomial to the wavelet signature; (**d**) wavelet signature (wavelet variance as a function of scale); and (**e**) interpretation of the wavelet signature based on target structural characteristics.

At each point in space (at each pixel location of the analyzed image), we obtain, in the log–log variance/scale place, a characteristic signature of the process, which reflects process parameters, such as field roughness, correlation structures and intermittency. This data structure is called "2D wavelet spectrum" (WS), and it is an extension of the method developed in **Chapter 3**. In more detail, the input field (e.g., vegetation height image) is decomposed in the wavelet frame basis using four dyadic scales. Local estimates of the wavelet variance are obtained by convolving the square of the wavelet coefficients with a B-spline smoothing function (Equation 2).

$$WS(s,i,j) = \left(c_{x,s}(i,j)^2 + c_{y,s}(i,j)^2\right) \otimes \beta_{i,j} \qquad \text{Equation 2}$$

Each signature $\log_2$WS ($\text{LiDAR}_{\text{CHM}}$WS or TDX_{DSM}WS) is interpolated in scale with a step of $\frac{1}{4}$ and fitted by a 3rd degree polynomial function. This function provides a good approximation to the wavelet signature (**Chapter 3**). Four polynomial coefficients for each pixel of the input field constitute finally the

dimensionally reduced features that describe the 2D wavelet spectrum. Two-point statistics was generated by deriving four polynomial coefficients: for LiDAR CHM ($\mathrm{LiDARCHM_{P0}}$, $\mathrm{LiDARCHM_{P1}}$, $\mathrm{LiDARCHM_{P2}}$ and $\mathrm{LiDARCHM_{P3}}$) and for TanDEM-X DSM ($\mathrm{TDXDSM_{P0}}$, $\mathrm{TDXDSM_{P1}}$, $\mathrm{TDXDSM_{P2}}$ and $\mathrm{TDXDSM_{P3}}$). Pixel based analysis was undertaken to explore sensitivity of 2D wavelet spectra to canopy structure heterogeneity through a gradient of varying vegetation structure (primary forest, secondary forest, mixed-scrub and grassland) (see Section 4.4.3).

4.4.6. Separability

To assess statistically the separability between four classes afforded by the wavelet spectra polynomial representation the Jeffries-Matusita (JM) distance. The JM distance of a pair of probabilistic distributions indicates the average distance between two classes density functions and it features a saturating behaviour with increasing separation (Alexander & Inggs, 1999). This fact makes it more suitable for dealing with a multi-class problem, because it avoids bias when taking averages due to an easily separable class. It is therefore suitable for the problem at hand, which has four features and four classes. The JM Equation 3) is derived from the Bhattacharyya distance (BD) Equation 4) (Alexander & Inggs, 1999). The JM distance ranges between 0 and $\sqrt{2}$ with highest values indicating greater class separability (Alexander & Inggs, 1999).

$$JM_{ij} = \sqrt{2(1 - e^{-BD})} \qquad \text{Equation 3}$$

where BD:

$$BD = \frac{1}{8}\left(M_i - M_j\right)^T \left[\frac{C_i + C_j}{2}^{-1}\right]\left(M_i - M_j\right) + \frac{1}{2} ln \left[\frac{\left|\frac{C_i + C_j}{2}\right|}{\sqrt{|C_i||C_j|}}\right] \qquad \text{Equation 4}$$

Where i is the class with mean vector M_i and co-variance matrix C_i.

Pairwise JM resulted in six JM distances, which are averaged and normalized by dividing the theoretical maximum JM distance of $\sqrt{2}$. The normalized average JM

distance was used as a parameter to indicate overall class separability (Alexander & Inggs, 1999). Upper and lower bounds of the probability of the classification error $P_e(i,j)$ are given by Alexander & Inggs (1999) Equation 5).

$$\frac{1}{16}(2 - JM_{i,j}^2)^2 \;\leq\; P_E(i,j) \;\leq\; 1 - \frac{1}{2}(1 + \frac{1}{2}JM_{i,j}^2) \qquad \text{Equation 5}$$

The JM distances are computed for the six combination of class pairs among grassland, mixed-scrub, secondary forest, primary forest, and feature vectors $\overrightarrow{v_{x,y}} = \{P_0, P_1, P_2, P_3\}$, where P_i are the polynomial coefficients of the wavelet spectra averaged over the training set plots, defined as described in Section 3.3. Morever, to investigate the dependence of class separability on scale, the JM distance is also computed for each scale of the signature separately $\langle W^2 \rangle = f(scale)$ derived from the polynomial coefficients. In this case, the feature space is one-dimensional.

4.5. Results and Interpretation

4.5.1. LiDAR and TanDEM-X Textural Correlation Analysis to Assess Coupling of Topographic and Canopy Structures

Canopy structure (roughness) measures derived from 3D datasets can provide information on landscape disturbance and recovery (Weishampel, et al., 2007) but can be affected by environmental factors (Wedeux & Coomes, 2015) such as the underlying topography especially in steep terrain (Véga, et al., 2015). Understanding of topographic structure is important to gain a better insight on the processes that play a role and the extent to which they influence the 3D information provided by LiDAR and InSAR. This is especially relevant as only the LiDAR provides both a DSM and DTM, and thus the possibility to calculate a CHM; TanDEM-X only provides a DSM.

The wavelet variance, being a two-point statistic proxy of the structure function, bears information on the dominant correlation patterns associated with either topographic or canopy structures, these happening at different scales and can also give insight into the impact of topography and canopy structure by comparison

with the available LiDAR DTM which carries information on ground topography (Figure 5a). To test this we performed an analysis over the 6.95 km transect in primary and disturbed forest, considering the LiDAR and TanDEM-X data.

The LiDAR DTM (red) signature reveals the trend of a process with smooth texture at short scales and long memory (correlated patterns) up to 200 m (Figure 5a). This scale corresponds to the onset of regular (almost periodic) patterns induced by the topography from the hilly terrain, which is reflected on the LiDAR DSM (black) and the TanDEM-X DSM (green), while the LiDAR DSM (black) carries strong information of short scale texture, with correlation length of tens of meters. Importantly, this texture patterns is also present (exactly overlaid) in the LiDAR CHM (blue) signature, revealing that within the short scale range (between 1 and 10 m) the textural information is related to canopy structure and not to topography. The TanDEM-X DSM (green) is also sensitive to these short scales structures due to canopy variation (i.e., variance greater than LiDAR DTM) but with lower separation with respect to variance due to topography (LiDAR DTM).

The wavelet co-variance holds information on the textural correlation between datasets, these being the LIDAR DTM, DSM and CHM and the TanDEM-X DSM (Figure 5b). The LiDAR DTM-DSM (red) confirms the presence of structures (periodic patterns) in the DTM texture at correlation length of 200 m (scale 2^8), which are reflected onto the DSM texture. At shorter scales, the texture correlation between LiDAR DTM and TanDEM-X DSM (black) is one order of magnitude lower, especially at scales typical of canopy width and gaps. This fact reinforces the point that although the TanDEM-X DSM is affected by the DTM noise, information on vegetation structure can still be detected as it happens at a different scale range. However, there is a striking feature in the LiDAR DTM/CHM co-variance (green) that reveals that there is also a textural reflection of topographic structures onto the LiDAR CHM, although at two orders of magnitude less important. Still, even if it is a weak coupling, this could mean that the LiDAR CHM has a component that follows the strong topographic features at scale of 200 m. This coupling could

confirm the fact that forest in valleys is higher than forest on ridges. This is due to several factors such as: (a) higher soil fertility and moisture availability in valleys; and (2) more need for forest in valleys to grow taller to reach light (light competition) (Eichhorn, 2006).

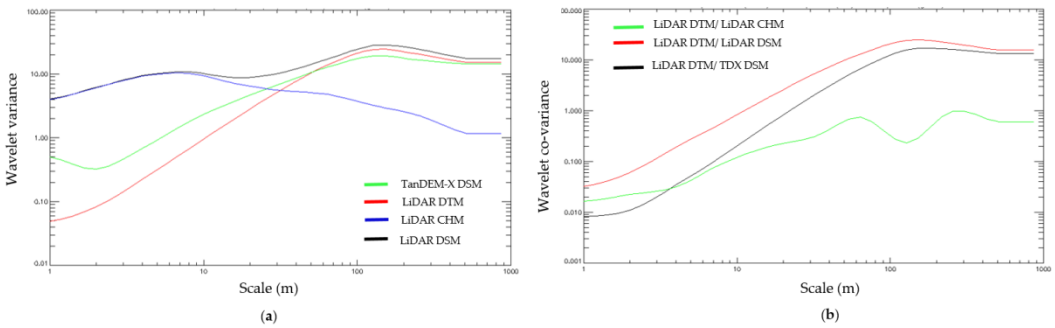

Figure 5. (**a**) Wavelet variance as a function of 10 dyadic scales (2 m to 1000 m) computed over a 6.95 km transect in intact (PF) and disturbed secondary forest (SF). TanDEM-X DSM (green) and LiDAR derived datasets (DSM: black, CHM: blue and DTM: red). The figure indicates how the information related to canopy structure provided by the LiDAR CHM (apparent with higher wavelet variance at short scale ≅ 10 m) is reflected onto the TanDEM-X DSM within the same scale range. Whereas, structure due to topography as provided by the LiDAR DTM are captured in the region around the wavelet variance maximum at longer scales (≅ 200 m), and are reflected onto the TanDEM-X DSM within the same scale range. Therefore, the TanDEM-X DSM contains both textural components due to forest canopy structure and elevation variation, these however appearing at largely different scale domains. (**b**) Wavelet co-variance providing information on pairwise textural correlation between datasets: LiDAR DTM, DSM and CHM versus TanDEM-X DSM. LiDAR DTM/LiDAR CHM (green); LiDAR DTM/LiDAR DSM (red) and LiDAR DTM/TDX DSM (black). The textural correlation between two datasets can be appreciated as being low at short scales and higher at long scales. Abbreviations: Canopy Height Model (CHM); Digital Surface Model (DSM) and Digital Terrain Model (DTM).

The results is key to determine the potential of TanDEM-X DSM for detecting canopy heterogeneity over larger areas compared to airborne LiDAR since TanDEM-X provides global coverage (Bräutigam, et al., 2015). Moreover, as opposed to a CHM the characterization of canopy heterogeneity does not depend on the availability of ground topography (DTM) but relies on the canopy roughness information provided from a DSM which does not penetrate deep enough into the canopy to reach the ground (in the presence of dense tropical forest) and therefore is restricted to a layer located somewhere within the upper canopy (Kugler, et al., 2010). Limitations due to resolution are to be taken into account since this is lower for TanDEM-X and it does not enable to resolve single crowns as in the high resolution airborne LiDAR. The results have implications on the utility of LiDAR CHM but most importantly the potential of TanDEM-X DSM, which can provide complementary information on canopy roughness.

Further analysis was undertaken at short scales (between scale 2^0 and 2^4). Longer scales were not considered since the ground topography was found to play an increasingly important role in affecting the process. Future research which aims to link textural variations to forest parameters (e.g., crown dimensions, height and above-ground biomass) should take into account the influence of topography to avoid bias in the estimation of these parameters which could be caused by the underlying relief rather than structural parameters (Proisy, et al., 2012).

4.5.2. Canopy Structural Heterogeneity Based on 2D Wavelet Spectra

Airborne LiDAR CHM is optimal to gain understanding of the processes driving the wavelet signature due to the high resolution (1 m) and thus, the ability to resolve single crowns. Individual spectrum data points, one in each of the four land cover types (each corresponding to the local wavelet variance as a function of scale, i.e., a wavelet signature) were considered in order to help in the interpretation of wavelet spectra of a LiDAR CHM. Each spectrum sample corresponds to a local wavelet variance estimate at one point in space and for all scales (i.e., a wavelet

signature). The interpretation of the wavelet signatures is based on two main considerations: (a) extent to which the process presents self-similarity (correlation length); and (b) wavelet variance absolute values for a set of landscape heterogeneity cases is illustrated in Figure 6.

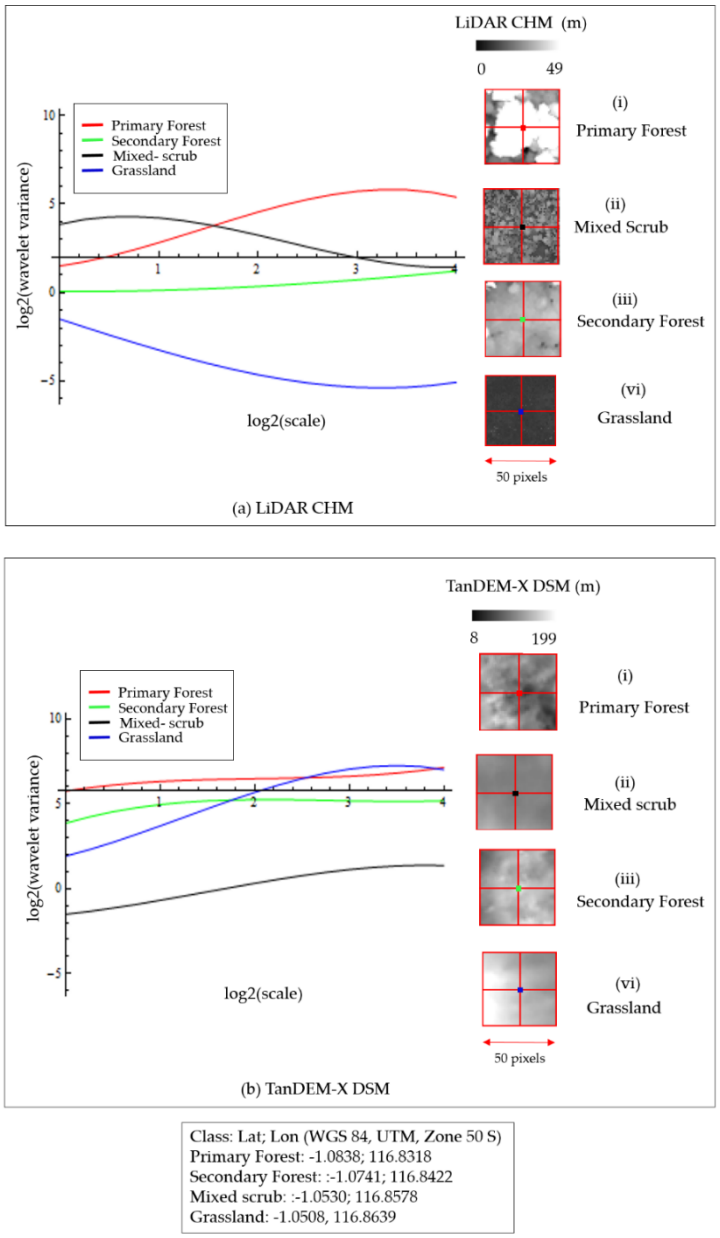

Figure 6. Wavelet signatures based on: (a) LiDAR CHM; and (b) TanDEM-X DSM based on one pixel taken in: primary forest (PF) (red), mixed-scrub (MS) (black), secondary forest (SF) (green) and grassland (GR) (blue). Colored squares within the LiDAR CHM or TanDEM-X DSM subsets indicate the pixel selected for the

analysis: 1 pixel (1 x 1 m^2 in LiDAR CHM and 4.6 x 4.6 m^2 in TanDEM-X DSM. Interpretation of the signature should take into account the location of the maxima (sill) or correlation length which indicates the point in terms of scale where the process autocorrelation decays to zero. The process "roughness" when considering the process smoothed at a given scale is indicated by the wavelet variance values at that scale, with higher wavelet variance indicating greater process roughness. Wavelet signature that do not present a correlation length (flat signature) is typical of a white noise processes which means that the process is self-similar at all scales indicating homogeneity. Similarities and differences between wavelet signatures must be considered in terms of correlation properties (correlation length), which are indicated by functional relations such as maxima and slope, and process variance as a function of scale, which is indicated by the wavelet variance magnitude.

Wavelet signatures for a multi-layered, complex old-growth forest patch (PF) (red line) dominated by a large emergent crown (crown diameter in the range of 18 m) show the typical trend of stationary noise with an exponential autocorrelation function (increasing variance with scale, asymptotically converging to the process variance). Wavelet variance for primary forest ranges between 1.5 and 5.4 with a maxima (correlation length) around scale 2^3 (8 m). Of course, this figure must not be interpreted as a crown width measure, but as the neighborhood within the crown where the canopy height variations are still correlated. This can be verified by interpretation of inset (Figure 6a(i)) showing the presence of a large emergent crown surrounded by coalescing large crowns.

The flat wavelet signature for a pixel selected in secondary forest (Figure 6a(iii) composed of interlocking crowns of similar height (homogeneous structure) with a lack of emergent trees is markedly different from that of the heterogeneous primary forest. The signature is typical of a white noise process meaning that the process is scale invariant and also presents no correlation length meaning that the process is self-similar at all scales considered and this is due to the homogeneity of the forest

patch, it does not present correlated features. The wavelet variance (in this case proportional to the scale variance) is lower compared to that of primary forest (range between 0.06 and 1.2).

The mixed-scrub class signature (black line) reveals the presence of non-stationarity with full multi-scale correlation patterns (decreasing variance with increasing scale), and a first correlation length at short scale (2 m). This is because the size of crowns located in mixed-scrub (as seen in Figure 6a(ii)) is much lower (1–2 m) compared to the size of emergent tree crowns in primary forest (Figure 6a(i)).

The grassland class wavelet signature also presents a white noise process, with the lowest process variance. The corresponding LiDAR CHM pixel selected is shown in (Figure 6a(vi)) and is clearly dominated by a layer that is texturally homogeneous and featureless.

The corresponding TanDEM-X DSM analysis does not match with the LiDAR CHM analysis. This highlights the fact that the sensor resolution is of key importance in textural measures. The two forest classes (primary forest and secondary forest) (red and green line) behave in a similar way, with the signatures revealing white noise processes (no correlation length) however in terms of wavelet variance values the primary forest class presents always higher values compared to secondary forest. The similarity between the wavelet signatures for these two classes is due to the fact that now single canopies cannot be resolved, and the correlated patterns appearing at 1 m resolution in the LiDAR CHM signatures are now not visible.

Nonetheless, the primary forest process features a higher process variance (Figure 6b(i)), meaning that still some discrimination between primary forest and secondary forest is possible with the one-point statistic. The mixed-scrub signature (Figure 6b(ii)) is again white noise and presents the lowest process variance. Again, this is due to the fact that smaller crowns cannot be resolved. Importantly, the grassland signature (Figure 6b(vi)) reveals a stationary correlated process, with a sill (signature maximum) around 8 m (scale 2^3). This is ascribed to the influence of

topography. Indeed, as these areas are dominated by surface scattering, from the spatial statistic (texture) point of view, the main dependence comes from the terrain height variations, whereas, in forested areas, volume scattering moves the PCH upwards towards the canopy upper layer and limits penetration capabilities.

4.5.3. Interpretation of Wavelet Measures of Structural Heterogeneity Based on Height Variance

4.5.3.1. Wavelet Signatures Polynomial Fit

Probability distributions (PDF) for the first wavelet polynomial coefficient (P_0) derived from the 3rd order fitted polynomial are found in Figure 7. P_0 is the intercept with the y-axis in the log–log variance–scale plot, therefore it is a good approximation to the variance at short scale. From Section 4.1 we assume that most of the variation due to canopy structures occurs at short scale and thus, P_0 holds more information compared to the other polynomial coefficients (P_1, P_2 and P_3).

By visual inspection of Figure 7, the following comments can be made. Overlap between classes is evident both in the LiDAR and in the TanDEM-X especially for the two forest classes. In the LiDAR CHM case, primary forest PDF presents a bimodal distribution, both modes having high means but low variance. The primary forest looks therefore texturally rough but more homogeneous. The secondary forest PDF is also bi-modal, but with higher variance in the two modes, these being heavily merged. The first mode presents lower P_0 values. Therefore, the secondary forest looks in some instance texturally less rough, but highly non-homogeneous.

The PDF of the MS class presents similar characteristics (bi-model, high variance) but with increasing textural non-homogeneity. Grassland PDF is also bi-modal with distinct low mean, this being the most texturally flat class. It is noticeable how in all cases the LiDAR CHM, due to high resolution, manages to split texturally each class into two characteristic components. Similar considerations can be made in the TanDEM-X case, with the following differences although the variances of the PF and SF PDFs are almost equal. Therefore, the two classes appear

with the same degree of textural homogeneity. The first mode of the MS PDF is strongly shifted towards low mean value. The MS class is again texturally split. But due to lower resolution, the lower mode overlaps part of the smoother GR class.

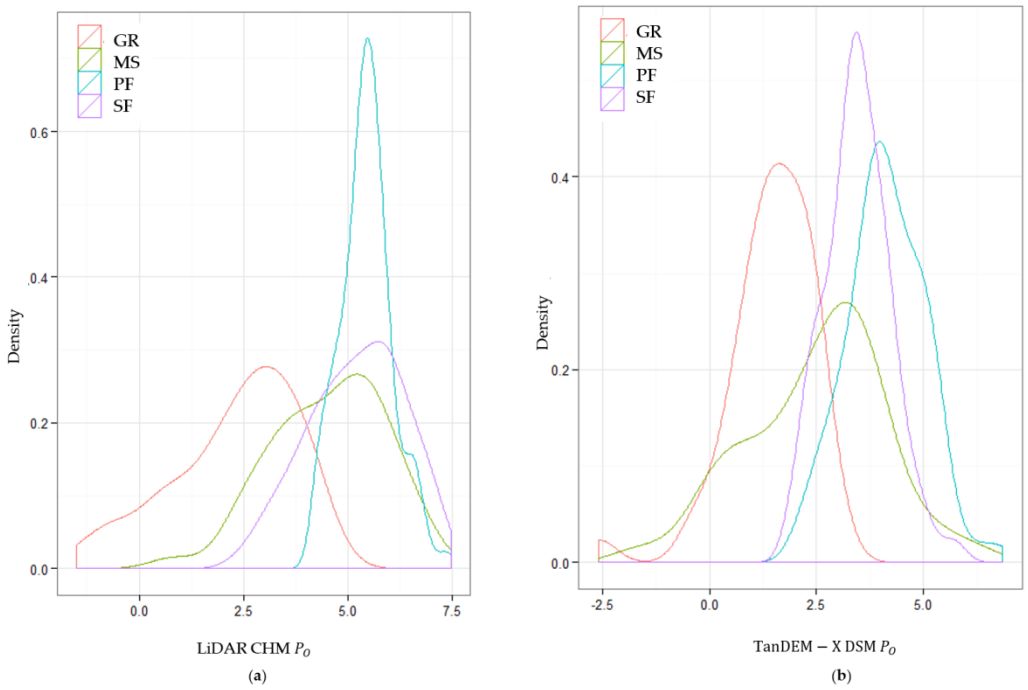

Figure 7. Probability distribution (PDF) of the first coefficient P_0 in the polynomial approximation of the wavelet signature by class (grassland- GR, mixed-scrub- MS, primary forest- PF and secondary forest- SF): (**a**) LiDAR CHM P_0 PDF; and (**b**) TanDEM-X DSM P_0 PDF. Greater information was observed using one-point statistic of P_0 compared to using one point-statistic of each P_1, P_2 and P_3. P_0 is the intercept with the y-axis in the log-log wavelet variance-scale plot, therefore it is a good approximation of the wavelet variance at short scale.

4.5.3.2. Regression Analysis

In order to gain insight into the measures provided by the wavelet spectra and their mapping onto the physical characteristics of the observed random field (forest structural heterogeneity), a regression analysis was performed between the LiDAR CHM standard deviation and the LiDAR CHM P_0. P_0 is the constant term of the wavelet variance polynomial approximation. Therefore, it provides a figure of the

overall variance (energy) carried by the wavelet representation. P_0 is also the intercept with the y-axis in the log–log variance–scale plot, therefore it is a good approximation to the variance at short scale.

We found that the LIDAR CHM P_0 is well correlated with the standard deviation of the LiDAR CHM ($R^2 = 0.78$, N = 315) (Figure 8a) and the TanDEM-X DSM P_0 is also well correlated with the standard deviation of the TanDEM-X DSM ($R^2 = 0.72$, N = 315) (Figure 8b). This means that the two-point statistic (P_0) at short scale of the process carries the same information as the one-point statistic (standard deviation) of the same process. Moreover, the one-point statistic of the TanDEM-X DSM is also equivalent to the CHM two-point statistic. This point confirms that, at least at first order, the properties of the CHM process are reflected onto the TanDEM-X DSM process.

On the other hand, the LiDAR CHM standard deviation was weakly correlated with TanDEM-X P_0 ($R^2 = 0.34$, N = 315). This case indicates that the TanDEM-X DSM process is not related in a simple way to the CHM process, but it is the result of the superposition of several random processes, such as terrain topography and InSAR phase signal to noise ratio. Therefore, the textural dependency of the DSM cannot be measured only by a simple one-point statistic, or a one-scale two point statistic, but the full multi-scale measures (wavelet spectra) must be called into play.

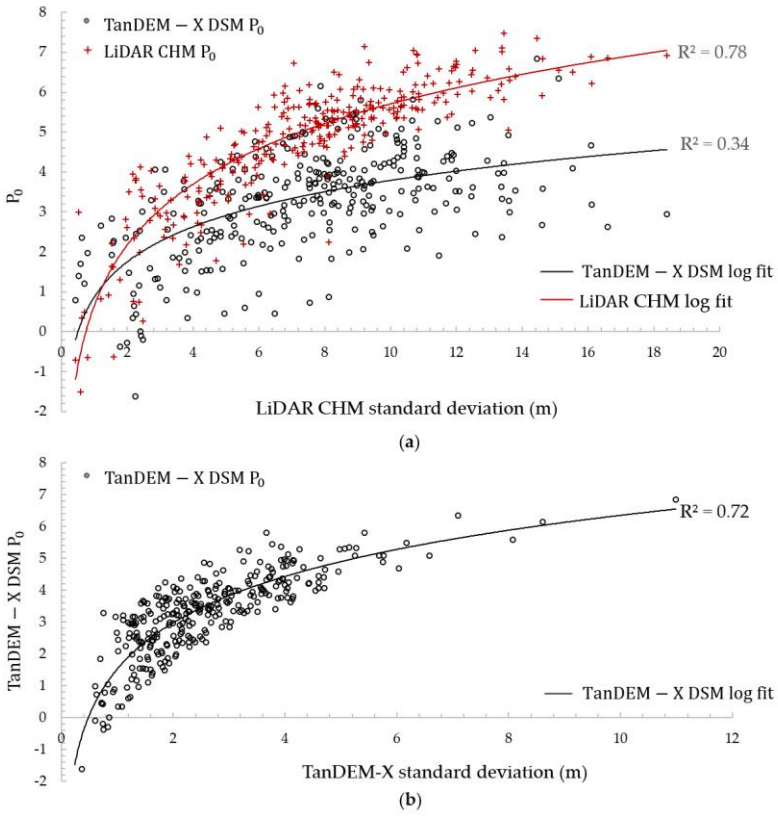

Figure 8. Logarithmic relationship between: (**a**) LiDAR CHM standard deviation (m) and LiDAR CHM P_0 (red cross) (R^2 = 0.78, N = 315), and LiDAR CHM standard deviation (m) and TanDEM-X DSM P_0 (black circle) (R^2 = 0.34, N = 315). (**b**) TanDEM-X DSM standard deviation (m) and TanDEM-X P_0 (R^2 = 0.72, N = 315).

Finally, notice that the correlation between the two-point statistic P_0 and the one-point statistic (standard deviation) of the same process (Figure 8a) is in line with the claim that the wavelet variance is an asymptotic unbiased estimator of the process variance (Percival & Walden, 2000). Indeed, given the wavelet frame of choice that acts a differential operator, the wavelet variance is tantamount to Equation 6):

$$\langle W(x,\tau)^2\rangle = \langle (f(x) - f(x+\tau))^2\rangle \; \tau \to \infty \xrightarrow{yields} 2(\langle f^2\rangle - \langle f\rangle^2) = 2VAR(f) \qquad \text{Equation 6}$$

Often in old-growth tropical forest height differences between individual trees is significant as a result of the presence of emergent trees (Hoekman & Varekamp, 2001). The results are in line with findings based on optical sensors that indicate that texture is driven by the variation in vertical structure (presence of emergent trees) of the canopy and gives rise to canopy texture (Ouma, et al., 2008). Stands with a high variance in tree height have a rougher upper canopy compared to those with lower variance (Ouma, et al., 2008). However, in DEMs provided by ranging or interferometric sensors (e.g., from LiDAR or InSAR), texture is not related to shadowing effects but to the gradient of height information. The area covered by large emergent trees (> 35 m) in secondary forest (burned) plots is significantly different from primary forest ($p < 0.01$, N = 222). This is a good indicator to explain why secondary forest presents a lower canopy roughness compared to primary forest.

4.5.3.3. LiDAR CHM and TanDEM-X Polynomial Coefficients and Standard Deviation Frequency Distributions

LiDAR CHM (height) frequency distribution (FD) in a 23 x 23 pixels (0.05 ha) area presenting low LiDAR CHM P_0 (0.12 ± 0.65) (mean ± standard deviation) (SF) was compared with an area presenting high P_0 (5.6 ± 1.2) (PF) (Figure 9b). Indeed, the area with lowest P_0 (SF) presents a more homogeneous height distribution, ranging between 21.1 and 27.9 m (mean ± standard deviation) (25.9 m ± 1.1 m) (Figure 9). Conversely, higher P_0 (black line) (Figure 9b) corresponds to a more heterogeneous structure comprising tree heights ranging between 11.8 m and 48.3 m (34.6 m ± 10.7 m) (Figure 9a).

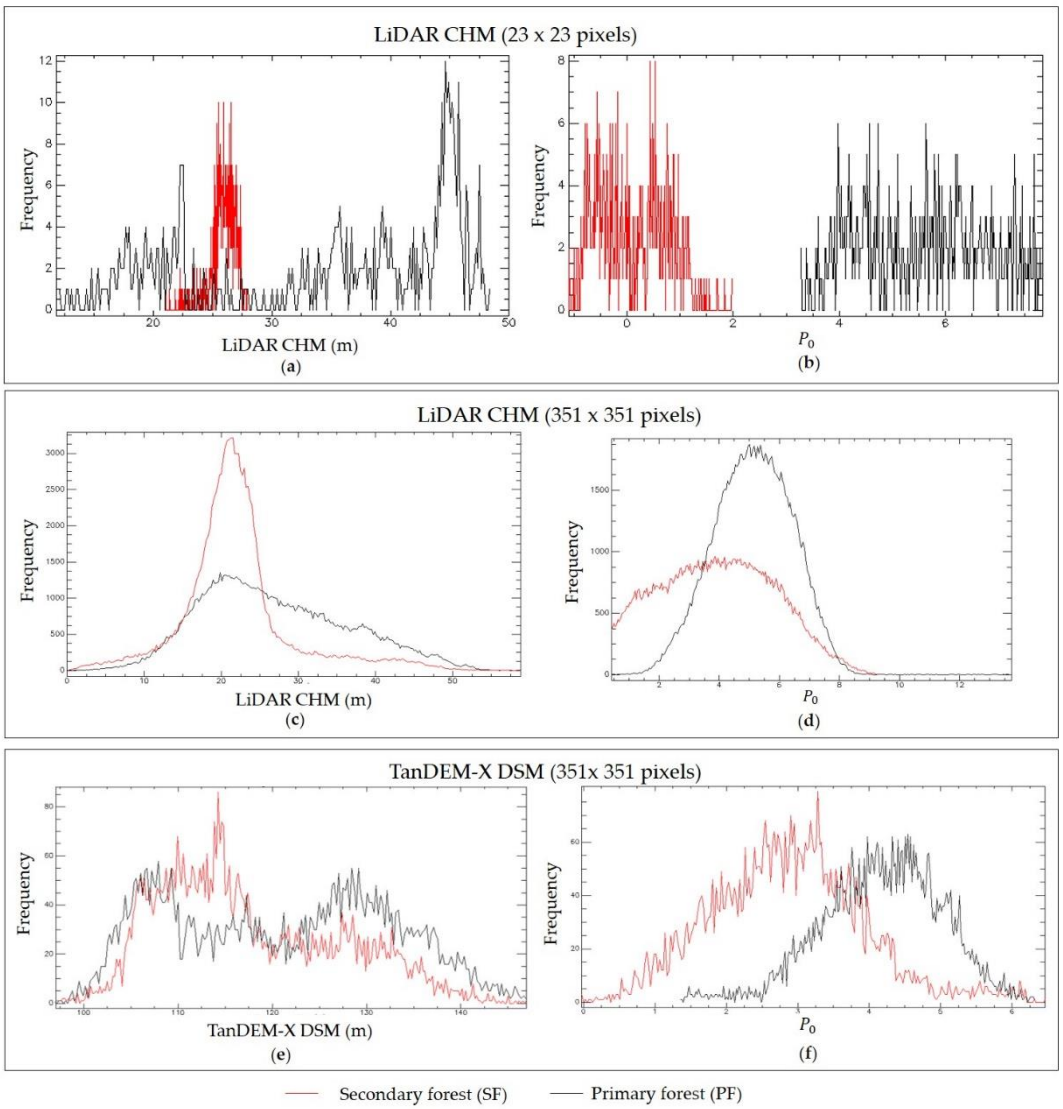

Figure 9. LiDAR CHM, TanDEM-X DSM and corresponding P_0 frequency distributions (FD) for primary forest (intact) (PF) (black line) and secondary forest (SF) (red line): (a) LiDAR CHM FD (23 x 23 pixels); (**b**) LiDAR CHM P_0 FD (23 x 23 pixels); (**c**) LiDAR CHM FD (351 x 351 pixels); (**d**) LiDAR CHM P_0 FD (351 x 351 pixels); (**e**) TanDEM-X DSM (m) FD (351 x 351 pixels); and (**f**) TanDEM-X DSM P_0 FD (351 x 351 pixels).

Lower tree height standard deviation (in this case provided by LiDAR CHM) observed in SF is often associated with young even aged stands of mono-dominant species (Ouma, et al., 2008). Another independent dataset such as field data would

be required to confirm this assumption. The forest successional gradient ranging from intact to burnt and ultimately regrowth and the variance of the CHM has been observed in other studies based on optical remote sensing, whereby the presence of emergent crowns caused a significant shadowing effect on the lower vegetation in PF influencing texture from spectral information (Ouma, et al., 2008).

Analysis taking into account 351 x 351 pixels plots of PF and SF was explored (Figure 9c-f). At this scale the LiDAR CHM FD indicates that the SF heights are no more restricted to the 21–27 m range like in the sub-hectare case (Figure 9a). However, there is a clear predominance around 22 m in the SF (Figure 9c). The SF also presents a long tail (not present in the sub-hectare case), which corresponds to patches that have not been burned within the burned matrix. Instead, homogeneous patches are areas where forest was affected by fire, and, after 17 years, a forest successional stage with a more uniform structure replaced heterogeneous old-growth formations. Because of the complex composition unburned small forest islands patches surrounded by burned forest, they will be more prone to fire disturbance since future fires will be facilitated by the more open canopy (Cochrane, 2003). Instead the PF presents a distribution ranging from 0 to 59 m (mean ± standard deviation: 27 ± 9.5 m) (Figure 9c). At hectare scales the PF is still very heterogeneous and multi-layered, a characteristics observed in many tropical forests studies due to the high diversity of species (Malhi & Román-Cuesta, 2008).

Similar, effects can be noticed in the TanDEM-X DSM (Figure 9f) where SF P_0 ranges between -0.02 and 6.5 (mean ± standard deviation: 2.9 ± 1.0), while PF P_0 ranges between 1.3 and 6.3 (mean ± standard deviation: 4.2 ± 0.8). In this case, the one-point statistical separation between PF and SF is less evident due to two reasons: coarser resolution (4.6 m); approximation of the top canopy spatial variation provided by location of the coherence PCH, this in turn depending on the canopy volume density and the sensor's parameters (Balzter, et al., 2007). However, notice that the distribution based on TanDEM-X DSM P_0 still bears information related to structural differences between PF and SF.

We can conclude that textural variation between SF and PF, as measured by one-point statistic (LiDAR CHM height FD) depends on the scale of observation and the disturbance conditions (e.g., presence of unburned forest patches within a burned forest matrix). This process has been observed in other tropical forest settings where, unburned forest patches were still present within the burned forest (Cochrane & Schultze, 1998; Cochrane & Schultze, 1999). In this particular case, they formed connected ribbons of old-growth forest along streams (Eichhorn, 2006) and they were not burned since the flammability in the presence of higher moisture is lower compared to those areas further away from water sources (Cochrane, 2003).

LiDAR CHM wavelet spectrum image (P_0) (Figure 10b) visual interpretation confirms the results from the FDs. Figure 10a shows a false colour image of the LiDAR CHM, where the red line marks the boundary between PF and SF to illustrate how forest height varies across the LiDAR extent. Figure 10b shows the corresponding LiDAR CHM P_0. Lower LiDAR CHM P_0 (brown) indicates more homogeneous, even height forest patches while, high P_0 is represented in yellow. The onset of the more homogeneous forest patches is clearly dominant in the region designated as the burned SF area of the SWPF to the North of the red line boundary. The TanDEM-X DSM (m) is shown in (Figure 10c) and the corresponding P_0 is illustrated in (Figure 10d) with low values in brown and high values in dark green. The results are further confirmed by class separability in the feature space of the wavelet spectra descriptors (Section 4.5.4).

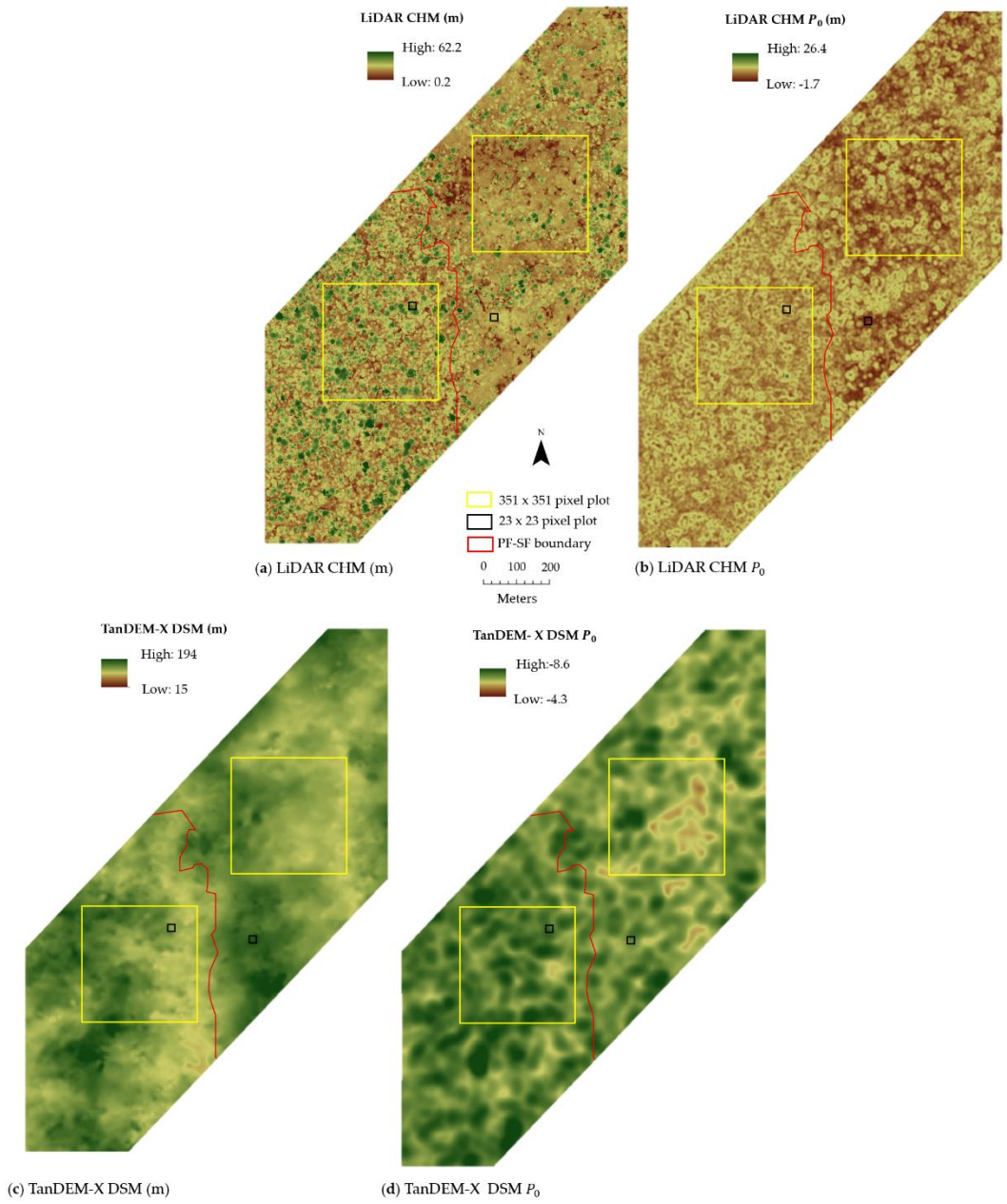

Figure 10. (**a**) LiDAR CHM; (**b**) LiDAR CHM wavelet spectrum image (P_0); (**c**) TanDEM-X DSM; and (**d**) TanDEM-X DSM wavelet spectrum image (P_0). The red line marks the boundary between secondary forest (SF) and primary forest (PF) according to data supplied by the Indonesian Ministry of Forestry (Indonesian Ministry of Forestry, 2015). The onset of homogeneous (in terms of height distribution) forest patches, characteristics of the burnt secondary forest, is clearly visible in the LIDAR CHM (a) to the North of the boundary line, and it is well

detected by areas of lower LiDAR CHM P_0 (brown) in (b) and lower TanDEM-X P_0 (brown) corresponding to secondary forest. Sample plots used in the FD analysis reported in Figure 9: 23 x 23 pixel plots (black squares) and 351 x 351 pixel plots (yellow squares).

4.5.4. LiDAR CHM and TanDEM-X DSM 2D Wavelet Spectra Class Separability

Jeffries-Matusita (JM) distance was performed based on the maximum number of common samples for each class pairs: grassland/mixed-scrub (GR/MS: 44), grassland/secondary forest (GR/SF: 44), grassland/primary forest (GR/PF: 44), mixed-scrub/secondary forest (MS/SF: 49), mixed scrub/primary forest (MS/PF: 49), and secondary forest/primary forest (SF/PF: 96).

4.5.4.1. Scale by Scale Class Separability

$\text{LiDAR}_{\text{CHM}}$ Wavelet Signature ($\text{LiDAR}_{\text{CHM}}$WS) separability (see Section 4.4.5 for WS definition) at different scales was performed on pairwise JM to assess the scale at which class separability was greater (Figure 11a). The JM distance ranges between 0 and $\sqrt{2}$ with highest values indicating greater class separability. Best separability between GR/MS ($JM_{\text{GR/MS}}$ = 0.82), GR/SF ($JM_{\text{GR/SF}}$ = 1.0) and GR/PF ($JM_{\text{GR/PF}}$ = 1.26) was achieved at 2.4 m (scale $2^{1.25}$), while the best separability between class pairs MS/SF ($JM_{\text{MS/SF}}$ = 0.49) and SF/PF ($JM_{\text{SF/PF}}$ = 0.81) was achieved at 2.8 m (scale $2^{1.5}$). Best separability between MS/PF occurred at 1.4 m (scale $2^{0.5}$) ($JM_{\text{MS/PF}}$= 0.78).

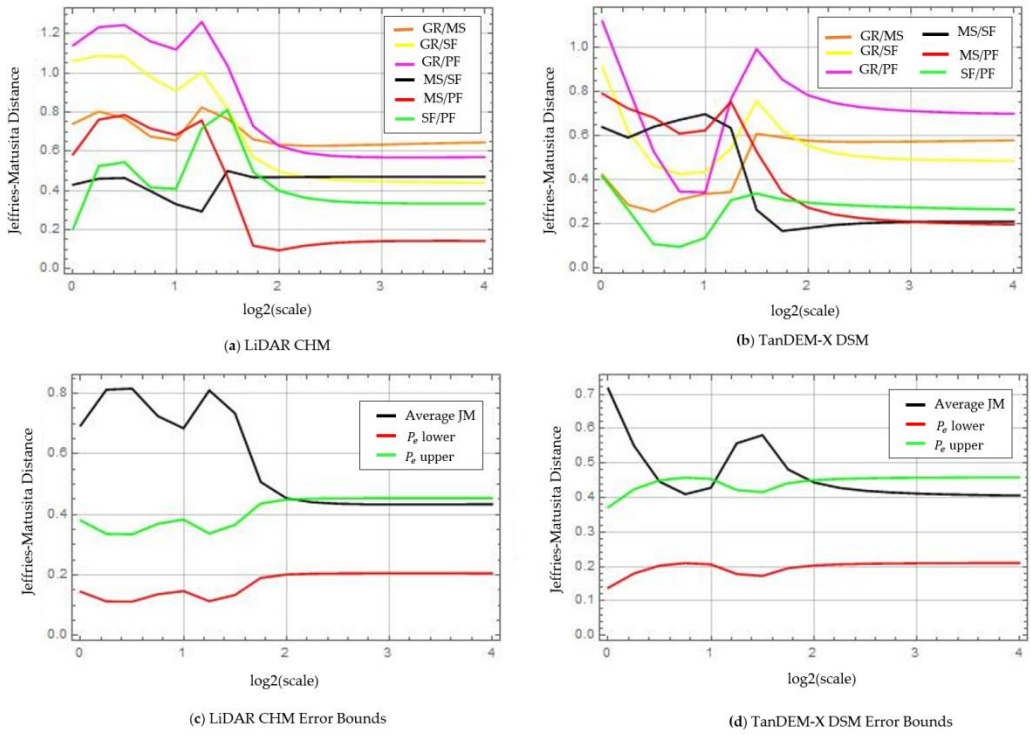

Figure 11. Scale by scale pairwise Jeffries Matusita (JM) distance trend for primary forest (PF), secondary forest (SF), mixed scrub (MS) and GR (grassland) at four dyadic scales: (**a**) LiDAR$_{\mathrm{CHM}}$WS; (**b**) TDX$_{\mathrm{DSM}}$WS ($n_{\mathrm{GR/MS}}$ = 44; $n_{GR/SF}$ = 44; $n_{GR/PF}$ = 44, $n_{MS/SF}$ = 49, $n_{MS/PF}$ = 49 and $n_{SF/PF}$ = 96); (**c**) LiDAR$_{\mathrm{CHM}}$WS average JM; and (**d**) TDX$_{\mathrm{DSM}}$WS average JM with associated error bounds (P_e lower and P_e upper).

Separability results considering TDX$_{\mathrm{DSM}}$WS scale by scale (Figure 11b) indicate that the highest separability between class pairs is achieved at 4.6 m (scale 20) for class pairs GR/SF ($JM_{\mathrm{GR/SF}}$ = 0.91), GR/PF ($JM_{\mathrm{GR/PF}}$ = 1.1), MS/PF ($JM_{\mathrm{MS/PF}}$ = 0.80) and SF/PF ($JM_{\mathrm{SF/PF}}$ = 0.41), while the highest separability between class pairs GR/MS ($JM_{\mathrm{GR/MS}}$ = 0.61) is achieved at 13 m (scale 21.5) and at 9.2 m (scale 21) for class pair MS/SF ($JM_{\mathrm{MS/SF}}$ = 0.70).

LiDAR$_{\mathrm{CHM}}$WS outperforms the TDX$_{\mathrm{DSM}}$WS due to its higher resolution. Nonetheless, textural information derived from the TDX$_{\mathrm{DSM}}$WS can still provide a certain degree of separability. Results also confirm that information at higher scales does not bear significant information on class separability and even the first few

scales contain limited information when taken singularly. Analysis of the full WS is therefore essential to achieve improved separability.

4.5.4.2. Full Wavelet Signature (WS) Class Separability

Class separability results based on the full $\text{LiDAR}_{\text{CHM}}$WS and TDX_{CHM}WS using the JM distance are found in Table 2.

Table 2. JM distance separability between four classes considering full WS: TDX_{DSM}WS; and $\text{LiDAR}_{\text{CHM}}$WS. Range between 0 and $\sqrt{2}$ ($n_{GR/MS}$ = 44; $n_{GR/SF}$ = 44; $n_{GR/PF}$44, $n_{MS/SF}$ = 49, $n_{MS/PF}$ = 49 and $n_{SF/PF}$ = 96).

	Class	GR	MS	SF	PF
TDX_{DSM}WS	GR		1.29	1.35	1.39
	MS	1.29		1.23	1.26
	SF	1.35	1.23		1.18
	PF	1.39	1.26	1.18	
$\text{LiDAR}_{\text{CHM}}$WS	GR		1.29	1.35	1.39
	MS	1.29		1.31	1.32
	SF	1.35	1.31		1.36
	PF	1.39	1.32	1.36	

Class separability based on $\text{LiDAR}_{\text{CHM}}$WS is high between all classes. Highest separability is achieved between GR and PF ($JM_{\text{GR/PF}}$ = 1.39) and lowest separability between GR and MS ($JM_{\text{GR/MS}}$ = 1.29). Results indicate that the separability between SF and PF ($JM_{\text{SF/PF}}$ = 1.36) is higher compared to the separability between MS and SF ($JM_{\text{MS/SF}}$ = 1.31). Instead the spatial configuration for GR is markedly separable from both SF and PF and this is reflected in the JM ($JM_{\text{GR/SF}}$ = 1.35 and $JM_{\text{GR/PF}}$ = 1.39).

TDX_{DSM}WS achieves highest separation between GR and PF as well ($JM_{\text{GR/PF}}$ = 1.39) and lowest separation between SF and PF ($JM_{\text{SF/PF}}$ = 1.18). Compared to the $\text{LiDAR}_{\text{CHM}}$WS, the separability using TDX_{DSM}WS is lower for the pairs MS/SF, MS/PF, SF/PF, and PF/MS, while identical separability was found between GR and all other classes. The analysis highlights the lower JM separability results considering a scale by scale analysis (0.1 ≤ JM ≤ 1.26 for LiDAR CHM; 0.1 ≤ JM ≤ 1.1 for TanDEM-X

DSM) (Section 4.5.4.1), compared to separability considering the full wavelet signature (1.29≤ JM ≤ 1.39 for LiDAR CHM; 1.18 ≤ JM ≤ 1.39 for TanDEM-X DSM).

Statistical evaluation based on $\mathrm{TDX_{DSM}}$WS and $\mathrm{LiDAR_{CHM}}$WS is found in Table 3. The results for $\mathrm{TDX_{DSM}}$WS are reported as follows: P_e lower bound P_e upper bound (%), where P_e is the expected classification error. The lowest P_e is achieved between GR/PF and between MS/PF (0.06%–2.47%), while the highest $P_e$was found between GR/MS (2.13%–17.68%) followed by SF/PF (2.32%–15.22%). $\mathrm{LiDAR_{CHM}}$WS results achieved indicate the lowest P_e between classes GR/PF (0.02-1.23%), while highest P_e between MS/SF (1.31%–11.46%) followed by GR/MS (0.65%–8.07%).

Table 3. Class separability statistical evaluation based on pairwise JM distance: P_e lower bound; P_e upper bound (%) (N = 176, n = 44).

Metric	P_e **(%)**	**Class Pair**					
		GR/MS	**GR/SF**	**GR/PF**	**MS/SF**	**MS/PF**	**SF/PF**
$\mathbf{TDX_{DSM}WS}$	Lower	3.13	0.18	0.06	0.18	0.06	2.32
	Upper	17.68	4.29	2.47	4.29	2.47	15.22
$\mathbf{LiDAR_{CHM}WS}$	Lower	0.65	0.23	0.02	1.31	0.44	0.38
	Upper	8.07	4.77	1.23	11.46	6.60	6.18

Figure 12 highlights results using $\mathrm{LiDAR_{CHM}}$WS and $\mathrm{TDX_{DSM}}$WS representing wavelet signature (WS) averaged for 16 sample plots for each of the four classes considered. SF $\mathrm{LiDAR_{CHM}}$WS shows consistently lower wavelet variance (smoother spatial distribution), compared to PF with separation increasing at longer scales (>4 m). The increasing separation between the two classes at longer scales is an indication that the heterogeneity of PF is best detected when considering a larger area, since in this case the texture related patterns are the separate crowns. Correlation length is similar for both PF and SF (8 m) which indicates that the averaging of the signatures for 35 x 35 m^2 plots leads to the loss of information in terms of correlation length. This is possibly because the areas of SF within a 35 x 35 m^2 plot are composed of a mix of burned and unburned forest and, in particular, the unburned forest patches are similar in structure to the old growth PF.

GR, which is effectively a homogeneous layer of grass, exhibits the lowest wavelet variance among all classes and a longer correlation length (4 m). This is because GR is dominated by surface scattering (proven by high coherence values). While, MS, being a composite of surface and volume scattering, shows lower wavelet variance compared to SF but higher than GR. Both these low energy processes tend to a flat scale-independent functional relationship, which is indicative of a white noise process.

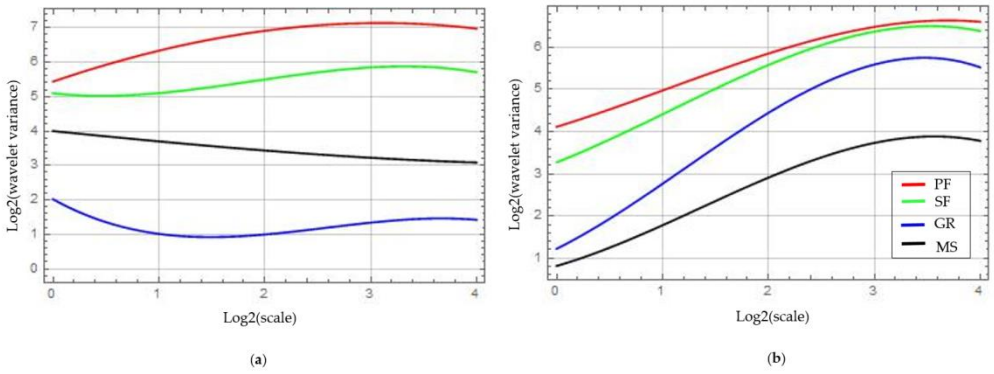

Figure 12. Average wavelet signatures for four classes: primary forest (PF) (red), secondary forest (SF (green), grassland (GR) (blue) and mixed-scrub (MS) (black) (n = 16, N = 64): (**a**) $\overline{\text{X}}\text{LiDAR}_{\text{CHM}}\text{WS}$ (scale: 2^0 = 1 m; 2^1 = 2 m; 2^2 = 4 m; 2^3 = 8 m; 2^4 = 16 m); and (**b**) $\overline{\text{X}}\text{TDX}_{\text{DSM}}\text{WS}$ (scale: 2^0 = 4.6 m; 2^1 = 9.2 m; 2^2 = 18.4 m; 2^3 = 36.8 m; 2^4 = 73.6 m).

$\text{TDX}_{\text{DSM}}\text{WS}$ (Figure 12b) indicates that wavelet variance is highest for PF followed by SF, GR and MS. This is in accordance with results derived from $\text{LiDAR}_{\text{CHM}}\text{WS}$ aside for the wavelet variance between GR, which is higher than for MS (the opposite compared to the LIDAR CHM case). Therefore, it is the lack of volume (tree canopies) contributes to the higher penetration of TanDEM-X in grassland areas. Intuitively, the penetration of TanDEM-X to derive ground topography in lower vegetation or bare areas is greater because of lack of attenuation due the presence of volume. SF $\text{TDX}_{\text{DSM}}\text{WS}$ is consistently lower compared to PF but the difference is reduced at longer scales, where SF and PF separation is reduced significantly.

Discrepancies are related to the difference in penetration depth of the two instruments and thus, the information that they provide. TanDEM-X DSM perceives the upper canopy roughness penetrating into the volume by several m (depending on the vegetation density and sensor configuration) but not reaching the ground surface in dense tropical forest. This assumption was confirmed in our context by estimating the fractional phase center height $fch = \frac{\varphi}{\beta h}$(where β is the vertical wave number of the interferometer) from the vegetation height h provided by the LiDAR CHM along a 6.95 km transect in intact (PF) and disturbed secondary forest (SF) (see also Section 4.5.1). The PDF of the fch reveals the presence of two peaks, the first holding the majority of the population located at 0.8, and the second at 0.5. It has been found in some cases that a rather surprising penetration depth was achieved even in tropical forest due to clumpiness of canopy where gaps allow more penetration even at short wavelength (X-band) (Treuhaft, et al., 2015). Higher penetration from LiDAR compared to TanDEM-X has been observed in dense tropical forest in the Amazon (Treuhaft, et al., 2015). TanDEM-X phase conversion to a DSM is limited by the penetration depth at X-band, with the availability of future missions such as TanDEM-L (Krieger, et al., 2009), penetration depth into the canopy will be greater as this increases with wavelength (Balzter, 2001). This will provide a similar kind of information on ground topography similarly to a DTM generated from LiDAR returns and the possibility to generate CHMs using a combination of TanDEM-X/L over a wide area coverage (Eineder, et al., 2014).

4.6. Discussion

The understanding of forest canopy heterogeneity has impact on several ecological process including productivity and nutrient cycling (Wedeux & Coomes, 2015). Relationship between forest structure and textural properties is still not clearly understood (Sun & Ranson, 1998; Malhi & Román-Cuesta, 2008). This study provides increased understanding in canopy heterogeneity arising from fire

disturbance and, in particular, the ability to detect areas of SF based on their structural arrangement.

Tropical forests structural heterogeneity is driven by a combination of processes: underlying topographic structure and canopy structure (Véga, et al., 2015). De-coupling the two processes to gain a better understanding of variations in canopy structure alone was considered by analysis of wavelet variance and wavelet co-variance. This was achievable since the two processes are characterized by different dominant frequencies: high frequency components for canopy structure and low frequency components for topographic structure. Both the LiDAR CHM and the TanDEM-X DSM were affected by topographic features but only at longer scales ($>2^3$), while, at shorter scales (2^0–2^3), the dominant process was linked to canopy structure alone.

Secondly, height standard deviation (derived from high resolution LiDAR CHM) was found by regression analysis to be the main driver affecting wavelet based texture, as measured by the first coefficient of the signature polynomial approximation (P_0). Analysis reveals a logarithmic relationship between height standard deviation and P_0 for LiDAR CHM ($R^2 = 0.77$) and, with lower correlation ($R^2 = 0.34$), for TanDEM-X DSM. Results were visually confirmed from aerial photography showing areas with low LiDAR CHM P_0 corresponding to homogeneous patches with lack of tall (or limited) emergent trees, a condition stemming from the lower amount of shadowing cast by these.

LiDAR CHM standard deviation can be linked to successional stage, with more complex PF presenting higher height standard deviation compared to disturbed SF due to the presence of tall emergent trees. Results are in accordance with research indicating that height difference between individual trees can be significant, due to the presence of emergent trees, especially in old-growth tropical forests (Hoekman & Varekamp, 2001) and that disturbed secondary forests are less structurally complex compared to old-growth forest (Brown & Lugo, 1990). The addition of

ground data information (e.g., fire history) on the forest condition could help the interpretation in term of the processes that generate such heterogeneity.

Potential of the wavelet signatures and wavelet spectra (WS) space-scale analysis was exemplified by selecting test cases on a high resolution dataset (airborne LiDAR CHM) to gain a better understanding as to the reasons behind wavelet variance values and their connection with statistical properties of the underlying process, such as correlation length. The interpretation of 1 m resolution LiDAR CHM was advantageous as the single crowns were resolvable thus increasing the level of detail compared to the lower resolution TanDEM-X DSM (approximately 4.6 m resolution). Visual interpretation indicates that wavelet variance is sensitive to target heterogeneity while correlation length is linked to the process self-similarity, with the limiting case of white noise with no correlation beyond zero lag.

$\mathrm{LiDAR_{CHM}WS}$ and $\mathrm{TDX_{DSM}WS}$ two-point statistic was successful to separate thematic classes. $\mathrm{LiDAR_{CHM}WS}$ JM distance (with asymptotic value of $\sqrt{2}$) ranged within $1.29 \leq JM \leq 1.39$ (lowest between MS/GR) and generally (apart from separability between GR and all other classes) lower separability was achieved with $\mathrm{TDX_{DSM}WS}$ ($1.18 \leq JM \leq 1.39$) (lowest between SF/PF).

Scale by scale separability analysis indicates that short scales (between scales 1.4 m and 2.8 m) are best for discriminating classes using $\mathrm{LiDAR_{CHM}WS}$ with increasingly reduced separability at longer scales. In the case of $\mathrm{TDX_{DSM}WS}$, scale by scale separability is highest between 4.6 m and 13 m. The reduced separability using $\mathrm{TDX_{DSM}WS}$ is related to two main factors: lower spatial resolution of radar compared to LiDAR; difference in information provision of the vertical forest structure due to the lower penetration depth into the canopy (higher attenuation) of TanDEM-X compared to LiDAR in tropical forests (Treuhaft, et al., 2015). TanDEM-X observations offer the major advantage of global coverage (Bräutigam, et al., 2015) as opposed to a restricted spatial coverage available from airborne LiDAR instruments. Therefore, despite the reduced resolution at the expenses of spatial

coverage, 2D wavelet spectra derived from TanDEM-X DSM are still able (to a certain extent) to provide some information on vegetation structure.

The method also provided evidence of the potential and limitation of 3D information provided by sensors with different characteristics. Moreover, regarding structural information extraction the improved performance of using two-point statistics as opposed to one-point statistics was demonstrated. 3D information is more suitable for the characterization of areas that cannot be discriminated by two-dimensional datasets (e.g., backscatter). Requirement for 3D information is therefore suggested for the characterization of vegetation structure, in particular in view of the potential to discriminate between PF and SF. Furthermore, provision of a higher resolution DSM derived from InSAR (e.g., TanDEM-X in SpotLight mode at approximately 2 m resolution) could provide significant improvements in the characterization of canopy structure.

4.7. Conclusions

We found that two-point statistic applied to both TanDEM-X InSAR and LiDAR observations was effective for the discrimination of a range of thematic classes based on the Jeffries–Matusita (JM) distance. In particular, increased separability performance was found by employing the full wavelet signature (WS) compared to using each decomposition scale individually. This points to the importance of the use of multi-scale texture metrics such as these for extracting as much information from the data as possible. Of particular interest is the significant separability between PF and SF, even 17 years after the fire event.

Remote sensing instruments that provide 3D information such as TanDEM-X InSAR and LiDAR observations can be used to extract information on canopy structure. In particular, we highlight the potential of TanDEM-X DSM, which will be available globally (WorldDEM™) (but at a lower resolution of 12 m) (Airbus Defence and Space, 2014) as opposed to airborne LiDAR acquisitions. These acquisitions, albeit they provide finer details, are limited in terms of area coverage, and currently less widely available and relatively costly (De Sy, et al., 2012).

The limitations of the method are not dictated by the statistical estimation, algorithmic or computational approach, but lie in the instrumental area, i.e. the spatial resolution of the dataset available, with higher resolution performing better to characterise different forest structures. TanDEM-X provides enough resolution as to potentially warrant the application of the approach over hotspots of forest disturbance. A global DEM product (WorldDEM™) is available; however, this will probably not be sufficient to provide information related to different forest structure. Instead, constrains on the LiDAR are related to the sensor coverage in terms of area which in our case only covers a portion of the site and is seldom available for large areas (e.g. comparable to a TanDEM-X scene).

Efforts to monitor global-scale degraded forest were not directly considered as the aim of the research, this concerning the test of novel methods for pattern recognition by exploiting available datasets. Augmenting the outreach of the approaches to global level would require further tests in other sites with different characteristics. The approach, as noted in Chapter 3, was not focused on providing an operational nor an automated framework for monitoring degradation, while only by taking further steps in the research this could potentially be achieved.

Requirements to monitor the increase in areas of degraded forest at the expense of primary forests due to fires, a process that will be exacerbated by ENSO in the future, call for novel methods and datasets to characterize canopy structure. The test case undertaken in this work highlights the suitability of two-point spatial statistics, based on a wavelet space-scale analysis, using DEMs derived from LiDAR or InSAR observations as a tool for detecting and mapping landscape-level vegetation heterogeneity.

The following chapter adds a temporal dimension to the analysis by using more than one data acquisition and by focusing on changes in structure (forest volume) due to forest disturbance.

4.8. Acknowledgements

Elsa Carla De Grandi is supported by the Principal's Career Development Scholarship and the School of GeoSciences (University of Edinburgh). The authors would like to acknowledge the software providers Sarmap SA and EXELIS VIS (Sarscape 5.0). Data processing was undertaken in ENVI IDL and Wolfram Mathematica. Data providers: DLR (TanDEM-X AO VEGE6702), Indonesian Ministry of Forestry (land cover map), Dirk Hoekman (Wageningen University) for providing SAR expertise, the LiDAR data and aerial photography. The authors would also like to thank Lan Qie (University of Leeds) for providing information related to the study site.

4.9. References

- Airbus Defence and Space, 2014. *WorldDEM Technical Product Specification 1.0.* [Online]. Available at: http://www.engesat.com.br/wp-content/uploads/455-201404_worlddem_technicalspecs_i1 [Accessed 11 November 2015].
- Alexander, L. A. & Inggs, M. R., 1999. *The investigation into the effects of speckle filters on classification.* Hamburg, Proceedings of the IEEE International Geosciences and Remote Sensing Symposium, pp. 1226-1228.
- Asner, G. P. et al., 2002. Estimating Canopy Structure in an Amazon Forest from Laser Range Finder and IKONOS Satellite Observations. *Biotropica,* 34(4), pp. 483-492.
- Balzter, H., 2001. Forest mapping and monitoring with interferometric synthetic aperture radar (InSAR). *Progress in Physical Geography,* 25(2), pp. 159-177.
- Balzter, H., Rowland, C. & Saich, P., 2007. Forest canopy and carbon estimation at Monks Wood National Nature Reserve, UK, using dual-wavelength SAR interferometry. *Remote Sensing of Environment,* 108(3), pp. 224-239.
- Barbier, N. et al., 2010. The variation of apparent crown size and canopy heterogeneity across lowland Amazonian forests. *Global Ecology and Biogeography,* 19(1), p. 72–84.
- Berenguer, E. et al., 2014. A large-scale field assessment of carbon stocks in human-modified tropical forests. *Global Change Biology,* 20(12), p. 3713–3726.
- Bongers, F., 2001. Methods to assess tropical rain forest canopy structure: an overview. *Plant Ecology,* Volume 153, p. 263–277.

- Bradshaw, G. A. & Spies, T. A., 1992. Characterizing Canopy Gap Structure in Forests Using Wavelet Analysis. *The Journal of Ecology,* 80(2), pp. 205-215.
- Bräutigam, B. et al., 2015. *Quality assessmenet for the first part of the TanDEM-X Global Digital Elevation Model.* Berlin, Germany, The International Archives of the Photogrammetry, Remote Sensing and Spatial Information Sciences, pp. 1137-1143.
- Brearley, F. Q. et al., 2004. Structure and floristics of an old secondary rain forest in Central Kalimantan, Indonesia, and a comparison with adjacent primary forest. *Forest Ecology and Management,* 195(3), pp. 385-397.
- Brown, S. & Lugo, A. E., 1990. Tropical secondary forests. *Journal of Tropical Ecology,* 6(1), pp. 1-32.
- Cai, W. B. S. et al., 2014. Increasing frequency of extreme El Niño events due to greenhouse warming. *Nature Climate Change,* 4(2), pp. 111-116.
- Chisholm, R. A., Wijedasa, L. S. & Swinfield, T., 2016. The need for long-term remedies for Indonesia's forest fires. *Conservation Biology Letters,* 30(1), pp. 5-6.
- Cochrane, M., 2003. Fire science for rainforests. *Nature,* 421(6926), pp. 913-919.
- Cochrane, M. A. & Schultze, M. D., 1998. Forest fires in the Brazilian Amazon. *Conservation Biology,* 12(5), pp. 948-950.
- Cochrane, M. A. & Schultze, M. D., 1999. Fires as a recurrent event in tropical forests of the Eastern Amazon. *Biotropica,* 31(1), pp. 2-16.
- Couteron, P., Pelissier, R., Nicolini, E. A. & Paget, D., 2005. Predicting tropical forest stand structure parameters from Fourier transform of very high-resolution remotely sensed canopy images. *Journal of Applied Ecology,* 42(6), pp. 1121-1128.
- Davis, A., Marshak, A. & Wiscombe, W., 1994. Wavelet-based multifractal analysis of non-stationary and/or intermittent geophisical signals. In: E. Foufoula-Georghiou & P. Kumar, eds. *Wavelets in Geophysics.* New Yor, NY, USA: Academic, p. 249–298.
- De Sy, V. et al., 2012. Synergies of multiple remote sensing data sources for REDD+ monitoring. *Current Opinion in Environmental Sustainability,* 4(6), p. 696–706.
- Delang, C. & Li, W. M., 2013. Forest Structure. In: C. Delang & W. M. Li, eds. *Ecological Succession on Fallowed Shifting Cultivation Fields: A Review of the Literature.* Heidelberg: Springer, pp. 9-35.
- Eichhorn, K. A. O., 2006. *Plant diversity after rain-forest fires in Borneo.* PhD Thesis ed. Leiden: Nationaal Herbarium Nederland.

- Eineder, M. et al., 2014. *TanDEM-L. Satellite Mission Proposal for Monitoring Dynamic Processes on the Earth's Surface,* Cologne: German Aerospace Center.
- Frazer, G. W., Wulder, M. A. & Niemann, K., 2005. Simulation and quantification of the fine-scale spatial pattern and heterogeneity of forest canopy structure: A lacunarity-based method designed for analysis of continuous canopy heights. *Forest Ecology and Management,* 214(1), p. 65–90.
- Gallardo-Cruz, J. M. J. A. et al., 2012. Predicting Tropical Dry Forest Successional Attributes from Space: Is the Key Hidden in Image Texture?. *PLoS ONE,* 7(2), p. e30506.
- Garrity, S. R. et al., 2012. Estimating plot-level tree structure in a deciduous forest by combining allometric equations, spatial wavelet analysis and airborne LiDAR. *Remote Sensing Letters,* 3(5), pp. 443-451.
- Gerwin, J., 2002. Degradation of forests through logging and fire in the easter Brazilian Amazon. *Forest Ecology and Management,* 157(1), pp. 131-141.
- Giam, X., Clements, G. R., Aziz, S. A. & Chong, K. Y., 2011. Rethinking the 'back to wilderness' concept for Sundaland's forests. *Biological Conservation,* 144(12), p. 3149–3152.
- Goldammer, H. G., 2015. Fire Management in Tropical Forests. In: L. Pancel & M. Köhl, eds. *Tropical Forestry Handbook.* Berlin: Springer-Verlag, pp. 1-42.
- Goldammer, J. G., 1999. Forests on Fire. *Science,* 284(5421), pp. 1782-1783.
- Goldstein, R. M. & Werner, C. L., 1998. Radar interferogram filtering for geophysical applications. *Geophysical Research Letters,* 25(21), pp. 4035-4038.
- Grace, J., Mitchard, E. & Gloor, E., 2014. Perturbations in the carbon budget of the tropics. *Global Change Biology,* 20(10), p. 3238–3255.
- Hajnsek, I., Kugler, F., Lee, S.-K. & Papathanassiou, K., 2009. Tropical- Forest-Parameter Estimation by Means of Pol-InSAR: The INDREX-II Campaign. *IEEE Transactions on Geoscience and Remote Sensing,* 42(7), pp. 481-493.
- Harris, N. L. et al., 2012. Baseline Map of Carbon Emissions from Deforestation in Tropical Regions. *Science,* 336(6088), pp. 1573-1576.
- Hoekman, D. H. & Varekamp, C., 2001. Observation of Tropical Rain Forest Trees by Airborne High-Resolution Interferometric Radar. *IEEE Transactions on Geoscience and Remote sensing,* 39(3), pp. 584-594.
- Indonesian Ministry of Forestry, 2015. [Online]. Available at: http://webgis.dephut.go.id/ditplanjs/ [Accessed 20 September 2015].

- International Tropical Timber Organization, 2002. *ITTO guidelines for the restoration, management and rehabilitation of degraded and secondary tropical forests,* Yokohama, Japan: International Tropical Timber Organization.
- Jordan, C. F. & Farnworth, E. G., 1982. Natural vs. Plantation Forests: A Case Study of Land Reclamation Strategies for the Humid Tropics. *Environmental Management,* 6(6), pp. 485-492.
- Kaasalainen, S. et al., 2015. Combining Lidar and Synthetic Aperture Radar Data to Estimate Forest Biomass: Status and Prospects. *Forests,* 6(1), pp. 252-270.
- Kartawinata, K., Abdullhadi, R. & Partomihardjo, T., 1981. Composition and structure of a lowland dipterocarp forest at Wanariset, East Kalimantan. *Malaysian Forester,* 44(2-3), pp. 397-406.
- Kennel, P., Tramon, M., Barbier, N. & Vincent, G., 2013. Canopy height model characteristics derived from airbone laser scanning and its effectiveness in discriminating various tropical moist forest types. *International Journal of Remote Sensing,* 34(24), pp. 8917-8935.
- Kent, R. et al., 2015. Airborne LiDAR Detects Selectively Logged Tropical Forest Even in an Advanced Stage of Recovery. *Remote Sensing,* 7(7), pp. 8448-8367.
- Krieger, G. et al., 2009. *The Tandem-L Mission Proposal: Monitoring Earth's Dynamics with High Resolution SAR Interferometry.* Pasadena, CA, USA, Proceedings of the IEEE International Geosciences and Remote Sensing Symposium, pp. 1-6.
- Krieger, G. et al., 2007. TanDEM-X: A Satellite Formation for High-Resolution SAR Interferometry. *IEEE Transactions on Geoscience and Remote Sensing,* 45(11), pp. 3317-3341.
- Kugler, F. & Hajnsek, I., 2011. *Forest characterisation by means of TerraSAR-X and TanDEM-X (polarimetric and) interferometric data.* Vancouver, BC, Canada, Proceedings of the IEEE International Geosciences and Remote Sensing Symposium.
- Kugler, F., Lee, S.-K., Hajnsek, I. & Papathanassiou, K., 2015. Forest Height Estimation by Means of Pol-InSAR Data Inversion: The Role of the Vertical Wavenumber. *IEEE Transactions on Geoscience and Remote Sensing,* 53(10), pp. 5294-5311.
- Kugler, F., Sauer, S., Lee, S.-K. & Papathanassiou, K. a. H. I., 2010. *Potential of TanDEM-X for forest parameter estimation.* Aachen, Germany, EUSAR, pp. 178-181.

- Lertzman, K. & Fall, J., 1998. From forest stands to landscape: spatial scales and the roles of disturbances. In: D. L. Peterson & V. T. Parker, eds. *Ecological scale: theory and applications.* New York: Columbia University Press, pp. 339-368.
- Lewis, S. L., Edwards, D. P. & Galbraith, D., 2015. Increasing human dominance of tropical forests. *Science,* 349(6250), pp. 827-832.
- Lim, K., Treitz, P. W. M., St-Onge, B. & Flood, M., 2003. LiDAR remote sensing of forest structure. *Progress in Physical Geography,* 27(1), pp. 88-106.
- MacKinnon, K., Hatta, G., Halim, H. & Mangalik, A., 1997. *The Ecology of Kalimantan.* 1st ed. Republic of Singapore: Periplus Editions.
- Malhi, Y. & Román-Cuesta, R. M., 2008. Analysis of lacunarity and scales of spatial homogeneity in IKONOS images of Amazonian tropical forest canopies. *Remote Sensing of Environment,* 112(5), pp. 2074-2087.
- Mallat, S., 2008. *A Wavelet Tour of Signal Processing.* 3rd Edition ed. New York, NY: Academic Press.
- Mietten, J., Stibig, H.-J. & Achard, F., 2014. Remote sensing of forest degradation in Southeast Asia—Aiming for a regional view through 5–30 m satellite data. *Global Ecology and Conservation,* Volume 2, pp. 24-36.
- Mitchard, E. T. A. et al., 2014. Markedly divergent estimates of Amazon forest carbon density from ground plots and satellites. *Global Ecology and Biogeography,* 23(8), pp. 935-946.
- Ouma, Y. O., Tetuki, J. & Tateishi, R., 2008. Analysis of co-occurrence and discrete wavelet transform texture for differentiation in very high resolution optical-sensor imagery. *International Journal of Remote Sensing,* 29(12), pp. 3417-3456.
- Page, S. E. et al., 2002. The amount of carbon released from peat and forest fires in Indonesia during 1997. *Nature,* 420(6911), pp. 61-65.
- Palace, M. et al., 2008. Amazon Forest Structure from IKONOS Satellite Data and the Automated Characterization of Forest Canopy Properties. *Biotropica,* 40(2), pp. 141-150.
- Pan, Y. et al., 2011. A Large and Persistent Carbon Sink in the World's Forests. *Science,* 333(6045), pp. 988-993.
- Percival, D. B. & Walden, A. T., 2000. Wavelet Methods for Time Series Analysis. In: 1st, ed. *Wavelet Methods for Time Series Analysis.* Cambridge: Cambridge University Press, p. 594.

- Potapov, P. et al., 2008. Mapping the World's Intact Forest Landscapes by Remote Sensing. *Ecology and Society,* 13(2), p. 51.
- Praks, J., Antropov, O. & Hallikainen, M., 2012. LIDAR-Aided SAR Interferometry Studies in Boreal Forest: Scattering Phase Center and Extinction Coefficient at X- and L-Band. *IEEE Transactions on Geoscience and Remote Sensing* , 50(10), pp. 3831-3843.
- Proisy, C. et al., 2012. Biomass Prediction in Tropical Forests: The Canopy Grain Approach. In: L. Fatoyinbo, ed. *Remote sensing of biomass : principles and applications.* Online: InTech, pp. 1-18.
- Proisy, C., Couteron, P. & Francois, F., 2007. Predicting and mapping mangrove biomass from canopy grain analysis using Fourier-based textural ordination of IKONOS images. *Remote Sensing of Environment,* 109(3), pp. 379-392.
- Roughgarden, J., Running, S. W. & Matson, P. A., 1991. What Does Remote Sensing Do For Ecology?. *Ecology,* 72(6), pp. 1918-1922.
- Sarmap, 2012. *SARscape.* [Online]. Available at: http://www.sarmap.ch/pdf/SARscapeTechnical.pdf [Accessed 2 November 2015].
- Siegert, F., Ruecker, G., Hinrichs, A. & Hoffmann, A., 2001. Increased damage from fires in logged forests during droughts caused by El Nino. *Nature,* 414(6862), pp. 437-440.
- Slik, J. W. F. et al., 2008. Tree diversity, composition, forest structure and aboveground biomass dynamics after single and repeated fire in a Bornean rain forest. *Oecologia,* 158(3), p. 579–588.
- Slik, J. W., Verburg, R. W. & Keßler, P. J. A., 2002. Effects of fire and selective logging on the tree species composition of lowland dipterocarp forest in East Kalimantan, Indonesia. *Biodiversity and Conservation,* 11(1), pp. 85-98.
- Solberg, S., Lohne, T.-P. & Karyanto, 2015. Temporal stability of InSAR height in a tropical rainforest. *Remote Sensing Letters,* 6(3), pp. 209-217.
- Sun, G. & Ranson, K. J., 1998. Radar modelling of forest spatial patterns. *International Journal of Remote Sensing* , 19(9), pp. 1769-1791.
- Toma, T., Ishida, A., Matius & Paulus, 2005. Long-term monitoring of post-fire aboveground biomass recovery in a lowland dipterocarp forest in East Kalimantan, Indonesia. *Nutrient Cycling in Agroecosystems,* 71(1), p. 63–72.
- Treuhaft, R. et al., 2015. Tropical-Forest Biomass Estimation at X-Band From the Spaceborne TanDEM-X Interferometer. *IEEE Geosciences and Remote Sensing Letters,* 12(2), pp. 239-243.

- van der Sanden, J. H. D. H., 1999. Potential of Airborne Radar to Support the Assessment of Landcover in a Tropical Rainforest. *Remote Sensing of Environment,* 68(1), pp. 26-40.
- van Nieuwstadt, M. G., 2002. *Trail by fire. Postfire development of a tropcial dipterocarp forest.* Thesis ed. Utrecht, NL: Utrecht University.
- Véga, C. et al., 2015. Aboveground-Biomass Estimation of a Complex Tropical Forest in Indian Using LiDAR. *Remote Sensing,* 7(8), pp. 10607-10625.
- Walsh, R. P. D., 1996. Drought frequency changes in Sabah and adjacent parts of northern Borneo since the late nineteenth century and possible implications for tropical rain forest dynamics. *Journal of Tropical Ecology,* 12(3), pp. 385-407.
- Wedeux, B. & Coomes, D., 2015. Landscape-scale changes in forest canopy structure across a partially logged tropical peat swamp. *Biogeosciences,* 12(22), p. 6707–6719.
- Weishampel, J. F. et al., 2007. Forest canopy recovery from the 1938 hurricane and subsequent salvage damage measured with airborne LiDAR. *Remote Sensing of Environment,* 109(2), p. 142–153.
- Wulder, M. & Franklin, S. E., 2003. *Remote Sensing of Forest Environments: Concepts and Case Studies.* 1st ed. Dordrecht, The Netherlands: Springer.
- Yassir, I., van der Kamp, J. & Buurman, P., 2010. Secondary succession after fire in Imperata grasslands of East Kalimantan, Indonesia. *Agriculture, Ecosystems and Environment,* 137(1), p. 172–182.
- Yeager, C. P., Marshall, A. J. & Stickler, C. M. C. C. A., 2003. Effects of fires on Peat Swamp and Lowland Dipterocarp Forests in Kalimantan, Indonesia. *Tropical Biodiversity* , 8(1), pp. 121-138.

5. Object-Based Structural Change Detection from TanDEM-X Digital Surface Models to Map Tropical Forest Disturbance and Re-Growth: A Case Study in the Republic of Congo

Abstract

TanDEM-X Digital Surface Models (DSMs) are sensitive to the forest vertical structure function, and therefore have considerable potential for mapping deforestation, forest degradation and re-growth. The capability to detect forest loss and gain was assessed by acquiring two TanDEM-X datasets during the dry season (December) separated by 1 year (2012-2013) in tropical forest located in the Republic of Congo. From the interferometric phase the relative height difference (ΔDSM) was computed. An object-based change detection algorithm was then used to extract deforestation/degradation objects (negative changes or $\Delta DSM_{negative}$) and re-growth objects (positive changes or $\Delta DSM_{positive}$). Each object is characterised by its sample mean and standard error of the mean, thus providing a better signal to noise ration with respect to a pixel-based change detection algorithm. Change magnitude of all detected $\Delta DSM_{negative}$ objects is on average -7.1 ± 1.4 m with an average area equal to 0.28 ± 0.61 ha. While, $\Delta DSM_{positive}$ objects are on average 2.4 ± 0.3 m, with an average area equal to 7.51 ± 14.32 ha. The statistical significance of the changes was assessed by the effect size index (E_{size}), which measures the distance of the object sample mean in comparison with no-change objects, given by undisturbed lowland and swamp forest control plots. $\Delta DSM_{negative}$ objects magnitude is highly significant (98% of changes with E_{size}≥ 1.5). For $\Delta DSM_{positive}$ objects the statistic also indicates that the changes are highly significant (98% changes with E_{size} ≥ 1.5), but on average E_{size} values are smaller and more outliers are present with respect to the $\Delta DSM_{negative}$ objects. This can be explained by the abrupt dynamics of deforestation/degradation events compared to the slower post-disturbance re-growth within 1 year. Further criteria based on object change magnitude and area were set to maximise the probability that $\Delta DSM_{negative}$ objects were true deforestation/forest degradation and $\Delta DSM_{positive}$ objects were post-disturbance re-growth. $\Delta DSM_{negative}$ objects were validated using two Pléiades scenes by manual delineation and two-users expert knowledge achieving a 87.6% hit rate (12.3% miss

rate) (N= 89). Validation of post-disturbance re-growth still requires further research. We conclude that TanDEM-X DSM differencing holds great potential for forest structural changes for several reasons: (a) it provides change magnitude (both positive and negative) which is not directly related to tree height change but can be considered a proxy measure of disturbance intensity; and (b) small-scale disturbance can be detected (< 1 ha) and (c) the method is sensitive to forest height change but independent from terrain elevation.

5.1. Introduction

Africa is of great importance since it hosts approximately 7.45 million km^2 of tropical forest (Grace, et al., 2014) (approximately 20% of the total global rainforest area) (Mayaux, et al., 2013). The largest portion of contiguous moist lowland humid and swamp forest (1.78 million km^2) (Mayaux, et al., 2013) and the second largest tract after the Amazon Rainforest (Laporte, et al., 1998; Malhi, et al., 2013) is located in Central Africa.

Moreover, it hosts rich biodiversity, supporting livelihoods by providing resources such as timber, goods and medicines (Megevand, et al., 2013), playing an important role in governing the global climatic system (Maynard & Royer, 2004; OSFAC, 2015), acting as an important carbon store and source (Grace, et al., 2014).

Carbon stocks in the Congo Basin are significant and account for about 25% of the total tropical carbon stocks (Saatchi, et al., 2011). As an important carbon sink and source, the Congo Basin is a priority area in international agreements such as Reducing Emissions from Deforestation and Forest Degradation initiatives (REDD+) set up under the UN Framework Convention on Climate Change (UNFCCC) that aims to curb climate change (UNFCCC, 2015).

Future climatic changes could pose major challenges for vulnerable African rainforests as models predict 3-4°C temperature increase, major changes in precipitation amount and patterning through the year, and a direct effect from the increase in CO_2 concentrations (which might enable an increased forest productivity and enhance photosynthesis) leading to potential forest expansion in the Congo

Basin (Cernusak, et al., 2013), but exactly how tropical forests will respond to these changes is still unclear (Malhi, et al., 2013).

Rapid deforestation and forest degradation driven by agricultural expansion, commercial logging, plantation development, mining, industrialization and urbanization is widespread across these areas (Duveiller, et al., 2008). Recent estimates indicate a tree cover loss equal to 471.38 kha between 2001-2014 (the highest loss occurred in 2014) and a tree cover gain reaching 559.82 kha (2001-2012) (considering a 30% canopy density threshold) (Hansen, et al., 2013). The rate of annual forest change for the period 1990-2015 was comparatively low for countries in the Congo Basin. For instance, the rate of annual forest changes was lower for the Republic of Congo (-0.1%) in comparison to Indonesia (-1.1%) and Brazil (-0.4%) (FAO, 2015).

Forest degradation, which is considered an anthropogenically driven change in carbon stocks (Herold, et al., 2011) and structure (Grainger, 1993), while still remaining "forest" and maintaining canopy cover above a threshold which is attributable to forest but does not imply a land use conversion (Herold, et al., 2011), is more challenging to detect and there are limited approaches to derive it in comparison to deforestation which makes this process vastly unaccounted for (Houghton, 2010). Recent estimates indicate that between 2005-2010 forest degradation made up 25% of the combined emissions from deforestation and forest degradation (Pearson, et al., 2017).

In some countries forest degradation has been identified as a predecessor of deforestation (Ahrends, et al., 2010) but there has been limited evidence for this in Africa (Mayaux, et al., 2013) and thus, this indicates that degraded forest are not necessarily converted to non-forest. This is widely observed in location where small scale disturbance due to selective logging or shifting cultivation is the prevalent form of forest disturbance (e.g.; in the Congo Basin).

Remote sensing provides the most suitable, cost effective approach for providing forest disturbance estimates in vast and inaccessible tracts of tropical forests in developing countries (Herold & Johns, 2007).

Deforestation mapping is prevalently accomplished using space-borne optical sensors (e.g. LANDSAT), with the ever increasing recognition and successful provision of the ability of radar instruments to provide forest area change estimates (deforestation) (Shimada, et al., 2014) independently from cloud cover, haze and daylight conditions (Lillesand, et al., 2008) especially in equatorial South America, the Congo River basin, and Southeast Asia where cloud cover annual frequency is > 80% (Wilson & Jetz, 2016) a fact that decreases the probability of cloud free acquisitions from optical sensors.

Despite the striking advantages over optical remote sensing, REDD+ initiatives have made comparatively limited use of Synthetic Aperture Radar (SAR) remote sensing to extract deforestation and forest degradation estimates (De Sy, et al., 2012) due to lack of consistent, freely available data acquired at time intervals which enable the detection of rapidly occurring phenomena (e.g. forest degradation) and slow vegetation re-growth.

Notably, Interferometric Synthetic Aperture Radar (InSAR) has been far less exploited due to data availability limitations, cost, methodological and computational complexity. In particular forestry applications are penalised by lack of consistent multi-temporal datasets which enable to track changes at regular intervals and the lack of suitable single-pass, fully-polarimetric, multi-baseline interferometric spaceborne sensors (e.g. before the TanDEM-X mission) which would be able to acquire data without the limitation of temporal decorrelation that affects repeat-pass acquisitions (Hanssen, 2001).

The use of single-pass InSAR is set to provide a valuable contribution to mapping and monitoring deforestation but particular focus should be directed to assess its potential for monitoring forest degradation.

5.1.1. Background: Interferometric Synthetic Aperture Radar (InSAR) for Forest Monitoring

InSAR exploits the ability to acquire two SAR images from two slightly different position and by measuring the phase difference between the two images to

provide a third dimension (Bamler & Hartl, 1998; Rosen, et al., 2000) and the generation of Digital Elevation Models (DEMs), these being highly suitable for the detection of forest structure changes (e.g. removal of vegetation).

DEMs from InSAR provide a relative height (or phase centre height- PCH) located somewhat within the vegetation volume (Balzter, 2001) depending on the sensor's frequency (deeper within vegetation volume for lower frequency); acquisition geometry and the temporal interval between acquisitions (in the case of repeat-pass interferometry) (Balzter, 2001).

The shift in the PCH is also dependent on environmental factors (e.g. rainfall and seasonality) (Praks, et al., 2012), and the target properties (e.g. canopy density and presence of canopy gaps) (Treuhaft, et al., 2015) which influence signal attenuation and the scattering mechanisms (Balzter, et al., 2007).

Dual-wavelength airborne SAR airborne systems have been employed to provide Digital Terrain Models (DTMs) (from P-band or L-Band) (Mura, et al., 2001; Neef, et al., 2005) and Digital Surface Models (DSMs) (from X-band) (Balzter, 2001; Neef, et al., 2005) to estimate tree height (or Canopy Height Models) (Balzter, et al., 2007) or to discriminate between landcover classes (Mura, et al., 2001).

DTMs are not as readily available (Balzter, et al., 2007) especially for large areas covering tropical forest. Other sources to provide DTMs (e.g. LiDAR) (Sadeghi, et al., 2016) are not widely acquired in tropical environments due to prohibitive costs in contrast to the more well studied boreal and temperate forests which are sometimes covered by national LiDAR surveys.

DEMs derived from spaceborne sensors at different wavelength (Shuttle Radar Topographic Mission at C-band and TanDEM-X or CosmoSkyMed at X-Band) have been used to delineate clear cuts in boreal forests (Solberg, et al., 2013), to detect canopy gaps due to forest degradation in tropical forest using the difference between Cosmo Sky-Med and SRTM DEMs (Deutscher, et al., 2013) and to map deforestation/forest degradation and re-growth in woodlands in Tanzania (Solberg, et al., 2014), in Australia and peat swamp forest in Indonesia (Tanase, et al., 2015) using a combination of SRTM and TanDEM-X.

In the absence of a dual-wavelength (long and short) spaceborne system with similar capabilities to airborne instruments, exploitation of multiple DSMs acquisitions over the same area can be exploited to detect relative height changes (deforestation, forest degradation and re-growth) in support of REDD+ initiatives (Solberg, et al., 2015) .

Particularly important in this context is the TanDEM-X (TerraSAR-X add-on for Digital Elevation Measurement) mission which acquires data at X-band (λ = 0.031 m, 9.65 GHz) and is currently the only available single-pass spaceborne interferometer to provide three-dimensional information (DEMs) without the limitation of temporal decorrelation between acquisitions. This is achieved by two-twin satellites flying in formation, that acquire data simultaneously (Kugler, et al., 2014; Martone, et al., 2012) and at high spatial resolution (< 5 m).

The physics behind the exploitation of X-band interferometric DSMs for forest monitoring hinges on the concept of penetration depth, which is a measure of the amount of vertical layer where the wave propagates before extinction (Cloude, 2010). For forest types that are less dense (e.g. boreal forests) and in dry conditions penetration depth is usually high (Garestier, et al., 2008; Hajnsek, et al., 2009). Instead, in denser tropical forests, at X-band, the low penetration results in the PCH being located closer to the top of the canopy (Izzawati, et al., 2006) and this can be exploited to provide a more accurate DSM.

Although, in some cases deeper penetration has been observed in tropical forest and this might have been linked to the clumpiness of the canopy and the development of gaps in the neighbouring clustered canopies (Treuhaft, et al., 2015).

In the context of dense tropical forest (assuming low penetration of the signal), since the PCH is located very close to the top of the canopy, the removal of forest through disturbance will lead to the PCH moving lower within the vertical profile thus, revealing processes such as deforestation (and forest degradation) given by a change in the target structure. Consequently, differences between two InSAR derived DSMs can provide estimates of the relative change in height.

Instead, for less dense forests, higher penetration of the signal into the canopy leads to the location of the PCH closer to the ground. Consequently, the shift in the phase centre will be less marked compared to a denser tropical forest.

The sensitivity of InSAR to structure is optimal for the detection of forest degradation since the change in forest structure caused by degradation cannot often be detected by optical sensors or SAR backscatter. In the case of optical instruments, saturation of the optical signal occurs due to fast re-growth of vegetation with canopy gaps closure occurring within 50 days after disturbance (Verhegghen, et al., 2015). In the case of microwave instruments the changes in backscatter are limited in magnitude and often masked by speckle and effects related to ground moisture (especially at longer wavelength due to increased penetration into the canopy) (Liesenberg, et al., 2016).

Most importantly, SAR backscatter and optical data, even if they do detect degradation, will very rarely have sufficient sensitivity to estimate its magnitude; comparison of InSAR datasets from multiple dates however, can provide a relative change in height, which is an indicator of the magnitude of disturbance.

The size of disturbance patches from small scale agriculture and selective logging of trees means that some of these changes can be missed by the most commonly available medium scale products (e.g. Hansen Forest Cover Loss (HFCL) with a 30 m resolution (MMU = 0.09 ha) (Hansen, et al., 2013).

Moreover, in optical remote sensing imagery subtle loss of canopy cover cannot be detected as it involves changes that are related to three-dimensional forest structure (Lucas, et al., 2014). This dimension is not accessible to optical sensors, since the radiation does not penetrate past the upper canopy.

TanDEM-X high resolution (< 5 m) affords increased probability of detection of small scale forest disturbance in the Congo Basin where, this process is often limited in size (~0.25 ha) (Wilkie, et al., 1998), in contrast with large scale commercial forest conversion occurring in the Brazilian Amazon (e.g. for cattle pasture and soya cultivation) (Fearnside, 2001) or in South-East Asia (e.g. palm oil and paper pulp plantations) (Mietten, et al., 2014). Case in point is the detection of canopy gaps (e.g.

removal of large trees may cause canopy gaps on average 719 m^2 (equal to 0.07 ha = 34 TanDEM-X pixels when geocoded with 4.6 m pixel spacing) (Pearson, et al., 2014) and small-scale disturbance (e.g. due to shifting cultivation). However, small canopy gaps are considered challenging to detect because of intrinsic noise (e.g. phase noise in the case of InSAR).

In summary, TanDEM-X provides several advantages that are well suited for mapping deforestation and, most importantly, forest degradation as well as forest re-growth: (a) Penetrate cloud cover and haze; (b) Limited penetration at X-band in dense tropical forest to provide accurate "top of canopy" estimates (DSM); (c) Detect small-scale disturbances (< 1 ha) due to high spatial resolution; (d) Magnitude of forest structure changes (forest degradation and re-growth) as well as land use conversion (deforestation).

Considering the aforementioned research gaps and requirements, we propose and demonstrate the potential of an object-based change detection approach using multiple TanDEM-X DSM acquisitions to map changes (and potentially to provide support for REDD+ initiatives) due to small scale disturbance in the tropical forests of the Congo Basin. In this setting persistent cloud cover severely restricts the availability of optical datasets and SAR backscatter is unable to detect three-dimensional changes (vertical structure as a function of space coordinates).

The following assumptions were made:

(a) Areas of no change exhibit similar DSM height between two dates.
(b) Changes due to deforestation, forest degradation and re-growth exhibit a change in DSM height between two dates.

5.2. Study Site

The study area is located around the town of Ouesso, Republic of Congo (UL: 15° 56'20.02'' E, 1° 44'42.83" N) covering 25 x 40 km^2 (Figure 1a). The area is dominated by dense humid semi-evergreen forest from the Guinean-Congolese region (White, 1983) (primary and logged) and extensive swamp forest around the Sangha River, a major tributary of the Congo River. The study site is partitioned

into community development areas, production (logging concessions) and protection areas which occupy respectively 0.6%, 10.8% and 3.4% of the study area (Figure 1b) (World Resources Institute, 2013).

The site has historically been prone to a high level of forest degradation from selective logging for commercial purposes and currently from extensive shifting cultivation that started in the 1990s (La Porte et al. 2004). Clearings are reported to be on average no greater than 1 ha and are concentrated in proximity of Ouesso (department capital and a centre for bushmeat trade) and Mboko, along the N2 road network and the Sangha River.

The Ngombé and Pokola logging concessions (Laporte, et al., 2004) are also situated within the study site where, selective logging of valuable tree species has been undertaken on rotation between 1985 and 2008 (Figure 1b).

Whilst, the long legacy of forest disturbance is still appreciable, this has created a mosaic landscape composed of areas of secondary and degraded forest spreading outwards from the main road networks which developed into a rural complex mosaic composed of old clearings, cropland, degraded forest and re-growth. The impact is still detectable visually by the presence of abandoned logging roads and primary road networks in some areas but rapid forest recovery makes it difficult to identify areas where selective logging occurred in the past.

The climate is classified as Tropical Wet Climate (Am) (Peel, et al., 2007) reaching peak precipitation in November (208 mm) and the lowest precipitation during July (45.9 mm) (World Bank, 2016). Total annual precipitation is 1597 mm (World Bank, 2016). Average yearly temperature is 24.8 °C and it is relatively constant throughout the year with highest temperature occurring in March (25.9 °C) and lowest temperature in July (23.5 °C) (World Bank, 2016). Soil type ranges from Haplic Ferralsols (FRha or FRX) to Umbric Gleysols (GLum) which is dominant in swamp forest (Jones, et al., 2013). Elevation in the study area varies between 320 m and 540 m asl with areas of higher elevation located towards the south-west of the study site inside the Ngombé logging concession while, swamp forest is located in areas with lowest elevation around the Sangha River (Figure 1a).

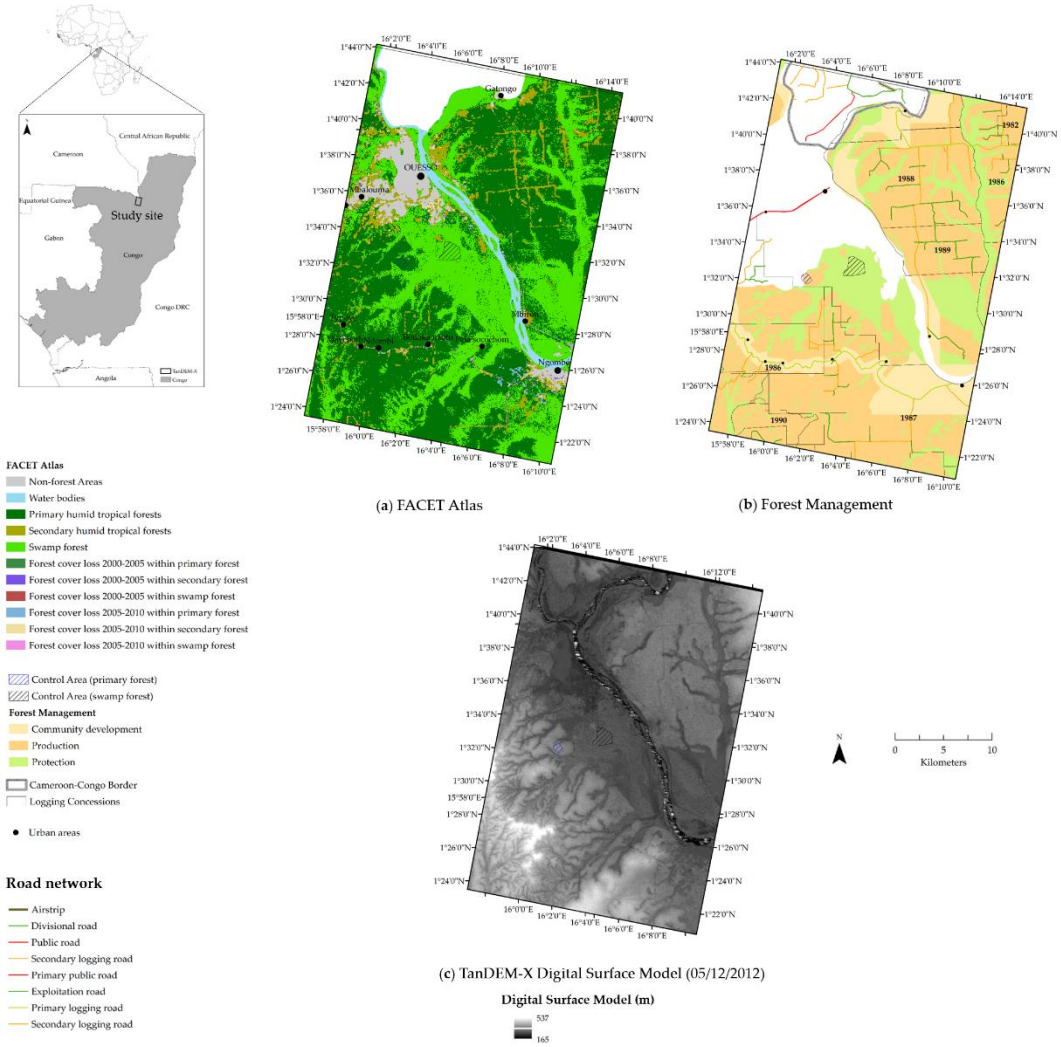

Figure 1. (**a**) Study area covered by TanDEM-X (approximately 1000 km²) situated around the Sangha Department capital of Ouesso in the Republic of Congo (RoC) (UL: 15° 56′ 54.55″ E, 1° 44′ 30.50″ N) overlaid on a landcover classification map (FACET Atlas: Forêts d'Afrique Centrale Évaluées par Télédétection) at 60 m resolution (OSFAC, 2012) showing the main landcover classes and forest cover loss between 2000-2010 (Potapov, et al., 2012). (**b**) The study site is divided into community areas (0.6% of the study area), protection areas (3.4% of the study area) and production areas (10.8% of the study area). The study area hosts two logging concession (black outline) with logging activities within the Pokola and Ngombé concessions taking place between the 1980s until 2008 (World Resources Institute, 2013). Control areas located within the protection area classified as lowland

primary forest (black) and swamp forest (blue) were selected to provide no-change areas for the analysis. (**c**) TanDEM-X Digital Surface Model acquired on 05/12/2012 (t_1).

5.3. Datasets

5.3.1. TanDEM-X

Two single polarisation TanDEM-X scenes in bistatic/StripMap mode (supplied by DLR through the VEGE03030 Announcement of Opportunity) were acquired on 05/12/2012 and on 25/12/2013, at HH polarization, 47° incidence angle in descending mode (Table 1). The effective baselines ($B_\perp$) ranged from 52 m (t_2) to 95.3 m (t_1) (corresponding to height of ambiguity between 164 m and 88.6 m respectively).

Data processing was undertaken using ENVI/SARScape software 5.0 interferometric module (Sarmap, 2016) from co-registered Single Look Complex (CoSSC) data and included the following steps: (a) importing; (b) multi-looking (2 range and 2 azimuth looks, corresponding to a slant range pixel size of 3.69 x 3.73 m); (c) interferometric workflow (interferogram generation and flattening, adaptive local frequency filter using the Goldstein filter (Goldstein & Werner, 1998) and coherence generation) and (d) geocoding to Geo-Global Lat/Lon with 3.33 10^{-5} degree pixel size (approximately 4.6 m).

Processing to obtain a DSM was also undertaken using the interferometric workflow implemented in SARScape 5.0 (Sarmap, 2016) following the procedure outlined: (a) phase unwrapping using the Minimum Cost Flow algorithm which enables to resolve the 2π ambiguity (Costantini, 1998); (b) phase to height conversion and (d) geocoding to Geo-Global Lat/Lon, Datum WGS 84 at 4.2 10^{-5} degrees pixel spacing (equivalent to 4.6 m pixel spacing in WGS84, UTM Zone 33 N). The DSM generated corresponds to the superimposition of the bare earth topography (DTM) and vegetation volume (PCH) which represents an approximation of the "top of the canopy" (or DSM) and is located within the top layer of the forest volume (Balzter, 2001). The resulting processed TanDEM-X DSM acquired on 05/12/2012 is shown in Figure 1c.

Accumulated precipitation data from the Tropical Rainfall Measuring Mission (TRMM) was used as reference data to ensure no influence of rainfall (Table 1).

Table 1. TanDEM-X StripMap mode configuration for 2 dates acquired at HH polarisation, descending orbit direction and right look direction. Tropical Rainfall Measuring Mission (TRMM) precipitation data for a period of 48 h before the acquisition date (GIOVANNI, 2016).

Acquisition	Date	$B_{\perp}$ (m)	Inc. Angle (°)	HoA (m)	Range (km)	Rainfall (mm)*
t_1	05/12/2012	95.3	48.05	88.6	718.59	0
t_2	25/12/2013	52	47.68	164	718.51	7.6

* based on TRMM accumulated rainfall for a period of 48 h before the acquisition date. $B_{\perp}$: effective baseline, HoA: Height of Ambiguity.

5.3.2. Optical Data

Very High Resolution (VHR) optical data acquired by the Pléiades satellite sensor on 22/02/2013 (4 bands pan-sharpened at 0.5 m resolution) (Astrium, 2012) and on 17/12/2013 (available from Google Earth at 2 m resolution) (Table 2). Pléiades Standard Ortho data was corrected for viewing angle and ground effects by Airbus Space and Defence and geocoded to WGS84/ UTM Zone 33 N (Astrium, 2012).

Employing Google Earth (GE) as a source for validation has been highlighted in Dorais & Cardille (2011) given that high resolution imagery enables clear interpretation of landcover and disturbance (Mermoz & Le Toan, 2016) and can be an effective tool when ground data is not available. High resolution optical imagery has clear advantages since it can cover a larger area compared to point estimates which are often not representative and more subjective compared to visual interpretation of high resolution optical data. Moreover, ground-based repeat survey to track forest disturbance (especially degradation) are rarely undertaken and often do not match well with the remote sensing data acquisitions.

A limitation for the use of GE is the availability of only a single date high resolution image which is not appropriate for change detection validation (Dorais & Cardille, 2011).

Table 2. Ancillary VHR optical Pléiades data used for validation of the TanDEM-X change map (Astrium, 2012; Google Earth , 2016).

Time	Sensor	Date	Resolution (m)	TanDEM-X Date
t_1	Pléiades	22/02/2013	0.5	05/12/2012
t_2	Pléiades (GE)	17/12/2013	2	25/12/2013

5.4. Methods

5.4.1. Method Outline

Figure 2 outlines the methodological approach. The approach departs from the classical statistical decision theory where the detector is driven by knowledge of the signal and noise characteristics in terms of their Probability Density Functions (PDFs). In other words, the detector works on random samples and tries to decide to which population (one or many) the sample belongs to. For instance, in the case of a simple two hypothesis testing framework for random signal in noise, the likelihood ratio test (Neyman Pearson theorem) (Neyman & Pearson, 1933) affords a detector where the probability of detection is maximized for a given probability of false alarm (Kay, 1998). Implementation of these types of detectors calls for the estimation of the relevant PDFs using a training dataset.

Instead of single samples (pixels) we consider objects, these being defined by the spatial relationship (continuity) of their constituent samples, i.e. by their morphological properties. Once an object is identified and labelled, then the detection step (the assignment to signal or noise, in our case change/no-change) is provided by the mean of the constituent samples (E) and the mean of control plots (C) and related standard errors.

Whereas, in the statistical detection theory the distribution of the sample is of importance, here the distribution of the mean value estimates plays a role. The

advantage of dealing with an object-oriented approach is therefore that the variance of the estimates used for detection, due to propagation of error and the intrinsic variance of the samples in the object, is much smaller than the one related to the samples in the object.

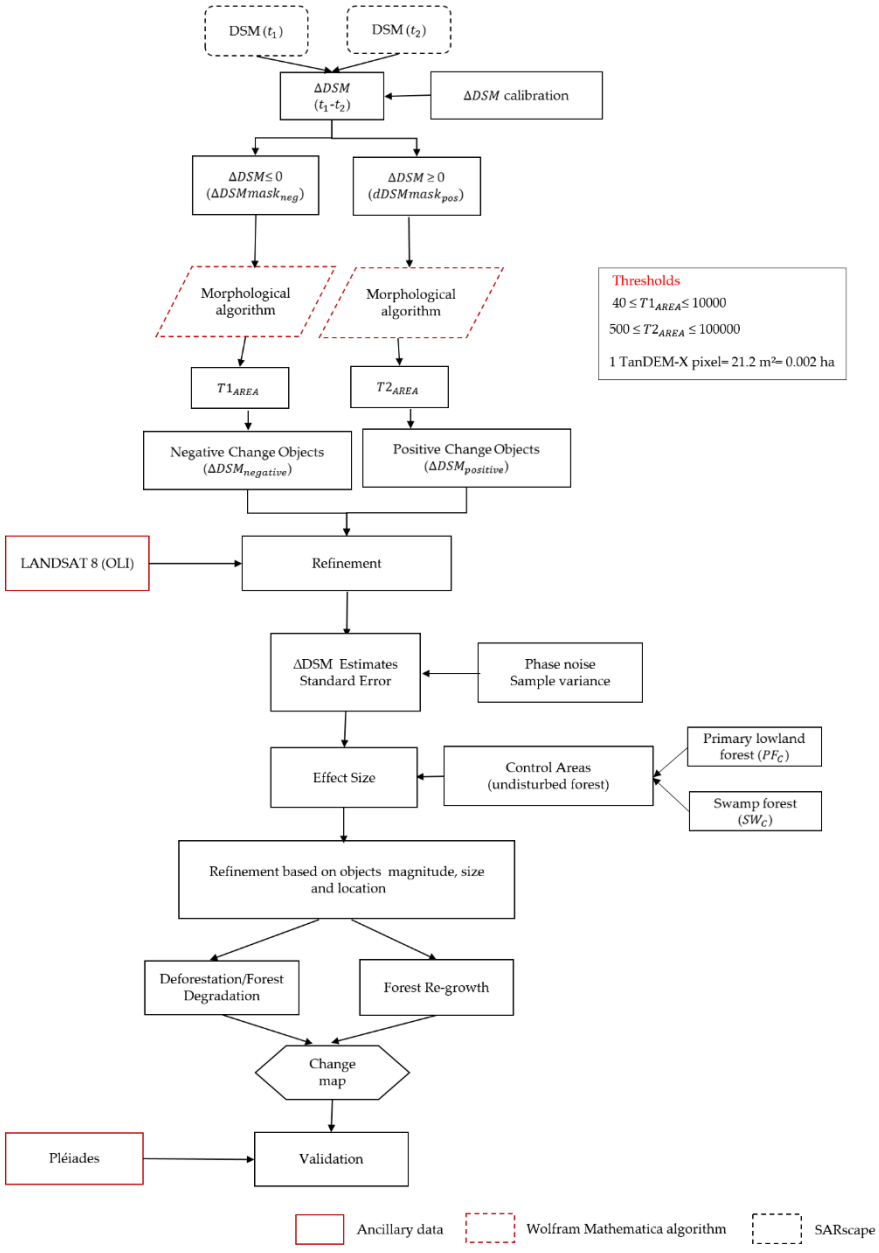

Figure 2. Methodology flowchart including DSM difference processing; DSM difference calibration; morphological algorithm implementation; post-processing and refinement; error propagation estimates and object-based validation relying on VHR Pléiades imagery.

5.4.2. TanDEM-X Digital Surface Model Difference Generation and Calibration

The object-based change detection method uses two dates: 05/12/2012 ($TDXt_1$) and 25/12/2013 ($TDXt_2$) separated by approximately 1 year and acquired in the same season (December) with the aim to minimise seasonality and rainfall influences (Table 1). The difference dataset (ΔDSM) is obtained by differencing between two co-registered DSMs in slant range geometry at $TDXt_1$ and $TDXt_2$ (Figure 2).

The ΔDSM dataset presents a tilt between far and near range, which was estimated with a tilt angle φ_{tilt}= 5.76 × 10^{-4} degrees and resulting in a height difference over the swath of 7.1 cm. The tilt is due to the propagation of small errors in the line of sight baseline determination combined with different effective baselines ($B_\perp$) in the two data takes. Theoretically, the φ_{tilt} in a DSM can be estimated from Equation 1 (Wermuth, et al., 2014):

$$\varphi_{tilt} = \frac{\Delta B_{los}}{B_\perp} \qquad \text{Equation 1}$$

For the ΔDSM dataset:

$$\varphi_{tilt} = \Delta B_{los} \left(\frac{1}{B1_\perp} - \frac{1}{B2_\perp}\right) \qquad \text{Equation 2}$$

Where ΔB_{los} is the baseline error in line of sight; $B1_\perp$ is the effective baseline at $TDXt_1$and $B2_\perp$ is the effective baseline at $TDXt_2$.

Considering the effective baseline values for the TanDEM-X dataset ($B1_\perp$= 52 m and $B2_\perp$= 95.3 m) and assuming an error of the line of sight baseline of 1 mm (in line with the results in (Wermuth, et al., 2014) we have: φ_{tilt}= 0.00059°, matching the estimated value from measurement.

To correct the tilt, the DSM difference as a function of range pixel coordinate j, $\Delta DSM(j)$ is modelled as a zero mean random process $\widehat{\Delta h}$ affected by a systematic error (trend), which is linear in the range coordinate j:

$$\Delta DSM(j) = \widehat{\Delta h}(j) + mj + q \qquad \text{Equation 3}$$

The trend is first estimated taking the average of N realisations of the ΔDSM profile in the cross-range direction over a small neighbourhood where the statistic is stationary. The average profile is then fitted by a trend line (Equation 4) (Figure 3):

$$y(j) = mj + q \qquad \text{Equation 4}$$

The dataset is then de-trended (brought to zero mean) line by line by subtracting to each pixel the trend line (Equation 5):

$$pdetrended(i,j) = p(i,j) - m\,j - q \qquad \text{Equation 5}$$

Where $p(j)$ is the pixel at position j in line i.

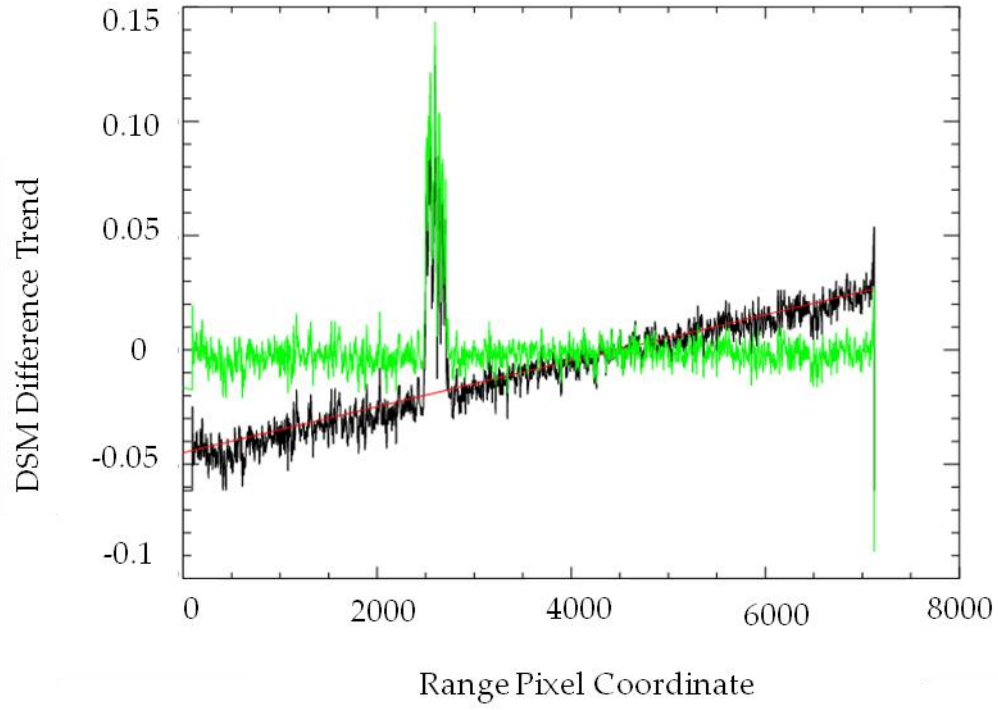

Figure 3. Original trend profile (black), fitted trend line (red) (Equation 4) and corrected (de-trended) range profile (green) (Equation 5). The peak between 2000 and 3000 pixels arises because of an area of very low precision in the DSM (river). This singularity does not influence the estimation of the trend.

5.4.3. Object-Based Change Detection Using a Morphological Algorithm

The calibrated ΔDSM was used as the starting point for an object-based change detection. Note that ΔDSM does not indicate the "true" vegetation height difference but the difference of the PCH, which are somewhere within the vegetation volume (Balzter, 2001) and closer to the true "top of canopy" at X-band for dense tropical forest.

Object-based change detection was sub-divided into two phases: (a) detection of negative changes, these being ascribed to loss of vegetation volume over ground (deforestation/forest degradation) and (b) detection of positive changes, these being ascribed due to gain in vegetation volume (re-growth).

The calibrated ΔDSM was converted into an image maintaining all negative values and masking all positive values (ΔDSM_{mask_neg}) while, a second image was generated by masking all negative values and keeping only the positive changes (ΔDSM_{mask_pos}).

A morphological segmentation algorithm implemented in Wolfram Mathematica 10 (Wolfram, 2016), was applied to each ΔDSM_{mask} image. The output is an array where each pixel in the image is labelled by an integer index representing the connected foreground image component in which the pixel lies (Wolfram, 2016). Morphological algorithms are well suited for extracting the spatial relationships between groups of pixels rather than the information for a single pixel (Soille & Pesaresi, 2002).

An area threshold ($40 \leq T1_{AREA} \leq 10000$ pixels equivalent to 0.08 ha $\leq T1_{AREA} \leq$ 21.16 ha) was set to the ΔDSM_{mask_neg} output to extract negative change objects ($\Delta DSM_{negative}$). In this case, the Minimum Mapping Unit (MMU) ≅ 0.08 ha (40 TanDEM-X pixels) was chosen to maximise the detection of small-scale changes and based on the following considerations: a) clearings size which are usually < 1 ha (lower threshold in the range 0.2-0.3 ha) as a result of shifting agriculture in the Congo Basin (Aweto, 2012) and b) size of selective logging gaps due to the removal

of a limited number of trees per hectare . In summary, the threshold was selected as a compromise to fully make use of the high resolution and knowledge related to the process scale based on published literature.

The morphological algorithm was run again on the ΔDSM_{mask_pos} output to extract positive changes. An area threshold (500 ≤$T2_{AREA}$≤ 100000 pixels equivalent to 1.06 ≤$T2_{AREA}$≤ 211.6 ha). This setting was reached by successive approximations by testing several upper and lower area thresholds and running the algorithm iteratively to identify the most suitable one to extract positive change objects ($\Delta DSM_{positive}$).

The upper area threshold was set to 100000 pixels since it was evident from visual inspection of VHR optical imagery that areas of re-growth tended to form large clusters. Setting a lower value of the upper threshold would have made the algorithm miss most of the positive change areas.

5.4.3.1. Objects Refinement

Objects refinement was essential to: a) remove objects inside water bodies; b) remove objects detected due to co-registration miss-matches.

a) A mask was extracted from LANDSAT 8 OLI (01/11/2013) by setting a threshold to the SWIR 1 (Band 6) which enabled a satisfactory delineation of the river system. The river mask was buffered by setting a 20 m threshold and change objects located within the buffered zone, were removed from the analysis since they did not constitute actual vegetation changes but were linked to problems with phase unwrapping over low coherence (γ) areas at both acquisition dates ($\gamma(t_1)$ = 0.47 ± 0.17; $\gamma(t_2)$ = 0.49 ± 0.19) and low DSM precision at both dates $SD(h_\varphi)(t_1)$ = 26.02 ± 7.19 m; $SD(h_\varphi)$ (t_2) = 46.34 ± 13.61 m) (Figure 4).
b) Objects located within a 10 m buffer from the margin of the output ΔDSM image were also removed since they were not considered "true" changes but were related to possible co-registration miss-matches between the two TanDEM-X DSMs.

5.4.4. Standard Error of the Mean Height Difference

We consider the variance of the mean estimator (SEOM) in a set of height difference samples being the result of two components: (1) phase noise and (2) variance of the samples. Other sources of error, such as phase unwrapping errors, are supposed to be second order effects and are not accounted for.

Each sample in the set (height estimate) is affected by an error induced by phase noise whose standard deviation ($SD\varphi$) can be related to the coherence by a Cramer-Rao bound (Cloude, 2010) (Figure 4) (Equation 6):

$$SD\varphi = \sqrt{\frac{1 - |\gamma|^2}{2|\gamma|^2}} \qquad \text{Equation 6}$$

Where φ is the phase and γ is the interferometric coherence.

The standard deviation of the height estimate $SD(h_\varphi)$ is computed by SARscape for each pixel in the DSM dataset (Sarmap, 2016). The phase error propagates to the height estimate error as:

$$SD(h_\varphi) = SD\varphi \frac{\lambda R \sin\vartheta}{4\pi B_\perp} \qquad \text{Equation 7}$$

Where λ is the wavelength, R is the slant range distance, ϑ is the local incidence angle and $B_\perp$ is the effective baseline.

Lower coherence values result in a lower measurement precision and vice versa (Sarmap, 2016).

With N independent samples in an object of the DSM at one date (h_i) with variance $VAR(h_i)$, each with additive white Gaussian noise with variance $VAR(h_{\varphi i})$, the variance of the samples and the noise propagate to the variance of the mean estimator ($\hat{h}$) in the following way:

The sample mean is:

$$\hat{h} = \langle h \rangle = \frac{\sum h_i}{N} \qquad \text{Equation 8}$$

The variance of the samples propagates to the variance of the sample mean as:

$$VAR(\hat{h}_1) = VAR\left(\frac{\sum h_i}{N}\right) = \frac{\sum VAR(h_i)}{N^2} = \frac{VAR(h_i)}{N} \quad \text{Equation 9}$$

For additive noise:

$$VAR(\hat{h}_2) = \frac{\sum VAR(h_{\varphi i})}{N^2} \quad \text{Equation 10}$$

Therefore, the overall variance $VAR(\hat{h})$ of the mean estimator is:

$$VAR(\hat{h}) = \left(\frac{\sum VAR(h_{\varphi i})}{N^2} + \frac{VAR(h)}{N}\right) \quad \text{Equation 11}$$

Where $VAR(h\varphi_i)$ is the phase variance of the single sample i and $VAR(h)$ is the variance of the samples in the object.

For the difference of the DSMs at two dates (t_1 and t_2), the Standard Error of the Mean height difference (SEOM) is:

$$SD(\widehat{\Delta h}) = \sqrt{VAR(\hat{h}_1) + VAR(\hat{h}_2)} \quad \text{Equation 12}$$

Where $\Delta h = h_1 - h_2$ with h_1 and h_2 being DSM height at t_1 and t_2 respectively.

5.4.5. Accuracy of DSM Difference Estimates

Accuracy of the DSM difference estimates is reported by confidence limits of the mean $\hat{h} \pm \delta$, with δ = t SEOM ($SD(\widehat{\Delta h})$), with Student's t =1 for 68% confidence level (CL) and t = 1.96 for 95% CL (degrees of freedom greater than 200). The confidence limits characterise the accuracy of the ΔDSM estimates within the detected objects achievable by the proposed method.

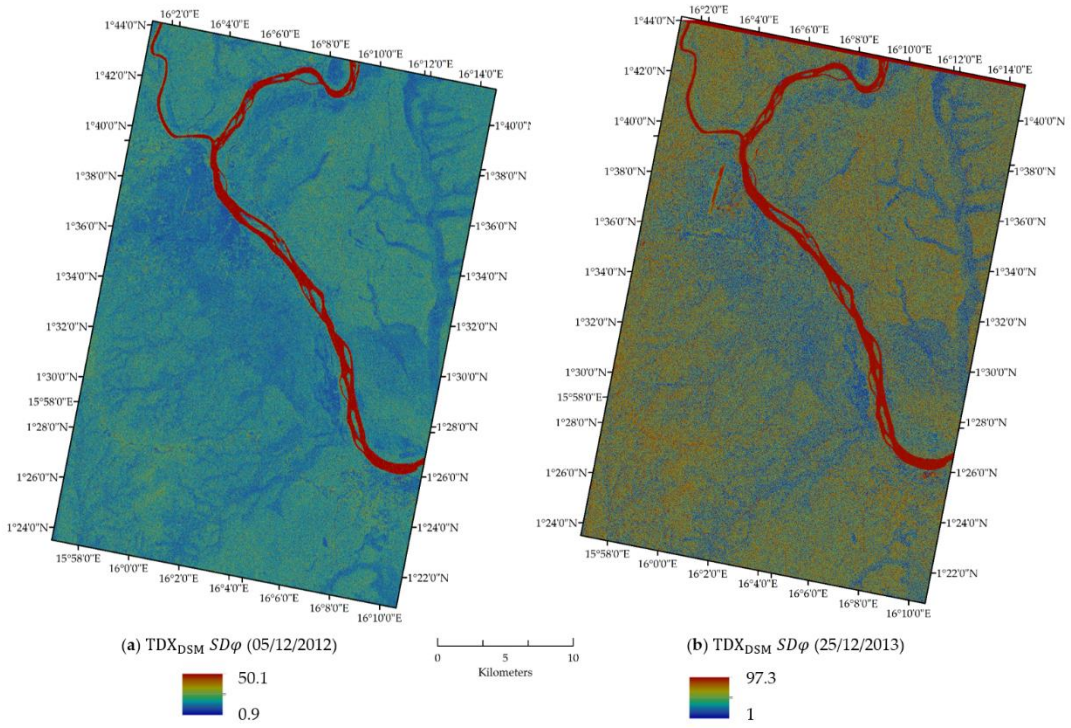

Figure 4. TanDEM-X standard deviation of height estimates derived from phase noise ($SD(h_\varphi)$) for two dates provided by SARScape 5.0 (Sarmap, 2016): (**a**) $TDXt_1$: 05/12/2012 and (**b**) $TDXt_2$: 25/12/2013. Higher $SD(h_\varphi)$ values (m) indicate lower measurement precision. Notice that areas of lowland forest present higher $SD(h_\varphi)$ values (lower precision) while, areas of swamp forest, agriculture and bare fields (dark blue) have a higher precision. This is related to the sensitivity of the interferometer in areas where there is less volume decorrelation. The river presents the lowest precision in the scene (highest $SD(h_\varphi)$) (red). Overall higher precision was achievable at $TDXt_1$ ($B_\perp$= 95.3 m) compared to $TDXt_2$ ($B_\perp$= 52 m).

5.4.6. Effect size and Confidence Intervals

The effect size (E_{size}) is the magnitude of the difference between groups (Sullivan & Fein, 2012) and is a true measure of the significance of the difference. E_{size} is used instead of *p- values* as it reports the size of the effect. Moreover, the *p-value* when considering a large number of samples (in the experimental and/or control groups) will usually always produce a significant difference and therefore, is not suitable in our case. E_{size} was computed between two groups: experimental

group (E) which corresponds to either $\Delta DSM_{positive}$ or $\Delta DSM_{negative}$ and a control group (C) corresponding to either a primary lowland forest control plot (PF_C) or swamp control plot (SW_C) (Cohen, 1992) (Equation 13):

$$E_{size} = \frac{\mu_E - \mu_C}{\sigma_{pooled}} \quad \text{Equation 13}$$

Where: μ_E is the mean of the change polygons in the experimental group, μ_C is the mean of the control plots and σ_{pooled} is the pooled standard deviation between the experimental and the control groups (Nakagawa & Cuthill, 2007) (Equation 14):

$$\sigma_{pooled} = \sqrt{\frac{(N_E - 1)SD_E^2 + (N_c - 1)SD_C^2}{N_E + N_C - 2}} \quad \text{Equation 14}$$

Where: N_E is the number of samples in the experimental group; N_C is the number of samples in the control group; SD_E is the standard deviation in the experimental group and SD_C is the standard deviation in the control group.

The E_{size} measures the distance between the sample mean values in the experimental group with respect to the sample mean value in a control group, in units of their pooled standard deviation. One way to interpret the E_{size} is to consider the statistic of the difference of two sample means $d = \mu_E - \mu_C$, these being normally distributed and independent. Their difference will also be normally distributed with a standard deviation $\sigma_d = \sqrt{\frac{\sigma_E^2 + \sigma_C^2}{2}}$ and mean value $\hat{\mu}$. Shifting d to zero mean and normalising by σ_d, the probability to have $P(\mu_E - \mu_C) > 0$ can be computed as a function of E_{size} (Moore & McCabe, 2005):

$$P(\mu_E - \mu_C) > 0 = P\left(\frac{\mu_E - \mu_C - \hat{\mu}}{\sigma_d}\right) > \frac{-\hat{\mu}}{\sigma_d} = -E_{size} \quad \text{Equation 15}$$

From Equation 15 the probability that a new sample in the experimental population will be above the mean of the control population is:

$$P(\mu_E - \mu_C) > 0 = 1 - CDF\ (\aleph(0,1, -E_{size}) \quad \text{Equation 16}$$

where CDF is the cumulative distribution function and ℵ(0,1) is the standard normal distribution.

For example, E_{size}= 1.45 indicates that in 93% of cases in a new experiment the mean value will be above the mean value of the control group.

The interpretation reported in the literature as Cohen's U_3 (Cohen, 1988) does not indicate how distant in the new sample from the control mean. Therefore, in the context of our detection problem it is more appropriate to consider the relationship between E_{size} and the probability that a new sample is assumed to be in the experimental population when indeed it is a control value (a Type I error). Given the normal distribution with equal variance of the two populations, a threshold was set within the overlap area at the intersection point of the PDFs. The error is given by integrating the PDF of the control population up to the intersect point (x):

$$\aleph(\mu_E, \sigma, x) = \aleph(\mu_E, \sigma, x) \xrightarrow{yields} x = \frac{\mu_E + \mu_C}{2} \qquad \text{Equation 17}$$

$$P(\,Type\ I\ error) = (1 - CDF\left(\aleph\left(\mu_C, \sigma, \frac{\mu_E + \mu_C}{2}\right)\right) = \frac{1}{2}(2 - Ercf\left(\frac{\mu_C - \mu_E}{2\sqrt{2}\sigma}\right) \qquad \text{Equation 18}$$

where $Ercf$ is the complementary error function.

This relationship allows us to compute the probability of Type I error for a range of E_{size} values (Figure 5).

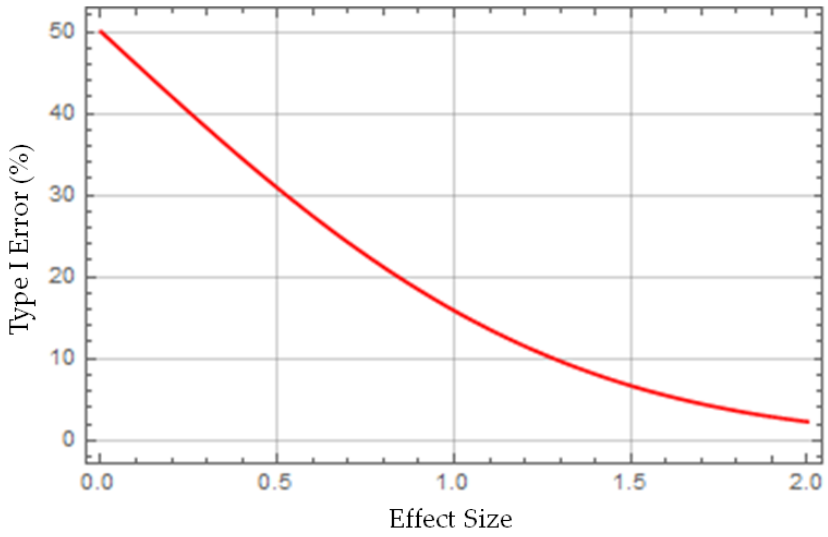

Figure 5. Probability of Type I error as a function of effect size.

For E_{size}= 1.5 the probability of Type I error is 6.6% (detecting as true change a sample that is noise). Based on this interpretation, a threshold E_{size}= 1.5 was set in the development of the change detection.

The margin of error (or confidence interval) (CI) on the effect size was used to estimate the amount of variation with respect to the "true" value and indicates the estimate resulting in case of repeatedly taking samples of the same size (Equation 19) (Hedges & Olkin, 1985):

$$\sigma[E_{size}] = \sqrt{\frac{N_E + N_C}{N_E \times N_C} + \frac{{E_{size}}^2}{2(N_E + N_C)}} \qquad \text{Equation 19}$$

Considering a 95% confidence interval (95% CI) $\boldsymbol{E_{size}}$ ranges between $\boldsymbol{E_{size_{lower/upper}}}$ (Equation 20) (Nakagawa & Cuthill, 2007):

$$E_{size\,lower/upper} = E_{size} \pm 1.96 \times \sigma[E_{size}] \qquad \text{Equation 20}$$

5.4.7. Object refinement based on magnitude, area and location

The statistics computed for all objects were used to choose a criteria for discarding objects which were not likely to be "true" disturbance events and for keeping for further analysis a subset that maximised the link between

$\Delta DSM_{negative}$ and $\Delta DSM_{positive}$ objects. The resulting subsets were used further in the analysis.

1. $\Delta DSM_{negative}$ objects: $\Delta DSM_{negative}$ objects refinement was undertaken by: a) defining a threshold related to the size of the objects by choice of the 3rd quartile of the distribution (representing the upper 75th of the distribution) (Q_3= 100 pixels); b) the magnitude of change threshold was based on the 3rd quartile (Q_3= -7 m). Discarded objects (subset A) were defined as objects which satisfied both area ≤ 100 pixels AND $|\Delta DSM_{negative}| \leq 7$. Subset B was considered for further analysis and included objects that satisfied the area threshold (> 100 pixels) but not necessarily the magnitude threshold. Effect size $\geqslant$ 1.5 was set as explained in section 5.4.6.
2. $\Delta DSM_{positive}$ objects: the spatial location of $\Delta DSM_{positive}$ objects with respect to $\Delta DSM_{negative}$ was considered. It was assumed that areas of post-disturbance re-growth were more likely to be located in proximity to $\Delta DSM_{negative}$ objects and consequently, we set a minimum distance from the centroid of each $\Delta DSM_{negative}$ object to the $\Delta DSM_{positive}$ objects centroid to < 500 m (subset B) and discarded objects located ≥ 500 m from $\Delta DSM_{negative}$ objects (subset A). Effect size $\geqslant$ 1.5 was set as explained in section 5.4.6.

5.4.8. Validation

a) False positives were assessed using two control plots (C) to verify that the changes that were detected from TanDEM-X were "true" changes and not due to noise. We considered an area of undisturbed primary lowland forest (PF_C) (77 ha) and undisturbed swamp forest (SW_C) (302 ha) (Figure 1). The areas were "undisturbed" within the time-frame of the analysis, it was challenging to delineate an area of "true" primary forest (as defined in the "Intact Forest Landscape" definition) (Potapov, et al., 2008), as there were no protected areas in the study site and most of the site was occupied by logging concessions. The reliability of this

assumption is also constrained by the lack of ground data covering the area at the time of data acquisition. Two independent datasets supported our assumption: 1) no forest cover loss was identified by Hansen et al. (2013) for the period 2000-2013 inside the control plots and b) no forest loss took place according to the FACET Atlas (2000-2010)(OSFAC, 2012).

b) An object-based oriented validation approach using an independent dataset was chosen, this being in line with the object-based change detection method (Elrajubi et al., 2014). An object-based validation implies that the validity criterion is the miss-hit matching of a spatial geometrical property, this being the intersection of the digitised contour (objects) delineating the test object (area of change detected by the radar analysis) and a reference object (area of change in the independent Pléiades dataset).

The hit rate (%) is the percentage of objects that are interpreted by the Pléiades scenes as changes and that geometrically intersect the $\Delta DSM_{negative}$ objects; while the miss rate (%) is the proportion of objects with no intersection between the Pléiades validation dataset and the $\Delta DSM_{negative}$ objects (Ryan, et al., 2012). Objects intersection was calculated using the "intersect" function available in ArcGIS 10.1 (ESRI, 2016).

No attempt is made to compare other pixel-based properties, such as total change area, or statistic of the forest height distribution. An object-based validation was deemed appropriate since it would enable us to assess the performance of our method.

Validation dataset selection relied on a combination of expert knowledge for the interpretation of remote sensing optical imagery (Pléiades) and manual delineation of changes by two users (Elsa De Grandi and Edward Mitchard). Validation was restricted to a 9500 ha section of the study site located around the town of Mboko due to limitations in data availability (Figure 6).

A validation dataset (DEF/DEG) was generated by delineating disturbance events (N = 89) occurring between February 2013 (22/02/2013) (3 months after

$TDXt_1$) and December 2013 (27/12/2012) (a few days after $TDXt_2$) based on two Pléiades scenes corresponding as closely as possible to the TanDEM-X acquisitions.

We delineated sub-hectare clearings as well as larger clearings (> 1 ha) (total area delineated: 67.72 ha, mean ± standard deviation: 0.75 ± 1.02 ha) to develop a dataset that took into account of the area threshold set for $\Delta DSM_{negative}$ objects (40 pixels ≅ 0.08 ha) (section 5.4.3). The validation was undertaken only for $\Delta DSM_{negative}$ objects.

The delineation of new deforestation/degradation events was challenging since: 1) clearings edges were not well defined and they were often overlapping with older clearings; 2) clearings were occupied by remnant vegetation before complete vegetation removal was undertaken. Once the objects were validated those that were "true" changes (intersected with both TanDEM-X and Pléiades or hit rate). This provided an independent check which could enable us to verify whether the TanDEM-X miss rate was due to: 1) omission from the analysis; 2) incorrect interpretation of the change occurring between the two Pléiades scenes; 3) due to the time elapsed between the TanDEM-X difference and the two Pléiades scenes.

No ground data was collected for the validation. Given the extent of the area to validate, the forest temporal dynamics, which would call for historical data, and the type of detection method, which is not based on physical properties (e.g. forest height), it was deemed that such an effort could have only marginally improved the accuracy, albeit providing one more independent assessment piece of information, since it would not be based on remote sensing imagery (Desclée, et al., 2006).

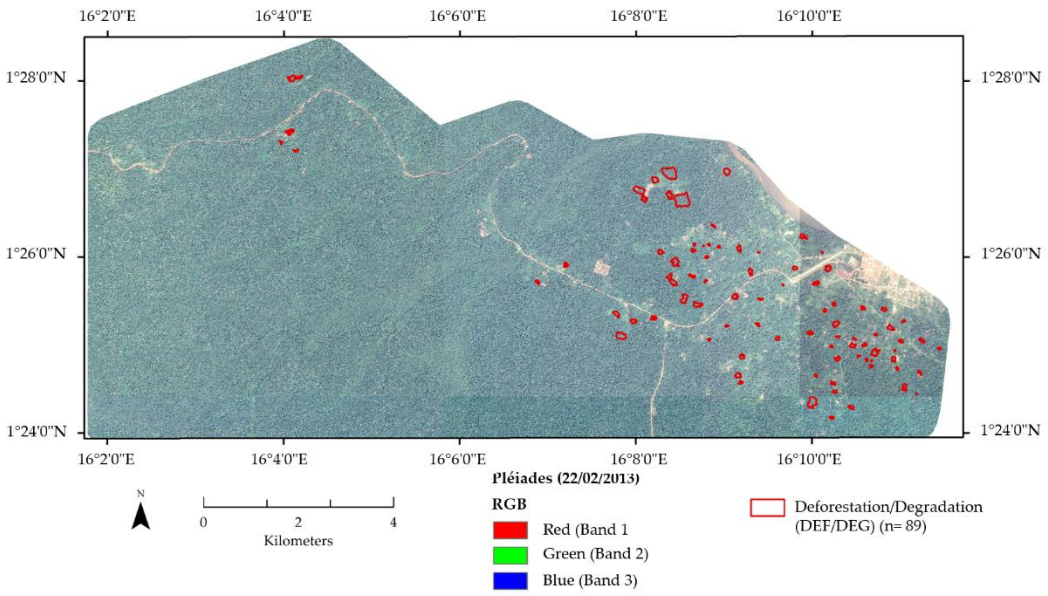

Figure 6. Pléiades data (22/02/2013) with overlaid deforestation/degradation validation objects (DEF/DEG) (red outline) delineated from visual interpretation and expert knowledge captured between two Pléiades scenes (date 1: 22/02/2013 and date 2: 17/12/2013).

5.4.9. Dependence of DSM Difference Estimates on Sensor's Parameters

We analyse from a theoretical (modelling) point of view the difference of two estimates of DSM of the same natural target, provided by two InSAR observations with slightly different instrumental parameters, these being the effective baseline, incidence angles, and range distances (Table 1). The effective baseline is the instrument's parameter that could affect more the DSM difference, and its impact needs to be considered.

Two scattering scenarios were considered in the analysis:

1) A dense forest, featuring high extinction at X-band and that can therefore be modelled as a random volume with no return from the ground. This situation will correspond to the no-change case represented by the lowland primary forest and the swamp forest control plots.

The fractional phase centre height is computed assuming a simple Random Volume model (RV) with exponential vertical structure function (Cloude, 2010):

$$\gamma_{vol} = \frac{P_1(e^{P_2 h} - 1)}{P_2(e^{P_1 h} - 1)} \quad \text{Equation 21}$$

Where: $P_1 = \frac{2\sigma_e}{cos\vartheta}$ and $P_2 = P_1 + i\beta_z$ and $\beta_z = \frac{4\pi B_\perp}{\lambda R \sin\vartheta}$

γ_{vol} is the complex coherence; h is the volume height; σ_e is the extinction; β_z is the vertical wavenumber; $B_\perp$ is the effective baseline; ϑ is the incidence angle and R is the range distance.

The fractional phase centre height is computed from the phase of the complex coherence and it is a function of extinction, volume height and vertical wavenumber (Cloude, 2010):

$$\phi_{center} = \frac{Arg[\gamma_{vol}]}{h\beta_z} \quad \text{Equation 22}$$

The DSM difference (ΔDSM) is computed from ϕ_{center} and it is a function of volume height h_v, extinction σ_e (assumed constant between the two data takes) and vertical wavenumbers β_1, β_2 that include the instrument's parameters of the two observations, (i.e. baseline, range distance and incidence angle):

$$\Delta DSM = \phi_c(h_v, \sigma_e, \beta_1)h_v - \phi_c(h_v, \sigma_e, \beta_2)h_v \quad \text{Equation 23}$$

2) A less dense forest which could represent the case of degraded forest or forest re-growth, can be modelled to include a return from the ground. In this case, the Random Volume over Ground (RVoG) model was used (Cloude, 2010).

For the purpose, Equation 21 is modified to include the return from the ground in the form of the effective volume to ground scattering ratio (μ) (Cloude, 2010):

$$\gamma = \frac{\gamma_{vol} + \mu}{1 + \mu} \quad \text{Equation 24}$$

5.5. Results

5.5.1. DSM Difference

Figure 7 illustrates an example of forest dynamics mapped by the ΔDSM along a transect including a gradient from undisturbed lowland forest (1) to forest volume loss (2) followed by forest volume gain (3) and forest volume loss (4). Notice that the fluctuations within each segment are due to forest structure variability and signal noise while relative differences between deforestation and re-growth and stable segments are due to the intensity of the forest change event. Forest change magnitude in (2) and (4) can be associated to a different degree of forest volume loss.

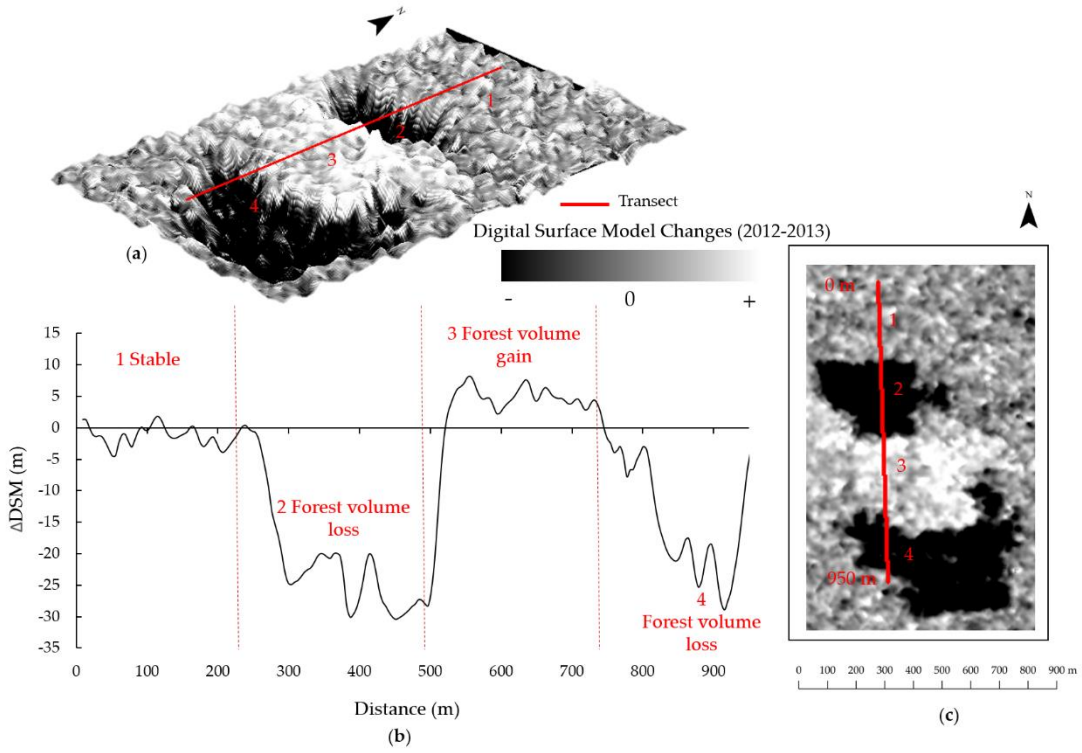

Figure 7. (**a**) Three-dimensional TanDEM-X ΔDSM representation showing changes along a 950 m transect across (1) undisturbed lowland forest, (2) forest volume loss, (3) forest volume gain and (4) forest volume loss. (**b**) Corresponding transect showing the magnitude of changes and (**c**) ΔDSM image illustrating the transect location.

The algorithm successfully extracted positive (green outline) and negative change objects (red outline) (Figure 8). Preliminary assessment shows that generally, negative change magnitude is higher compared to positive change and more clearly appreciable in high resolution optical imagery (Figure 8i and Figure 8ii).

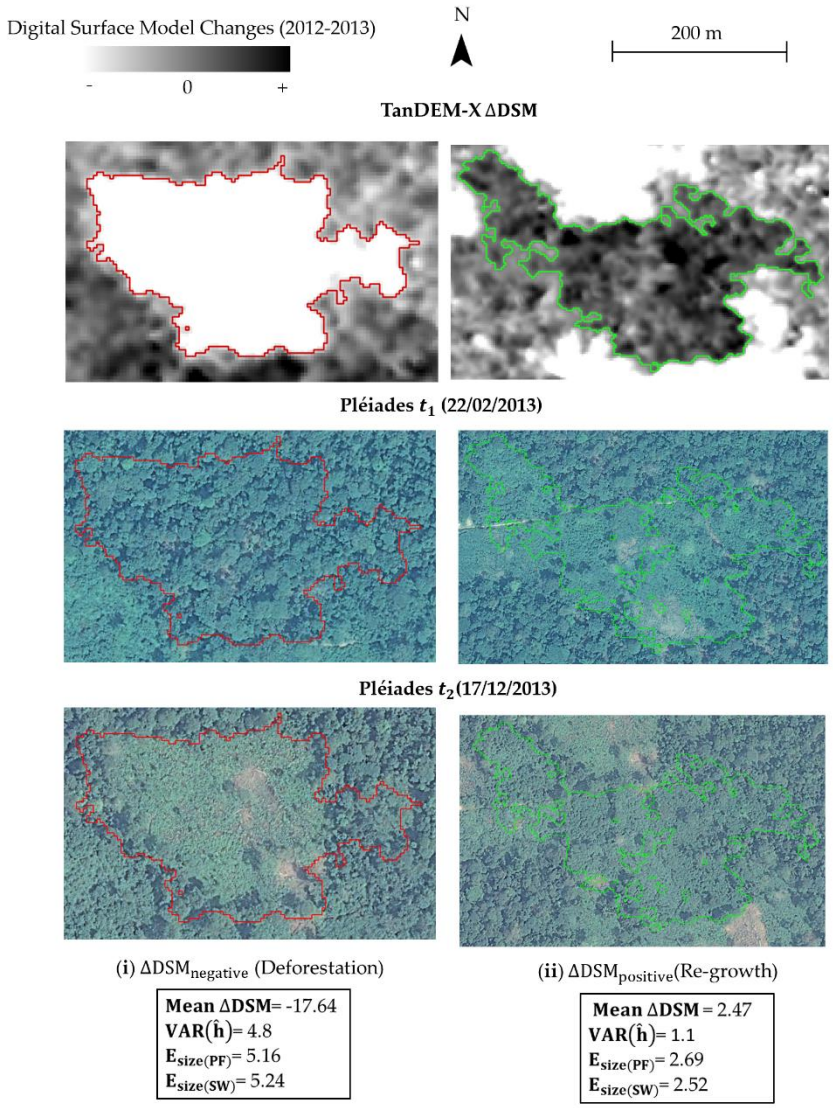

Figure 8. (**i**) $\Delta DSM_{negative}$ object (red) and (**ii**) $\Delta DSM_{positive}$ object (green) overlaid on the image and on two Pléiades scenes taken at t_1(22/02/2013) and t_2 (17/12/2013).

5.5.2. DSM Difference Magnitude and Area Statistics

The $\Delta DSM_{negative}$ objects magnitude distribution is very distinct from both the control areas (undisturbed lowland primary forest (PF_C) and swamp forest (SW_C) (Table 3). This indicates that the detected changes are caused by anthropogenic

disturbance. The magnitude distribution presents a thick tail (high kurtosis) (k= 10.9) and low median ($\tilde{x}$= -6.8 m) (Table 3), but with values beyond the lower quartile (Q_3) extending to -19.7 m. This pattern arises from the fact that these changes are due to continuous smooth transition from one forest state to the next, and only in a some cases (the extreme values in the distribution) by a single abrupt event indicating complete removal of vegetation (forest to non-forest conversion). The continuous transition can be given by the remnant forest patches or partial re-growth at t_2, and/or onset of forest disturbance at t_1. These different natural drivers of DSM change call for further investigation of the change statistic of related object properties, such as area.

The $\Delta DSM_{positive}$ magnitude distribution is less distinct from the control plots than $\Delta DSM_{negative}$ objects. However, the median ($\tilde{x}$= 2.4) and the quartiles (Q_1= 2.2 and Q_3= 2.6) are well separated from the respective values in the control plots distributions ($PF_C Q_1$= 0.9; $SW_C Q_1$= 0.8 and $PF_C Q_3$= 1.9; $SW_C Q_3$= 1.6).

The distribution of magnitude values is much wider for $\Delta DSM_{negative}$ objects (n= 4168) (deforestation/forest degradation) than for $\Delta DSM_{positive}$ objects (re-growth) (n= 772) (Figure 9). Overlap exists between the median of the changes and the values in the tails of the control distributions. Kurtosis for $\Delta DSM_{positive}$ objects (k = 2.5) is much lower compared to $\Delta DSM_{negative}$ objects (k = 10.9), which indicates that the distribution is more homogeneous given the presence of a lower amount of outliers.

Figure 9b and Figure 9c show boxplots presenting $\Delta DSM_{negative}$ objects (red) and $\Delta DSM_{positive}$ objects (green) by 10 area categories. The area distribution shows that the larger $\Delta DSM_{negative}$ objects have a higher change magnitude and smaller objects present a lower change magnitude. Instead for $\Delta DSM_{positive}$ objects there is no link between the magnitude of change and the object area.

For $\Delta DSM_{negative}$ objects the distribution in terms of area presents a much lower median ($\tilde{x}$= 0.16 ha) compared to $\Delta DSM_{positive}$ objects ($\tilde{x}$= 3.65 ha) and the mean object size is similarly smaller for $\Delta DSM_{negative}$ objects (0.28 ± 0.61 ha) compared to $\Delta DSM_{positive}$ objects (7.51 ± 14.32 ha).

Data in Table 3 reports kurtosis of the area distribution, which indicates the presence of a large number of outliers (thick tails) in the $\Delta DSM_{negative}$ area distribution (k= 272.34) compared to the relatively more evenly distributed areas for $\Delta DSM_{positive}$ objects (k= 63.01). The $\Delta DSM_{negative}$ area distribution is characterised by a high number of outliers, these being the result of two distinct processes: selective logging and shifting cultivation. Instead, the relatively more even-size distribution of $\Delta DSM_{positive}$ objects indicates that many areas can be associated with clusters of re-growth which are generally large in size. Small $\Delta DSM_{negative}$ objects down to 0.08 ha were detected as well as some very large scale clearing events (up to 14.85 ha), which are more likely to be deforestation.

$\Delta DSM_{positive}$ objects (re-growth) are more challenging to detect since the height variation range is narrower due to slow vegetation growth within 1 year (1.6 m ≤$\Delta DSM_{positive}$≤ 4.4 m) (Table 3). Moreover, there is less separation with the surrounding areas (lowland primary forest and swamp forest) (as shown by the comparison of magnitude values and the control plots in Table 3). It was therefore key to consider the spatial relationship (neighbourhood distance) between $\Delta DSM_{positive}$ objects and $\Delta DSM_{negative}$ objects to improve post-disturbance re-growth detection (section 5.5.7).

The control areas can be considered stable (especially old growth forests which have reached climax indicating a biological steady state) (Hartshorn, 1980) but present a natural variability due to canopy unevenness and due to the presence of treefall gaps or seasonality (leaf on/leaf off).

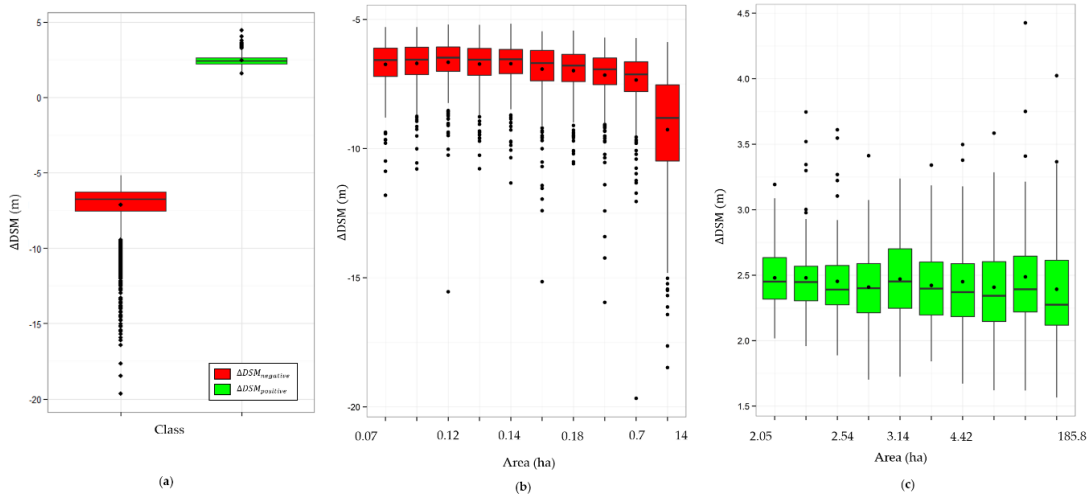

Figure 9. (**a**) Mean $\Delta DSM_{negative}$ objects boxplots (red) (n= 4168) and mean $\Delta DSM_{positive}$ objects boxplots (green) (n= 772). (**b**) Mean $\Delta DSM_{negative}$ objects by 10 area categories and (**c**) mean $\Delta DSM_{positive}$ objects (green) by 10 area categories.

Table 3. $\Delta DSM_{negative}$ objects (n= 4168), $\Delta DSM_{positive}$ objects (n= 772), lowland primary forest (PF_C) (n= 510) and swamp forest (SW_C) (n= 1161) magnitude and area statistics (mean ± standard deviation: $\mu \pm \sigma$; median: $\tilde{x}$; kurtosis: k; minimum: Min; maximum: Max; lower quartile: Q_1 and upper quartile: Q_3.

ΔDSM magnitude (m)							
Object	$\boldsymbol{\mu \pm \sigma}$	$\boldsymbol{\tilde{x}}$	$\boldsymbol{k}$	**Min**	**Max**	$\boldsymbol{Q_1}$	$\boldsymbol{Q_3}$
$\boldsymbol{PF_C}$	1.5 ± 0.8	1.3	0.6	0.05	4.6	0.9	1.9
$\boldsymbol{SW_C}$	1.2 ± 0.6	1.2	2.7	0.02	4.8	0.8	1.6
$\boldsymbol{\Delta DSM_{negative}}$	-7.1 ± 1.4	-6.8	10.9	-19.7	-5.2	-7.5	-6.3
$\boldsymbol{\Delta DSM_{positive}}$	2.4 ± 0.3	2.4	2.5	1.6	4.4	2.2	2.6
ΔDSM Area (ha)							
$\boldsymbol{\Delta DSM_{negative}}$	0.28 ± 0.61	0.16	272.34	0.08	14.85	0.12	0.23
$\boldsymbol{\Delta DSM_{positive}}$	7.51 ± 14.32	3.65	63.01	2.05	185.8	2.66	6.38

5.5.3. Accuracy of DSM Difference Estimates

Estimates of the mean ΔDSM objects, sorted by increasing value and associated confidence limits at 95% and 68% confidence level (CL) are shown in Figure 10. The confidence limits are defined as ± t × Standard Error of the Mean (SEOM), with Student t-test (t= 1 for 68% CL and t= 0.96 for 95% CL), since the degrees of freedom are greater than 200.

The confidence limits characterise the accuracy of the ΔDSM estimates within the detected objects achieved by the proposed method. However, it is important to notice that these estimates do not correspond to a measure of vegetation physical properties, such as tree heights. They correspond to a change of the scattering physical phenomena, these being, for instance, a decrease or increase in the PCH, or the combined influence of the volume and surface scattering. Therefore, in the perspective of change detection, the importance of the confidence limits should be considered more in connection with the possibility of achieving enough accuracy in order to be able to separate true changes from noise. This is further assessed by an effect size index (section 5.5.4).

Analysis of the SEOM indicates that, in the case of $\Delta DSM_{negative}$ objects, the SEOM is linearly dependent on the mean values, with a coefficient of proportionality equal to 0.4 and a maximum deviation of 10 m (Figure 10). Instead, for $\Delta DSM_{positive}$ objects the SEOM is fairly constant with respect to the mean values, this being related to lower range of the mean $\Delta DSM_{positive}$ values (from 1.6 m to 4.4 m) and the higher homogeneity of the samples within the objects (Table 3).

SEOM statistics are reported in Table 4. SEOM for $\Delta DSM_{negative}$ shows greater variability with several outliers (high kurtosis) (k= 30.41) (Table 4). This is due to the DSM variability within objects depending on two processes: complete removal of vegetation (deforestation) and partial loss of forest cover (forest degradation) where the former results in a larger change compared to the latter. Instead, lower SEOM variability is observed for $\Delta DSM_{positive}$ objects (k= 14.39).

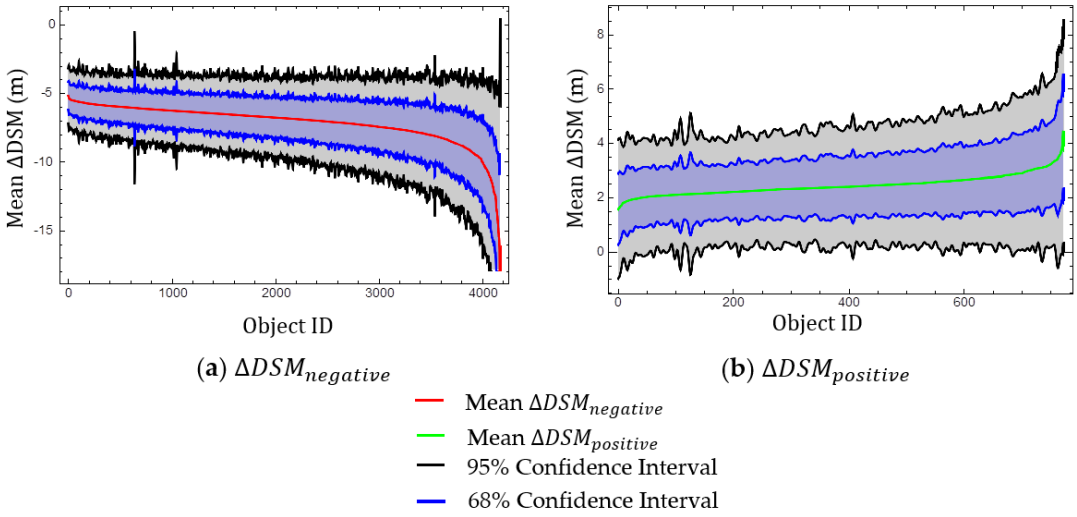

Figure 10. (**a**) Mean $\Delta DSM_{negative}$ objects magnitude (red) and associated confidence intervals (CI) ± 68% (blue) and ± 95% (black). (**b**) Mean $\Delta DSM_{positive}$ objects magnitude (green) and associated confidence intervals (CI) ± 68% (blue) and ± 95% (black).

Table 4. Standard error of the mean (SEOM ($SD(\hat{h})$) statistics (mean ± standard deviation: $\mu \pm \sigma$ (m); median: $\tilde{x}$ (m); lower quartile: Q_1; upper quartile: Q_3 and kurtosis: k for $\Delta DSM_{negative}$ objects (N= 4168) and $\Delta DSM_{positive}$ objects (N= 772).

Class	$\mu \pm \sigma$	$\tilde{x}$	Q_1	Q_3	k
$\Delta DSM_{negative}$	1.74 ± 0.72	1.55	1.3	1.97	30.41
$\Delta DSM_{positive}$	1.19 ± 0.27	1.14	1.02	1.31	14.39

5.5.4. Effect Size

Effect size (E_{size}) indices, based on the standardised difference of means, were calculated to assess the significance of the changes in comparison to two stable areas: undisturbed lowland primary forest (PF_C) and swamp forest (SW_C). E_{size} statistics are reported in Figure 11 and Table 5.

E_{size} between $\Delta DSM_{negative}$ objects and PF_C ranges from 0.84 to 7.26 ($\mu \pm \sigma$: 5.2 ± 0.69) and for SW_C ranges from 0.86 to 7.99 ($\mu \pm \sigma$: 5.58 ± 0.84). The results indicate that deforestation/degradation changes are highly significant (98% changes with

E_{size} ≥ 1.5) and can be considered well above the intrinsic noise within the two control areas representing natural forest variability. It is to be noted that there is one outlier with E_{size} < 1.5 in the $\Delta DSM_{negative}$ dataset.

E_{size} for $\Delta DSM_{positive}$ objects compared to PF_C ranges from 0.73 to 3.41 ($\mu \pm \sigma$: 2.53 ± 0.4) and from 0.67 to 3.16 ($\mu \pm \sigma$: 2.36 ± 0.38) compared to SW_C. This statistic also indicates that changes are highly significant (98% change with E_{size} ≥ 1.5) but on average E_{size} values are smaller and more outliers are present with respect to $\Delta DSM_{negative}$. Notice that outliers (E_{size} < 1.5) were removed from $\Delta DSM_{negative}$ objects (n= 1) and from $\Delta DSM_{positive}$ objects (n= 17) for further analysis.

E_{size} sorted by increasing values is reported in Figure 12. $\Delta DSM_{negative}$ objects and the associated 95% confidence interval (CI) is shown in Figure 12a (compared to PF_C) and in Figure 12b (compared to SW_C). While, E_{size} for $\Delta DSM_{positive}$ objects and the associated ± 95% CI is shown in Figure 12c and Figure 12d. Table 6 reports statistics (mean, minimum and maximum) of the resulting 95% CI values for PF_C ($\Delta DSM_{negative}$: μ= 0.67 and $\Delta DSM_{positive}$: μ= 0.085). Comparison with the swamp forest control plot (SW_C) is similar ($\Delta DSM_{negative}$: μ= 0.71 and $\Delta DSM_{positive}$: μ= 0.083).

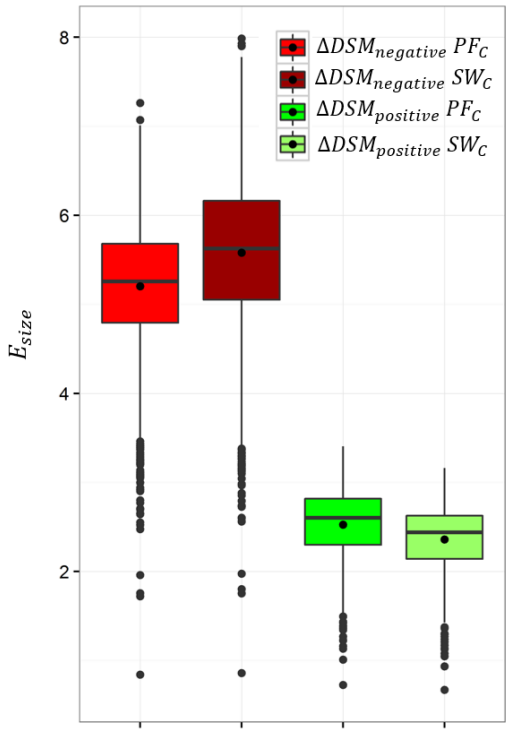

Figure 11. Effect size of objects $\Delta DSM_{negative}$ (red shades) and $\Delta DSM_{positive}$ objects (green shades) with respect to two control plots: lowland primary forest (PF_c) and swamp forest (SW_C).

Table 5. Effect size (E_{size}) statistics for $\Delta DSM_{negative}$ objects (N= 4168) against control plots and for $\Delta DSM_{positive}$ objects (N= 772) against control plots (PF_C and SW_C).

ΔDSM	$\mu \pm \sigma$	$\tilde{x}$	Min	Max	Q_1	Q_3
PF_C						
$\Delta DSM_{negative}$	5.2 ± 0.69	5.26	0.84	7.26	4.79	5.68
$\Delta DSM_{positive}$	2.53 ± 0.4	2.60	0.73	3.41	2.3	2.82
SW_C						
$\Delta DSM_{negative}$	5.58 ± 0.84	5.63	0.86	7.99	5.05	6.16
$\Delta DSM_{positive}$	2.36 ± 0.38	2.44	0.67	3.16	2.14	2.63

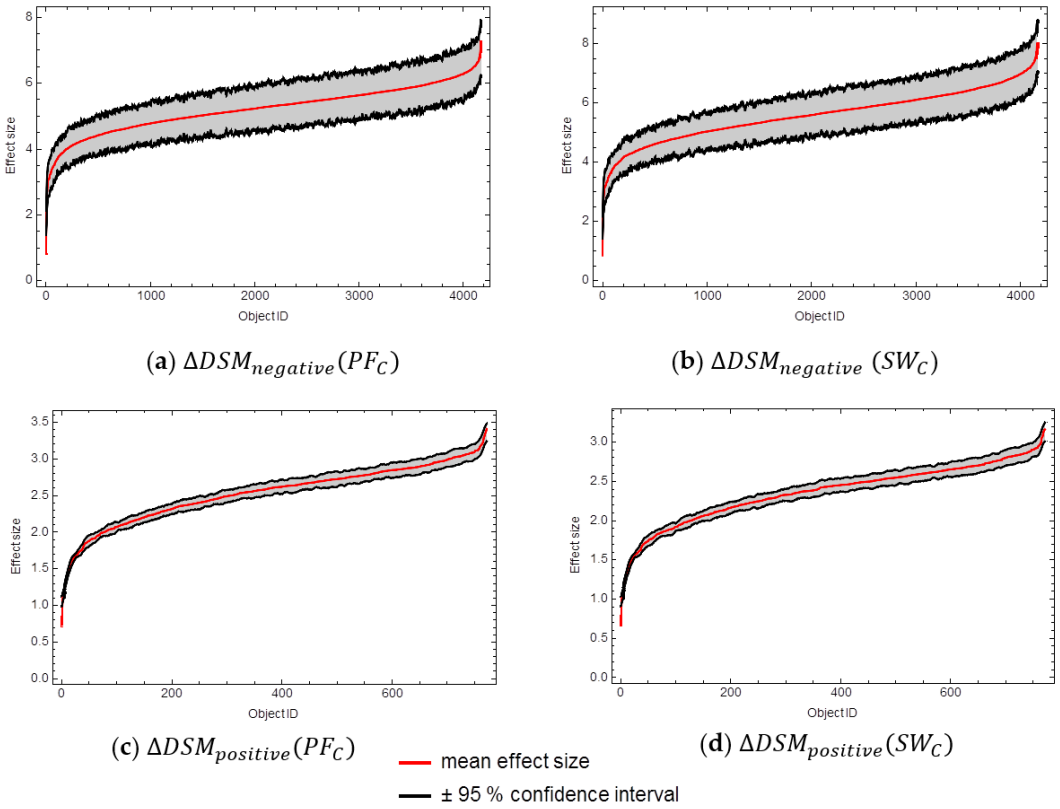

(**a**) $\Delta DSM_{negative}(PF_C)$ (**b**) $\Delta DSM_{negative}$ (SW_C)

(**c**) $\Delta DSM_{positive}(PF_C)$ (**d**) $\Delta DSM_{positive}(SW_C)$

Figure 12. Mean effect size (red) ± 95% confidence interval (black) for $\Delta DSM_{negative}$ objects compared to (**a**) lowland primary forest control plot (PF_c) and (**b**) swamp forest control plot (SW_C). Mean effect size (red) ± 95% confidence interval (black) for $\Delta DSM_{positive}$ objects compared to (**c**) lowland primary forest control plot (PF_C) and (**d**) swamp forest control plot (SW_C).

Table 6. Statistics of the ± 95% confidence interval (CI) for $\Delta DSM_{negative}$ objects (N= 4168) and control plots and for $\Delta DSM_{positive}$ objects (N= 772) and two control plots (PF_C and SW_C).

	$\boldsymbol{\mu}$	Min	Max
$\boldsymbol{\Delta DSM_{negative}\,(PF_C)}$	0.67	0.06	1.18
$\boldsymbol{\Delta DSM_{negative}\,(SW_C)}$	0.71	0.06	1.27
$\boldsymbol{\Delta DSM_{positive}\,(PF_C)}$	0.085	0.01	0.14
$\boldsymbol{\Delta DSM_{positive}\,(SW_C)}$	0.083	0.01	0.13

5.5.5. Dependence of ΔDSM Estimates on Sensor's Parameters

Based on the modelling approach outlined in section 5.4.9, estimate of the impact on ΔDSM of different baselines between the two acquisitions is reported here.

In the case of the random volume only, ΔDSM was computed from Equation 23 as a function of extinction and parameterised by random volume height (Figure 13). The maximum difference is in the order of -1 m (decrease in PCH), and occurs for low extinction and 50 m volume height (red line in Figure 13). The -1 m difference corresponds to the mean of the distribution of samples taken within the primary lowland forest control area. Therefore, ΔDSM within a stable forest area can be affected in this order of magnitude by difference in instrumental parameters.

For increasing extinction, the PCH moves towards the top of the volume, and the dependence on interferometers sensitivity (β_z) decreases, resulting in lower or negligible ΔDSM. The same effect occurs for a lower volume height (30 m) (green line in Figure 13), where for all extinction values the range of ΔDSM is reduced to only a fraction of meter.

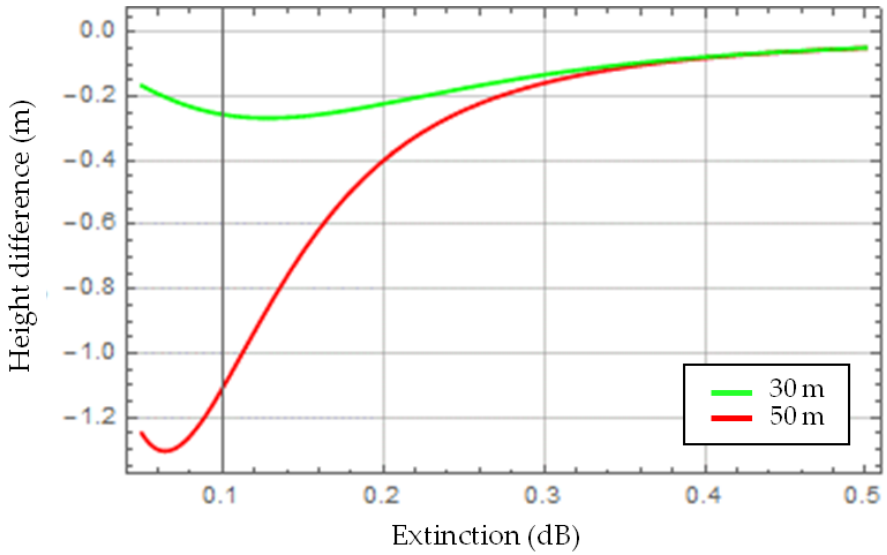

Figure 13. DSM height difference (m) between two observations as a function of extinction (dB) for a volume height of 30 m (green) and 50 m (red).

In the case of the RVoG model, ΔDSM height difference was computed from Equation 23 (but using the model in Equation 24) as a function of the surface to

volume scattering ratio (μ), for a volume height equal to 30 m and parameterised by two extinction values: 0.05 dB (red) and 0.3 dB (green) (Figure 14).

With lower extinction (0.05 dB), the PCH is set around the middle of the volume (15 m), and there is low dependence on β_z for small surface scattering component (small negative DSM difference). However, when the surface component weighs in more, the DSM difference becomes positive and increases. This indicates that for a sparser forest an increase in DSM can be due to the influence of ground return, and it is proportional to this return.

For higher extinction, when the PCH is pushed towards the top of canopy, the DSM difference becomes larger and negative (up to - 1 m) when the surface contribution is small. However, it is pushed to positive values when the surface component starts to weigh in, reaching an asymptotic difference of approximately 1.5 m.

We can conclude from the analysis that the range of DSM differences related to instrumental parameters is of the order of ± 1 m, with the positive values due to the influence of surface return.

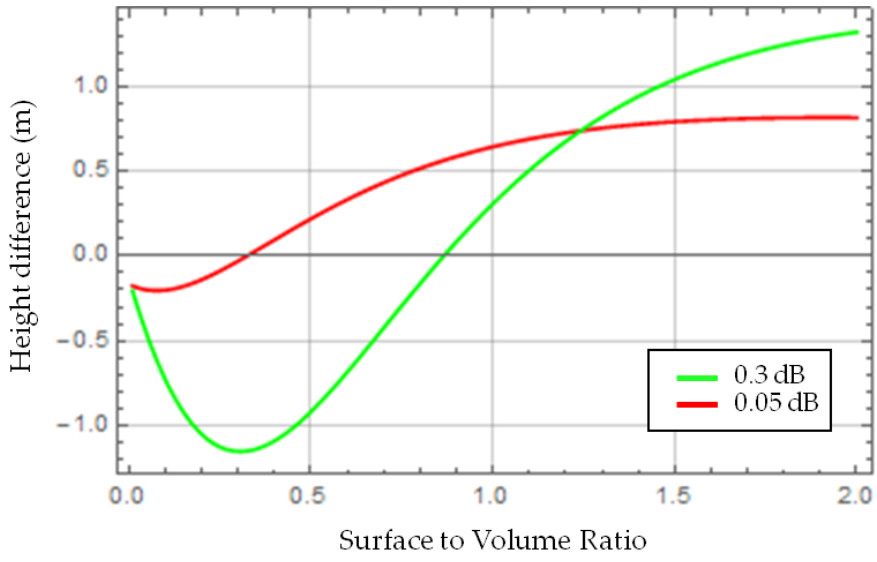

Figure 14. DSM height difference as a function of the surface to volume scattering ratio and parameterised by extinction: 0.05 dB (red) and 0.3 dB (green).

5.5.6. Negative Change Objects Refinement Based on Magnitude and Area Properties

Investigation related to the magnitude of change and size of objects was carried out by partitioning the $\Delta DSM_{negative}$ dataset into two subsets (A and B) by setting specific thresholds in term of $\Delta DSM_{negative}$ objects magnitude and area properties.

The reason behind this was to improve the likelihood of detecting "true" changes due to small scale shifting agriculture and separate them from possible changes due to selective logging.

A noticeably large proportion of the objects detected were ≤ 100 TanDEM-X pixels (≤ 0.2 ha), these being located primarily inside a logging concession.

Threshold choice was based on statistical evaluation of randomly selected $\Delta DSM_{negative}$ objects (n= 382) located within the Ngombé logging concession. A threshold related to the size of the object was selected by choice of the 3rd quartile of the distribution (representing the upper 75th of the distribution) (Q_3= 100 TanDEM-X pixels) and the magnitude threshold was similarly based on the 3rd quartile (Q_3= -7 m).

Subset A was defined as objects which satisfied both area ≤ 100 TanDEM-X pixels AND $|\Delta DSM_{negative}|$ ≤ 7 (Figure 15). While, subset B consisted of objects that satisfied the area threshold (> 100 TanDEM-X pixels) but not necessarily the change magnitude threshold. The reason behind the criteria chosen is that the larger objects (> 100 pixels) are more likely to be "true" anthropogenic clearings even if $|\Delta DSM|$ is ≤ 7 m. This is because a large area, if only partially cleared, will present a lower change magnitude compared to an area which is completely deforested. This effect was also verified by visual inspection of VHR optical imagery, where a set of disturbance objects corresponded to complete clearing and others where vegetation was only partially removed hence the lower mean magnitude change.

Figure 15 reports boxplots for subset A and B and Table 7 reports the associated magnitude and area statistics. Further analysis was undertaken by considering only subset B, since these objects were more likely to be due to anthropogenic deforestation/forest degradation linked to shifting cultivation (rather

than due to selective logging, noise, shadowing effect or linked to seasonality). These objects were also more suitable for the analysis aimed at extracting post-disturbance re-growth (see section 5.5.7). Subset A objects were considered "true" changes compared to the control plots (see section 5.5.4), but the origin of these changes requires further investigation.

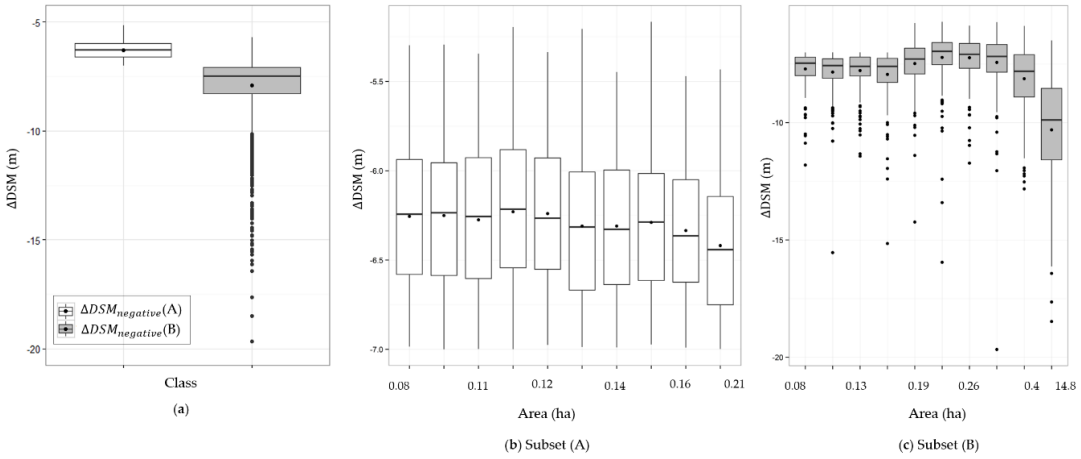

Figure 15. $\Delta DSM_{negative}$ subset A (n= 2030) (white) and $\Delta DSM_{negative}$ subset B (n= 2137) (grey) boxplots illustrating (**a**) $\Delta DSM_{negative}$ magnitude (m); (**b**) $\Delta DSM_{negative}$ subset A binned into 10 area categories and (**c**) $\Delta DSM_{negative}$ subset B binned into 10 area categories.

Table 7. $\Delta DSM_{negative}$ subset A (n= 2030) and B (n= 2137) magnitude (m) and area (ha) statistics (mean ± standard deviation: $\mu \pm \sigma$; median: $\tilde{x}$; minimum: Min; maximum: Max; upper quartile: Q_1; lower quartile: Q_3 and kurtosis: k.

$\Delta DSM_{negative}$ magnitude (m)							
Subset	$\mu \pm \sigma$	$\tilde{x}$	**Min**	**Max**	Q_1	Q_3	k
A	-6.3 ± 0.4	-6.3	-7	-5.2	-6.6	-6	-0.8
B	-7.9 ± 1.5	-7.5	-19.7	-5.7	-8.3	-7.1	8.8
$\Delta DSM_{negative}$ area (ha)							
Subset	$\mu \pm \sigma$	$\tilde{x}$	**min**	**max**	Q_1	Q_3	k
A	0.14 ± 0.03	0.13	0.08	0.21	0.11	0.16	-0.49
B	0.41 ± 0.83	0.23	0.08	14.85	0.15	0.35	146.49

5.5.7. Distance between Positive and Negative Objects

The spatial location of $\Delta DSM_{positive}$ objects can be used to infer probability of false detection. $\Delta DSM_{positive}$ objects located in areas of swamp forest as indicated by visual inspection of the FACET map (OSFAC, 2012), or located in relatively isolated areas not in proximity of road networks or logging roads, were deemed likely to be false detections and not related to re-growth after disturbance. The distance between $\Delta DSM_{positive}$ and $\Delta DSM_{negative}$ subset B was taken as a condition to confirm the onset of post-disturbance re-growth following shifting cultivation.

The distribution of minimum distance between $\Delta DSM_{positive}$ objects (n= 755) and $\Delta DSM_{negative}$ subset B (n= 2137) is shown in Figure 16 and ranges from 34 m to 2544 m (742 ± 542 m) (blue distribution).

The threshold selection is based on the minimum distance distribution shown in Figure 16 (blue). The distribution (estimated by a smoothed histogram) is multi-modal (blue). Fitting a Gaussian function around the first mode (short distance) gives a mean value of 300 m and standard deviation of 200 m (red). Objects with a distance below the 3rd quartile of the normal distribution (d< 500 m) are retained as post-disturbance re-growth ($\Delta DSM_{positive}$ subset B).

The summary statistics from the two subsets corresponding to $d \geq 500$ m (subset A) and $d < 500$ m (subset B) are shown in Table 8. Subset A (n= 428) minimum distance ranged from 501 m to 2544 m (mean ± standard deviation: 1095 ± 467 m). While, subset B (n= 327) minimum distance ranged from 34 m to 497 m (mean ± standard deviation: 278 ± 119 m). Further analysis was undertaken by considering only subset B. Subset B magnitude changes ranged from 1.6 m to 4.4 m (mean ± standard deviation: 2.6 ± 0.4 m) and area ranging from 2.07 ha to 185.8 ha (8.88 ± 18.11 ha). Figure 17 shows the final change map after the analysis refinement based on magnitude, area and distance thresholds.

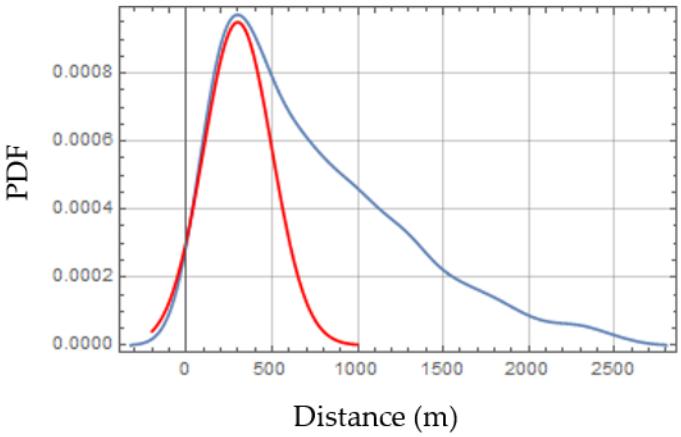

Figure 16. Minimum distance (m) between $\Delta DSM_{positive}$ objects and $\Delta DSM_{negative}$ objects multi-modal distribution (blue) (estimated by a smoothed histogram) (dataset A+B). A normal distribution (red) is fitted around the first mode at 300 m. Objects with a distance within the 3rd quartile of the normal distribution (d< 500 m) are considered further as post-disturbance re-growth while objects with d≥ 500 m are discarded.

Table 8. Minimum distance (m) statistics between $\Delta DSM_{positive}$ objects centroids (N= 755) and $\Delta DSM_{negative}$ objects centroids (N= 2137) for subset A (n= 428) and subset B (n= 327).

Dataset	Min	Q_1	$\tilde{x}$	$\mu \pm \sigma$	Q_3	Max
A+ B	34	304	610	742 ± 542	1052	2544
A	501	712	988	1095 ± 467	1342	2544
B	34	182	265	278 ± 119	385	497

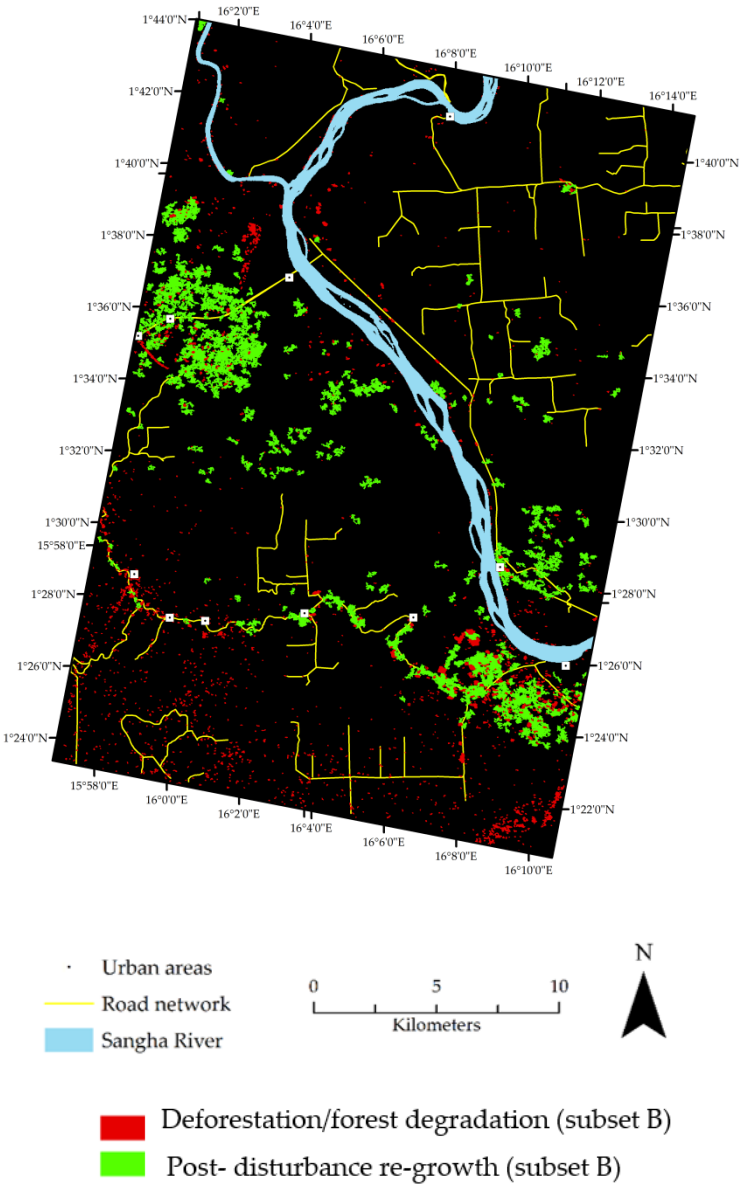

Figure 17. Change map showing TanDEM-X $\Delta DSM_{negative}$ objects (deforestation/forest degradation) (red) (subset B) and $\Delta DSM_{positive}$ objects (post-disturbance re-growth) (subset B) (green).

5.6. Validation

Validation of $\Delta DSM_{negative}$ objects by comparison with optical imagery is detailed below. For validation we used the refined $\Delta DSM_{negative}$ subset B. 78 out of the 89 disturbed areas delineated manually (DEF/DEG) using two Pléiades imagery intersected (some only partially) the TanDEM-X change objects (87.6%) while, 11

objects (12.3%) were not intersected. A sample of DEF/DEG objects ranging from 0.2 ha to 2.1 ha that were detected by both TanDEM-X and Pléiades imagery (red) are shown in Figure 18.

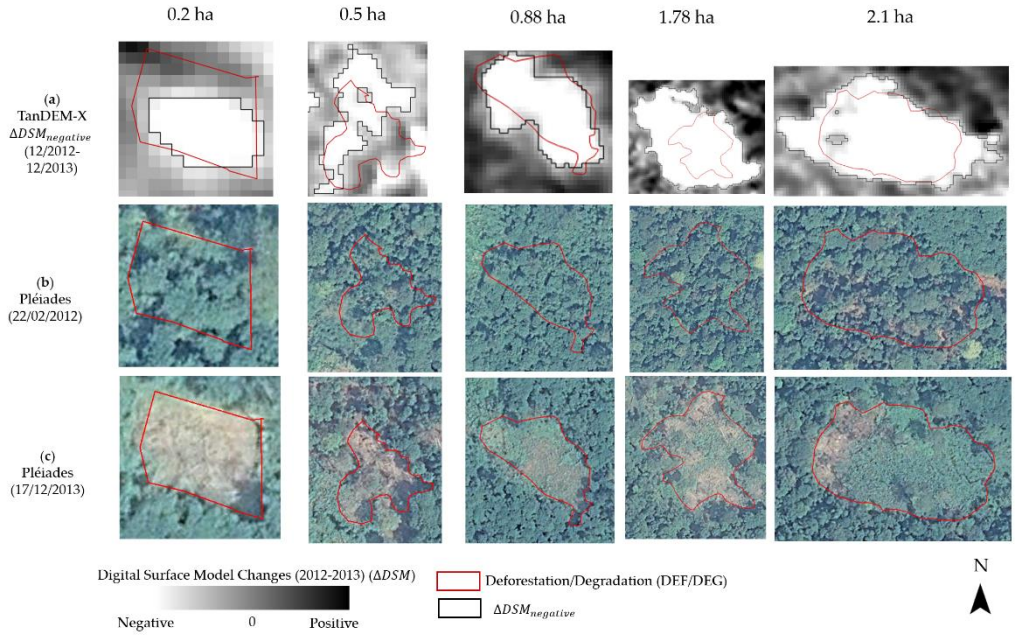

Figure 18. Sample of manually delineated deforestation/forest degradation objects (DEF/DEG) (red) detected by both TanDEM-X change detection and Pléiades overlaid on (**a**) ΔDSM image (extracted changes outlined in black); (**b**) Pléiades at t_1 (22/02/2012) and (**c**) Pléiades at t_2 (17/12/2013).

5.7. Discussion and Interpretation

5.7.1. Negative and Positive Change Objects Magnitude and Area

Our approach was not aimed at quantifying the absolute vegetation height changes because a PCH shift cannot be directly linked to a change of vegetation height since it is influenced by a range of variables (e.g. vegetation horizontal structure or canopy density) and it is not a one-to-one relationship with a single bio-physical parameter. The estimation of forest height by InSAR phase requires the availability of a DTM (seldom available in tropical forest) in combination with the TanDEM-X DSM. In principle, height could be estimated using P-band SAR tomography, a technique that exploits multi-baseline data to slice the volume and

estimate the vertical structure function (Papathanassiou, et al., 2016). This technique could also provide estimates of AGB based on the sliced HV backscatter (Minh, et al., 2014). However, these approaches are at the moment still limited to ad-hoc experiments using airborne Pol-InSAR instruments.

Our approach seeks to give a relative estimate of change within 1 year and to spatially map areas of change without the use of an auxiliary DTM which was not available and would have only covered a fraction of the study site. The advantage of the approach is that it is computationally simple, requires only single-polarisation, single-baseline InSAR acquisitions, but at the same time it is statistically robust. Issues related to the findings are discussed next.

The PCH shift between two dates are much lower (mean ± standard deviation: 2.4 ± 0.3 m) for $\Delta DSM_{positive}$ objects (re-growth) in comparison to abrupt $\Delta DSM_{negative}$ events (deforestation/forest degradation) (mean ± standard deviation: -7.1 ± 1.4 m) (Table 3) and consequently, more challenging to detect.

In terms of species composition following disturbance, the Congo Basin is often dominated by monospecific *Musanga cecropides* appearing as a continuous and homogeneous layer (Lebrun & Gilbert, 1954) with growth rates in the range of up to 15 m in 3 years (Mayaux, et al., 1999). Considering a scenario dominated by monospecific *Musanga cecropides* post-disturbance re-growth, we would expect plots with maximum tree height increase in the range of 5 m/year. Our analysis shows average $\Delta DSM_{positive}$ magnitude about half those values (2.4 ± 0.3 m). This apparent discrepancy is due to the fact that the $\Delta DSM_{positive}$ magnitude estimates provided by TanDEM-X do not correspond to single tree height differences but to phase center differences, these being dependent on penetration depth at X-band in sparser vegetation (hence lower PCH sensitivity to forest volume for sparser vegetation) and on sensor's parameters.

Mean $\Delta DSM_{negative}$ objects magnitude ranges from -19.7 m to -5.2 m (Table 3) which suggests a gradient of vegetation removal. A possible reason for this can be linked to short fallow cycle within slash-and-burn agriculture, and frequent use of

the same areas, which means that vegetation is usually not able to recover to pre-disturbance levels (Chazdon, 2003) and hence trees do not reach significant height.

Large $\Delta DSM_{negative}$ objects that present high magnitude change can be undoubtedly linked to primary forest conversion to non-forest (deforestation) for agriculture. While, smaller and lower magnitude $\Delta DSM_{negative}$ objects (subset A) (between -7 and 0 m and area below 100 pixels) are more likely to be the result of other disturbance drivers (e.g. selective logging). 98% of all $\Delta DSM_{negative}$ objects extracted (including those < 100 TanDEM-X pixels) were significantly different from the control areas (as shown by the effect size index results) (section 5.5.4) indicating that they are in all likelihood genuine deforestation/forest degradation events and not false detections. Even small-scale disturbance (down to 0.08 ha) (subset A) (Table 7) were significant but these could not be validated using Pléiades data.

$\Delta DSM_{negative}$ objects (subset B) were considered most likely deforestation/degradation due to shifting agriculture. The area was 0.41 ± 0.83 ha (mean ± standard deviation) (N= 2137) with validated objects area by comparison with Pléiades data equal to 0.75 ± 1.04 ha (mean ± standard deviation) (Figure 18) proving unambiguous evidence.

$\Delta DSM_{positive}$ objects area (subset B) associated with post-disturbance re-growth was 8.88 ± 18.11 ha (mean ± standard deviation) (N= 327) consisting of multiple vegetation successional growth stages clustered together (Figure 8).

The larger area for $\Delta DSM_{positive}$ objects is due to the fact that areas that were identified as a single re-growth event are effectively a combination of more re-growth stages which have developed, for instance at different times (e.g. over many years of shifting cultivation practices); but because of the limited changes in growth within 1 year these events are clustered into a single object by the morphological algorithm since it aims to group together pixels which present similar spatially contiguous values (Wolfram, 2016). The $\Delta DSM_{positive}$ objects extracted can be defined as rural-complex, an area where a mix of secondary forest, degraded forest and fallow fields have been re-growing for a significant amount of time already (Laporte, et al., 2004).Considerations on the area extent of post-disturbance re-

growth events and how the different successional stages can be separated requires further investigation. At this stage we can predict that a DSM time-series combined with textural (structural) analysis within each object (multi-temporal spatial statistics) could provide means to partition re-growth stages that in our implementation are merged into a single object.

The standard error of the mean (SEOM) and associated confidence limits characterise the accuracy of the ΔDSM estimates within the detected objects achievable by our method. However, it is important to notice that these estimates do not correspond to measures of vegetation physical properties, such as tree height. These correspond to a change in the physics of the scattering phenomena, these being for instance a decrease or increase in the PCH, or the combined influence of the volume and surface scattering. Therefore, the importance of these confidence limits should be considered related to the possibility of achieving sufficient accuracy to be able to separate true change from noise. This was further assessed by an effect size index (see section 5.5.4).

Effect size (E_{size}) was used to assess the significance of change objects with respect to two no-change control plots. The choice of an effect size index as opposed to a significance t-test was advantageous since this index reports the magnitude of difference between two groups (change and no-change) (Sullivan & Fein, 2012) as opposed to a test of significance that only checks the hypothesis of a mean value being greater. In the context of change detection, the effect size can be interpreted in terms of Type I error, as explained in section 5.4.6.

The average E_{size} for $\Delta DSM_{negative}$ objects is 5.2 ± 0.69 (PF_C); 5.58 ± 0.84 (SW_C) and 2.53 ± 0.4 (PF_C), 2.36 ± 0.38 (SW_C) for $\Delta DSM_{positive}$ objects. E_{size} was ≥ 1.5 for 98% of $\Delta DSM_{negative}$ objects and for 98% of $\Delta DSM_{positive}$ objects.

$\Delta DSM_{positive}$ objects effect size values are lower than those from the $\Delta DSM_{negative}$ case because of the time elapsed between the two TanDEM-X dates (1 year) is short with respect to the time-scale at which vegetation re-growth occurs. This process would take several decades to achieve changes comparable deforestation/forest degradation in terms of magnitude (e.g. in the range of 10-20 m

for clear cuts for instance). This is confirmed by the statistics of the $\Delta DSM_{positive}$ objects which have a lower magnitude (on average half the magnitude of $\Delta DSM_{negative}$) as reported in Table 3.

This does not imply that all objects detected are either deforestation/forest degradation or re-growth but it suggests that detected objects are statistically separable compared to stable forest areas. The link behind the change was established by validating a sample of $\Delta DSM_{negative}$ objects using high-resolution Pléiades imagery while the $\Delta DSM_{positive}$ objects were not validated.

5.7.2. Factors Influencing DSM Change Magnitude

The estimated DSM changes are inevitably influenced by various errors (noise), in addition to changes in the characteristics of the forest (deforestation/forest degradation or re-growth). More precisely, we address here the problem of identifying sources of PCH changes occurring even if the forest is stationary (i.e. within the boundaries of natural variability). We can summarise parameters affecting the PCH into four categories: (a) forest vertical structure and spatial distribution when in a stationary situation within the sampling time; (b) environmental conditions (seasonality and rainfall); (c) instrument related (baseline, incidence angle and range distances differences between acquisitions) and (d) phase noise.

a) Forest vertical structure and spatial distribution (forest density):

PCH location is dependent on the forest density, which in turn is related to extinction for wave scattering. PCH moves closer to the ground for sparser forest due to canopy gaps or if the canopy is clumped together leaving gaps enabling greater signal penetration (Treuhaft, et al., 2015) and increased contribution from surface scattering. In the present work, forest density was considered high (highest density and homogeneity is found in swamp forest) but decreasing for degraded forest. Vegetation density and gaps might have also influenced the DSM (and as a consequence ΔDSM) since, in particular in old-growth primary forest the presence of large emergent trees cast shadows on the

surrounding vegetation, thus modulating the local extinction and incidence angle. Shadowing effects were noticed in interferometric coherence derived from airborne sensors over tropical forest (Hoekman & Varekamp, 2001).

b) Environmental conditions (seasonality and rainfall):

Seasonality effects can be considered negligible in the tropical evergreen forests of the Congo Basin (as opposed to temperate and boreal forest where leaf-off condition leads to higher penetration within the canopy and consequently lowers the PCH) (Praks, et al., 2012).

We also hypothesise that smaller changes (change magnitude between 0 and -7 m and area ≤ 100 pixels) (subset A in could be linked to disturbance due to damage from selective logging or to seasonality (e.g. transition from leaf on/leaf off conditions) which have been observed in the study area (Gond, et al., 2013). The study area falls within the so-called Sangha River Interval (located between 14-18° E covering a 400 km wide area) which is reported to host semi-deciduous forest presenting high photosynthetic activity and low endemism (Maley, 2002; Gond, et al., 2013). In this area, some trees at least could have more leaves at one date - through both scenes were captured in the same season (dry season, both December).

The effect of rainfall was considered minimal in the study since both the datasets were acquired in December (dry season) (Philippon, et al., 2016; World Bank, 2016) which in the Congo Basin is relatively weak. Rainfall 48 h before the data acquisition was low (t_1= 0 mm and t_2= 7.6 mm) (GIOVANNI, 2016) (Table 1).

The exact reason and influence of the above-mentioned parameters on the changes detected cannot be fully explained nor validated with a high degree of confidence using VHR optical data and requires further information related to logging operations in the area. We do not exclude the link to natural die-back of trees damaged during past logging operations or recent legal/illegal logging especially as these changes are mostly located inside the Pokola and Ngombé

logging concessions (supposedly currently inactive) exploited in the past between 1960-1999 (and in some areas between 2000-2008) (Mertens, et al., 2011) so usually in proximity to old logging roads. There are currently no studies in semi-deciduous tropical forests similar to those in the Congo Basin using TanDEM-X so this does not enable a clear conclusion to be drawn to support the influence of seasonality.

c) Sensor's parameters (baseline, incidence angles and range distances):

Baseline differences could have affected the resulting changes and this can be attributable to the sensitivity of the interferometer. Baselines from the TanDEM-X acquisitions used for the analysis were 95.3 m ($TDXt_1$) and 52 m ($TDXt_2$) resulting in higher precision for the former dataset. The acquisitions were chosen among those provided by DLR to ensure the most similar acquisitions based on seasonality (dry season) and similarity between acquisition parameters (incidence angle).

A modelling approach (see section 5.5.5) was used to assess the impact of different baseline choice, incidence angles and range distance on the resulting change estimates of the same natural targets. The maximum difference is of the order of 1 m (decrease in PCH), and occurs for lower extinction and 50 m volume height. Notice that a -1 m difference corresponds to the mean of the distribution of samples taken within the primary forest control area. Therefore, DSM changes within a stable forest area can be ascribed to differences in instrumental parameters.

d) Phase noise:

Phase noise, estimated from the absolute volume of the coherence, was accounted for as one component in the error propagation affecting the estimate of the SEOM (section 5.5.3).

5.7.3. Deforestation, Forest Degradation and Re-growth Spatial Patterns

TanDEM-X DSM object-based change detection enables both positive and negative PCH shifts to be mapped and consequently the spatial relationship between the two processes can be inferred. This capability was exploited to increase the likelihood of the $\Delta DSM_{positive}$ objects to effectively belong to post-disturbance re-growth occurring after shifting cultivation. $\Delta DSM_{positive}$ objects which were < 500 m from $\Delta DSM_{negative}$ objects (subset B) were considered more likely to be post-disturbance re-growth.

The minimum distance between the two processes was variable and ranged from 34 m to 497 m (mean ± standard deviation: 278 ± 119 m) (subset B in Table 8). We believe that this is related to the fact that the analysis spanned only 1 year with only 2 acquisitions available. In other words, correlation in space of the two categorical events (deforestation/forest degradation and re-growth) may only be achieved by proper sampling in time. However, this could not be verified due to lack of a dense time-series.

A possible influence on the estimation of the minimum distance concerns the method used. The distance between $\Delta DSM_{positive}$ and $\Delta DSM_{negative}$ objects was calculated by considering the minimum distance between the objects centroids. $\Delta DSM_{positive}$ objects shape was not as regular as $\Delta DSM_{negative}$ objects; for instance objects along road networks were elongated as they followed a linear feature. This pattern would have introduced a bias in the distance calculation. Other approaches should be tested in the future.

Given the process dynamics arising from clearing, abandonment and re-clearing with a close coupling between deforestation and post-disturbance forest re-growth (Skole, et al., 2004) denser time-series spanning several years would provide finer detailed information on the spatial patterns and enable a better understanding of whether deforestation/forest degradation is expanding from road networks towards primary forest or whether old clearings are primarily re-

used (and how long is the time elapsed between field abandonment and re-clearing).

Forest changes can be classified as "diffuse" or "corridor" patterns according to (Mayaux, et al., 2013). The "diffuse" pattern of disturbance consist of isolated small openings (traditional shifting cultivation) while, the "corridor" pattern of disturbance is characterised by contiguous patches along road networks (either old logging roads or forest clearings).

Visual interpretation of the final change map shows "corridor" patterns associated with $\Delta DSM_{positive}$ objects (post-disturbance re-growth) in accordance with Mayaux et al. (2013) mainly located along road networks, which link the main rural communities (Sessions, 2007), within abandoned logging roads and also within the logging concessions (Figure 17). Instead, the $\Delta DSM_{negative}$ objects, were often isolated within the lowland forest within currently inactive logging concessions and can be classified as having a "diffuse" pattern (Figure 17).

In the Northern Congo selective logging is one of the major forest degradation drivers with the most visually perceptible damage related to logging roads (Gullison & Hardner, 1993). Here logging roads construction rates have increased dramatically through time (from 156 km/year between 1976-1990 and 660 km/year from 2000 onwards) (Laporte, et al., 2007). The legacy derived from the presence of old inactive logging roads (often re-vegetating) is still visually appreciable in the TanDEM-X ΔDSM image. A study based on optical data found that median persistence of logging roads was 4 years and after 20 years complete disappearance was observed in the Northern Republic of Congo (Kleinschroth, et al., 2015).

Extracting re-growing vegetation developing on abandoned road networks was challenging. Old logging re-vegetating roads were visually identified in the ΔDSM image but it was not possible to extract most of these areas using the morphological algorithm since growth was often limited in terms of magnitude and fragmented within 1 year. However, the dataset and the approach used

holds potential for extracting these features by considering a longer time-frame (e.g. > 1 year). This will provide higher change magnitude that would be better segmented thanks to the increased contrast with the surrounding stable areas.

On the contrary, canopy gaps closure observed by optical remote sensing can occur within 50 days after disturbance (Verhegghen, et al., 2015); in this case, canopy gaps due to selective logging might have been detected (subset A in Table 7) but there is no way to validate this assumption using the available data. The combination of ancillary information related to previous selective logging operations inside the logging concessions might help to validate these changes but this is rarely made available from logging companies. We therefore, partitioned the detected changes into changes that have a higher chance of being "true" and due to shifting agriculture (subset B in Table 7) and changes that could be related to other drivers including selective logging (magnitude between -7 and 0 m and area ≤ 100 TanDEM-X pixels) (subset A in Table 7) (see section 5.5.6).

5.7.4. Validation Using High Resolution Optical Data

High resolution optical imagery has become the norm for validating other remote sensing studies (Mermoz & Le Toan, 2016) and in particular the use of freely available Google Earth imagery (Dorais & Cardille, 2011). This is often preferred due to reasons related to area coverage and lack of possibility to collect ground data in remote and inaccessible tropical forest.

a) $\Delta DSM_{negative}$ *(deforestation/forest degradation) subset B (n*= 2137*)*:

- 78 (87.6%) out of the 89 disturbed areas delineated manually (DEF/DEG) using two Pléiades imagery intersected (some only partially) the TanDEM-X change objects. This proves a good performance of the method.
- 11 out of 89 (12.3% miss rate) DEF/DEG objects detected in the optical dataset were missed by the TanDEM-X change map. This can be explained either by an

omission error in the detection algorithm or a commission error during the visual interpretation of the optical data.

- Visual interpretation of the $\Delta DSM_{negative}$ objects indicates that these were both non-forest (or young secondary forest or degraded forest) in both Pléiades acquisitions. The reason for the TanDEM-X detecting these was because the acquisition of the first TanDEM-X scene occurred about 3 months before the first Pléiades acquisition. We verified this using an independent data product. We used the Hansen et al. (2013) forest loss dataset and verified visually that some of the change areas that were detect by TanDEM-X are not visible between the two Pléiades dates.
- Changes detected by TanDEM-X were generally larger in size compared those observed by comparison of two Pléiades images and this can be attributed to two distinct approaches affected by a different set of errors: a computational automatic change detection algorithm using TanDEM-X DSMs against the user defined manual delineation of deforestation events using Pléiades. The validation method was aimed at assessing the performance of the TanDEM-X change detection; other validation methods should be used to compare change properties such as area or change magnitude.

b) $\Delta DSM_{positive}$ *(post-disturbance re-growth)*:

- Pléiades imagery was not sufficient for the validation of forest re-growth since the spectral properties of re-growth at various stages are visually similar after 1 year. The only way to validate these should involve height change estimates that are only available from three-dimensional remote sensing datasets (e.g. repeat LiDAR surveys or repeat drone based digital elevation models) and/or through repeat ground-based height estimates, detailed visual assessment and knowledge of species composition changes.

5.8. Conclusion and Future Work

Technological advancement in spaceborne SAR and InSAR satellites now enables the provision of unprecedented datasets in terms of: (a) increased resolution; (b) revisit time and (c) 3D (height as a function of space coordinates) information. The TanDEM-X mission encapsulates these advantages (high resolution 3D information at 11 days revisit time). Albeit, the 11 day revisit is possible only if the acquisitions are ordered in advance, systematic revisit times are far lower.

We highlight the potential of using an object-based approach as an alternative to a pixel-based approach, which provides objects encapsulating either negative or positive DSM changes occurring between two TanDEM-X acquisitions.

The approach provided significant information in terms of: (a) forest structure change magnitude and (b) area changes linked to deforestation, forest degradation and to a certain extent post-disturbance re-growth at high resolution (< 5 m) in tropical forest where optical remote sensing is hindered by cloud cover. This is a significant step forward compared to SAR backscatter pixel-based change detection, which is limited by the ability of scattering physics to sense the forest vertical structure function, and by speckle noise precluding the detection of subtle processes (e.g. degradation and re-growth).

Of particular significance is the potential for detection of post-disturbance re-growth (on a yearly basis), which we appear to have been detected to a certain extent despite having only a single year of data but this could not be validated due to lack of appropriate validation datasets. This ability to map and assign a magnitude value to re-growth will need further investigation by employing longer DSM time-series, as the changes in PCH will increase with time and will be outside of the noise level and greater compared to no-change areas.

The potential of InSAR for tropical forest monitoring has relatively been little researched given the limited availability of operating spaceborne satellite missions (even less so single-pass interferometers such as TanDEM-X, as this is the first such

satellite mission) and in particular for the detection of changes that are spatially and temporally limited (e.g. forest degradation).

Understanding PCH modulation with target properties (e.g. density) and the impact of external influences (seasonality and meteorological conditions) remains currently still vastly unexplored. Currently, there is still a significant gap in understanding new datasets and thus, methods are being developed rapidly but are not yet operational.

It is widely suggested to the remote sensing community to incorporate 3D information from InSAR to support international restoration/conservation initiatives for the provision of activity data (e.g. REDD+), in particular in areas where cloud cover and rapid spectral reflectance recovery is an issue for optical sensors and as SAR backscatter is not sensitive enough to detect 3D structural changes, such as more subtle degradation and re-growth patterns (Global Forest Observations Initiative, 2016).

The approach can be applied to pairs of InSAR DSMs (or a longer time-series) which can currently only be provided by TanDEM-X with sufficient spatial resolution and phase noise variance to afford the results obtained in the present study. Testing the approach on Sentinel-1 InSAR (repeat pass interferometry) is of great interest, but performance would be limited by the interferometer configurations (baselines), and the ability to have enough coherence due to temporal decorrelation. On the other hand, increased data availability would lay the possibility of covering a larger area of the tropics. Denser and longer TanDEM-X DSMs time-series could in principle provide improved mapping of the events dynamics in future work.

For this purpose, Sentinel-1 Interferometric Wide Swath mode (IWS) data (at a reduced spatial resolution 5 x 20 m) is also foreseen to provide interferometric data with advancements in forest monitoring, although restricted to repeat-pass acquisitions (European Space Agency, 2013).

The future launch of TanDEM-L aims to provide a global DEM (closer to ground topography by operating at longer wavelength) (Moreira, et al., 2015).

Synergy between TanDEM-X and TanDEM-L holds great potential for the generation of a global vegetation height (Eineder, et al., 2014).

Finally, the DSM differencing approach by InSAR could be extended by incorporating ground-based above-ground biomass estimates that would allow conversion from forest volume change to biomass change and thus used for REDD+ sampling schemes to estimate carbon stock loss.

5.9. Acknowledgments

Elsa Carla De Grandi is supported by the Principal's Career Development Scholarship and the School of GeoSciences (University of Edinburgh). The author was granted the Elizabeth Sinclair Irvine Bequest Fund by the School of GeoSciences, University of Edinburgh, UK to carry out the work. Dr Edward Mitchard is supported by a NERC Fellowship. The authors would like to acknowledge the software providers Sarmap SA and EXELIS VIS (Sarscape 5.0). Data processing was undertaken in ENVI IDL, SARscape and Wolfram Mathematica 11.0. Data providers: DLR (TanDEM-X AO VEGE6702) and Airbus Defence (Pléiades imagery), Google (Google Earth imagery). Dr Astrid Verhegghen (Joint Research Center) is acknowledged for providing insight on the tropical forests of the Congo Basin.

5.10. References

- Ahrends, A. et al., 2010. Predictable waves of sequential forest degradation and biodiversity loss spreading from an African city. *Proceedings of the National Academyy of Sciences,* 107(33), p. 14556–14561.
- Astrium, 2012. *Pléiades Imagery User Guide.* [Online]. Available at: http://www.cscrs.itu.edu.tr/assets/downloads/PleiadesUserGuide.pdf [Accessed 26 September 2016].
- Aweto, A., 2012. *Shifting cultivation and secondary succession in the tropics.* 1st ed. Ibadan, Nigeria: CABI.
- Balzter, H., 2001. Forest mapping and monitoring with interferometric synthetic aperture radar (InSAR). *Progress in Physical Geography,* 25(2), pp. 159-177.

- Balzter, H., Rowland, C. & Saich, P., 2007. Forest canopy and carbon estimation at Monks Wood National Nature Reserve, UK, using dual-wavelength SAR interferometry. *Remote Sensing of Environment,* 108(3), pp. 224-239.
- Bamler, R. & Hartl, P., 1998. Synthetic Aperture Radar Interferometry. *Inverse Problems,* 14(4), pp. 1-54.
- Cernusak, L. A. et al., 2013. Tropical forest responses to increasing atmospheric CO2: current knowledge and opportunities for future research. *Functional Plant Biology,* 40(6), p. 531–551.
- Chazdon, R. L., 2003. Tropical forest recovery: legacies of human impact and natural disturbances. *Perspectives in Plant Ecology Evolution and Systematics,* 6(1-2), pp. 51-71.
- Cloude, S., 2010. *Polarization applications in remote sensing.* Oxford, UK: Oxford University Press.
- Cohen, J., 1988. *Statistical power analysis for the behavioral sciences.* 2nd ed. Hillsdale, NJ: Lawrence Earlbaum Associates.
- Cohen, J., 1992. A Power Primer. *Psychological Bulletin,* 112(1), pp. 155-159.
- Costantini, M., 1998. A novel phase unwrapping method based on network programming. *IEEE Transactions on Geoscience and Remote Sensing,* 36(3), pp. 813-821.
- De Sy, V. et al., 2012. Synergies of multiple remote sensing data sources for REDD+ monitoring. *Current Opinion in Environmental Sustainability,* 4(6), p. 696–706.
- Desclée, B., Bogaert, P. & Defourny, P., 2006. Forest change detection by statistical object-based method. *Remote Sensing of Environment,* 102(1), pp. 1-11.
- Deutscher, J. P. R., Gutjahr, K. & Hirschmugl, M., 2013. Mapping Tropical Rainforest Canopy Disturbances in 3D by COSMO-SkyMed Spotlight InSAR-Stereo Data to Detect Areas of Forest Degradation. *Remote Sensing,* 5(2), pp. 648-663.
- Dorais, A. & Cardille, J., 2011. Strategies for Incorporating High Resolution Google Earth Databases to Guide and Validate Classifications: Understanding Deforestation in Borneo. *Remote Sensing,* 3(6), pp. 1157-1176.
- Duveiller, G., Defourny, P., Desclée, B. & Mayaux, P., 2008. Deforestation in Central Africa: Estimates at regional, national and landscape levels by advanced processing of systematically-distributed Landsat extracts. *Remote Sensing of Environment,* 112(5), pp. 1969-1981.

- Eineder, M. et al., 2014. *Surface, TanDEM-L. Satellite Mission Proposal for Monitoring Dynamic Processes on the Earth's,* Cologne: German Aerospace Center.
- Elrajubi, O. M.; El-Feghi, I. & Saghayer, M.A.B., 2014. Hit-or-Miss Transform as a Tool for Similar Shape Detection. I*nternational Journal of Computer, Electrical, Automation, Control and Information Engineering*, 8(6), pp.993-996.
- ESRI, 2016. *Intersect (Analysis).* [Online]. Available at: http://webhelp.esri.com/arcgisdesktop/9.2/index.cfm?TopicName=Intersect_%28Analysis%29 [Accessed 7 November 2016].
- European Space Agency, 2013. *Sentinel-1 User Handbook.* [Online]. Available at: https://sentinel.esa.int/web/sentinel/user-guides/sentinel-1-sar/revisit-and-coverage [Accessed 21 June 2016].
- FAO, 2015. *The Global Forest Resources Assessment (FRA) 2015. Terms and Definitions,* Rome, Italy: Food and Agriculture Organization of the United Nations.
- Fearnside, P. M., 2001. Soybean cultivation as a threat to the environment in Brazil. *Environmental Conservation,* 28(1), pp. 23-38.
- Garestier, F., Dubois-Fernandez, P. C. & Papathanassiou, K. P., 2008. Pine Forest Height Inversion Using Single-Pass X-Band PolInSAR Data. *IEEE Transactions on Geoscience and Remote Sensing,* 46(1), pp. 59-68.
- GIOVANNI, 2016. *GIOVANNI.* [Online]. Available at: http://giovanni.sci.gsfc.nasa.gov/ [Accessed 2 March 2016].
- Global Forest Observations Initiative, 2016. *Integration of remote-sensing and ground-based observations for estimation of emissions and removals of greenhouse gases in forests: Methods and Guidance from the Global Forest Observations Initiative,* Rome: Food and Agriculture Organization of the United Nations.
- Goldstein, R. M. & Werner, C. L., 1998. Radar interferogram filtering for geophysical applications. *Geophysical Research Letters,* 25(21), pp. 4035-4038.
- Gond, V. et al., 2013. Vegetation structure and greenness in Central Africa from Modis multi-temporal data. *Philisophical Transactions of the Royal Society B,* 368(20120309), pp. 1-8.
- Google Earth , 2016. *Google Earth PRO.* [Online]. Available at: https://www.google.com/earth/ [Accessed 2 January 2016].
- Grace, J., Mitchard, E. & Gloor, E., 2014. Perturbations in the carbon budget of the tropics. *Global Change Biology,* 20(10), p. 3238–3255.
- Grainger, A., 1993. *Controlling tropical deforestation.* 1st ed. London.: Earthscan Publications Ltd.

- Gullison, R. E. & Hardner, J. J., 1993. The effects of road design and harvest intensity on forest damage cause by selective logging: empirical results and a simulation model from the Bosque Chimanes, Bolivia. *Forest Ecology and Management,* 59(1-2), pp. 1-14.

- Hajnsek, I., Kugler, F., Lee, S.-K. & Papathanassiou, K., 2009. Tropical- Forest-Parameter Estimation by Means of Pol-InSAR: The INDREX-II Campaign. *IEEE Transactions on Geoscience and Remote Sensing,* 42(7), pp. 481-493.

- Hansen, M. et al., 2013. High-Resolution Global Maps of 21st Century Forest Cover Change. *Science,* 342(6160), pp. 850-853.

- Hanssen, R. F., 2001. *Radar Interferometry. Data Interpretation and Error Analysis.* 1st ed. Dordrecht, The Netherlands: Kluwer.

- Hartshorn, G. S., 1980. Neotropical Forest Dynamics. *Biotropica,* 12(2), pp. 23-30.

- Hedges, L. & Olkin, I., 1985. *Statistical Methods for Meta-Analysis.* 1st ed. New York: Academic Press.

- Herold, M. & Johns, T., 2007. Linking requirements with capabilities for deforestation monitoring in the cotext of the UNFCCC-REDD process. *Environmental Research Letters,* 2(5), p. 045025.

- Herold, M. et al., 2011. A review of methods to measure and monitor historical carbon emissions from forest degradation. *Unasylva,* 62(238), pp. 16-24.

- Hoekman, D. H. & Varekamp, C., 2001. Observation of Tropical Rain Forest Trees by Airborne High-Resolution Interferometric Radar. *IEEE Transactions on Geoscience and Remote Sensing,* 39(3), pp. 584-594.

- Houghton, R. A., 2010. How well do we know the flux of CO2 from land-use change?. *Tellus B,* 62(5), p. 337–351.

- Izzawati, Wallington, E. & Woodhouse, I., 2006. Forest Height Retrieval From Commercial X-Band SAR Products. *IEEE Transactions on Geoscience and Remote Sensing,* 44(4), pp. 863-870.

- Jones, A. et al., 2013. *Soil Atlas of Africa.* 1st ed. Luxembourg: European Commission, Publications Office of the European.

- Kay, S. M., 1998. *Fundamentals of Statistical Signal Processing, Volume II: Detection Theory.* 1st ed. Englewood Cliffs, NJ: Prentice Hall.

- Kleinschroth, F. et al., 2015. Legacy of logging roads in the Congo Basin: How persistent are the scars in forest cover?. *Ecosphere,* 6(4), pp. 1-17.

- Kugler, F., Schulze, D. H. I., Pretzsch, H. & Papathanassiou, K., 2014. TanDEM-X Pol-InSAR Performance for Forest Height Estimation. *IEEE Transactions on Geoscience and Remote Sensing,* 52(10), pp. 6404-6422.

- Laporte, N., Goetz, S., Justice, C. & Heinicke, M., 1998. A new landcover map of central Africa from multi-resolution, multi-temporal AVHRR data. *International Journal of Remote Sensing,* 19(18), pp. 3537-3550.

- Laporte, N. T. et al., 2004. Towards an operational forest monitoring system for Central Africa. In: G. Gutman, et al. eds. *Land Change Science: Observing, Monitoring and Understanding Trajectories of Change on the Earth's Surface.* The Netherlands: Kluwer Academic Publishers, pp. 97-110.

- Laporte, N. T. et al., 2007. Expansion of Industrial Logging in Central Africa. *Science,* 316(5830), p. 1451.

- Lebrun, J. & Gilbert, G., 1954. *Une classification écologique des forêts du Congo.* 1st ed. Bruxelles: National Institute for Agronomic Study of the Belgian Congo (INEAC).

- Liesenberg, V., de Souza Filho, C. R. & Gloaguen, R., 2016. Evaluating Moisture and Geometry Effects on L-Band SAR Classification Performance Over a Tropical Rain Forest Environment. *IEEE Journal of Selected Topics in Applied Earth Observations and Remote Sensing,* 9(12), pp. 5357-5368.

- Lillesand, T., Kiefer, R. & Chipman, J., 2008. *Remote Sensing and Image Interpretation.* 6th ed. Hoboken, NJ: John Wiley & Sons.

- Lucas, R. M. et al., 2014. Mapping forest growth and degradation stage in the Brigalow Belt Bioregion of Australia through integration of ALOS PALSAR and Landsat-derived foliage projective cover data. *Remote Sensing of Environment,* Volume 155, pp. 42-57.

- Maley, J., 2002. A Catastrophic Destruction of African Forest about 2,500 Years Ago Still Exerts a Major Influence on Present Vegetation Formations. *IDS Bulletin,* 33(1), pp. 13-30.

- Malhi, Y. et al., 2013. African rainforests: past, present and future. *Philosophical Transactions of the Royal Society B,* 368(1625), p. 20120312.

- Martone, M. et al., 2012. Coherence evaluation opf TanDEM-X interferometric data. *ISPRS Journal of Photogrammetry and Remote Sensing,* Volume 73, pp. 21-29.

- Mayaux, P. et al., 2013. State and evolution of the African rainforests between 1990 and 2010. *Philosophical Transactions of the Royal Society B,* 368(1625), p. 20120300.

- Mayaux, P., Richards, T. & Janodet, E., 1999. A vegetation map of Central Africa derived from satellite imagery. *Journal of Biogeography,* 26(2), pp. 353-366.

- Maynard, K. & Royer, J. F., 2004. Effects of ''realistic'' land-cover change on a greenhouse-warmed African climate. *Climate Dynamics,* 22(4), p. 343–358.
- Megevand, C. et al., 2013. *Deforestation Trends in the Congo Basin,* Washington, D.C.: The World Bank.
- Mermoz, S. & Le Toan, T., 2016. Forest Disturbances and Regrowth Assessment Using ALOS PALSAR Data from 2007 to 2010 in Vietnam, Cambodia and Lao PDR. *Remote Sensing,* 8(217), pp. 1-22.
- Mertens, B. et al., 2011. *Atlas Forestier Interactif Du Congo,* Washington, DC: World Resources Institute.
- Mietten, J., Stibig, H.-J. & Achard, F., 2014. Remote sensing of forest degradation in Southeast Asia—Aiming for a regional view through 5–30 m satellite data. *Global Ecology and Conservation,* Volume 2, pp. 24-36.
- Minh, D. H. T. et al., 2014. Relating P-Band Synthetic Aperture Radar Tomography to Tropical Forest Biomass. *IEEE Transactions on Geoscience and Remote Sensing ,* 52(2), pp. 967-979.
- Moore, D. & McCabe, G. P., 2005. *Introduction to the Practice of Statistics.* 5th ed. New York, NY: W. H. Freeman & Co.
- Moreira, A. et al., 2015. Tandem-L: A Highly Innovative Bistatic SAR Mission for Global Observation of Dynamic Processes on the Earth's Surface. *EEE Geoscience and Remote Sensing Magazine,* 3(2), pp. 8-23.
- Mura, J. C. et al., 2001. *Identification of the tropical forest in Brasilian Amazon based on the DEM difference from P- and X-band interferometric data.* Sydney, Australia, Proceedings of the International Geoscience and Remote Sensing Symposium, p. 789–791.
- Nakagawa, S. & Cuthill, I. C., 2007. Effect size, confidence interval and statistical significance: a practical guide for biologists. *Biological Reviews,* 82(4), pp. 591-605.
- Neef, T. et al., 2005. Tropical Forest Measurement by Interferometric Height Modeling and P-Band Radar Backscatter. *Forest Science,* 51(6), pp. 585-594.
- Neyman, J. & Pearson, E. S., 1933. On the Problem of the Most Efficient Tests of Statistical Hypotheses. *Philosophical Transactions of the Royal Society of London. Series A, Containing Papers of a Mathematical or Physical Character,* Volume 231, pp. 289-337.
- OSFAC, 2012. *FACET: Monitoring the forests of Central Africa using remotely sensed data sets (Forêts d'Afrique Centrale Évaluées par Télédétection),* OSFAC.
- OSFAC, 2015. *The Forests of the Congo Basin- Forests and climate change.* 1st ed. Belgium: Weyrich.

- Papathanassiou, K., Pardini, M. & Hajnsek, I., 2016. *Volume structure characterisation by means of multi-baseline Pol-InSAR: status and challanges.* Beijing, China, IEEE, pp. 7531-7532.
- Pearson, T. R. H., Brown, S. & Casarim, f. M., 2014. Carbon emissions from tropical forest degradation caused by logging. *Environmental Research Letters,* 9(3), pp. 1-11.
- Pearson, T. R. H., Brown, S., Murray, L. & Sidman, G., 2017. Greenhouse gas emissions from tropical forest degradation: an underestimated source. *Carbon Balance and Management,* 12(3), pp. 1-11.
- Peel, M. C., Finlayson, B. L. & A, M. T., 2007. Updated world map of the Koppen-Geiger climate classification. *Hydrology and Earth System Sciences Discussions,* 4(2), pp. 439-473.
- Philippon, N. et al., 2016. Analysis of the diurnal cycles for a better understanding of the mean annual cycle of forests greenness in Central Africa. *Agriucltural and Forest Meteorology,* Volume 223, pp. 81-94.
- Potapov, P. et al., 2012. Quantifying forest cover loss in Democratic Republic of the Congo, 2000–2010, with Landsat ETM+ data. *Remote Sensing of Environmen,* 1(22), p. 106–116.
- Potapov, P. et al., 2008. Mapping the World's Intact Forest Landscapes by Remote Sensing. *Ecology and Society,* 13(2), p. 51.
- Praks, J., Antropov, O. & Hallikainen, M., 2012. LIDAR-Aided SAR Interferometry Studies in Boreal Forest: Scattering Phase Center and Extinction Coefficient at X- and L-Band. *IEEE Transactions on Geoscience and Remote Sensing ,* 50(10), pp. 3831-3843.
- Rosen, P. et al., 2000. Synthetic Aperture Radar Interferometry. *Proceedings of the IEEE,* 88(3), pp. 333-382.
- Ryan, C. et al., 2012. Quantifying small-scale deforestation and forest degradation in African woodlands using radar imagery. *Global Change Biology ,* 18(1), p. 243–257.
- Saatchi, S. S. et al., 2011. Benchmark map of forest carbon stocks in tropical regions across three continents. *PNAS,* 108(24), p. 9899–9904.
- Sadeghi, Y., St-Onge, B., Leblon, B. & Simard, M., 2016. Canopy Height Model (CHM) Derived From a TanDEM-X InSAR DSM and an Airborne Lidar DTM in Boreal Forest. *IEEE Journal of Selected Topics in Applied Earth Observations and Remote Sensing,* 9(1), pp. 381-397.

- Sarmap, 2016. *SARscape Guide.* [Online]. Available at: https://www.harrisgeospatial.com/docs/pdf/sarscape_help.pdf [Accessed 20 May 2016].
- Sessions, J., 2007. *Forest Road Operations in the Tropics.* 1st ed. New York: Springer.
- Shimada, M. et al., 2014. Newglobal forest/non-forest maps fromALOS PALSAR data (2007–2010). *Remote Sensing of Environment,* Volume 155, pp. 13-31.
- Skole, D. L. et al., 2004. Pattern to process in the Amazon Region. In: G. Gutman, et al. eds. *Land Change Science.* Dordrecht : Springer Netherlands, pp. 77-95.
- Soille, P. & Pesaresi, M., 2002. Advances in Mathematical Morphology Applied to Geoscience and Remote Sensing. *IEEE Transactions on Geoscience and Remote Sensing ,* 40(9), pp. 2042-2055.
- Solberg, S., Astrup, R. & Weydahl, D. J., 2013. Detection of Forest Clear-Cuts with Shuttle Radar Topography Mission (SRTM) and TanDEM-X InSAR Data. *Remote Sensing,* 5(11), pp. 5449-5462.
- Solberg, S. et al., 2015. Monitoring forest carbon in a Tanzanian woodland using interferometric SAR: a novel methodology for REDD+. *Carbon Balance and Management,* 10(14), pp. 1-14.
- Solberg, S., Næsset, E., Gobakken, T. & Bollandsås, O.-M., 2014. Forest biomass change estimated from height change in interferometric SAR height models. *Carbon Balance and Management,* 9(1), pp. 1-12.
- Sullivan, G. & Fein, R., 2012. Using Effective Size-or why the P Value Is Not Enough. *Journal of Graduate Medical Education,* 4(3), pp. 279-282.
- Tanase, M. A. I. I., Lowell, K., Karyanto, O. & Santoro, M., 2015. Detecting and Quantifying Forest Change: The Potential of Existing C- and X-Band Radar Datasets. *PLoS ONE,* 10(6), p. e0131079.
- Treuhaft, R. et al., 2015. Tropical-Forest Biomass Estimation at X-Band From the Spaceborne TanDEM-X Interferometer. *IEEE Geoscience and Remote Sensing Letters,* 12(2), pp. 239-243.
- UNFCCC, 2015. *Conference of the Parties (COP): Adoption of the Paris Agreement. Proposal by the President,* Geneva, Switzerland: United Nations Office.
- Verhegghen, A., Eva, H. & Achard, F., 2015. *Assessing forest degradation from selective logging using time series of fine spatial resolution imagery in Republic of Congo.* Milan, Italy, Proceedings of the IEEE International Geoscience and Remote Sensing Symposium , pp. 2044-2047.

- Wermuth, M. et al., 2014. Two Years of TanDEM-X Baseline Determination. *International Journal of Space Science and Engineering,* 2(1), pp. 35-48.

- White, F., 1983. *The vegetation of Africa: a descriptive memoir to accompany the Unesco/AETFAT/UNSO vegetation map of Africa,* Paris, France: Unesco.

- Wilkie, D., Curran, B., Tshombe, R. & Morelli, G. A., 1998. Modelling the Sustainability of Subsistence Farming and Hunting in the Ituri Forest of Zaire. *Conservation Biology ,* 12(1), pp. 137-147.

- Wilson, A. M. & Jetz, W., 2016. Remotely Sensed High-Resolution Global Cloud Dynamics for Predicting Ecosystem and Biodiversity Distributions. *PLoS Biology,* 14(3), pp. 1-20.

- Wolfram, 2016. *Morphological Components.* [Online]. Available at: https://reference.wolfram.com/language/ref/MorphologicalComponents.html [Accessed 18 June 2016].

- World Bank, 2016. *Climate Change Knowledge Portal.* [Online]. Available at: http://sdwebx.worldbank.org/climateportal/countryprofile/home.cfm?page=country_profile&CCode=COG&ThisTab=ClimateBaseline [Accessed 15 November 2016].

- World Resources Institute, 2013. *Congo Basin Forest Atlases.* [Online]. Available at: http://www.wri.org/our-work/project/congo-basin-forests/congo#project-tabs [Accessed 20 January 2016].

6. Summary and Implications

6.1. Summary

The chapter summarises the findings from **Chapter 3**, **4** and **5**. Implications and suggestions for future research developments for mapping and monitoring degraded forests through the structural information provided by SAR and InSAR observations are reported.

6.1.1. Chapter 3

Spatial statistic of SAR backscatter at C- and L-band was extracted using a wavelet analysis technique. The analysis sought to assess the capability of these textural measures to discriminate between intact forest (IF) and degraded forest (DF) as well as other landcover types including forest-agriculture mosaic (FAM) and forest-savanna (FS). These classes were mapped independently using ancillary datasets and expert knowledge to provide a 'ground truth' dataset against which to develop the statistics.

There were two specific sets of analyses to address the objectives of **Chapter 3**, these are covered separately below, followed in each case by a summary of what was found:

1. **Qualitative interpretation of the wavelet statistics related to landcover classes (IF, DF, FAM and FS)**

   ENVISAT ASAR backscatter findings:

   - IF, DF and FAM signatures reveal correlated stationary random processes with correlation length at short scales (~ 42 m for IF and DF and ~ 60 m for FAM)
   - FS signature indicates non-stationarity with increasing variance with scale, due to the presence of intermittency (trees within grassland).

- In terms of separability based on scale by scale distance between signatures, IF and DF are well separated from FAM and FS at scales up to 2^2. However, separation between IF and DF appears weak at all scales.

ALOS PALSAR backscatter findings:

- At HH polarization the signature functional form is similar to the ENVISAT ASAR signatures, although with reduced wavelet variance magnitude. This feature indicates that L-band HH scattering is influenced by the upper canopy layer variations, in the same way as C-band, only less so due to deeper penetration into the forest volume.
- At HV polarization the signatures of IF and DF reveal the onset of a white noise process (no textural features). This happens because depolarization is caused by volume scattering and therefore the sensitivity to upper surface variation is lost. HV polarization is therefore not useful in the present context, and is not analyzed further.

2. **Functional analysis by means of polynomial approximations of the wavelet signatures to improve separability between IF and DF**

Findings:

- The two main functional forms that were useful for differentiating IF and DF are the signature sill (first maximum) and the inflection point, these corresponding to correlation length and the onset of anti-correlations. These two forms are identified numerically by the zero-crossings of the first and second derivative of a polynomial approximation.
- For, ENVISAT ASAR backscatter, the two functional parameters (first and second derivative) of the IF and DF signatures are both statistically different at 0.05 confidence level.
- In contrast, for ALOS PALSAR backscatter (L-band, HH polarization), the difference between IF and DF signatures was not statistically significant.

- ALOS PALSAR backscatter (HH polarization) is sensitive to the large scattering elements in the top layer of the canopy, and therefore, develops sensitivity to the forest structure in a similar way to C-band VV, although with less strength due to the increased penetration.
- It is hypothesized that the success of C-band is due to the low penetration into the canopy, the backscatter return comes primarily from the top of the canopy components, and it is modulated by local incidence angle variation and extinction (micro-topography effect). In this environment the roughness of the upper canopy is a good indicator of the level of disturbance. The L-band penetration is too high to capture the upper canopy roughness alone and is also influenced by the ground return.

6.1.2. Chapter 4

This chapter aimed to assess the capability of DSMs derived from TanDEM-X data to detect the difference between primary forest (PF), secondary forest (SF), mixed-scrub (MS) and grassland (GR) which developed from a well-mapped large forest fire in Indonesian Borneo. The link between forest canopy structure, measured by LiDAR CHM and TanDEM-X DSM spatial statistic provided by wavelet spectra in the space-scale domain was analysed. Ways of de-coupling the dependence on forest structure and topography were sought with the goal of arriving at estimates of thematic class separability based on TanDEM-X DSM wavelet spectra.

Four main analysis were performed:

1. **TanDEM-X DSM dependence on forest structure and topography**

   The adopted wavelet acts as a differential operator. Therefore, at the scales where (locally) variation of topographic height is negligible, the wavelet variance will only be sensitive to the variation of forest canopy height. The topographic component will not depend on the absolute value of topographic height within the range of scales where the signal can be modelled by the sum of a constant (topography) and of a random process (canopy height).

Findings:

- Topographic features are characterized by wavelet variance analysis (wavelet signatures) of LiDAR DTM, revealing smooth texture patterns up to 200 m with regular (almost periodic patterns) arising beyond 200 m (low frequencies). These patterns are also visible in the LiDAR DSM and the TanDEM-X DSM wavelet signatures, as expected since these data include the DTM information.
- Forest canopy structural features are characterized by wavelet signature of LiDAR CHM, revealing that these features are reflected in short scale (between 1-10 m) (high frequencies) textural information. Importantly, these high frequency textural patterns are also appreciable in LiDAR DSM and TanDEM-X DSMs, this setting the stage for forest structural measures also based on this data.
- Wavelet co-variance provides indication on the textural correlation between LiDAR and TanDEM-X datasets. At shorter scales, the texture correlation between LiDAR DTM and TanDEM-XDSM is one order of magnitude lower, especially at scales typical of canopy width and gaps. This fact reinforces the point that although the TanDEM-X DSM is affected by the DTM noise, information on vegetation structure can still be detected as it happens at a different scale range.

2. Connection between the spectrum polynomial approximation at short scale and the forest height variance.

The variance of the LiDAR CHM and TanDEM-X DSM observations is estimated locally (in space) by the first polynomial coefficient (P_0) of the fitted wavelet spectrum. From P_0 statistics consideration were derived about the link between the natural process (forest height) variance and the wavelet measures.

Findings:

- LiDAR CHM P_0 is well correlated with the process standard deviation (R^2 = 0.77, N = 315).
- TanDEM-X DSM P_0 is well correlated with the process standard deviation (R^2 = 0.72, N = 315).
- LiDAR CHM standard deviation was weakly correlated with TanDEM-X P_0 (R^2 = 0.34, N = 315). This case reinforces the fact that the TanDEM-X DSM process is not related in a simple way to the CHM process, but it is the result of the superposition of several random processes, such as terrain topography and InSAR phase signal to noise ratio.
- The area occupied by large emergent trees (> 35 m) is a good indicator to explain why SF presents a lower canopy roughness compared to PF and to explain the resulting texture appreciable in LiDAR and TanDEM-X observations. It was found that, the area occupied by large emergent trees (>35 m) in SF plots is significantly different from PF (p < 0.01, N = 222).

3. Class separability provided by 2D wavelet spectra

LiDAR Wavelet Spectrum ($\mathrm{LiDAR_{CHM}WS}$) and TanDEM-X Wavelet Spectrum ($\mathrm{TDX_{DSM}WS}$) separability at 4 scales of decomposition was performed based on pairwise Jeffries-Matusita (JM) distance and expected classification error (P_e) was calculated.

Findings:

- Separability by considering each decomposition scale individually indicates that information at all scales when taken singularly do not bear significant information to discriminate landcover classes.
- Analysis of the full wavelet spectrum (i.e. either all dyadic scales or the spectrum polynomial functional representation) was essential to improve separability.

- Higher JM separability was found using the full wavelet spectrum (LiDAR: 1.29 ≤JM≤ 1.39; TanDEM-X: 1.18 ≤JM≤ 1.39) compared to using each decomposition scale individually (LiDAR: 0.1 ≤JM≤ 1.26; TanDEM-X: 0.1 ≤JM≤ 1.1).
- Class separability based on the full $\text{LiDAR}_{\text{CHM}}$WS is high between all class pairs (most importantly, JM distance= 1.36 between PF and SF).
- Class separability based on the full TDX_{DSM}WS is high between all class pairs (most importantly, JM distance= 1.18 between PF and SF).
- The JM separability difference between pairs MS/PF, MS/SF and SF/PF for LiDAR and TanDEM-X was 0.06, 0.08 and 0.18 respectively.
- Expected classification error (P_e) between PF and SF ranged between 2.32%-15.22% (TanDEM-X) and 0.38%-6.18% (LiDAR).
- The highest $P_e$using TDX_{DSM}WS was found between the class pair GR/MS (P_e lower bound: 3.13% and P_e upper bound: 17.68%).
- The highest P_e using $\text{LiDAR}_{\text{CHM}}$WS was found between the class pair MS/SF (P_e lower bound: 1.31% and P_e upper bound: 11.46%).

6.1.3. Chapter 5

Chapters 3 and **4** considered the texture of single time acquisitions to distinguish disturbed forest, undisturbed forest and other landcover types. **Chapter 5** took a different approach, using InSAR DSMs as in **Chapter 4**, but using two acquisitions a year apart to map negative and positive DSM changes ($\Delta DSM_{negative}$ and $\Delta DSM_{positive}$) which could be related to deforestation/forest degradation and re-growth.

A crucial point is that ΔDSM depend only on shifts of the phase center height (PCH) due to changes of the vegetation volume, while the component due to ground return is a constant. Therefore, influence of terrain elevation on the change estimates is minimized (residuals are due to instrument configuration). Objects within the ΔDSM data are searched and labeled using a neighboring point similarity criterion. Object changes are detected by comparison of first order statistic with

control areas of no change. The object-based algorithm performed well in terms of improved signal to noise ratio, and for the capability of affording measures, such as object areas. The approach allowed to identify vegetation loss events, estimate their size and strength and to validation them. Gain events were also mapped, although with less statistical evidence due to much smaller dynamics, and their validation could not be performed due to lack of reference data.

Six main analyses were performed:

1. **A shift in TanDEM-X PCH (ΔDSM) provides estimates of forest loss (complete or partial loss associated with deforestation and forest degradation respectively) and forest gain (forest re-growth) between 2012-2013.**

   Findings:

   - Mean ΔDSM loss ranged from -19.7 to -5.2 m (-7.1 ± 1.4 m).
   - Mean ΔDSM gain ranged from 1.6 to 4.4 m (2.4 ± 0.3 m).
   - Small scale ΔDSM loss (< 1 ha) was detected successfully due to high resolution (ΔDSM loss area was 0.28 ± 0.61 ha).
   - Average size of ΔDSM gain objects was 7.51 ± 14.32 ha.
   - Deforestation/forest degradatation statistics (subset B) (mean ± standard deviation): -7.9 ± 1.5 m (magnitude); 0.41 ± 0.83 ha (area).
   - Post-disturbance re-growth statistics (subset B) (mean ± standard deviation): 2.6 ± 0.4 (magnitude); 8.88 ± 18.11 ha (area).

2. **Accuracy of the ΔDSM estimates using Standard Error of the Mean (SEOM).**

   Findings:

   - SEOM (mean ± standard deviation) was 1.74 ± 0.72 for $\Delta DSM_{negative}$ and 1.19 ± 0.27 for $\Delta DSM_{positive}$.

3. **Effect size (E_{size}) index, based on the standardised difference of means, was calculated to assess the significance of the $\Delta DSM_{negative}$ and $\Delta DSM_{positive}$**

objects in comparison to two stable areas: undisturbed lowland primary forest (PF_C) and swamp forest (SW_C).

Findings:

- E_{size} statistics ($\Delta DSM_{negative}\ PF_C$) (mean ± standard deviation): 5.2 ± 0.69 and $\Delta DSM_{negative}\ SW_C$ statistic: 5.58 ± 0.84.
- E_{size} statistics ($\Delta DSM_{positive}\ PF_C$) (mean ± standard deviation): 2.53 ± 0.4 and $\Delta DSM_{positive}\ SW_C$ statistic: 2.36 ± 0.38.
- For E_{size}= 1.5 the probability of Type I error is 6.6% (detecting as true change a sample that is noise).
- Based on this interpretation, a threshold E_{size}= 1.5 was set in the development of the change detection for both $\Delta DSM_{negative}$ and $\Delta DSM_{positive}$ objects.

4. **DSM changes dependence on sensor's parameters (baseline, incidence angle, and range distances).**

   Findings:

   - Modelling results indicate that the maximum difference is of the order of 1 m (decrease in PCH), and occurs for lower extinction and 50 m volume height. Notice that a -1 m difference correspond to the mean of the distribution of samples taken within the control area. Therefore, DSM changes within a stable forest area can be ascribed to differences in instrumental parameters.

5. **Visual interpretation of the change map.**

   Findings:

   - Positive changes (post-disturbance re-growth) distribution can be classified as "corridor" patterns (Mayaux, et al., 2013) clustered around road networks and urban areas.
   - Negative changes (deforestation/forest degradation) detected can be visually interpreted as having a "diffuse" pattern (Mayaux, et al., 2013) located inside

logging concessions but in some cases located around post-disturbance re-growth areas.

- Old logging re-vegetating roads were visually identified in the ΔDSM image but it was not possible to extract them using the morphological algorithm since re-growth magnitude was often relatively low and fragmented within a 1 year period.

6. **Validation of the $\Delta DSM_{negative}$ objects was undertaken by manually delineating deforestation/degradation change objects (DEG/DEF) using two very high resolution Pléiades scenes.**

   Findings:

   - 78 out of 89 (87.6% hit rate) DEG/DEF objects were detected by the TanDEM-X change map.
   - 11 out of 89 (12.3% miss rate) DEF/DEG objects detected in the optical dataset were missed in the TanDEM-X change map. This can be explained either by an omission error in the detection algorithm or a commission error during the visual interpretation of the optical data.
   - Changes detected by TanDEM-X were generally larger in size compared those observed by comparison of two Pléiades images and this can be attributed to two distinct approaches affected by a different set of errors: a computational automatic change detection algorithm using TanDEM-X DSMs against the user defined manual delineation of deforestation/forest degradation events using Pléiades scenes.
   - $\Delta DSM_{positive}$ objects validation was not undertaken and it requires further research including ancillary remote sensing datasets (e.g. LiDAR).

6.2.Implications

The implications from the results can be partitioned as follows: a) methodological implications for future remote sensing research and b) implications for mapping and monitoring forests.

6.2.1. Methodological Implications

a) Wavelet based spatial statistic measures of SAR backscatter and InSAR DSMs to distinguish intact forest from degraded/secondary forest:

Discrimination between intact and degraded forest using optical remote sensing is known to be challenging due the inability to detect the three-dimensional distribution of plant material (Lucas, et al., 2014). It is also challenging using one-point statistic of SAR backscatter data due to speckle noise (Oliver & Quegan, 2004), signal saturation and moisture influence (e.g. Liesenberg, et al., 2016).

This thesis is based on the principle that a connection can be established by physical considerations from the forest structural characteristics and the spatial statistic of the SAR signal, this being not only the backscatter, but more importantly, also the InSAR DSM. Grounded on this principle, space-frequency analysis provided by a wavelet representation was adopted as the tool that could provide the best numerical results in terms of signal processing quality factors.

In the specific thematic context, the passage from one-point to two-point statistic, and from 2D intensity data to 3D elevation data has confirmed that considerable improvements could be achieved for discrimination between intact forest and disturbed forest compared to one-point measures of backscatter alone (Luckman, et al., 1997; van der Sanden & Hoekman, 1999).

It is to be noted that the proposed method for deriving measures of forest spatial distributional properties, which on a perceptive standpoint could be called "textures", rests on a solid mathematical ground provided by the theory of random processes, and on a solid physics ground, provided by wave scattering theory. In this sense, it departs considerably from other approaches for spatial measures, such as edge density, shape grammars, Boolean models or co-occurrence matrices (Petrou

& García Sevilla, 2006). As for all methods based on physical-mathematical principles, as opposed to empirical solutions, the implication is that interpretation of the results can be guided by known statistical concepts (i.e. process variance and co-variance, correlation). The rigorous underlying statistical theory also implies that the method be extensible either to different thematic contexts, or to different (future) remote sensing observations (e.g. Sentinel-1 or CosmoSkyMed).

Techniques based on wavelet spectra with SAR imagery and in particular with InSAR DSMs have, to the best of our knowledge, never been used in the thematic context of detecting degraded forest (or secondary forest). **Chapter 3** and **Chapter 4** have contributed to testing these techniques on SAR backscatter and InSAR DSMs respectively.

Chapter 3 showed greater discrimination based on spatial statistical measures at shorter wavelength (ENVISAT ASAR C-band VV backscatter) compared to longer wavelength (ALOS PALSAR L-band HH backscatter). This suggests that the relevant structural properties are better captured by textural measures at shorter wavelength because of lower penetration within the canopy and consequently improved ability to characterise upper canopy roughness. The result has implications for future application using other short wavelength SAR sensors, for instance ESA C-Band Sentinel-1 or X-band SAR (e.g. TerraSAR-X or TanDEM-X backscatter). Notice that, on the contrary, when considering one-point statistic of intensity that longer wavelengths are better for forest/non-forest mapping (van der Sanden, 1997). A combination of C-band texture and L-band backscatter could improve classification accuracy.

Furthermore, wavelet signature cross-correlation techniques used in **Chapter 3** can be applied to Sentinel-1 backscatter time-series to track canopy structure changes through time. The same technique can be in principle tested on multiple TanDEM-X DSM acquisitions as well.

Chapter 4 also employed wavelet-based textural measures to capture information on the upper canopy structure (roughness) to discriminate between a structurally complex primary forest and forest recovering after the 1997/1998 El

Niño driven forest fires as well as other landcover classes (mixed-scrub and grassland).

The main limiting factor for mapping disturbed forest by InSAR DMS spatial statistic is resolution in range-azimuth, rather than in height. This point is confirmed by comparison with spatial statistic afforded by the higher resolution LiDAR CHM data (1 m). This obstacle implies that future research should exploit higher resolution TanDEM-X imaging modes (such as SpotLight), super-resolution techniques based on multi-temporal data, or future spaceborne interferometers acquiring higher resolution data. However, this will inevitably result in a reduced extent covered.

b) TanDEM-X DSM differencing method to map deforestation and forest degradation

The use of an object-based change detection approach has major implications for the detection of forest changes. The approach enables us to extract contiguous objects characterised by a decrease in Phase Centre Height (PCH) based on the mean values estimates as opposed to a pixel-based approach which would consider the distribution of samples. The advantage of dealing with an object-oriented approach is that the variance of the estimates used for detection, due to propagation of error and the intrinsic variance of the samples in the object, is much smaller than the one related to the samples in the object.

The magnitude of changes within the object reflects disturbance intensity whereby, a higher ΔDSM decrease can be linked to deforestation and a lower magnitude can be associated with forest degradation. Finding the appropriate threshold to distinguish between complete deforestation and degradation requires further work based on coherence analysis.

c) TanDEM-X DSM differencing method to map forest re-growth

Forest re-growth changes were more challenging to detect compared to forest loss. This can be explained by (a) forest re-growth is a much slower processes, and

we only had one year of difference; (b) spatial and phase resolution of the sensor does not match single tree growth; (c) the measured DSM difference is only a proxy to forest volume change. It does not follow linearly an increase in forest volume, because it does not depend only on height, but on other variables, mainly the vertical structure function (demonstrated in **Chapter 5**). Tracking significant, long-term forest recovery requires high accuracy, high resolution and approximately a minimum 1 year time-lag between two acquisitions to be detected.

The results have major implications and are promising since forest re-growth is usually not detectable using optical spectral reflectance as the three-dimensional distribution of the plant material cannot be observed (Lucas, et al., 2014) and SAR backscatter is not sensitive enough to subtle changes due to removal of plant material and attaining similar values to undisturbed forest at the wavelengths available currently (e.g. Mitchard, et al., 2011). Moreover, the approach is promising as a changes in PCH is proportional to a change in forest biophysical parameters.

The approach developed in **Chapter 5** provides an initial step to detect and map post-disturbance re-growth and given the important implications it requires further work, refining the methods and testing it using denser time-series involving more than two steps.

d) TanDEM-X DSM differencing method to provide carbon stock changes

The method could be used for REDD+ projects sampling schemes to provide carbon stock loss due to degradation, an area of considerable interest as no current satellite systems provide such data.

IPCC Good Practice Guidance states that emissions need to be reported as the activity area by the emission factor (Penman, et al., 2003). TanDEM-X difference approaches would be able to provide the emission factor per unit of ΔDSM (m) instead of per unit area (ha) (Solberg, et al., 2015). A pre-requisite for this is that the InSAR height needs to be proportional to AGB and stable over time (Solberg, et al., 2015). A linear relationship between InSAR height and AGB was found for a boreal forest site (Solberg, et al., 2014) and for miombo woodland (Solberg, et al., 2015) but

this approach has not yet been tested in more structurally diverse tropical forest (e.g. in the Congo Basin tropical forests), a priority area for REDD+ projects to be developed. However, the scope of the PhD was not to assess the relationship between AGB and InSAR height since this would require ground-based AGB estimates which were not available for the site. This should be considered in future research.

e) Independence of forest height changes from terrain elevation in the TanDEM-X DSM differencing method

Chapter 5 demonstrated that using a pair of multiple TanDEM-X observations we could map (spatially) and measure the magnitude of changes in forest height in the resolution element (forest volume) independently from the stable topographic component. This has implications for extraction of the signal due to canopy volume (as terrain elevation contributes to the DSM, albeit at low spatial frequency, as demonstrated in **Chapter 4)**.

Removing the terrain elevation component from a DSM without the use of an external DTM has implications for the extraction of canopy height variation alone which could only otherwise be accomplished using an auxiliary DTM (e.g. from LiDAR). Given that there are currently no high resolution DTMs available from spaceborne radar (aside from a low resolution 90 m C-band DEM provided by the Shuttle Radar Topographic Mission) or spaceborne LiDAR which are able to provide topography information, the approach used in **Chapter 5** is a key outcome with major implications to study vegetation structure.

The forthcoming launch of NASA's Global Ecosystem Dynamics Investigation (GEDI) mission will provide topography information (Qi & Dubayah, 2016) which could potentially be used in combination with TanDEM-X but currently removal of terrain elevation through TanDEM-X differences is the only available option. Currently, TanDEM-X is also the only available single-pass spaceborne interferometer (Krieger, et al., 2007) and source of radar based DSMs.

Given the promising research findings there is great potential for mapping those changes that are due to complete or partial forest loss (deforestation/forest degradation) and gain (forest re-growth) using three-dimensional spaceborne radar so planning future missions that acquire data in single-pass interferometric mode should be considered a priority as well as using the current data provided by TanDEM-X.

6.2.2. Implications for Forest Mapping and Monitoring

The UN Framework Convention on Climate Change (UNFCCC) has recognised the contribution of forest degradation (in addition to deforestation) as an important part in global carbon emissions by including it into the Reducing Emissions from Deforestation and Forest Degradation scheme (REDD+) (UNFCCC, 2008; UNFCCC, 2015). Forest degradation emissions are reported to have contributed to 25% of the total emission from deforestation and forest degradation (2005-2010 estimates) (Pearson, et al., 2017). Efforts to reduce and eventually reverse deforestation and forest degradation to provide about 20% of the reduction in greenhouse gases are crucial but the capacity to estimate these operationally is still lacking with methodologies lagging behind data availability.

So far, optical sensors capabilities have been extensively researched and are routinely used to support deforestation mapping (e.g. PRODES from INPE using Landsat) (Souza, et al., 2013) and globally (Hansen, et al., 2013). Attempts have also been made to use optical data to map forest degradation (Stone & Lefebvre, 1998; Souza, et al., 2005; Hirschmugl, et al., 2014), but with mixed results so far. Fundamentally, optical data cannot see through the top layer of the canopy, so sub-canopy degradation will remain invisible unless accompanied by secondary features such as logging roads (see **Chapter 1**).

SAR is not currently used much for operational forest monitoring despite its many well established advantages. Its use is likely to be further enhanced by the large amount of freely available data from ESA Sentinel-1 (European Space Agency, 2013), increase in commercial data availability (e.g. TanDEM-X), increased

automated processing and as algorithms will be further developed (Global Forest Observations Initiative, 2014).

The use of InSAR to support REDD+ projects is even less developed (especially as TanDEM-X, the only spaceborne single-pass interferometer has only been available since 2010) (Krieger, et al., 2007) and requires much research. In this context, **Chapter 4** and **Chapter 5** provide important developments and increased understanding of the role of InSAR for this purpose.

Whilst, the PhD thesis was not set up to directly contribute to REDD+ initiatives, it seeks to improve understanding of how canopy structure changes are reflected in spatial statistics of SAR backscatter and InSAR DSM and the potential of InSAR DSM change detection. This has implication for the future use of SAR and InSAR approaches that can be fed into international initiatives once these approaches can be considered robust enough to be used operationally.

As well, as for international initiatives such as REDD+ projects, local scale conservation projects could also benefit from the use of SAR and InSAR remote sensing to provide estimates of deforestation as well as forest degradation and re-growth.

Conservation and restoration practices have been primarily targeted towards the conservation of intact forests (Lewis, et al., 2015) but as the proportion of these is set to be decrease in the future due increased pressure, for instance, impacts of forest fires due to El Niño patterns that are forecasted to become more frequent and of increased magnitude (Cai, et al., 2014), timber extraction from extensive areas of forest granted to logging concessions (e.g. in the Congo logging concessions occupy 42.9% of the land area) (Nasi, et al., 2012) there is a need for conservation and restoration efforts to target these areas too. Moreover, the combination of multiple degradation drivers affecting the same area (e.g. selective logging followed by fire disturbance) exacerbates the vulnerability to future disturbance events (Siegert, et al., 2001). This has also been recently observed in the Congo Basin, where dry conditions driven by El Niño have increased forest flammability leading fires to spread from logging concessions (Verhegghen, et al., 2016).

Knowledge on the location and extent (as well as changes in carbon stocks) of degraded forest is crucial to inform forest management (e.g. it can provide estimates of the ability of forests to recover after disturbance), conservation (e.g. provide information on conservation value based on the magnitude of degradation) (**Chapter 5**) and to prioritise areas suitable for restoration projects (**Chapter 3**, **4** and **5**).

More specifically, **Chapter 5** has shown the potential of high resolution InSAR (< 5 m resolution) for detecting shifting cultivation and the magnitude of change in areas where this is undertaken by small holders at sub-hectare scales primarily (~ 0.25 ha in certain areas of the Congo Basin) (Wilkie, et al., 1998) to hectare scales (Brown & Lugo, 1990). The higher resolution of TanDEM-X (4.6 m) makes it suitable to detect small scale changes (1 TanDEM-X pixel = 0.002 ha) which is much lower compared to changes detected by the 30 m resolution (0.09 ha) Hansen's Global Forest Cover product (Hansen, et al., 2013).

In principle, TanDEM-X is able to detect canopy gaps from selective logging of trees which are reported to be on average 719 m^2 (0.07 ha) in the Congo Basin (Pearson, et al., 2014) (gaps can be larger if a set of commercially valuable trees are clustered together) (Van Gemerden, et al., 2003) (if the acquisitions are taken at appropriate time before and after the event). Furthermore, areas with increased number of samples in higher resolution imagery are more likely to belong to a 'true change' rather than attributed to instrument noise. Whilst, smaller changes (< 100 TanDEM-X pixels) were detected in **Chapter 5** these could not be validated using the auxiliary data (provision of data related to logging would be required for this purpose).

Our approach also detects and validates (using VHR optical data and ensures significance of changes compared to no-change areas) much smaller changes (≅ 100 TanDEM-X pixels = 0.2 ha) compared to the PRODES products for instance (minimum mapping unit = 6.25 ha) (Shimabukuro, et al., 2012). The advantage of the approach used in **Chapter 5** consists in detecting the magnitude of change which is not reported by the Hansen's Global Forest Cover Loss dataset for instance (this

only provides a yearly binary change/no change product). It is important to note that our approach has been tested only for a selected site while Hansen's product is available globally.

Chapter 3 and **Chapter 5** focused on the Congo Basin tropical forests which are reportedly not as well studied compared to other tropical forest areas (Malhi, et al., 2013). In the Congo Basin, small scale processes (e.g. selective logging and shifting cultivation) are widespread (e.g. a total of over 49 million ha have been allocated to forest concessions) (Marquant, et al., 2015) so monitoring these processes needs to be urgently addressed (Verhegghen, et al., 2016) using novel remote sensing approaches.

Two of the countries considered in the PhD thesis host extensive logging concessions and are dominated by shifting agriculture. For instance, in Cameroon the area allocated to forest concessions (e.g. a total of 87 Forest Management Units) covered 5.5 million ha (Mertens, et al., 2011) and in the Republic of Congo this is 19.9 million ha (2011 estimates) (Mertens, et al., 2011). Shifting cultivation in the Congo Basin is considered the third largest land use (438,801 km^2) (Nasi, et al., 2009).

Here, there is comparatively less research undertaken related to detecting degraded and regenerating forest especially using SAR and InSAR as forest degradation drivers are more challenging to detect compared to the better studied Brazilian Amazon (e.g. operational mapping undertaken by INPE) (Souza, et al., 2013) where the majority of disturbance is related to deforestation for industrial purposes as opposed to smaller-scale degradation occurring in Africa (e.g. selective logging consists in the extraction of ~1 stem/ha) (Hall, et al., 2003) and small scale shifting agriculture (Laporte, et al., 2004). Therefore, the work has implications and benefits for improved mapping and monitoring of African tropical forest disturbance from SAR and InSAR. **Chapter 3** and **Chapter 4** have implications as a starting point for improved classification of degraded forest based on wavelet signatures and wavelet spectra, these providing two-point statistic of either

backscatter or DSM. Moreover, **Chapter 3** highlights that one-point statistic (variance) of SAR backscatter alone is not sufficient for this detection.

Chapter 5 demonstrated the use of an object-based change detection approach to map negative and positive forest changes exploiting DSM differences between two acquisitions. Single-pass acquisitions limits the effect of temporal decorrelation with the main source of decorrelation due to forest volume (Martone, et al., 2016) which enabled changes to be linked primarily to forest loss (deforestation or forest degradation) and forest gain (forest re-growth). The future provision of classifications including the extent of degraded forests will be beneficial to forest managers and the provision of maps related to forest re-growth will be useful to assess the ability (and the rate) of forests recovery after deforestation or degradation events. Provision of such products requires further research.

The research was not aimed at providing AGB or carbon stocks changes for tropical forests, which is still considered a major challenge due to SAR backscatter saturation at 60–100 Mg/ha at L-Band (Carreiras, et al., 2012) (depending on sensor's parameters and forest type primarily). This saturation point is much lower than the mean AGB estimated in tropical forests (e.g. mean AGB equal to 429 Mg/ha and in the intact forest of the Congo Basin) (Lewis, et al., 2013).

The approach suggested in **Chapter 5** does open up a method for detecting height changes, which could be related to AGB. However, the method provides only a starting point to the solution of the problem. Indeed, the differential DSM provides changes of the phase centre height (PCH) within the forest volume, this being a fractional measure, not true forest height. To arrive at true height change estimates the PCH must be related to at least true height at time zero. However, difficulties remain in retrieving forest height from spaceborne X-band InSAR in tropical forests since penetration is not enough to estimate the phase ground return (Kugler, et al., 2014). Moreover, conversion from height to AGB would still be needed. All in all, but the problem of detecting AGB changes would call for more field data and potentially multi-date aircraft LiDAR data.

Other problems arise from the fact that SAR backscatter is not directly related to AGB (Woodhouse, et al., 2012), and the non one-to-one mapping of InSAR derived forest height to AGB. The BIOMASS mission (P-band, λ= 69 cm) (Le Toan, et al., 2011) will provide increased AGB dynamic range retrieved from SAR thanks to the higher sensitivity of P-band to larger tree components (e.g. trunk and large branches) as sensitivity to AGB increases with wavelength (Dobson, et al., 1992), and will thus represent a real step forward for SAR mapping of AGB change.

6.3. Future Research and Improvements

a) Disturbed forest classification using spatial statistic of SAR backscatter or InSAR DSMs

The use of SAR backscatter and interferometric phase wavelet spectra spatial statistic was successful (with associated limitations and external factors influences taken into consideration) for the discrimination between intact and disturbed forest (degraded forest through selective logging or after a fire event). Classification itself was not performed as the ability to use all the information derived from wavelet-based approaches requires new classification methods to be developed and should be considered for future work (**Chapter 3** and **Chapter 4**). It is however to be noted that the wavelet spectrum provides local estimates of the two-point SAR statistic for each pixel in the dataset. This feature would enable a pathway to the implementation of classical classification algorithms.

b) Forest degradation and re-growth mapping improvements

Employing a longer time-lag between acquisitions (more than one year tested in **Chapter 5**) could in principle be a way to assess the stage of forest recovery. If over a large area forest gain matches a magnitude equal to forest loss, as measured in the case of deforestation, then it will have achieved a similar structure to undisturbed forest in terms of PCH and can be used to give an approximation of the time taken for forest to recover relative to a pre-disturbance baseline. However, this can only be achieved from 2010 when

TanDEM-X was launched until present, which is a relatively short time-frame for significant forest recovery to have occurred.

While, a long time-series with a shorter sampling (e.g. 5 months) might be effective to detect shorter term re-growth. This is however, restricted by the fact that, according to our analysis, ΔDSM gain between 0-1 m will be within the sensor noise level and therefore cannot be considered a significant change. This figure might be different using other TanDEM-X configurations (e.g. much longer baselines to improve the interferometer sensitivity).

The possibility to detect individual successional stages within the post disturbance re-growth objects (rural-complex) will also need to be tested by employing for instance a pixel-based approach or by using texture within the objects extracted.

Considering the significant potential of InSAR to map two significantly challenging processes (forest degradation and forest re-growth) there is a need for future missions to be able to acquire InSAR data providing three-dimensional information over large, continuous areas, a considerable advantage over current LiDAR based three-dimensional datasets from either aircraft or satellites.

c) Digital Surface Model time-series

TanDEM-X DSM provides interferometric data time-series (dependent on data availability and acquisition parameters for the location of choice) acquired since the first acquisition phase in 2010 (Martone, et al., 2012). Future work, should seek to test the change detection algorithm using more data takes to provide yearly (or monthly depending on availability and algorithm performance) estimates of deforestation, forest degradation and re-growth for a set of locations. These data are highly suitable for test sites for national or sub-national scale REDD+ degradation monitoring, or Verified Carbon Standard style voluntary carbon projects: we hope a collaboration between such projects and researchers take up this opportunity. There has been much talk of using

repeat LiDAR for these purposes, but TanDEM-X DSMs may provide a much cheaper option providing less high resolution, but still suitable data.

6.4. References

- Brown, S. & Lugo, A. E., 1990. Tropical secondary forests. *Journal of Tropical Ecology*, 6(1), pp. 1-32.
- Cai, W. B. S. et al., 2014. Increasing frequency of extreme El Niño events due to greenhouse warming. *Nature Climate Change*, 4(2), pp. 111-116.
- Carreiras, J. M. B., Vasconcelos, M. J. & Lucas, R. M., 2012. Understanding the relationship between aboveground biomass and ALOS PALSAR data in the forests of Guinea-Bissau (West Africa). *Remote Sensing of Environment*, Volume 121, pp. 426-442.
- Dobson, C. M. et al., 1992. Dependence of Radar Backscatter on Coniferous Forest Biomass. *IEEE Transactions on Geoscience and Remote Sensing*, 30(2), pp. 412-415.
- European Space Agency, 2013. *Sentinel-1 User Handbook.* [Online]. Available at: https://sentinel.esa.int/web/sentinel/user-guides/sentinel-1-sar/revisit-and-coverage [Accessed 21 June 2016].
- Global Forest Observations Initiative, 2014. *Integrating remote-sensing and ground-based observations for estimation of greenhouse gases in forests.* [Online]. Available at: https://unfccc.int/files/methods/redd/submissions/application/pdf/redd_20140218_mgd_report_gfoi.pdf [Accessed 20 January 2014].
- Hall, J. S., Harris, D. J., Medjibe, V. & Ashton, M. S., 2003. The effects of selective logging on forest structure and tree species composition in a Central African forest: implications for management of conservation areas. *Forest Ecology and Management*, 183(1), p. 249–264.
- Hansen, M. et al., 2013. High-Resolution Global Maps of 21st Century Forest Cover Change. *Science*, 342(6160), pp. 850-853.
- Hirschmugl, M., Steinneger, M. & Gallaun, H. a. S. M., 2014. Mapping forest degradation due to selective logging by means of time-series analysis: Case studies in Central Africa. *Remote Sensing* , 6(1), p. 756–775.
- Krieger, G. et al., 2007. TanDEM-X: A Satellite Formation for High-Resolution SAR Interferometry. *IEEE Transactions on Geoscience and Remote Sensing*, 45(11), pp. 3317-3341.

- Kugler, F. et al., 2014. TanDEM-X Pol-InSAR Performance for Forest Height Estimation. *IEEE Transactions on Geoscience and Remote Sensing,* 52(10), pp. 6404-6422.

- Laporte, N. T. et al., 2004. Towards an operational forest monitoring system for Central Africa. In: G. Gutman, et al. eds. *Land Change Science: Observing, Monitoring and Understanding Trajectories of Change on the Earth's Surface.* The Netherlands: Kluwer Academic Publishers, pp. 97-110.

- Le Toan, T. et al., 2011. The BIOMASS mission: Mapping global forest biomass to better understand the terrestrial carbon cycle. *Remote Sensing of Environment,* 115(1), pp. 2850-2860.

- Lewis, S. L., Edwards, D. P. & Galbraith, D., 2015. Increasing human dominance of tropical forests. *Science,* 349(6250), pp. 827-832.

- Lewis, S. L. et al., 2013. Above-ground biomass and structure of 260 African tropical forests. *Philosophical Transactions of the Royal Society B,* 368(1625), p. 20120295.

- Liesenberg, V., de Souza Filho, C. R. & Gloaguen, R., 2016. Evaluating Moisture and Geometry Effects on L-Band SAR Classification Performance Over a Tropical Rain Forest Environment. *IEEE Journal of Selected Topics in Applied Earth Observations and Remote Sensing,* 9(12), pp. 5357-5368.

- Lucas, R. M. et al., 2014. Mapping forest growth and degradation stage in the Brigalow Belt Bioregion of Australia through integration of ALOS PALSAR and Landsat-derived foliage projective cover data. *Remote Sensing of Environment,* Volume 155, pp. 42-57.

- Luckman, A. J., Frery, A. C., Yanasse, C. C. F. & Groom, G. B., 1997. Texture in airborne SAR imagery of tropical forest and its relationship to forest regeneration stage. *International Journal of Remote Sensing,* 18(6), pp. 1333-1349.

- Malhi, Y. et al., 2013. African rainforests: past, present and future. *Philosophical Transactions of the Royal Society B,* 368(1625), p. 20120312.

- Marquant, B. et al., 2015. Chapter 1: The Importance of Central Africa's Forests. In: C. de Wasseige, M. Tadoum, R. Eba'a Atyi & C. Doumenge, eds. *The Forests of the Congo Basin: Forest and Climate Change.* Neufchâteau: Weyrich, Belgium, p. 128.

- Martone, M. et al., 2012. Coherence evaluation opf TanDEM-X interferometric data. *ISPRS Journal of Photogrammetry and Remote Sensing,* Volume 73, pp. 21-29.

- Martone, M., Rizzoli, P., Krieger & Gerhard, 2016. Volume Decorrelation Effect in TanDEM-X Interferometric SAR Data. *IEEE Geoscience and Remote Sensing Letters,* 13(12), pp. 1812-1816.

- Mayaux, P. et al., 2013. State and evolution of the African rainforests between 1990 and 2010. *Philosophical Transactions of the Royal Society B,* 368(1625), p. 20120300.
- Mertens, B. et al., 2011. *Atlas Forestier Interactif Du Congo,* Washington, DC: World Resources Institute.
- Mertens, B., Shu, G. N., Steil, M. & Tessa, B., 2011. *Interactive Forest Atlast of Cameroon. Version 3.0,* Washington, DC: World Resources Institute.
- Mitchard, E. T. A. et al., 2011. Measuring biomass changes due to woody encroachment and deforestation/degradation in a forest–savanna boundary region of central Africa using multi-temporal L-band radar backscatter. *Remote Sensing of Environment,* 115(11), pp. 2861-2873.
- Nasi, R., Billand, A. & Vanvliet, N., 2012. Managing for timber and biodiversity in the Congo Basin. *Forest Ecology and Management,* Volume 268, pp. 103-111.
- Nasi, R. et al., 2009. Chapter 12: A first look at carbon stocks and their variations in Congo Basin Forests. In: C. de Wasseige, et al. eds. *State of the Forests 2008.* Luxembourg: Publications Office of the European Union, p. 191–208.
- Oliver, C. & Quegan, S., 2004. *Understanding Synthetic Aperture Radar Images.* 2nd ed. Herndon, VA: SciTech Publishing.
- Pearson, T. R. H., Brown, S. & Casarim, F. M., 2014. Carbon emissions from tropical forest degradation caused by logging. *Environmental Research Letters,* 9(3), pp. 1-11.
- Pearson, T. R. H., Brown, S., Murray, L. & Sidman, G., 2017. Greenhouse gas emissions from tropical forest degradation: an underestimated source. *Carbon Balance and Management,* 12(3), pp. 1-11.
- Penman, J. et al., 2003. *Good Practice Guidance for Land Use, Land-Use Change and Forestry,* Hayama, Kanagawa (Japan): The Intergovernmental Panel on Climate Change (IPCC).
- Petrou, M. & García Sevilla, P., 2006. *Image Processing: Dealing with Texture.* 1st ed. Chichester, West Sussex, England: John Wiley & Sons.
- Qi, W. & Dubayah, R. O., 2016. Combining Tandem-X InSAR and simulated GEDI lidar obesrvations for forest structure mapping. *Remote Sensing of Enivironmnet,* Volume 187, pp. 253-266.
- Shimabukuro, Y. E. et al., 2012. The Brazilian Amazon monitorung program: PRODES and DETER projects. In: F. Achard & M. C. Hansen, eds. *Global Forest Monitoring from Earth Observation.* Boca Raton, FL: CRC Press/Taylor & Francis Group, p. 153–169.

- Siegert, F., Ruecker, G., Hinrichs, A. & Hoffmann, A., 2001. Increased damage from fires in logged forests during droughts caused by El Nino. *Nature,* 414(6862), pp. 437-440.
- Solberg, S. et al., 2015. Monitoring forest carbon in a Tanzanian woodland using interferometric SAR: a novel methodology for REDD+. *Carbon Balance and Management,* 10(14), pp. 1-14.
- Solberg, S., Næsset, E., Gobakken, T. & Bollandsås, O.-M., 2014. Forest biomass change estimated from height change in interferometric SAR height models. *Carbon Balance and Management,* 9(5), pp. 1-12.
- Souza, C. M. J., Roberts, D. A. & Cochrane, M. A., 2005. Combining spectral and spatial information to map canopy damage from selective logging and forest fires. *Remote Sensing of Environment,* 98(2), pp. 329-343.
- Souza, C. M. J. et al., 2013. Ten-Year Landsat Classification of Deforestation and Forest Degradation in the Brazilian Amazon. *Remote Sensing,* 5(11), pp. 5493-5513.
- Stone, T. A. & Lefebvre, P., 1998. Using multi-temporal satellite data to evaluate selective logging in Para, Brazil. *International Journal of Remote Sensing* , 19(13), pp. 517-2526.
- UNFCCC, 2008. *Report of the conference of the parties on its thirteenth session, held in Bali from 3 to 15 December 2007* , Bali: UNFCCC.
- UNFCCC, 2015. *Conference of the Parties (COP): Adoption of the Paris Agreement. Proposal by the President,* Geneva, Switzerland: United Nations Office.
- van der Sanden, J. & Hoekman, D. H., 1999. Potential of Airborne Radar to Support the Assessment of Landcover in a Tropical Rainforest. *Remote Sensing of Environment,* 68(1), pp. 26-40.
- van der Sanden, J. J., 1997. *Radar remote sensing to support tropical forest management.* PhD thesis ed. Wageningen: Tropenbos-Guyana Programme.
- Van Gemerden, B., Shu, G. N. & Han, O., 2003. Recovery of conservation values in Central African rain forest after logging and shifting cultivation. *Biodiversity and Conservation,* 12(8), pp. 1553-1570.
- Verhegghen, A. et al., 2016. The Potential of Sentinel Satellites for Burnt Area Mapping and Monitoring in the Congo Basin Forests. *Remote Sensing* , 8(986), pp. 1-22.
- Wilkie, D., Curran, B., Tshombe, R. & Morelli, G. A., 1998. Modelling the Sustainability of Subsistence Farming and Hunting in the Ituri Forest of Zaire. *Conservation Biology* , 12(1), pp. 137-147.

- Woodhouse, I. H. et al., 2012. Radar backscatter is not a 'direct measure' of forest biomass. *Nature Climate Change,* 2(8), pp. 556-557.

Appendix I: Published version of Chapter 3

Spatial Wavelet Statistics of SAR Backscatter for Characterizing Degraded Forest: A Case Study From Cameroon

Elsa C. De Grandi, *Member, IEEE*, Edward Mitchard, *Member, IEEE*, Iain H. Woodhouse, and Gianfranco D. De Grandi, *Fellow, IEEE*

***Abstract*—Forest degradation is an important issue in global environmental studies, albeit not yet well defined in quantitative terms. The present work addresses the problem, by starting with the assumption that forest spatial structure can provide an indication of the process of forest degradation, this being reflected in the spatial statistics of synthetic aperture radar (SAR) backscatter observations. The capability of characterizing landcover classes, such as intact and degraded forest (DF), is tested by supervised analysis of ENVISAT ASAR and ALOS PALSAR backscatter spatial statistics, provided by wavelet frames. The test is conducted in a closed semideciduous forest in Cameroon, Central Africa. Results showed that wavelet variance scaling signatures, which are measures of the SAR backscatter two-point statistics in the combined space-scale domain, are able to differentiate landcover classes by capturing their spatial distribution. Discrimination between intact and DF was found to be enabled by functional analysis of the wavelet scaling signatures of C-band ENVISAT ASAR data. Analytic parameters, describing the functional form of the scaling signatures when fitted by a third-degree polynomial, resulted in a statistically significant difference between the signatures of intact and DF. The results with ALOS PALSAR, on the other hand, were not significant. The technique sets the stage for promising developments for tracking forest disturbance, especially with the future availability of C-band data provided by ESA Sentinel-1.**

***Index Terms*—Degraded forest (DF), spatial statistics, synthetic aperture radar (SAR), texture, wavelet transform.**

I. Introduction

FORESTS play a fundamental role in the exchange of gases and energy between the atmosphere and biosphere. In particular, degraded forests (DFs) in tropical forest ecosystems are a large component of the global carbon balance, with the process of degradation representing a large but hard to quantify source of carbon, whereas regrowing DFs are also responsible for a significant carbon sink [1]. Recognition of the role of deforestation and forest degradation by the U.N. General Assembly has stressed the need for mapping the extent of deforested and degraded forests [2], in order to enable a successful system for reducing emission from deforestation and forest degradation (REDD+). The International Tropical Timber Organization estimated that there are up to 850 million ha of tropical forest which have already been degraded [3] due to intensive pressures such as logging, slash and burn agriculture, and shifting cultivation outside of protected areas.

Forest degradation in a remote sensing context can be defined from the ecological standpoint and at a conceptual level as an environmental change process, where a disturbance causes the system to evolve from an initial state toward a final state with loss of valuable properties (e.g., canopy cover or carbon stocks) or capacities (e.g., provision of fuelwood and other ecosystem services). This initial state constituted a spatially contiguous and unmanaged old-growth forest [intact forest (IF)]. If some of its structural and physical properties are affected by a major disturbance (logging, fire, insect infestation, timber harvest, or windthrow), then the system will change to a final state, characterized by a different forest type (i.e., secondary forest or disturbed forest).

A mapping between the ecological process of forest degradation and physical observables is needed to provide measures of its onset and extent. The basic tenet of the work presented in this paper is that the process of forest degradation will result in a change of the forest structure. As a consequence, the mapping was established by considering synthetic aperture radar (SAR) backscatter spatial statistics (texture) as a measure of forest structure, this in turn being one of the ecological variables that can be assumed to be a fingerprint of the degradation process. Different stages of the degradation process will result in changes of the statistics. For instance, removal of part of an old-growth forest will correspond to the transition from some stationary regime due to backscattering from the irregular top layer of the canopy [e.g., K-distributed with an exponential cosine autocorrelation function (ACF)] [4] to some nonstationary or intermittent regime. At the final stage of regrowth, when a secondary forest will have taken place, the statistics will revert back to stationary, albeit with different correlation properties due to the different horizontal structure.

This starting assumption is tested by supervised statistical analysis of spatial random fields (SRFs) provided by SAR observations at C- and L-band, i.e., calculating statistics over

Manuscript received September 30, 2014; revised February 14, 2015; accepted March 23, 2015. Date of publication May 07, 2015; date of current version August 11, 2015. This work was supported in part by the School of GeoSciences, University of Edinburgh, and in part by the Principal's Career Development Scholarship, University of Edinburgh. The work of E. Mitchard was supported by a Research Fellowship from the Natural Environment Research Council (NE/I021217/1).

E. C. De Grandi, E. Mithcard, and I. H. Woodhouse are with the School of GeoSciences, University of Edinburgh, Edinburgh EH9 3FF, U.K. (e-mail: E-De-Grandi@sms.ed.ac.uk; edward.mitchard@ed.ac.uk; i.h.woodhouse@ed.ac.uk).

G. D. De Grandi was with European Commission, Joint Research Center, Ispra 21027, Italy. He is now with Aberystwyth University, Aberystwyth SY23 3F, U.K. (e-mail: gid6@aber.ac.uk).

Color versions of one or more of the figures in this paper are available online at http://ieeexplore.ieee.org.

Digital Object Identifier 10.1109/JSTARS.2015.2420596

Appendix I

areas of interest based on expert knowledge and the interpretation of other satellite. The spatial statistics are derived from a signal representation in a wavelet frame basis. The analysis seeks to assess the capability of these textural measures to discriminate between intact and DF.

This paper is organized as follows. In Section II, the role of remote sensing for mapping forest degradation is explained. In Section III, the test site of the present work is described. Methods for SAR data processing and analysis are found in Section IV. Results are reported and discussed in Section V. Section VI summarizes the findings and gives concluding remarks.

II. Background and Context

Remote sensing plays a primary role for mapping and monitoring deforestation and forest degradation for REDD+ [5]. In particular, compared to deforestation, forest degradation is more difficult to detect using remote sensing [6], [7].

Mapping and monitoring of forest degradation has been accomplished using optical remote sensing due to the availability of Landsat [8], [9] and the distinct spectral response of DF [10]. Fine resolution optical sensors have been most successfully employed for mapping selective logging, including IKONOS [11] and RapidEye [12]; but to our knowledge, such methods have not been used to map actual forest degradation (as opposed to the presence of logging roads) in African forests.

Limitations of optical sensors have given impetus to the use of sensors independent of atmospheric conditions, such as SAR, which allows observations regardless of cloud cover and illumination conditions, but most importantly is sensitive to both forest vertical structure (through interferometry) and horizontal structure (through backscatter and coherence).

Five main aspects related to forest degradation have been the focus of research: 1) above-ground biomass and carbon stock changes using SAR backscatter (e.g., [13]); 2) classification of DF and particularly the contribution of texture (focus of the present research); 3) detection of the removal of single trees using very high resolution SAR imagery (e.g., [14]); 4) use of interferometric phase information to determine a change in the canopy structure which can be associated with removal of vegetation (e.g., [15]); and 5) use of coherence to provide information on canopy openness [16].

The future provision of Sentinel-1 (C-band) will enable to study forest degradation at increased revisit time leading to unprecedented levels of SAR data availability [17]. However, currently, data coverage is limited due to the recent launch of Sentinel-1.

A further topic of interest is the classification of DF, which can be accomplished with the addition of texture that provides complementary knowledge to intensity-only information [18].

The main research that has been employed in the domain of texture analysis for landcover classification includes the use of Haralick parameters based on gray-level cooccurrence matrix (GLCM) ([19]) and spectral analysis (or ACF, these being techniques in the Fourier transform domain). Notice that the ACF provides a two-point statistics, while GLCM is a second-order one-point one.

The limitations in using these methods for the classification of SAR data are twofold. First, direction constraints on GLCM and insensitivity to short-lived high frequencies in the Fourier transform limit the ability of these methods to quantify the evolution of statistical properties through scale [20]. Second, by their nature, SAR sensors are affected by both multiplicative noise and correlated noise: this means that simple relationships among neighboring pixels can either bear no information, being themselves just stationary white noise, or even provide false information; for instance, two constant reflectivity areas might be measured as two textured areas because of the presence of speckle. GLCM and ACFs are both highly sensitive to speckle noise. A way out suggested in related work such as in [21] is to apply these statistics after transforming the input signal to the logarithmic domain. This transform makes the multiplicative noise additive. However, introduces side effects such as compressing high dynamics features and boosting low-level noise, such as thermal noise.

Wavelet transforms provide a modern pathway to time-frequency (space-scale) analysis with better resolution in the combined domain, and superior computational efficiency on the discrete setting. Moreover, wavelet statistics can be normalized in such a way as to be compatible with multiplicative noise without recurring to the logarithmic transform (see Section IV-C)

The field of wavelets developed in the mid-1980s with research by [22]. Originally, wavelet transform developed in the field of geophysics applied to time-series analysis of one-dimensional (1-D) geophysical signals [23]; but since then have been applied in the field of remote sensing including landcover classification using SAR, which is becoming more popular [24].

Techniques based on the use of wavelet transform with SAR imagery have seldom been used in the thematic context of forest degradation. However, wavelet statistics of SAR backscatter in connection with textural analysis was proposed in a different thematic context in [25]and [26] and in general, its utility in image processing have been long understood [27].

III. Study Site

We center our study in Cameroon, a country of great interest for forest monitoring, since it is the African country with the highest percentage of previously logged forests [28]. Over a third of its territory is covered by moist tropical forest, part of the Congo Basin, and the area covered by active or previously active logging concessions extends over $71\,000\,\mathrm{km}^2$, about 40% of total forest area [29]. Cameroon is also a significant hotspot of other forms of forest degradation, including those related to agricultural encroachment, fuelwood extraction, and illegal logging [28]: it is more affected by these than its Congo basis neighbors as it has a significantly higher population density than neighboring Gabon, Democratic Republic of the Congo, or the Republic of Congo.

The study site encompasses semideciduous closed forest located in Deng Deng National Park and its surroundings in Lom et Djerem, Cameroon ($13°4'$ E, $5°28'39$ N). The study site extends for 100×100 km and is delimited by the Sanaga River to the west and the forest savanna transition zone to the

Appendix I

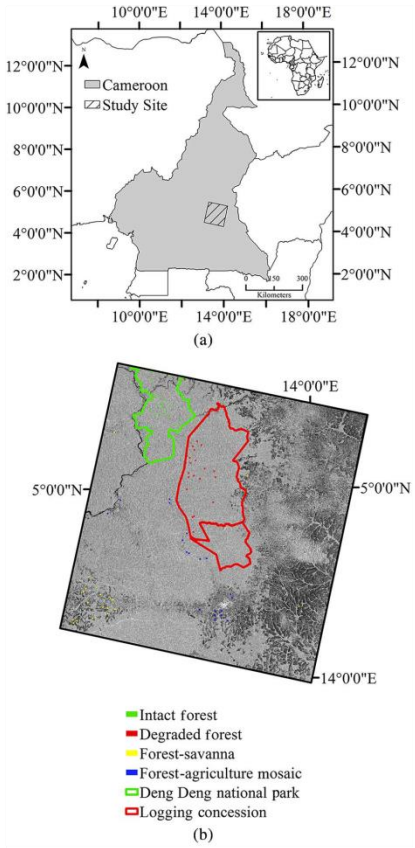

Fig. 1. (a) Study area within the extent of ENVISAR ASAR acquisitions (WGS84, UTM zone 33 N). (b) Location of all landcover samples (n = 20) used in the analysis overlaid on ENVISAT ASAR VV (WGS84, UTM projection-zone 33N). Data source: World Resources Institute and European Space Agency. The green shape outlines the Deng Deng National Park. The yellow shape outlines a logging concession. Red squares mark samples of DF within the concession, green squares mark IF samples in the National Park, yellow squares mark samples within FS and blue squares mark samples within FAM (see also Table II).

east (Fig. 1). The main urban center in the area of study is the region's capital Bertoua while, a high number of rural villages are distributed across the landscape contributing to the highest rate of rural population exploiting forest resources mainly in the form of slash and burn agriculture at small to medium scales [30]. The forest in the area is a semideciduous closed forest dominated by *Sterculiaceae* and *Ulmaceae* and extends to the north of the moist evergreen forest [31]. Human intervention is widespread in the area giving rise to several stages of DF and areas of regenerating forest developing into secondary formations characterized by *Musanga cecropioides* and *Albizia spp.* [32].

Another driver of forest degradation is selective logging within the forest management units (UFAs). The logging industry has been present in the area and exploited forest resources through the selective removal of a limited number of high-value trees. Even though the UFA had been exploited long in the past, the presence of old logging roads was still clearly visible in the 2010 Landsat and RapidEye imagery (and less evident in radar imagery).

The climate is classified as equatorial (Guinean type) with one major wet season (September–November) (monthly rainfall over 250 mm) and dry season with rainfall as low as 10 mm (December–February) [33]. Rainfall at the time of ENVISAT ASAR data acquisition (January 15, 2010) and ALOS PALSAR (August 3, 2010) can be considered negligible, since the data was acquired in the dry season. Topography in the study site is hilly to mountainous ranging from 597 to 1060 m with areas of more pronounced topography located to the north of the study site in the forest-savanna (FS) mosaic, whereas topography is more gentle in the areas of semideciduous forest (ranging between 597 and 700 m a.s.l.).

IV. Methods

Methods employed for the analysis of both ENVISAT ASAR (VV) and ALOS PALSAR (HH and HV) scenes comprise the following steps: 1) SAR data processing; 2) thematic class definition and supervised selection of a spatial test set for SAR statistics estimation (43×43 pixels windows) for each class; and 3) wavelet transform of the test set SRFs and wavelet coefficients statistics computation and interpretation.

A. SAR Data Processing

Nine ENVISAT ASAR IMS scenes were acquired between 2003 and 2010 at VV polarization, IS2 mode (23° incidence angle) over the study area. The datasets were processed using the basic processing module available with SARscape 5.0 software [34]. The scenes were multilooked, coregistered, radiometrically calibrated and radiometrically normalized (cosine correction) using a 90-m SRTM DEM, geocoded to WGS84, UTM projection (zone 33N) at 15-m pixel spacing. Importantly, the time-series was speckle filtered using "De Grandi multitemporal filter" available in SARscape 5.0 and based on the principles proposed in [35]. This step enables the reconstruction of the radar cross-section (RCS) with good preservation of its two-point spatial statistics, whereas abating the strength of the high-frequency noise induced by the fading process to a level inversely proportional to the number of samples in the series. It is therefore fundamental with respect to the capability of retrieving textural properties of the imaged target.

Most of the analysis presented here was then undertaken on a single ENVISAT ASAR scene (January 15, 2010), since it was acquired during the dry season with minimal influence from rainfall events and, correspondent with available ALOS PALSAR and RapidEye data.

Appendix I

Twelve ALOS PALSAR fine beam dual (FBD) were acquired between 2007 and 2010 at HH and HV polarizations and 34° incidence angle. This dataset was processed using the same approach as above.

Supplementary optical data for the interpretation of SAR imagery consisted of Landsat ETM+ (slc-off) at 30-m resolution acquired on January 18, 2011 covering the northernmost part of the study site and Landsat ETM+ (slc-on) data acquired on December 27, 2002 covering the southern part of the study area. The scenes were the only available which were not affected by extensive cloud cover and closest to the data of the SAR data acquisition. RapidEye at 5-m resolution was also acquired on December 17, 2010 for training purposes covering a selected area of UFA 10 065 and part of Deng Deng National Park. Contextual data consisting of UFAs, logging roads (digitized with the aid of Landsat), location of protected areas (e.g., Deng Deng National Park) were provided by [36]. The data were used to help with the selection of classes of interest through a supervised analysis.

B. Spatial Test Set Preparation by Supervised Analysis

A supervised analysis was chosen due to unavailability of ground truth data for 2010, thus the use of optical imagery and contextual information was used for training purposes. The analysis uses a 43×43 pixel window (corresponding to 645×645 m on ENVISAT ASAR and ALOS PALSAR geocoded scenes at 15 m pixel spacing). The classes selected correspond to the following: IF, DF, forest-agriculture mosaic (FAM), and FS. Four samples were used in parts of the analysis but twenty samples were selected for each class of interest to ensure a significant sample size for statistical analysis.

IF areas were selected based on contextual information including the extent of Deng Deng National Park and the absence of logging roads and urban centers in the areas chosen. The chosen areas are all located in the northern section of the Deng Deng National Park, which is known to be intact and has no sign of logging roads in any ancillary dataset.

DF was identified based on the presence of inactive logging roads (in 2010) which were clearly visible in both Landsat and RapidEye data at the time of the analysis and were also noticeable back in the 1980s Landsat imagery, thus indicating the long term pattern of disturbance of forest inside the logging concession. FAM could be clearly identified in both Landsat and RapidEye scenes as the most complex and heterogeneous class among those selected due to the presence of a mixture of forest, bare areas, and agricultural fields. The pattern of anthropogenic disturbance was also very clear due to the proximity to rural settlements. FS presented lower backscatter values in ENVISAT ASAR VV and ALOS PALSAR HH and HV scenes compared to dense forested areas.

C. Spatial Statistics From a Wavelet Frame Basis Representation

The spatial statistics of interest are derived from a signal (field) representation provided by a nonorthogonal oversampled discrete wavelet transform (DWT). The basis for this representation is generated by a wavelet frame [37]. The advantage of such an approach in connection with texture (spatial statistic) analysis is proven in [27]. In our case, the mother wavelet in the continuous scale-space domain is the first derivative of a box spline of order 3 [38] (see Fig. 2), with Fourier transform

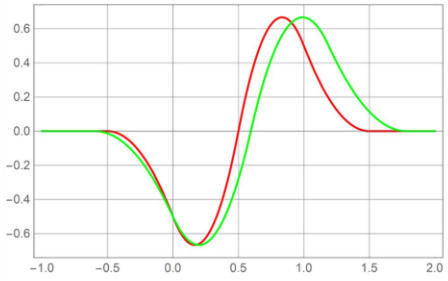

Fig. 2. Mother wavelet (red line) and the dilated by $2^{0.25}$ version (first and second voice).

$$\hat{w}(\omega) = -i\frac{\omega}{4}\left(\frac{\sin\left(\frac{\omega}{4}\right)}{\frac{\omega}{4}}\right)^4 e^{-i\frac{\omega}{2}}. \tag{1}$$

In the discrete case, the transform is implemented using a variant of the à trous algorithm [39], [40] with four voices per octave. The design of the multivoice scheme entails the following steps. For each voice in the first octave, a fractionally dilated wavelet is computed in the frequency domain from (1)

$$\Psi_{\mathrm{dil}}(\omega) = \frac{1}{\sqrt{2^d}} 2^d \Psi\left(2^d\omega\right) e^{-i\omega\left(\frac{1}{2}(2^d-1)\right)} \tag{2}$$

where the fractional dilation factor is $d = 0.25\ k, k = 0 \cdots 3$. The dilated wavelet is normalized by $\frac{1}{\sqrt{2^d}}$ to preserve the norms, and shifted by $e^{-i\omega\left(\frac{1}{2}(2^d-1)\right)}$ in such a way so as to match the zero crossings of the original mother wavelet.

Importantly, the multivoice scheme using the à trous algorithm can only be implemented with the $s^{-1/2}$ normalization to assure equal norms among the mother wavelets which sample the frequency lattice within one octave. In this way, wavelet coefficients corresponding to all voices and octaves carry comparable energy, and can be used in forming measures, e.g., two-point statistics of the signal.

The à trous algorithm [39], [40] calls for the approximation of the continuous space wavelet by means of an interpolating filter. This condition is expressed in the time and frequency domain by

$$\frac{1}{\sqrt{2}}\psi\left(\frac{t}{2}\right) = \sum\nolimits_n h[n]\,\phi(t-n) \tag{3}$$

$$\frac{2}{\sqrt{2}}\Psi_{\mathrm{dil}}(2\omega) = H_j(\omega)\,\Phi(\omega). \tag{4}$$

The high-pass filter coefficients for each fractionally dilated wavelet are computed from (4) by inverse discrete Fourier transform (DFT)

$$h_j[n] = \frac{1}{2\pi}\int_{-\pi}^{+\pi} H_j(\omega)\, e^{i\omega n} d\omega \tag{5}$$

Appendix I

where j is the voice index.

Each dilated high-pass filter h_j for each voice is finally used in a recursive à trous decomposition scheme to generate wavelet coefficients at the corresponding dyadic scales $2^{d+j}, j = 1 \ldots n$.

In case of analysis of a two-dimensional (2-D) field, the DWT is implemented by separable (row, columns) convolutions with a low-pass and a high-pass filter [40]

$$\begin{aligned} f_{s+1}(i,j) &= g_s(j)\, g_s(i) \otimes_j \otimes_i f_s(i,j) \\ c_{x,s+1}(i,j,v) &= h_s(j,v) \otimes_j f_s(i,j) \\ c_{y,s+1}(i,j,v) &= h_s(i,v) \otimes_i f_s(i,j) \end{aligned} \tag{6}$$

where $\bigotimes_j$ is the convolution operator over columns, and $\bigotimes_i$ is the convolution operator over lines, $f_1(i,j)$ is the input signal, h_s is high-pass filter at level s and voice v, g_s is low-pass filter (à trous filter) at level s, both filters being upsampled by dilation with s zeros.

In a nutshell, the multivoice scheme for v voices is implemented by applying the à trous algorithm, valid for power of two scales, v times starting from each fractionally dilated mother wavelet.

Importantly, the wavelet coefficients in (6) are normalized by smooth approximations of the input fields $\overline{f(i,j)_s}$ at the corresponding scale s. The smooth approximations are obtained by convolution with separable smoothing spline filters with unit norm (energy conserving) and dilated by a factor corresponding to the scale s. This position (as pointed out in [25]) is necessary to avoid influence on the wavelet statistics of the fading variable when multiplicative noise is developed, and to equalize the dynamic range of the variable of interest (RCS). Theoretical characterization (bias and variance) of estimators of normalized wavelet coefficients is given in [41].

The mother wavelet (Fig. 2) acts as a differential operator. It is this characteristic that establishes the bridge for reaching over to the spatial statistics of interest. Indeed, a wavelet which is a symmetric and odd function of the space coordinate (as the one considered here), when translated performs differences between averages of the signals around points whose distance is proportional to the dilation factor (scale). This leads to consider the following equivalence between local averages of the wavelet coefficients squared and a two-point statistic known as structure function of order 2

$$\langle {c_{x,s}}^2 \rangle \cong \langle (f(x+\tau) - f(x)^2 \rangle, \quad \text{where } s \overset{yields}{\longrightarrow} \tau \tag{7}$$

where $\langle\rangle$ is a spatial average operator.

In turn, this statistic leads to the characterization of stationary random processes, as well as of nonstationary processes with stationary increments (e.g., fractals) [42]). The wavelet variance as a function of scale provides in the log–log variance/scale plane a characteristic signature of the process and measures of the process parameters, such as correlation structures in stationary processes and the scaling exponent in 1/f processes.

Computationally, the wavelet scaling signature (WASS) is estimated from the wavelet coefficients of the 2-D DWT (6) within a 43×43 pixels window of the backscatter image centered around points of interest (see Section IV-B for the selection criteria)

$$\begin{aligned} WS_x(s) &= \langle c_{x,s}(i,j)^2 \rangle \\ WS_y(s) &= \langle c_{y,s}(i,j)^2 \rangle \end{aligned} \tag{8}$$

where the average is taken over the estimation window. The standard error of the wavelet variance estimator S^2 (8) is $\sigma_{S^2} = S^2 \sqrt{\frac{2}{n-1}}$, where n is the number of samples in the estimation window.

When a second realization of the input random field is available, this being acquired at a different date or with different sensor's configuration (e.g., polarization, incidence angle), a scaling signature can be constructed with the wavelet coefficients cross-correlation

$$\begin{aligned} WCRS_x(s) &= \frac{\langle c_{x,s^1}(i,j)\, c_{x,s^2}(i,j) \rangle}{\left(\langle c_{x,s^1}(i,j)^2 \rangle \langle c_{x,s^2}(i,j)^2 \rangle \right)^{1/2}} \\ WCRS_y(s) &= \frac{\langle c_{y^1}(s,i,j)\, c_{y^2}(s,i,j) \rangle}{\left(\langle c_{y,s^1}(i,j)^2 \rangle \langle c_{y,s^2}(i,j)^2 \rangle \right)^{1/2}}. \end{aligned} \tag{9}$$

In the case of spatial statistics, this signature provides an indicator of the textural difference of the observed random fields between acquisitions. For acquisitions at different dates, the wavelet cross-correlation extends the statistics to the time–space–frequency domain.

A second point of view leads us to consider the generation of a scale-dependent gradient field $\epsilon(s,x,y)$ from the wavelet coefficients, which in turn can be used as a random measure in intermittency analysis. Intermittency in our context can be generated in a random field by the presence of singularities such as edges and point targets. The normalized fourth moment of the gradient modulus (called the flatness factor) is taken in this case as an indicator of intermittency within the random field. Indeed, the fourth moment of a probability density function (pdf) (kurtosis) is related to the flatness of the distribution's tails. Since the wavelet frame is a differential operator, thick tails of the distribution indicate the presence of spikes or events with high derivative. The wavelet flatness factor signature (dependence on scale) is computed in a way similar to the wavelet scaling signature (9)

$$\begin{aligned} FlS_x(s) &= \frac{\langle c_{x,s}(i,j)^4 \rangle}{\langle c_{x,s}(i,j)^2 \rangle^2} \\ FlS_y(s) &= \frac{\langle c_{y,s}(s,i,j)^4 \rangle}{\langle c_{y,s}(s,i,j)^2 \rangle^2}. \end{aligned} \tag{10}$$

Finally, the gradient field modulus squared can be interpreted as the signal energy captured at every point visited by the translated and dilated wavelet in the space-scale lattice and within the resolution cell at that point (Heisenberg box [38]). Local estimates of the $\epsilon(s,x,y)$ field through the related wavelet coefficients provide a space–frequency analysis of the input random field energy, which is called the wavelet spectrum. The wavelet spectrum is computed by convolution of the wavelet

TABLE I
WAVELET RESOLUTION FOR THE FIRST FOUR VOICES

Scale	σ_{space}(m)	σ_{period}(m)	σ_{freq} (cycles /winl)
2^0	11.34	4.20	1513
$2^{0.25}$	13.48	5.19	1227
$2^{0.5}$	16.03	9.42	675
$2^{0.75}$	19.07	19.76	322
2	22.68	40.61	156

coefficients with a smoothing kernel (a cubic spline β_m, with support $\mathrm{m} = 25$ pixels)

$$Wspctr\,(s,i,j) = \left(c_{x,s}(i,j)^2 + \langle c_{y,s}(i,j)^2\rangle\right) \otimes \beta_m\,(i,j)\,. \tag{11}$$

Since $Wspctr\,(s,i,j)$ is a function of three variables, a three-dimensional (3-D) graphic representation is obtained by averaging in one direction (columns or rows). The spectrum is then pictured in a 2-D density plot, with space, scale on the x-, y-axis and a color palette to represent power density.

In space-scale (time–frequency) analysis, which underpins all the derived spatial statistics considered here, the most important factor is the combined resolution in the two dimensions of the domain. Wavelet provides adaptive resolution with increased frequency support and short-time spread at short scales, and decreased frequency support and wider time spread at long scales. It is important to quantify the combined resolutions and to put these measures in comparison with the order of magnitude of space variations expected in the physical phenomenon of interest (e.g., forest canopy horizontal distribution). The space and frequency spread of the wavelet was computed as follows.

The wavelet $\psi\,(s,x)$ at each scale s is normalized in such a way that $\|\psi\| = 1$ and shifted to be centered at $\mathrm{x} = 0$. In this way, the spread in space and frequency is

$$\sigma_x^2 = \int_{-\infty}^{+\infty} x^2\psi^2 dt \tag{12}$$

$$\sigma_\omega^2 = \int_{-\infty}^{+\infty} (\omega-\eta)^2\hat{\psi}^2 d\omega \tag{13}$$

where $\hat{\psi}$ is the Fourier transform of ψ and η is the center frequency.

The spread σ_x and σ_ω were computed for the first four voices (Table I).

In Table I, $\sigma_{space}\,(m)$ is the resolution in space related to the reference system of the geocoded SAR imagery with a pixel spacing of 15 m. $\sigma_{period}\,(m)$ is the resolution if frequency given as a period $T = \frac{2\pi}{\omega}$, where ω is the frequency in radians/m. $\sigma_{freq}\,(\mathrm{cycles/winl})$ is the resolution in frequency given as number of cycles within the estimation window length.

Values in the table can be interpreted as follows. First, notice that resolutions in the space-scale (time–frequency) plane were computed for the continuous wavelet transform, therefore, space is defined on the real numbers set, and the support of the mother wavelet at scale 1 is in $d = [-1, 1]$. Normalized values in the space domain are then converted in metric units with $d \triangle x\,[\mathrm{m}] = [-15, 15]$. Values at the next dyadic scales can be computed simply by multiplication (division) by 2.

With these figures in mind, let us imagine of considering a backscatter signal portraying intermittent hard targets (e.g., buildings) and periodic features (e.g., a forest canopy or ocean waves). Values $\sigma_{space}\,(\mathrm{m})$ tell us that we could distinguish, by the wavelet multiscale representation, the impulsive features if they are spaced apart a distance greater than these values. Values $\sigma_{period}\,(\mathrm{m})$ tell us that we could detect the periodic features if their period is greater than those values. Finally, the last column gives us an indication of how many oscillations of the periodic phenomena we could at most observe within an estimation window of 615 m.

In our thematic context, we could for instance conclude regarding space resolution: The first four voices do not provide useful information, being the resolution less than the sensor's one; intermittency patterns with characteristic spacing of $2^j \times 23$ m will be best detected at corresponding resonating scales 2^j. Regarding frequency resolution, the spatial frequency components of an homogeneous forest canopy, this developing with a characteristic period of some $2^j \times 40\,\mathrm{m}$ could be best measured at resonating scales 2^j.

D. Connection Between Wavelet Variance Analysis and Fourier Spectral Analysis

Relevance of two-point statistics in connection with SAR imagery textural characterization, in particular of the Fourier spectral analysis and the ACF, was pointed out in a seminal work published in the late 1980s [43]. This work was targeted to supervised classification, where textural class parameters were estimated from SAR spatial statistics. Analysis was carried out based on stationary Rayleigh statistics for the envelope of the received field, and under the condition of a delta correlated fading component. In this framework, a method was derived for the estimation of the underlying RCS ACF from experimental data, whereas no specific model for the surface fluctuations was proposed. This line of research was extended by a theoretical model for non-Rayleigh SAR scattering statistics, covering the case of correlations between scatterers in the resolution cell (or fluctuating cross-section), and finite illumination window [44], [45]. The surface fluctuations were described by a Gamma distribution and a Lorentzian spectrum (exponential ACF). This model is particularly relevant when imaging forest at the resolution afforded by instruments used in our experiments. These contributions were the springboard over which interest in space–frequency analysis of SAR backscatter took momentum [46]–[49].

Wavelet frame spatial statistical measures are rooted in the groundwork established by the classical Fourier ACF analysis adopted in those research works, but extend it in several respects: 1) by enabling space-scale analysis (through good localization in the space–frequency domain); 2) by the capability of dealing with nonstationary processes; and 3) providing statistically better and computationally more efficient estimators. The reader is referred to [50] for a discussion on this topic. It appears therefore interesting to establish, for those random processes described by the models mentioned above, the

Appendix I

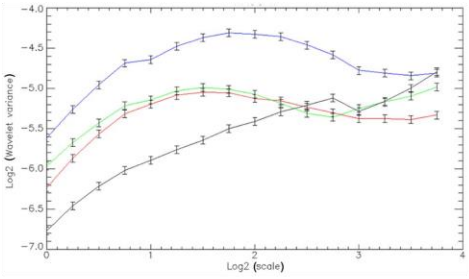

Fig. 3. Wavelet variance scaling signatures computed on single date ENVISAT ASAR VV backscatter (2010) for four classes of interest: FAM (blue), DF (red), IF (green), and FS (black). The error bars correspond to the standard error of the wavelet variance estimator.

TABLE II
FOUR LANDCOVER SAMPLES USED IN THE ANALYSIS (WGS84, UTM PROJECTION—ZONE 33 N)

Class	Center pixel coordinates
IF	329 220 E, 586 850 N
DF	344 085 E, 556 755 N
FAM	306 510 E, 543 045 N
FS	363 405 E, 558 060 N

connection between the wavelet space-scale statistics (wavelet variance and covariance) and the ACF based characterization.

For the purpose, analytical and numerical derivations were undertaken to illustrate the response of the wavelet scaling signatures to given correlation properties of the input SRF, including those assumed in the models in [44]. The gist of the analysis was based on the theory of linear filtering of random signals [51], which was exploited to link the spectral properties of the input signal to the statistics (variance) of the output process, this being filtered by the wavelet operator. Detailed analytical derivations and results would be outside the scope of the paper.

Suffice here to mention that for fractal RCS [52]–[54], the dependence of the wavelet variance on scale is linear in log–log scale, with the first derivative proportional to the spectral exponent. For a Gamma-distributed RCS with exponential ACF [44], the wavelet variance increases nonlinearly with the derivative at scale $s = 1$ linear in β (the inverse correlation length). While, the asymptotic value is proportional to the second moment of intensity.

V. ENVISAT ASAR RESULTS AND INTERPRETATION

A. Wavelet Variance Signatures

The graph in Fig. 3 shows the wavelet variance as a function of scale (four dyadic scales and four voices) for four classes of interest with corresponding estimation windows selected on ENVISAR ASAR VV backscatter geocoded data (Table II). Notice that in this set of classes and with respect to SAR backscatter, there are two radiometrically pure cases (intact and DF) and two mixed cases (FAM and FS). However, in terms of textural analysis, these classes can be handled as pure classes, in the sense that they can be characterized by separable measures.

The following observations can be made. Regarding the general trend with scale, signatures related to IF, DF, and FAM all show the fingerprint of a stationary random process with loss of correlation at short scales, a first maximum (sill) in a range of intermediate scales (corresponding to the correlation length concept in Fourier analysis), and a final segment with flattening out (white noise DF, FAM) or the presence of further correlation (or anticorrelation) structures (IF). A striking difference is provided by the FS signature which presents persistent increase with scale, a sign of a nonstationary process. This situation is due to the presence of strong radiometric nonhomogeneities within the estimation area (mixture), due to the intertwining of grassland and taller vegetation, as it will be documented later by wavelet spectra analysis (see Section V-D).

Regarding the separation between signatures (in terms of point-wise distance between variance values at each scale with respect to the estimation error), it is clear that between scales 2^0 and 2^2, the two radiometrically mixed classes (FAM and FS) are well separated between themselves and with respect to the union of more homogeneous classes (IF and DF). However, separation between IF and DF appears problematic, when based only on scale-by-scale differences between signature values. Statistical analysis on the probability distribution of the signatures' values for 20 samples of each class confirms these results.

The key to the solution of the problem stems from considering the functional dependence on scale of the signatures, as opposed to their point by point differences. For this purpose, the difference between IF and DF signatures were analyzed in more detail. The two functions (IF and DF signatures) appear to have a very similar form in the range of scales 2^0–2^2. However, the sill (first maximum) of the IF occurs at shorter scale than the DF one, or, in other words, there is a remarkable and consistent difference in the correlation length for the two classes [Fig. 4(a)]. Additionally, the IF signature shows persistent correlation/anticorrelation structures at longer scales, whereas the DF tends to flatten out.

A link between these two statistical correlation patterns and the underlying structure of the observed target can be conjectured in the following way. The IF structure is made up by layers of vegetation and in particular large emergent trees contribute to the signal. Instead, the DF has a relatively more homogeneous structure due to the removal of large emergent trees and the vegetation regrowth which has achieved a stage similar to the remnant vegetation from the intact stage. Let us remember that C-band radiation has a short penetration depth into a dense target, like this type of forest. Therefore, the RCS is spatially modulated by height changes and shadowing effects of a thin layer at top of canopy. Therefore, the IF return (which is more "rough") will decorrelate at shorter scales than the more homogeneous DF. On the other hand, the IF will retain some self-similar structures at longer scales, which will result in long scale memory as far as correlation is concerned. The results concerning the IF are in line with the dense homogeneous forest model in [51], where K-distributed clutter with an exponential cosine ACF is assumed. These considerations suggested a

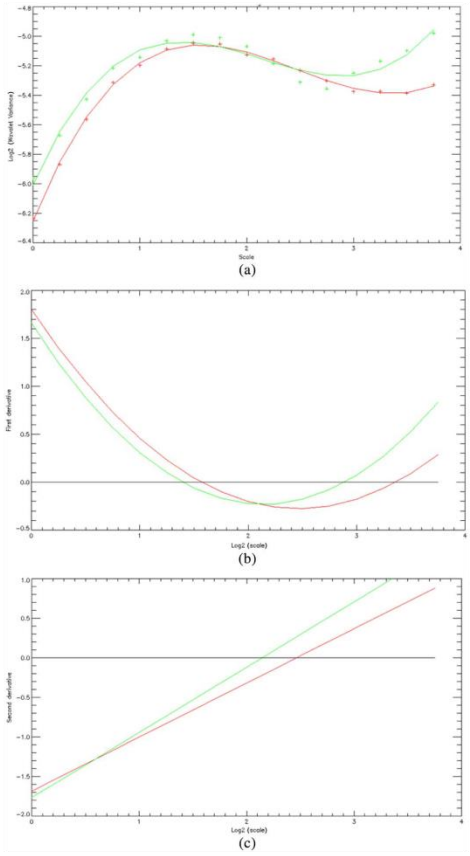

Fig. 4. (a) Wavelet scaling signature for two classes: IF (green cross), DF (red cross), and the fitted third-degree polynomial function (green and red solid lines for IF and DF, respectively). (b) First derivative of the IF (green) and DF (red) fitted wavelet scaling signatures. (c) Second derivative (slope) of the IF (green) and DF (red) fitted wavelet scaling signatures.

computational approach for the two-class pattern recognition problem based on signature functional analysis (described in Section V- B).

B. Wavelet Scaling Signatures Functional Analysis

Functional analysis of the wavelet scaling signatures was undertaken by fitting a polynomial function to the wavelet variance values for two classes of interest: IF (green) and DF (red) [Fig. 4(a)]. The wavelet scaling signatures points were fitted using a third-degree polynomial function of the form $y = ax^3 + by^2 + cx + d$. Two patterns can be noted in the graph: the first maximum (sill) of the IF signature occurs at shorter scale than the DF one; the presence of persistent correlations (anticorrelations) at long scales in the IF signature, whereas the DF signature tends to level off (uncorrelated noise). These two different functional dependences of the wavelet variance on scale can be described by the first and second derivatives of the fitting polynomial, as shown in Fig. 4(b) and (c). The zero crossing of the first derivative marks the onset of the sill point. The zero crossing of the second derivative marks the inflection point of the signature, this occurring always at longer scales for the DF class.

The combination of these functional parameters provides a consistent condition to discriminate between the two classes. This proposition was proven by a statistical hypothesis test of the difference of the parameters' mean values using 20 samples for each class of interest (H0: $\overline{x}_{DEG} - \overline{x}_{IF} = 0$). Concerning the first derivative zero crossings, the test resulted in one-sided p-value equal to 6.477×10^{-7}; thus, H0 was rejected indicating that there is a significant difference between the means at a 0.05 significance level. As to the zero crossings of the second derivative, the test gave a one-sided p-value equal to 0.003 with H0 rejected.

TABLE III
FLATNESS FACTOR STATISTICS FOR 20 SAMPLES OF EACH OF THE FOUR CLASSES OF INTEREST

Scale	DF		IF		FAM		FS	
	Mean	Stdev	Mean	Stdev	Mean	Stdev	Mean	Stdev
2^0	6.01	4.58	3.54	0.18	6.20	7.94	5.84	3.29
2^1	4.28	2.29	3.24	0.24	4.21	2.15	5.90	2.55
2^2	3.58	0.86	3.31	0.28	3.77	0.79	6.7	5.26
2^3	3.58	0.44	3.31	0.35	3.54	0.67	5.49	3.69
2^4	4.12	1.41	3.74	0.46	3.56	0.82	4.57	2.85

DF, degraded forest; IF, infact forest; FAM, forest agriculture mosaic; FS, forest-savanna.

C. Flatness Factor

The flatness factor [see (10)] intuitively gives an indication of the relative variability of the wavelet variance within the data samples, and therefore can indicate the presence of intermittency in the SAR signal, such as edges and point targets. As a guideline for the interpretation of the experimental data, we remind that for a wavelet frame that acts as a differentiator, and for Gaussian white noise as input, the flatness factor equals 3.

IF is the class which presents the lowest amount of intermittency at all scales, and less spread among samples, with flatness factor values around 3, thus pointing at a nearly Gaussian noise process (Table III).

The DF reveals some intermittency at short scales, also with large spread among samples (Table III). This result seems to contrast the conclusion derived from the scaling signature, which indicates the DF as a more homogeneous process than the IF. However, closer examination of the DF areas reveals that these high intermittency values are due to topographic effects (shadow, layover) which are present in some of the areas.

The FAM and FS classes both present intermittency of different importance, with the highest values and highest spread among samples for the FS (Table III). In both these cases, the intermittency is due to the presence of edges between two

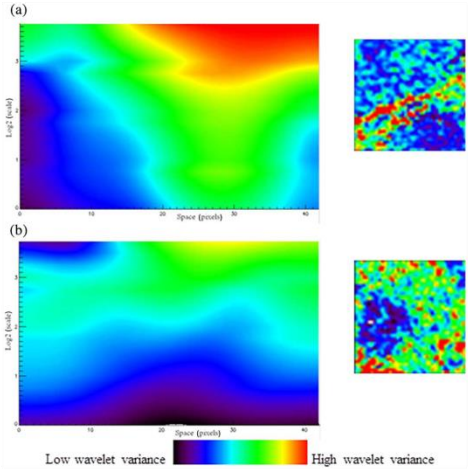

Fig. 5. Wavelet spectrum for (a) FS (in the northing direction) and (b) FAM (easting direction) showing the different textural properties of each class in the space-scale domain. The spectrum is estimated in a 43×43 pixels window (equivalent to 645×645 m in the ASAR geocoded dataset). The SAR backscatter within the corresponding windows (rendered in false color) is shown at the right of the spectra. These test cases highlight the capability of the wavelet space-scale representation to characterize radiometrically heterogeneous targets, such as a forest ribbon in (a) and the margin between bare soil and forest in (b).

homogeneous fields (e.g., soil and forest in FAM, and forest clusters in the FS). These singularities are of different strength, as a function of the related backscatter values, as indicated by higher flatness values with the FS class. The case of these nonstationary samples will be further analyzed using the wavelet spectrum in Section V-D.

D. Wavelet Space-Scale Signatures (Spectrum)

Analysis by wavelet spectrum of the two heterogeneous classes FS and FAM illustrates well the ability of this technique for localizing features in the combined space–frequency domain. The FS spectrum is shown in Fig. 5(a), this being represented in the northing direction. The backscatter in the estimation window (43×43 pixels) for FS and FAM is shown in false color in Fig. 5. A singularity (ridge) due to a forest ribbon is present in the image [Fig. 5(a)]. This feature is mapped onto the triangular area of higher variance values spreading in scale and around pixel 30 in space. Changes of the wavelet variance trajectory with scale are due to the intersection of the translated wavelet with the feature.

The FAM case [Fig. 5(b)] concerns an area with a diagonal edge marking the transition from bare soil to forest. In the spectrum (represented in the easting direction), the first segment (pixels 0–10) reveals a stationary signature (maximum at scale 2) that is due to the bare soil homogeneous region within this range, whereas the following spectrum values

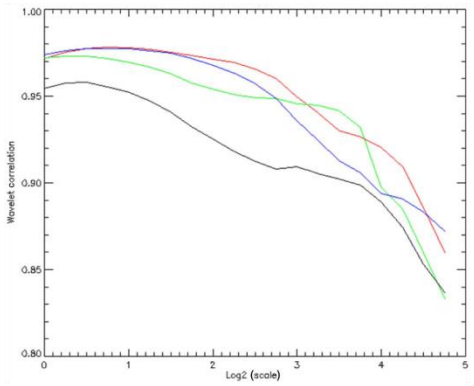

Fig. 6. Wavelet correlation between ENVISAT ASAR datasets acquired in 2006 and 2010 for four classes: DF (red), FS (green), IF (blue), and FAM (black).

indicate a nonstationary situation (increasing signature at all scale) corresponding to the presence of an edge.

E. Wavelet Covariance

The normalized wavelet covariance (correlation) signature (9) provides a measure of how the SAR backscatter within the estimation window (related to a specific landcover class) changes texturally between two dates and as a function of scale. It is therefore a spatiotemporal fingerprint of the SAR statistics. An example is shown in Fig. 6. The signature was computed with the same classes as the wavelet variance signature in Fig. 3 and refers to changes between acquisitions in 2006 and 2010. It can be observed that the wavelet variance of all classes loses correlation between the two dates, with lower correlation at longer scales. The changes at short scales may be influenced by residual speckle noise, whereas as scale increases, variation of the RCS spatial distribution comes into play. Class FAM (black) shows the highest decorrelation (highest temporal change) at all scales. This pattern depends obviously by temporal changes in the agricultural practices and bare soil extent. At short scales (up to 2^3), the statistics of class FS (green) shows more decorrelation than the ones of class intact and DF. Again, this is the other class where changes in the target can be expected. For class IF (blue), there appears to be more textural change in comparison with class DF. This feature must be further investigated to be able to connect it to vegetation changes.

VI. ALOS PALSAR Results and Interpretation

A. Wavelet Variance Signatures

The wavelet statistics analysis was also applied to L-band ALOS PALSAR at HH and HV polarizations. The signatures for the classes FS, IF, DF, and FAM can be found in Fig. 7(a) and (b). Differences of the wavelet statistics at HH and HV

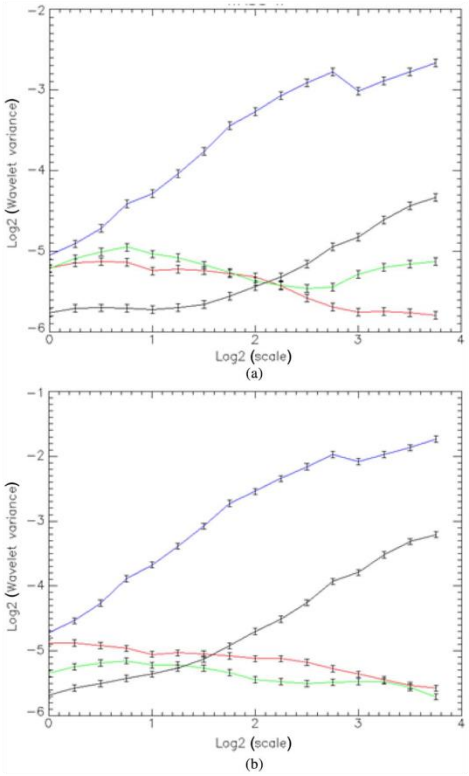

Fig. 7. (a) ALOS PALSAR HH and (b) ALOS PALSAR HV wavelet variance scaling signatures (four dyadic scales) for four classes of interest: FAM (blue), DF (red), IF (green), and FS (black) with corresponding error bars (black).

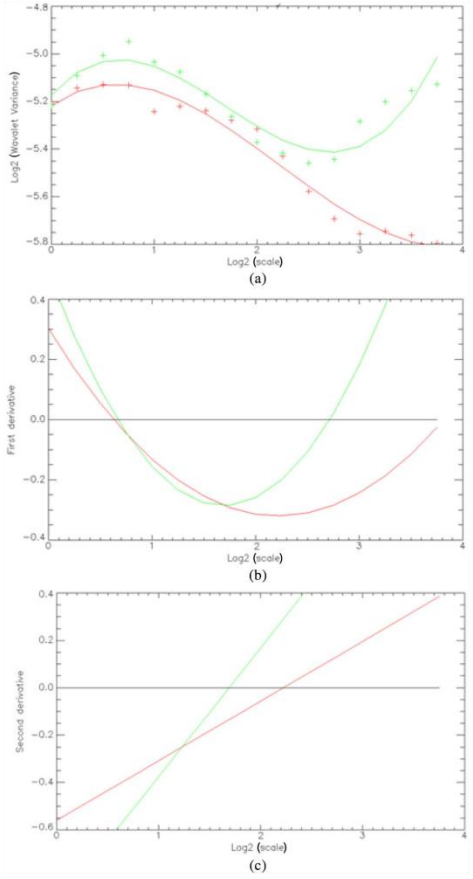

Fig. 8. (a) Wavelet scaling signature for two classes: IF (green cross) and DF (red cross) and the fitted third-degree polynomial functions (green and red solid lines). (b) First derivative of the fitted polynomial. (c) Second derivative of the fitted polynomial.

polarizations (in terms of absolute wavelet variance values and functional form) can be readily seen from the graphs.

At HH polarization, the scaling functional form of the signatures is similar to the one of ENVISAT ASAR VV, with the DF signature flattening out and the IF signature keeping memory of its structure [these trends are better highlighted with the fitted wavelet signatures in Fig. 8(a)]. While, at HV polarization, the signatures for the two classes reveal the onset of a white noise random process (no texture) and no significant difference between the two. We conclude that the HV return (volume scattering) does not provide spatial information that is useful to discriminate between DF and IF. From another standpoint, differences in biomass within and between intact and DF (if any) cannot be detected at this radiometric and spatial resolution by HV backscatter. On the other hand, the HH return is sensitive to the large scattering elements in the top layer of the canopy, and therefore, develops sensitivity to the forest structure in the same way as the C-band VV, although with less strength due to the increased penetration. The signatures of the two heterogeneous classes (FAM and FS), both at HH and HV, bear in a very strong way the tell-tale signs of nonstationarity, and even more so with respect to the ENVISAT ASAR case.

B. Wavelet Scaling Signatures Functional Analysis

This analysis is carried out only for HH polarization in view of IF and DF class separation, since the HV does not provide useful spatial information. The fitted wavelet signatures also confirm that the PALSAR HH is similar to the ASAR VV case in terms of functional form. However, the parameters that characterize univocally this dependence are different. Now,

Appendix I

the two classes present the same correlation length [Fig. 8(a)]. Therefore, the first zero crossing of the first derivative cannot be used as a marker [Fig. 8(b)]. On the other hand, now the second zero crossing is a good candidate, since it occurs at short scales for the IF, and at longer scales (if any) for the DF [Fig. 8(c)].

The inflection point (zero of the second derivative) appears to have the same role as in the case of ASAR. The significance of these observations was checked using a hypothesis test at 0.05 significance level of the differences of the mean values of these parameters (second zero crossing of the first derivative and zero crossing of the second derivative) using 20 samples for each class of interest.

The test reports that the H0 cannot be rejected in this case ($p = 0.109$). Therefore, functional analysis of wavelet signatures does not appear to be a viable solution for the textural discrimination of the two classes using ALOS PALSAR HH.

VII. Conclusion

Supervised analysis of SAR backscatter spatial statistics, as provided by a wavelet frame representation, was undertaken with the goal of assessing the capability of retrieving information about landcover differentiation, in particular, the ability to differentiate intact and DF in a closed semideciduous forest context. Test cases were developed using both C-band ENVISAT ASAR and L-band ALOS PALSAR datasets acquired on a site in Cameroon.

Results have shown that wavelet variance scaling signatures, which are measures of the SAR backscatter two-point statistics in the combined space-scale domain, are able to differentiate landcover classes by capturing their spatial distribution. This sensitivity extends the possibility of class discrimination based on intensity values distance, which is effective only for radiometrically pure classes or homogeneous targets, to the case of heterogeneous targets, these giving rise to texturally pure classes. Along this line, wavelet spectra were proven to be effective in characterizing heterogeneous landcover, such as FAM, by capturing the onset and the spatial location of singularities, such as edges.

Importantly, discrimination between IF and DF which is an important focus for conservation science was found to be enabled by functional analysis of the wavelet scaling signatures of C-band ENVISAT ASAR data. Analytic parameters, describing the functional form of the scaling signatures when fitted by a third-degree polynomial, resulted in a statistically significant difference between the signatures of the two classes. On the other hand, this outcome could not be replicated using the L-band ALOS PALSAR data.

Reasons for the inability to discriminate between intact and DF using ALOS PALSAR could be explained by the fact that L-band penetrates more into the canopy, and therefore, the observed backscatter texture is influenced more by the distribution of large scattering elements, and by the ground return. By contrast, C-band ENVISAT ASAR penetration is lower, and thus, the backscatter return comes primarily from the top of the canopy components, which produce a microtopography effect on the radar return due to their irregular vertical and horizontal distribution (e.g., emergent trees, which may be missing in degraded/regenerating forests). Additionally, differences in incidence angle and environmental/seasonal conditions between the C-band and L-band acquisitions could have influenced the differences in observed results.

The study area is characterized by DF that was disturbed by selective logging at least 15 years in the past. It is therefore notable that a SAR sensor at 15-m resolution can still distinguish between this DF stage and IF, based on textural features. Additional information could be retrieved from higher resolution sensors (e.g., Sentinel-1 or TanDEM-X).

In this specific environmental setting, the ENVISAT ASAR VV outperforms the ALOS PALSAR at HH and HV polarizations in terms of distinguishing between intact and DF. However, in a different environmental setting with other degradation patterns (e.g., more recent forest degradation patterns or in closed evergreen forest), the results could be different and therefore, testing the method in several areas will be undertaken in the future.

The performance of C-band ENVISAT ASAR for the purpose of discriminating between intact and DF is a promising result given the future availability of new C-band data provided by ESA Sentinel-1 mission.

Acknowledgment

The authors would like to acknowledge the software providers Sarmap SA (Sarscape 5.0) and the data providers: ESA (ENVISAT ASAR), Sarmap SA, JAXA (ALOS PALSAR), BlackBridge (RapidEye), and USGS (Landsat data).

References

[1] J. Grace, E. Mitchard, and E. Gloor, "Perturbations in the carbon budget in the tropics," *Global Change Biol.*, vol. 20, pp. 3238–3255, Feb. 2014.
[2] O. Mertz *et al.*, "The forgotten D: Challenges of addressing forest degradation in complex mosaic landscapes under REDD+," *Danish J. Geogr.*, vol. 112, no. 1, pp. 63–76, May 2012.
[3] I. D. Thompson *et al.*, "An operational framework for defining and monitoring forest degradation," *Ecol. Soc.*, vol. 18, no. 2, p. 20, Jun. 2013.
[4] C. J. Oliver, "The interpretation and simulation of clutter textures in coherent images," *Inverse Prob.*, vol. 2, pp. 481–518, Nov. 1986.
[5] Global Forest Observations Initiative. (2014, Jan.). *Integrating Remote-Sensing and Ground-Based Observations for Estimation of Emissions and Removals of Greenhouse Gases in Forests: Methods and Guidance from the Global Forest Observations Initiative* [Online]. Available: https://unfccc.int/files/methods/redd/submissions/application/pdf/redd_20140218_mgd_report_gfoi.pdf
[6] A. Ahrends *et al.*, "Predictable waves of sequential forest degradation and biodiversity loss spreading from an African city," *Proc. Natl. Acad. Sci. USA*, vol. 107, no. 33, pp. 1–6, Aug. 2010.
[7] M. S. Mon, N. Mizoue, N. Z. Htun, T. Kajisa, and S. Yoshida, "Factors affecting deforestation and forest degradation in selectively logged production forest: A case study in Myanmar," *Forest Ecol. Manage.*, vol. 267 no. 1, pp. 190–198, Mar. 2012.
[8] T. A. Stone and P. Lefebvre, "Using multi-temporal satellite data to evaluate selective logging in Para, Brazil," *Int. J. Remote Sens.*, vol. 19, no. 13, pp. 2517–2526, Jan. 1998.
[9] M. Hirschmugl, M. Steinneger, H. Gallaun, and M. Schardt, "Mapping forest degradation due to selective logging by means of time series analysis: Case studies in Central Africa," *Remote Sens.*, vol. 6, no. 1, pp. 756–775, Jan. 2014.
[10] C. M. Souza, Jr., D. A. Roberts, and M. A. Cochrane, "Combining spectral and spatial information to map canopy damage from selective logging and forest fires," *Remote Sens. Environ.*, vol. 98, no. 2–3, pp. 329–343, Oct. 2005.

Appendix I

[11] C. M. Souza, Jr., and D. Roberts, "Mapping forest degradation in the Amazon region with Ikonos images," *Int. J Remote Sens.*, vol. 26, no. 3, pp. 425–429, Feb. 2005.

[12] J. Franke, P. Navratil, V. Keuck, K. Peterson, and F. Siegert, "Monitoring fire and selective logging activities in tropical peat swamp forests," *IEEE J. Sel. Topics Appl. Earth Observ. Remote Sens.*, vol. 5, no. 6, pp. 1811–1820, Dec. 2012.

[13] E. T. A. Mitchard *et al.*, "Mapping tropical forest biomass with radar and spaceborne LiDAR in Lopé National Park, Gabon: Overcoming problems of high biomass and persistent cloud," *Biogeosciences*, vol. 9, no. 1, pp. 179–191, Jul. 2012.

[14] S. Kuntz *et al.*, "A multi-stage inventory scheme for REDD inventories in tropical countries," in *Proc. 34th Int. Symp. Remote Sens. Environ.*, Sydney, Australia, Apr. 2011, pp. 1–4.

[15] J. Deutscher, R. Perko, K. Gutjahr, M. Hirschmugl, and M. Schardt, "Mapping tropical rainforest canopy disturbances in 3D by COSMO-skymed spotlight InSAR-stereo data to detect areas of forest degradation," *Remote Sens.*, vol. 5, no. 2, pp. 648–663, Feb. 2013.

[16] M. Schlund, F. von Poncet, D. Hoekman, S. Kuntz, and C. Schmullius, "Importance of bistatic SAR features from TanDEM-X for forest mapping," *Remote Sens. Environ.*, vol. 151, pp. 16–26, Aug. 2014.

[17] E. Attema *et al.*, "Sentinel-1. The radar mission for GMES operational land and sea services," *ESA Bull.*, vol. 131, pp. 1–17, Aug. 2007.

[18] H. Benelcadi *et al.*, "Contribution of TerraSAR-X radar images texture for forest monitoring," in *Proc. IEEE Int. Geosci. Remote Sens. Symp. (IGARSS)*, Jul. 2012, pp. 6427–6430.

[19] R. M. Haralick and W. F. Bryant, "Documentation of procedures for textural/spatial pattern recognition techniques," Univ. Kansas, Lawrence, KS, USA, Final Rep. 278-1, 1976, 203pp.

[20] L. R. Sarker, J. Nichol, H. B. Iz, B. B. Ahmad, and A. A. Rahman, "Forest biomass estimation using texture measurements of high-resolution dual-polarization C-band SAR data," *IEEE Trans. Geosci. Remote Sens.*, vol. 51, no. 6, pp. 3371–3384, Jul. 2013.

[21] M. Beauchemin, K. P. B. Thomson, and G. Edwards, "Edge detection and speckle adaptive filtering for SAR images based on a second-order textural measure," *Int. J. Remote Sens.*, vol. 17, no. 9, pp. 1751–1759, Jun. 1996.

[22] I. Daubechies, "Orthonormal bases of compactly supported wavelets," *Commun. Pure Appl. Math.*, vol. 41, no. 7, pp. 909–996, Oct. 1988.

[23] P. Kumar and E. Foufoula-Georgiou, "Wavelet analysis for geophysical applications," *Rev. Geophys.*, vol. 35, no. 4, pp. 385–412, Nov. 1997.

[24] M. E. J. Cutler, D. S. Boyd, G. M. Foody, and A. Vetrivel, "Estimating tropical forest biomass with a combination of SAR image texture and Landsat TM data: An assessment of predictions between regions," *ISPRS J. Photogramm. Remote Sens.*, vol. 70, pp. 66–77, Jun. 2012.

[25] M. Simard, G. De Grandi, K. P. B. Thomson, and G. B. Benie, "Analysis of speckle noise contribution on wavelet decomposition of SAR images," *IEEE Trans. Geosci. Remote Sens.*, vol. 36, no. 6, pp. 1953–1962, Nov. 1998.

[26] G. D. De Grandi, R. M. Lucas, and J. Kropacek, "Analysis by wavelet frames of spatial statistics in SAR data for characterizing structural properties of forests," *IEEE Trans. Geosci. Remote Sens.*, vol. 47, no. 2, pp. 494–507, Feb. 2009.

[27] M. Unser, "Texture classification and segmentation using wavelet frames," *IEEE Trans. Image Process.*, vol. 4, no. 11, pp. 1549–1560, Nov. 1995.

[28] V. Bellassen and V. Gitz, "Reducing emissions from deforestation and degradation in Cameroon—Assessing costs and benefits," *Ecol. Econ.*, vol. 68, no. 1–2, pp. 336–344, Dec. 2008.

[29] B. Martens, N. S. Gideon, S. Matthew, and T. Bertrand. (2012). *Interactive Forestry Atlas of Cameroon. Version 3.0* [Online]. Available: http://data.wri.org/forest_atlas/cmr/report/cmr_atlas_v3_eng.pdf

[30] B. Martens and E. F. Lambin, "Land-cover-change trajectories in Southern Cameroon," *Ann. Assoc. Amer. Geogr.*, vol. 90, no. 3, pp. 467–494, Sep. 2000.

[31] FAO. (1985). *Forest Genetic Resources. Information -No.14. In Situ Conservation of Forest Genetic Resources in Cameroon* [Online]. Available: http://www.fao.org/docrep/006/r4968e/r4968e07.htm

[32] Y. Yako Tegechouang. (2010). *Contribution a la gestion des relations homme-plantation forestiere dans le sud et l'Est Cameroun: Cas des plantations de Pericopsis elata de bidou ii dans la reserve de la kienke sud et du bloc kebe dans la reserve de Deng-Deng* [Online]. Available: http://www.itto.int/files/user/cites/cameroon/M%C3%A9moire_gestion%20des%20relations%20homme_Plantations_Yako%2024_05_2010.pdf

[33] World Bank. (2014). *Climate Change Knowledge Portal* [Online]. Available: http://sdwebx.worldbank.org/climateportal/index.cfm?page=country_historical_climate&ThisRegion=Africa&ThisCCode=CMR

[34] Sarmap. (2007). *SARscape Technical Description* [Online]. Available: https://www.exelisvis.com/portals/0/pdfs/ENVI/SAR_tech_documents/SARscape_Technical_Description.pdf

[35] G. F. De Grandi, M. Leysen, J. S. Lee, and D. Schuler, "Radar reflectivity estimation using multiple SAR scenes of the same target: Technique and applications," in *Proc. IEEE Int. Remote Sens. Sci. Vis. Sustain. Develop. Geosci. Remote Sens. (IGARSS'97)*, Aug. 3–8, 1997, vol. 2, pp. 1047–1050.

[36] World Resources Institute. (2014). *Congo Basin Forest Atlases* [Online]. Available: http://www.wri.org/our-work/project/congo-basin-forests/congo#project-tabs

[37] I. Daubechies, *Ten Lectures on Wavelets*. Philadelphia, PA, USA: Society for Industrial and Applied Mathematics, 1992, ch. 3.

[38] S. Mallat, *A Wavelet Tour of Signal Processing*. New York, NY, USA: Academic, 1998, ch. 5.5, pp. 148–156.

[39] M. J. Shensa, "The discrete wavelet transform: Wedding the à trous and Mallat algorithms," *IEEE Trans. Signal Process.*, vol. 40, no. 10, pp. 2464–2482, Oct. 1992.

[40] S. Mallat, *A Wavelet Tour of Signal Processing*. New York, NY, USA: Academic, 1998, ch. 6.3, pp. 198–199.

[41] G. De Grandi, J.-S. Lee, and D. L. Schuler, "Target detection and texture segmentation in polarimetric SAR images using a wavelet frame: Theoretical aspects," *IEEE Trans. Geosci. Remote Sens.*, vol. 45, no. 11, pp. 3437–3453, Nov. 2007.

[42] A. Davis, A. Marshak, and W. Wiscombe, "Wavelet-based multifractal analysis of non-stationary and/or intermittent geophysical signals," in *Wavelets in Geophysics*, E. Foufoula-Georghiou and P. Kumar, Eds. New York, NY, USA: Academic, 1994, pp. 249–298.

[43] F. T. Ulaby, F. Kouyate, B. Brisco, and T. H. Williams, "Textural information in SAR images," *IEEE Trans. Geosci. Remote Sens.*, vol. 24, no. 2, pp. 235–245, Mar. 1986.

[44] C. J. Oliver, "A model for non-Rayleigh scattering statistics," *Opt. Acta Int. J. Opt.*, vol. 31, no. 6, pp. 701–722, 1984.

[45] C. J. Oliver, "The representation of correlated clutter textures in coherent images," *Inverse Prob.*, vol. 4, pp. 843–866, 1988.

[46] D. R. Sheen and L. P. Johnston, "Statistical and spatial properties of forest clutter measured with polarimetric synthetic aperture radar (SAR)," *IEEE Trans. Geosci. Remote Sens.*, vol. 30, no. 3, pp. 578–588, May 1992.

[47] L. Kurvonen and M. T. Hallikainen, "Textural information of multitemporal ERS-1 and JERS-1 SAR images with applications to land and forest type classification in boreal zone," *IEEE Trans. Geosci. Remote Sens.*, vol. 37, no. 2, pp. 680–689, Mar. 1999.

[48] M. J. Collins and J. Huang, "Uncertainties in the estimation of ACF-based texture in synthetic aperture radar image data," *IEEE Trans. Geosci. Remote Sens.*, vol. 36, no. 3, pp. 940–949, May 1998.

[49] F. Bujor, E. Trouve, L. Valet, J.-M. Nicolas, and J.-P. Rudant, "Application of log-cumulants to the detection of spatiotemporal discontinuities in multitemporal SAR images," *IEEE Trans. Geosci. Remote Sens.*, vol. 42, no. 10, pp. 2073–2084, Oct. 2004.

[50] D. B. Percival and A. T. Walden, *Wavelet Methods for Time Series Analysis*. Cambridge, U.K.: Cambridge Univ. Press, 2000, ch. 8.3, p. 306.

[51] B. Picinbono, *Random Signals and Systems*. Englewood Cliffs, NJ, USA: Prentice Hall, 1993, ch. 5.4.

[52] C. V. Stewart, B. Moghaddam, K. J. Hintz, and L. M. Novak, "Fractional Brownian motion models for SAR imagery scene segmentation," *Proc. IEEE*, vol. 81, no. 10, pp. 1511–1522, Oct. 1993.

[53] G. Franceschetti, A. Iodice, M. Migliaccio, and D. Riccio "Scattering from natural rough surfaces modeled by fractional Brownian motion two-dimensional processes," *IEEE Trans. Antennas Propag.*, vol. 47, no. 9, pp. 1405–1415, Sep. 1999.

[54] G. W. Wornell, "Wavelet-based representations for the 1/f family of fractal processes," *Proc. IEEE*, vol. 81, no. 10, pp. 1428–1450, Oct. 1993.

Elsa C. De Grandi (M'09) received the B.Sc. degree in physical geography and the M.Sc. degree (with distinction) in remote sensing and geography from Aberystwyth University, Aberystwyth, U.K., in 2011 and 2012, respectively. Currently, she is pursuing the Ph.D. degree in remote sensing of forests at the University of Edinburgh, Edinburgh, U.K.

She is a Co-Investigator of the German Aerospace Center (DLR) TanDEM-X science program. Her research interests include the use of synthetic aperture radar (SAR) to map forest changes and forest degradation in tropical forest.

Appendix I

Edward Mitchard (M'07) was born in U.K., in 1986. He received the Degree in biological sciences from the University of Oxford, Oxford, U.K., in 2007, and the Ph.D. degree in remote sensing of forests from the University of Edinburgh, Edinburgh, U.K., in 2011.

Currently, he is a Chancellor's Fellow with the University of Edinburgh, and previously held a NERC Fellowship there. He has authored extensively, including in *PNAS*, *Geophysical Research Letters*, and *Nature Climate Change*. His research interests include the use of remote sensing data (optical, radar, and lidar) to map aboveground biomass and vegetation type, and changes in these parameters.

Dr. Mitchard is also a Member of the European Geosciences Union and chairs the Technical Advisory Board of the Plan Vivo Foundation.

Iain H. Woodhouse received the B.Sc. degree (Hons.) from the University of Edinburgh, Edinburgh, U.K., the M.Sc. degree in remote sensing from Dundee University, Dundee, U.K., and the Ph.D. degree in atmospheric remote sensing from the Heriot-Watt University, Edinburgh.

He has worked with the Marconi Research Center and Wageningen University, Wageningen, The Netherlands. In 1999, he moved to the University of Edinburgh, where he is currently a Senior Lecturer in Radar Remote Sensing with the School of GeoSciences. He is a Principal Investigator on a number of projects related to quantitative measurements of forests from remote sensing, which are funded by NERC, DTI, DSTL, and the Forestry Commission. His research interests include retrieval of biophysical properties of vegetation using active remote sensing, specifically synthetic aperture radar (SAR), and lidar.

Dr. Woodhouse is a Member of the NERC Earth Observation Director's Advisory Board and the Group on Earth Observations (GEO) Capacity Building Committee and a Nonexecutive Director of Ecometrica Ltd. He was a Founding Member of the Edinburgh Earth Observatory (EEO), a research group within the School of GeoSciences.

Gianfranco D. De Grandi (M'90–SM'96–F'02) received a Doctorate degree (Hons.) in physics engineering from Politecnico Milano, Milan, Italy, in 1973.

From 1977 to 2012, he was with the European Commission Directorate General Joint Research Center, Ispra, Italy, where he performed research in signal processing for application areas such as gamma ray spectroscopy, data communications, and radar remote sensing. In 1985, he was a Visiting Scientist at Bell Communications Research, Morristown, NJ, USA, where he participated in the design of metrocore, one of the first research projects for Gbit rate metropolitan area networks. From 1997 to 2001, he served as an Assistant Professor with the Faculte' de Foresterie et Geomatique, Universite' Laval, Quebec, PQ, Canada. He was a Principal Investigator of Japan Aerospace Exploration Agency (JAXA) Global Boreal Forest Mapping project, the ALOS research program, and the Kyoto and Carbon (K&C) project. He is an Investigator of the German Aerospace Center (DLR) Tandem-X science program. Currently, he is a Visiting Scholar at the Aberystwyth University, Aberystwyth, U.K., where he is pursuing his research interests in SAR spatial statistics.

Appendix II: Published version of Chapter 4

remote sensing

MDPI

Article

Wavelet Based Analysis of TanDEM-X and LiDAR DEMs across a Tropical Vegetation Heterogeneity Gradient Driven by Fire Disturbance in Indonesia

Elsa Carla De Grandi [1,*], Edward Mitchard [1] and Dirk Hoekman [2]

[1] School of GeoSciences, University of Edinburgh, Edinburgh EH8 9YL, UK; edward.mitchard@ed.ac.uk
[2] Department of Environmental Sciences, Wageningen University, Wageningen 6708 PB, The Netherlands; dirk.hoekman@wur.nl
* Correspondence: E.De-Grandi@sms.ed.ac.uk; Tel.: +44-131-650-5103

Academic Editors: Ioannis Gitas, Clement Atzberger and Prasad S. Thenkabail
Received: 25 May 2016; Accepted: 1 August 2016; Published: 5 August 2016

Abstract: Three-dimensional information provided by TanDEM-X interferometric phase and airborne Light Detection and Ranging (LiDAR) Digital Elevation Models (DEMs) were used to detect differences in vegetation heterogeneity through a disturbance gradient in Indonesia. The range of vegetation types developed as a consequence of fires during the 1997–1998 El Niño. Two-point statistic (wavelet variance and co-variance) was used to assess the dominant spatial frequencies associated with either topographic features or canopy structure. DEMs wavelet spectra were found to be sensitive to canopy structure at short scales (up to 8 m) but increasingly influenced by topographic structures at longer scales. Analysis also indicates that, at short scale, canopy texture is driven by the distribution of heights. Thematic class separation using the Jeffries–Matusita distance (JM) was greater when using the full wavelet signature (LiDAR: $1.29 \leqslant JM \leqslant 1.39$; TanDEM-X: $1.18 \leqslant JM \leqslant 1.39$) compared to using each decomposition scale individually (LiDAR: $0.1 \leqslant JM \leqslant 1.26$; TanDEM-X: $0.1 \leqslant JM \leqslant 1.1$). In some cases, separability with TanDEM-X was similar to the higher resolution LiDAR. The study highlights the potential of 3D information from TanDEM-X and LiDAR DEMs to explore vegetation disturbance history when analyzed using two-point statistics.

Keywords: tropical forest; interferometric synthetic aperture radar; TanDEM-X; LiDAR; forest structure; fire; El Niño Southern Oscillation

1. Introduction

Tropical forests are the largest and most complex forest biome on the planet covering 16% of the global land surface where pressure exerted by anthropogenic activities is high and their role in the carbon budget is of great significance [1]. Forests are a substantial carbon sink sequestering 2.0 ± 0.4 Pg C/year globally (1990–2007 estimates) [2] and simultaneously a large carbon source through deforestation and forest degradation by contributing to approximately 7%–15% of anthropogenic emissions since 2000s [2]. The combination of deforestation, degradation, harvesting and peat fires has been estimated as 2.01 ± 1.1 Pg/annum [1]. The uncertainty on these numbers, and thus the total flux to/from the atmosphere, is considerable. Indeed, the uncertainty on both these numbers may be underestimated as we struggle to map forest carbon stocks accurately, let alone subtle changes in these stocks [3]. The disturbance regime, and rate of recovery following disturbance determines their effectiveness in sequestering carbon: therefore, it is important to reduce these uncertainties to allow for global-scale monitoring of the effectiveness of pledges made under the UNFCCC Paris Agreement (2015).

Degraded and secondary forests are a particular concern. They were estimated to make up 60% of the total area classified as forest in tropical regions covering 850 million ha in the year 2000 [4],

Appendix II

and this number has grown significantly since then. Most studies on changing biomass stocks are focused on intact forest and changes from intact forest to non-forest only [5]. These are very dynamic areas, suffering from anthropogenic degradation but also re-growing rapidly (regrowth may represent 1.8 ± 0.9 Pg/annum) [1]. We currently lack the tools to map these subtle changes well from satellite data, leading to these large uncertainties.

Secondary forests are now especially dominant in Southeast Asia. Until the 1960s, Southeast Asia was dominated by extensive tracts of high above-ground biomass lowland Dipterocarp forests which acted as a significant carbon sink [6]. Estimates indicate that only 12% of the remaining forests in Southeast Asia remained "intact" in 2000 [7]. The majority of natural old-growth forest areas are now considered disturbed due to different processes such as logging, conversion into degraded savanna and grassland or managed land [8,9]. The increased proportion of secondary forests (or successional communities) at the expenses of old-growth forests requires us to prioritize and re-focus conservation efforts on degraded forest [10]. In fact, after disturbance, forests still retain conservation values [11] and maintain appreciable biodiversity. In particular, tropical forests in Southeast Asia are considered some of the most valuable in this respect, since they host endangered species such as orangutans [12].

A major forest degradation driver is fire, which has been extensively and increasingly used in slash and burn practices and to induce clearing for industrial palm oil and paper-pulp plantations as it is the most convenient and efficient conversion method [8,13,14]. Humid tropical forest flammability is often exacerbated by human intervention (e.g., selective logging) [15–17]. Fire is mainly driven by moisture stress in dry conditions during El Niño Southern Oscillation (ENSO) events [15]. These have occurred in the past (notably the strong 1997–1998 event) and more recently (2015–2016), causing the alteration and degradation of tropical lowland and peat swamp forest in Southeast Asia [14]. These climatic anomalies will continue to threaten tropical forests in the future as these events become more frequent and of increased magnitude [18].

Drought conditions during the 1997–1998 ENSO resulted in a total of 2.6 million ha of forest being burned [16] and the release of 2.97–9.42 Gt CO_2 [19], thus acting as a source of CO_2, reducing above-ground biomass and diminishing the potential (at least in the early stages of regeneration) of the newly degraded forest to act as a carbon sink [20]. Most significantly, the 1997–1998 fires affected more severely those areas which had previously been disturbed by selective logging [16]. This indicates that previously disturbed forests (from logging or previous fires) are more susceptible to further disturbance and thus, it is important to locate these areas [21]. Fire can result in the alteration of stands in terms of structure and composition [17] by converting them from areas that have achieved high diversity to areas dominated by a few pioneer species [22]. The resulting vegetation spatial structural alterations (e.g., height, canopy cover and biomass) and composition (e.g., species diversity) after fire are complex to characterize [23] and there is no "coherent pattern of forest regeneration" [13]. Recovery to old-growth conditions is not always possible. The majority of degraded forests might not recover and potentially develop into scrubland or grassland dominated by *Imperata cylindrica* [13,21] (often permanently due to recurring fire management practices).

Given the above, techniques for wide area and spatial measures of vegetation structure and disturbance are evidently necessary. Remote sensing observations afford in principle a vehicle for providing such measures, but methods for doing this are still under development and there is space for considerable improvements to obtain the required information from satellite instruments. We give next a brief summary of the state of the art of remote sensing practices for vegetation spatial structure characterization. Finally, evidence for the potential in this context of wavelet based two-point statistics will be supplied using spatial Interferometric Synthetic Aperture Radar (InSAR) and airborne LiDAR observations of a fire-affected site in Indonesian Borneo.

1.1. Forest Structural Heterogeneity Derived from Remote Sensing

Undisturbed old-growth tropical forests are known to be complex, multi-layered environments where heterogeneity is driven prevalently by species diversity assemblages [24]. Further factors that

Appendix II

influence heterogeneity are related to disturbance processes. For example the development of canopy gaps as large trees die and fall over, either naturally or due to extreme events or anthropogenic influence, and compositional alterations caused by changing climate or local conditions [25]. Spatial patterns in tropical forests are determined by the size, shape and the distribution of the single canopy components (branches and leaves), which have a varying pattern dependent on the scale of observation [26]. Despite its importance in ecological processes, canopy spatial heterogeneity has not yet been fully quantified and lacks a standardized measurement approach given issues on the agreement of a definition [26]. Approaches that are best suited for this include those that are able to take into account the scale-dependence of the processes and are consequently best observed using space-scale analysis derived from two-point statistical measures (wavelet space-scale analysis) of 3D datasets [27]. 3D datasets suitable for such analysis, including Light Detection and Ranging (LiDAR) and Interferometric Synthetic Aperture Radar (InSAR) are now widely available from a range of airborne and spaceborne sources (e.g., the TanDEM-X satellite formation).

Moreover, the nature of the ecological processes (derived from environmental conditions, composition and disturbance processes) results in many cases in statistical non-stationarity of the random fields associated with the instrumental observations. In essence, statistical stationarity (or homogeneity when the independent variable is space) means that the statistical measures are invariant under translation. Non-stationarity in nature includes intermittency and scale invariance (fractal process) [28,29].

Canopy structure is significantly affected by the scale of observation [30]. At fine-scales, within a forest patch heterogeneity is visible while, at coarser scales, the clumping of canopies results in homogeneous patches with similar structure. In this case, heterogeneity between patches due to differences in structure can be appreciated [31].

Increased availability of fine resolution data provided by commercial satellites (in particular optical sensors such as those publicized through the Google Earth platform (e.g., QuickBird, WorldView and IKONOS) [32] have provided the increasing opportunity to explore canopy spatial arrangement and to resolve an unprecedented level of detail and the development of image processing algorithms that can extract single tree crowns [33] as well as manual delineation of tree crowns [34] but this has been more commonly done in the past using aerial photography [35].

Compositional changes (e.g., species succession) and structural changes (e.g., small canopy openings) due to disturbance (e.g., fire or selective logging) can be measured using ground data with point estimates (e.g., gap fraction and canopy openness) at recurring intervals after the occurrence of the disturbance event [36–42]. Accessibility limits the retrieval of such information in tropical forest and the ability to gather datasets spanning large areas [32]. Remote sensing observations offer a valuable, complementary tool to explore canopy structure variations due to degradation processes at larger scales in extensive, complex, heterogeneous and multi-layered tracts of tropical forests [30,43].

Optical sensors are most commonly employed due to their widespread availability (e.g., LANDSAT), but these observations are severely limited in the tropics due to frequent cloud cover and haze, which precludes the acquisition of data [44]. Moreover, these observations provide only two-dimensional information (projection of the structure from a volume onto a plane), lacking sensitivity to vertical structure, which is an important parameters in multi-layered tropical forests. Spectral properties provide limited sensitivity to differentiate successional stages given the rapid recovery of canopy cover after disturbance, which is reflected on the spectral signature of regenerating forest [45].

Improved understanding and characterization of forest structural arrangement arising from different forest types and forest patches at different successional stages can be improved using geometrical and textural properties of spectral signal from high resolution optical data [46]. Resolution <4 m has also been suggested as optimal for retrieving meaningful information related to canopy structure [47]. While datasets with resolution lower than 4 m are readily available from optical and airborne LiDAR sensors, they have limited spatial coverage [48]. Canopy texture derived from

Appendix II

high resolution optical imagery has been employed successfully for discrimination of forest types due to the ability to exploit the variation in illumination between crowns, this resulting in tonal variation between the sunlit and shadow canopy components using Fourier Transform Textural Ordination (FOTO) [32,47,49]. Lacunarity has also been explored for the analysis of spatial patterns derived from canopy arrangements in simulated LiDAR datasets [26] and in high resolution multi-spectral optical data [24].

Requirements to capture the complex three-dimensional structure can be best matched by airborne Light Detection and Ranging (LiDAR) [50] and Interferometric Synthetic Aperture Radar (InSAR) [51]. Forest spatial structure from LiDAR datasets has been extensively studied with the aim of characterizing forest types using texture metrics [23]. Also forest disturbance has been addressed using these techniques (e.g., selective logging: [52,53]). Canopy grain analysis from FOTO applied to LiDAR derived Canopy Height Model (CHM) and Digital Surface Model (DSM) was also used to generate metrics related to structure and to ultimately improve above-ground biomass prediction [32,54]. The extraction of single crowns from LiDAR has also been explored [55].

InSAR is also sensitive to three-dimensional vegetation structure, with capability of mapping the vegetation spatial distribution by the coherence modulus and the vertical distribution by the interferogram phase. TanDEM-X (and the twin satellite is a single-pass interferometer acquiring data at X-band (λ = 0.031 m, 9.65 GHz) and at high spatial resolution (approximately 5 m pixel spacing). Its unique configuration results in no temporal decorrelation [56], as this is typically high in multi-pass interferometers where acquisitions are normally at least days, if not longer apart. The availability of TanDEM-X data has spurred much research on forestry applications and in particular related to vegetation vertical structure (height) through interferometric phase and forest horizontal structure (canopy density) through backscatter and coherence. In this paper we concentrate on the first of these, as a Digital Surface Model (DSM) (WorldDEM^{TM}) [57] is provided globally so it is the easiest TanDEM-X data product to access and use. Indeed, TanDEM-X provides the first DSM with global coverage, at high resolution (<5 m), which could provide information on canopy heterogeneity. The DSM potential to characterize structural heterogeneity through texture based methods in tropical forests has, however, seldom been explored as far as we are aware.

DSMs are produced from TanDEM-X data using the coherence phase information, which incorporates three-dimensional spatial information on vegetation height superimposed on topography [51,58]. Sensitivity to sensor's parameters (e.g., polarization) and environmental conditions (e.g., rainfall events and seasonality) have also been noticed to influence the phase center height (PCH) but research has been predominantly focused on boreal or temperate forests. For instance, ground scattering is lower at VV polarization compared to HH [59]. Seasonality can also play a part in determining X-band penetration depth with deeper penetration occurring during leaf-off conditions [60]. Penetration depth decreases with increasing frequency, so at X-band penetration depth is lower compared to L-band [51]. In tropical forest, phase height was found to be higher for shorter forest (early succession) compared to taller forest stands [61].

Developing methods for the extraction of texture is a key priority to retrieve information on canopy conditions from forest structure [32]. However, texture derived from 3D InSAR datasets has not yet been explored to obtain information related to canopy heterogeneity and in particular for the analysis of differences in structure between landscapes, which are characterized by a gradient of heterogeneity derived from anthropogenic disturbance.

Spatial patterns, which from a cognitive point of view we can associate with forest heterogeneity, such as canopy clusters, canopy closure and voids, canopy roughness, vegetation density, and emergent trees, appear in statistical measures of the 3D observations (vegetation height as a function of northing and easting) in, for instance, signal energy which is highly variable both in space and frequency. Their characterization requires therefore a signal representation, which affords local energy estimation. Wavelet frames, which feature an optimal time-frequency (space-scale) resolution, are the ideal representation choice for the purpose [28].

Appendix II

1.2. Rationale

The full LiDAR waveform provides a measure of the forest vertical structure function, obtained by sampling in range time the returns from layers of elementary scattering elements which are distributed in height along the vegetation volume. When the full waveform is processed into a Canopy Height Model (CHM), the vertical structure measure is condensed in one value, namely the distance at each resolution point in space from the ground return to the top canopy return. It carries therefore a three-dimensional geometric characterization of the forest structure, one dimension being the vegetation height, and the other two dimensions being the spatial distribution of the heights (the horizontal structure).

The phase of the coherence can be exploited to derive a surface model (DSM), which incorporates spatial information on topography and vegetation height. This happens because on a vegetated surface the phase center height (PCH) moves up from the value corresponding to the ground, because of the contribution of the scattering elements in the vegetation volume [60]. When the DSM is located near the canopy surface, it carries information on those higher spatial frequencies that are generated by the forest horizontal structure, similarly to the LiDAR CHM and therefore can give an indication of canopy structure.

An intuitive view of the phenomenon in case of the non-stationary and intermittent random field provided by the primary forest canopy height, can be obtained in this way. Moving from one resolution element to the next, the radar beam will intercept different structural patterns of the heterogeneous canopy. As a consequence, the scattering volume dimension will change, because the local incidence angle and the extinction will change (different number density of scattering elements). Reasoning in terms of a piecewise random volume model, the net result of all changing factors will be a corresponding spatial change of the complex coherence and of the phase center height, and in turn on the phase to height conversion (DSM).

The aim of the work presented in this paper is to compare the information content of the spatial statistic (texture) of DEMs provided by two observational sensors, LiDAR and InSAR, these featuring complementary spatial resolution and mapping extent characteristics. The aim is pursued by providing a quantitative characterization of the mapping between observations (LiDAR and InSAR) and target spatial structure using two-point statistical measures. The approach is two-fold: first, LiDAR and InSAR textural correlation is used to assess coupling of topographic and canopy structures. Subsequently, space-frequency analysis (2D wavelet spectra) is applied to structure measures provided by LiDAR CHM and TanDEM-X DSM to test congruency of the measures carried out by the two sensors. Finally, thematic class separability based on the wavelet statistical measures is performed.

2. Study Site: Sungai Wain Protection Forest (SWPF), East Kalimantan (Indonesia)

Sungai Wain Protection Forest (SWPF) is located to the North of Balikpapan (116°46′14.08″E, 0°59′57.91″S), East Kalimantan (Indonesia) (Figure 1). The study site encompassed intact lowland Dipterocarp forest within the core of the SWPF surrounded by disturbed forest dominated by *Macaranga* sp. which developed after the 1997–1998 fires [62]. Cultivated areas are located to the North and to the East of the SWPF with mainly abandoned mixed rice fields, grassland which is dominated by the invasive *Imperata cylindrica* and scrub composed of a mix of vegetation at various stages of development. Intact lowland Dipterocarp forest in the SWPF reaches above-ground biomass up to 400 Mg/ha and heights up to 60 m [63] and on a large scale appears as homogeneous [62].

Elevation ranges between 30 and 140 m above sea level with an elevation gradient decreasing from North to South and terrain slope ranging from 0 to 30°. The soil type is classified as Alisols [41]. The climate is categorized as Tropical Wet [64], and is wet all year but has infrequent marked dry periods as a consequence of ENSO conditions. Its wet season, December to May, has peak rainfall in March (272 mm), with average annual precipitation equal to 2250 mm [65], and a rainfall minimum in July (147 mm during the dry season) [12]. The 1997–1998 ENSO, which affected the study area, was characterized by a lack of precipitation for several months, leading to fire which caused damage

to two thirds of the SWPF [41]. As well as altering the species composition of the forest, there were noticeable changes in forest structure such as an increase in canopy openness [41].

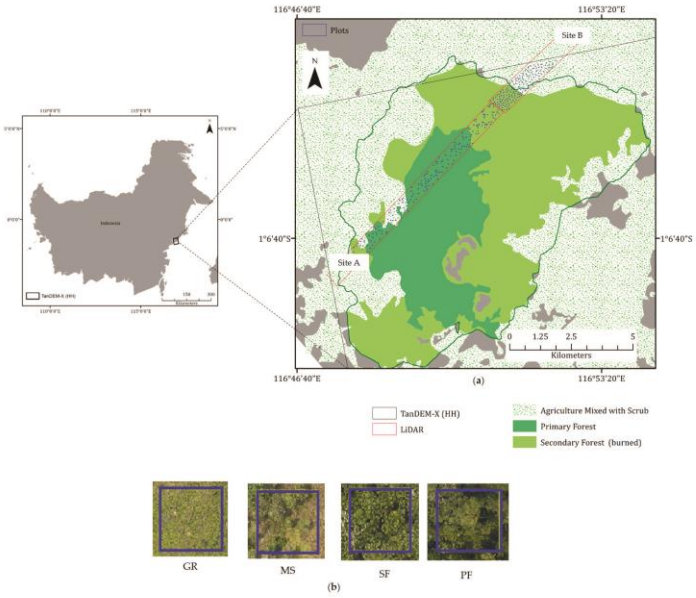

Figure 1. (**a**) Study site location and data extent overlaid on a land cover map provided by the Indonesian Ministry of Forestry [66]. TanDEM-X data extent (black box, only partially covered in this image), LiDAR site A and B (red) and 315 sample plots (35 × 35 m^2) (blue squares). LiDAR Site A is primarily covered by primary forest (PF) (undisturbed) while; Site B is dominated by secondary forest (SF) (disturbed), mixed scrub (MS) and grassland (GR); (**b**) Range of vegetation structures observed from high resolution aerial photography (0.5 m) (blue square: 35 × 35 m^2 plot).

3. Methods

3.1. TanDEM-X Data

TanDEM-X data was acquired on 11 December 2014 in StripMap bistatic mode (single polarization HH) at 41° incidence angle supplied through AO VEGE6702 by DLR (Figure 2). The scene covers 32 km W-E × 25 N-S km (UL Geo: 116°46′14.08″E, 0°59′57.91″S). A summary of the TanDEM-X acquisition configuration is found in Table 1. The data was processed using ENVI/SARScape 5.0 Interferometric module to generate coherence modulus and a Digital Surface Model (DSM) [67] and consists of the following steps: (a) interferogram generation (2 looks in azimuth and 2 looks in range); (b) retrieval of a subset of the SRTM-4 version DEM which covers the extent of the TanDEM-X acquisition; (c) interferogram flattening; (d) filtering using a Goldstein filter [68] and coherence generation; (e) phase unwrapping using the minimum cost flow algorithm; and (f) geocoding at 4.6 m resolution to WGS84 datum, Zone 50 South. A DSM was generated using the phase to height conversion by setting relaxed interpolation since the low coherence values meant that the phase was difficult to unwrap (Figure 2). The derived DSM was also geocoded at 4.6 m pixel spacing to WGS84 datum, UTM Zone 50 South. The DSM derived from TanDEM-X corresponds to the superimposition of

the bare earth (Digital Terrain Model—DTM) plus the vegetation and corresponds to the phase center height (PCH) which is located within the vertical structure of the target [51]. The location of the PCH depends on target parameters (e.g., vegetation spatial configuration such as volume density) and the sensor's parameters (e.g., frequency and polarization) [69].

Table 1. TanDEM-X acquisition configuration parameters.

Parameter	Value
Mode	StripMap bistatic
Acquisition Date	11/12/2014
Polarization	HH
Incidence Angle (°)	41
Resolution (azimuth, range) (m)	3.3 × 1.8
Ground resolution (m) at 41°	3.3 × 2.74
Effective Baseline (m)	223
HoA (m)	30.2
Orbit direction	Ascending
Look direction	Right

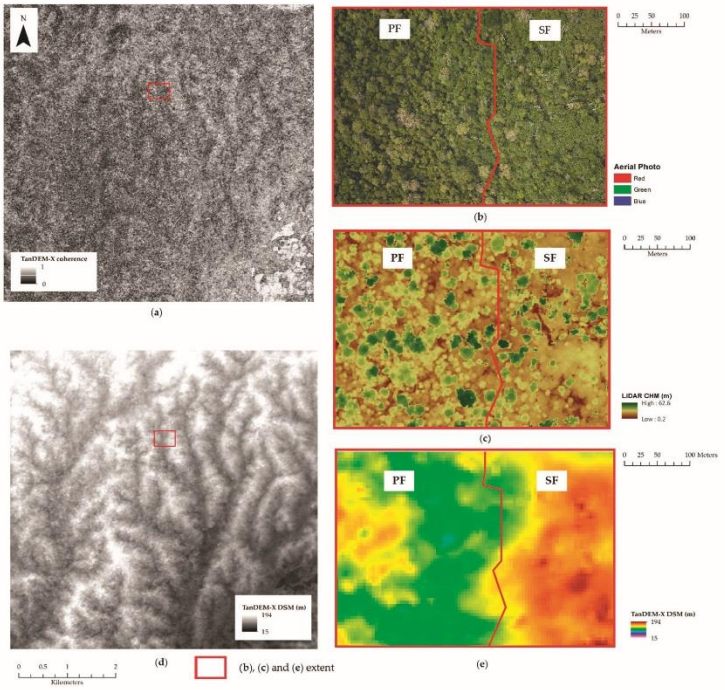

Figure 2. (**a**) TanDEM-X coherence modulus; (**b**) Aerial photo (0.5 m resolution); (**c**) Canopy Height Model (CHM) derived from airborne LiDAR (1 m resolution); (**d**) TanDEM-X DSM; and (**e**) TanDEM-X DSM subset. Boundary between primary forest (PF) and secondary forest (SF) (red line) according to the land cover map provided by the Indonesian Ministry of Forestry [66] is shown on the aerial photo (**b**); LiDAR CHM (**c**) and TanDEM-X DSM (**e**).

Appendix II

3.2. Reference Datasets

LiDAR data was acquired on 14 November 2014 using the Optech ORION M300 system (frequency: 55 Hz). The airborne LiDAR instrument was flown at an altitude of 700 m above ground level, scan angle of $\pm 18^{\circ}$, swath width of 455 m with an overlap of 227 m. The resulting point density was 5.75 points per m^2 (excluding overlap). The vertical accuracy for all LiDAR returns on clear ground was 0.08 m (standard error at 1 sigma). The data covers 9.7 $\times$ 0.7 km^2 (Site A) and 4.5 $\times$ 0.8 km^2 (Site B). The LiDAR products were geocoded to WGS84 datum, Zone 50 South. Lidar2dems open source software developed by Applied GeoSolutions was used to process the LiDAR data to provide the following: a Canopy Height Model (CHM) at 1 m resolution was generated by subtracting a Digital Terrain Model (DTM) from a Digital Surface Model (DSM) (Figure 2). The general term Digital Elevation Model (DEM) is used to refer to DSM, DTM or CHM.

A land cover map developed by the Indonesian Ministry of Forestry [66] was also used to distinguish between broad vegetation classes with additional visual inspection of aerial photography (Figure 1).

Aerial photos (AP) (0.5 m resolution) were acquired at the same time as the LiDAR overpass using a Trimble 80 megapixel medium format digital aerial camera. The APs were used as reference data to aid in the supervised analysis for the selection of classes of interest, since ground truth data was not available. The APs were deemed suitable to aid the selection of structural classes since they were able to capture illumination variability giving rise to textural differences derived from the spatial arrangement of canopy components (combination of sunlit or shadow areas), and so could be used to locate areas with different structural properties through visual inspection.

3.3. Vegetation Structural Class Selection

Analysis was performed in 315 virtual plots (35 $\times$ 35 m^2 = 0.12 ha) located in primary lowland *Dipterocarpaceae* forest (intact) (PF), secondary forest (disturbed) (SF), mixed scrub (MS) and grassland (GR). Figure 3 shows a representative sample of plots for each class visualized on a LiDAR CHM. A random sampling approach was devised within the extent of both the LiDAR and TanDEM-X datasets so that the number of non-overlapping plots of size 35 $\times$ 35 m^2 could be maximized without user interference. The choice of window size was determined from the knowledge of the landscape taking into account the spatial arrangement and size of canopies so that the variability was appropriately captured. It could not be smaller as the largest crown dimensions were in the range of 10–20 m in the intact primary forest (PF) and considering the random sampling approach ensured that the plots were not selected by the user so that the window was not centered on a single emergent crown, and if any larger plots might have contained a mixture of forest types, and the resolution of any eventual product using windows of this size would be reduced.

Class selection was based on a land cover map derived from Landsat developed by the Indonesian Ministry of Forestry [66] and on visual interpretation of high resolution aerial photography (0.5 m resolution). The class "mixed agriculture and scrub" described in the Indonesian Ministry of Forestry land cover map was broad and not representative of the condition in 2014 (as observed from aerial photography) thus, it was deemed appropriate to partition the class into two separate classes: grassland (GR) and mixed scrub (MS) based on visual inspection. The MS class is composed of a combination of *Imperata cylindrica* and presents taller re-growing vegetation such as shrubs and young trees which are not present in the grassland class (GR) which is prevalently colonized by *Imperata cylindrica*.

Landscape heterogeneity from 2D wavelet spectra was assessed based on randomly selected pixels which are representative of the chosen classes (PF, SF, MS and GR) to give insight into the target structure at four scales of decomposition based on a LiDAR CHM and TanDEM-X DSM (the figure in Section 4.2). The set of cases considered are as follows: (a) Emergent trees in a multi-layered heterogeneous (in terms of heights) matrix characteristic of old-growth forest (PF); (b) Relatively homogenous secondary forest patches composed by a carpet of crowns with high clumpiness. Absence of tall emergent trees but has reached full canopy cover (SF); (c) Early stage re-growth presenting

smaller tree crowns (2–3 m) closely packed but discernible from LiDAR (MS); (d) Homogeneous grassland (*Imperata cylindrica*) presenting low height with scattered small shrubs (GR).

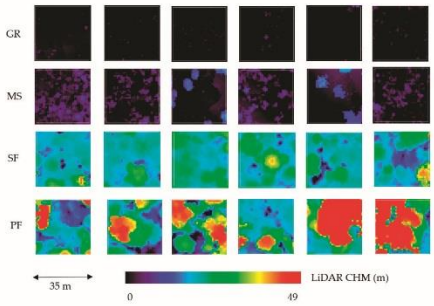

Figure 3. Sample classes derived from a LiDAR Canopy Height Model (CHM) (m) within 35 × 35 m^2 plots illustrating vertical structure arrangement (height) in: primary forest (intact) (PF), secondary forest (disturbed) (SF), mixed scrub (MS) and grassland (GR).

3.4. LiDAR and TanDEM-X Texture Correlation Analysis to Assess Impact of Topographic and Canopy Structures

Scaling (spectral) analysis of LiDAR and TanDEM-X datasets was performed in the wavelet domain along a profile covering 6.95 km in a north-south direction dominated by PF and SF. The aim of the analysis was to identify scales where textural patterns associated with topographic or canopy features develop within the different Digital Elevation Models (DEMs). The following two-point spatial statistics were computed in the wavelet domain [70]: (a) wavelet variance; and (b) wavelet co-variance (between LiDAR DTM/DSM, LiDAR DTM/CHM, and LiDAR DTM/TDX DSM). A wavelet representation is used instead of a Fourier one because the processes are multi-scale and non-stationary. The analysis provided an assessment of the relative influence on the signal texture of topographic structures and canopy structures, which is the main concern of the current study.

3.5. 2D Wavelet Spectra

Information on canopy structure is carried by datasets where vegetation height (or a proxy) is mapped as a function of space (e.g., LiDAR CHM or TanDEM-X DSM) (Figure 4). This mapping provides a two-dimensional random field, whose spatial (two-point) statistics condenses measures of the horizontal and vertical distribution of the forest. These random fields are analyzed using two-point statistics provided by the variance of a wavelet frame that acts as a differential operator (Equation (1)). This statistics, analogous to the structure function lends to the characterization of stationary random processes, as well as of non-stationary processes with stationary increments (e.g., fractals) [29].

$$\langle WS(s,\ x)^2 \rangle \cong \langle (f(x+s) - f(x)^2) \rangle \quad (1)$$

In particular, we consider exploiting the well-known properties of optimal space-frequency resolution of wavelets, and local (in space) estimates of the wavelet variance as a function of scale.

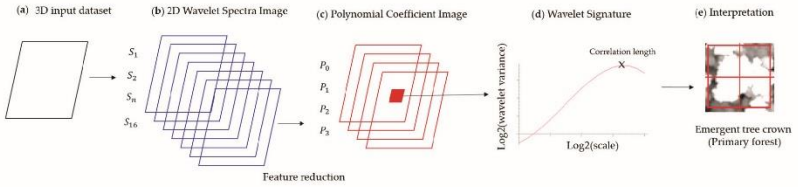

Figure 4. Flowchart illustrating the application of 2D wavelet spectra to 3D datasets for the analysis of landscape heterogeneity across a disturbance gradient: (**a**) 3D input dataset; (**b**) generation of 2D wavelet spectra image at four dyadic scales (16 scales in total); (**c**) feature reduction to four wavelet polynomial coefficients by fitting a 3rd order polynomial to the wavelet signature; (**d**) wavelet signature (wavelet variance as a function of scale); and (**e**) interpretation of the wavelet signature based on target structural characteristics.

At each point in space (at each pixel location of the analyzed image), we obtain, in the log–log variance/scale place, a characteristic signature of the process, which reflects process parameters, such as field roughness, correlation structures and intermittency. This data structure is called "2D wavelet spectrum" (WS), and it is an extension of the method developed by De Grandi et al. [70]. In more detail, the input field (e.g., vegetation height image) is decomposed in the wavelet frame basis using four dyadic scales. Local estimates of the wavelet variance are obtained by convolving the square of the wavelet coefficients with a B-spline smoothing function (Equation (2)).

$$WS\,(s,\ i,\ j)\ =\ \left(c_{x,s}\,(i,\ j)^2 + c_{y,s}\,(i,\ j)^2\right) \otimes \beta_{i,j} \tag{2}$$

Each signature $\log_2$WS ($\text{LiDAR}_{\text{CHM}}$WS or TDX_{DSM}WS) is interpolated in scale with a step of $\frac{1}{4}$ and fitted by a 3rd degree polynomial function. This function provides a good approximation to the wavelet signatures [70]. Four polynomial coefficients for each pixel of the input field constitute finally the dimensionally reduced features that describe the 2D wavelet spectrum. Two-point statistics was generated by deriving four polynomial coefficients: for LiDAR CHM (LiDARCHM_{P_0}, LiDARCHM_{P_1}, LiDARCHM_{P_2} and LiDARCHM_{P_3} and for TanDEM-X DSM (TDXDSM_{P_0}, TDXDSM_{P_1}, TDXDSM_{P_2} and TDXDSM_{P_3}). Pixel based analysis was undertaken to explore the sensitivity of 2D wavelet spectra to canopy structure heterogeneity through a gradient of varying vegetation structure (PF, SF, MS and GR) (see Section 3.3).

3.6. Separability

To assess statistically the separability between four classes afforded by the wavelet spectra polynomial representation the Jeffries–Matusita (JM) distance was computed. The JM distance of a pair of probabilistic distributions indicates the average distance between two classes density functions and it features a saturating behavior with increasing separation [71]. This fact makes it more suitable for dealing with a multi-class problem, because it avoids bias when taking averages due to an easily separable class. It is therefore suitable for the problem at hand, which has four features and four classes. The JM distance (Equation (3)) is derived from the Bhattacharyya distance (BD) (Equation (4)) [71]. The JM distance ranges between 0 and $\sqrt{2}$ with highest values indicating greater class separability [71].

$$JM_{ij}\ =\ \sqrt{2(1-e^{-BD})} \tag{3}$$

where BD:

$$BD\ =\ \frac{1}{8}\left(M_i - M_j\right)^T \left[\frac{C_i + C_j}{2}^{-1}\right]\left(M_i - M_j\right) + \frac{1}{2} ln\left[\frac{\left|\frac{C_i+C_j}{2}\right|}{\sqrt{|C_i|\,|C_j|}}\right] \tag{4}$$

where i is the class with mean vector M_i and co-variance matrix C_i.

Pairwise JM resulted in six JM distances, which are averaged and normalized by dividing the theoretical maximum JM distance of $\sqrt{2}$. The normalised average JM distance was used as a parameter to indicate overall class separability [71]. Upper and lower bounds of the probability of the classification error $P_e(i,j)$ are given by [71] (Equation (5)):

$$\frac{1}{16}(2 - JM_{i,j}^2)^2 \leqslant P_E(i,j) \leqslant 1 - \frac{1}{2}(1 + \frac{1}{2}JM_{i,j}^2) \quad (5)$$

The JM distances are computed for the six combination of class pairs among GR, MS, SF, PF, and feature vectors $\vec{v_{x,y}} = \{P_0, P_1, P_2, P_3\}$, where P_i are the polynomial coefficients of the wavelet spectra averaged over the training set plots, defined as described in Section 3.3. Moreover, to investigate the dependence of class separability on scale, the JM distance is also computed for each scale of the signature separately $\langle W^2 \rangle = f(scale)$ derived from the polynomial coefficients. In this case, the feature space is one-dimensional.

4. Results and Interpretation

4.1. LiDAR and TanDEM-X Textural Correlation Anaysis to Assess Coupling of Topographic and Canopy Structures

Canopy structure (roughness) measures derived from 3D datasets can provide information on landscape disturbance and recovery [25] but can be affected by environmental factors [53] such as the underlying topography especially in steep terrain [54]. Since the transect is characterized by low-lying undulating terrain (52.7 ± 3.2 m) and often the presence of mild slopes (12.1° ± 10°) and at higher elevation (81.4 ± 11.2 m) and slopes (12° ± 4.3°) in AG and MS plots (elevation: 64.9 ± 21.4 m, slopes: 11.9° ± 6.2°), understanding of topographic structure is important to gain a better insight on the processes that play a role and the extent to which they influence the 3D information provided by LiDAR and InSAR. This is especially relevant as only the LiDAR provides both a DSM and DTM, and thus the possibility to calculate a CHM; TanDEM-X only provides a DSM.

The wavelet variance, being a two-point statistic proxy of the structure function, bears information on the dominant correlation patterns associated with either topographic or canopy structures, these happening at different scales and can also give insight into the impact of topography and canopy structure by comparison with the available LiDAR DTM which carries information on ground topography (Figure 5a). To test this we performed an analysis over the 6.95 km transect in primary and disturbed forest, considering the LiDAR and TanDEM-X data. The LiDAR DTM (red) signature reveals the trend of a process with smooth texture at short scales and long memory (correlated patterns) up to 200 m. This scale corresponds to the onset of regular (almost periodic) patterns induced by the topography from the hilly terrain, which is reflected on the LiDAR DSM (black) and the TanDEM-X DSM (green), while the LiDAR DSM (black) carries strong information of short scale texture, with correlation length of tens of meters. Importantly, this texture patterns is also present (exactly overlaid) in the LiDAR CHM (blue) signature, revealing that within the short scale range (between 1 and 10 m) the textural information is related to canopy structure and not to topography. The TanDEM-X DSM (green) is also sensitive to these short scales structures due to canopy variation (i.e., variance greater than LiDAR DTM) but with lower separation with respect to variance due to topography (LiDAR DTM).

The wavelet co-variance holds information on the textural correlation between datasets, these being the LIDAR DTM, DSM and CHM and the TanDEM-X DSM (Figure 5b). The LiDAR DTM-DSM (red) confirms the presence of structures (periodic patterns) in the DTM texture at correlation length of 200 m (scale 2^8), which are reflected onto the DSM texture. At shorter scales, the texture correlation between LiDAR DTM and TanDEM-X DSM (black) is one order of magnitude lower, especially at scales typical of canopy width and gaps. This fact reinforces the point that although the TanDEM-X DSM is affected by the DTM noise, information on vegetation structure can still be detected as it happens

at a different scale range. However, there is a striking feature in the LiDAR DTM/CHM co-variance (green) that reveals that there is also a textural reflection of topographic structures onto the LiDAR CHM, although at two orders of magnitude less important. Still, even if it is a weak coupling, this could mean that the LiDAR CHM has a component that follows the strong topographic features at scale of 200 m. This coupling could confirm the fact that forest in valleys is higher than forest on ridges. This is due to several factors such as: (1) higher soil fertility and moisture availability in valleys; and (2) more need for forest in valleys to grow taller to reach light (light competition) [38].

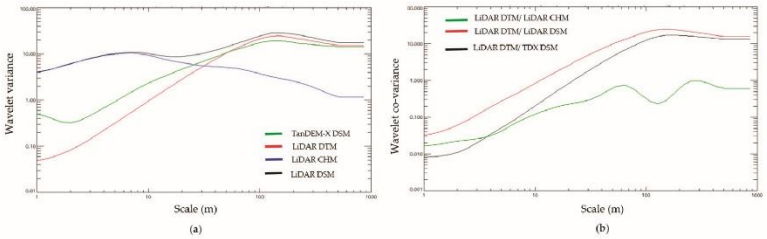

Figure 5. (**a**) Wavelet variance as a function of 10 dyadic scales (2 m to 1000 m) computed over a 6.95 km transect in intact (PF) and disturbed secondary forest (SF). TanDEM-X DSM (green) and LiDAR derived datasets (DSM: black, CHM: blue and DTM: red); (**b**) Wavelet co-variance providing information on textural correlation between datasets: LiDAR DTM, DSM and CHM and the TanDEM-X DSM. LiDAR DTM/LiDAR CHM (green); LiDAR DTM/LiDAR DSM (red) and LiDAR DTM/TDX DSM (black). Abbreviations: Canopy Height Model (CHM); Digital Surface Model (DSM) and Digital Terrain Model (DTM).

The results is key to determine the potential of TanDEM-X DSM for detecting canopy heterogeneity over larger areas compared to airborne LiDAR since TanDEM-X provides global coverage [57]. Moreover, as opposed to a CHM the characterization of canopy heterogeneity does not depend on the availability of ground topography (DTM) but relies on the canopy roughness information provided from a DSM which does not penetrate deep enough into the canopy to reach the ground (in the presence of dense tropical forest) and therefore is restricted to a layer located somewhere within the upper canopy [72]. Limitations due to resolution are to be taken into account since this is lower for TanDEM-X and it does not enable to resolve single crowns as in the high resolution airborne LiDAR. The results have implications on the utility of LiDAR CHM but most importantly the potential of TanDEM-X DSM, which can provide complementary information on canopy roughness.

Further analysis was undertaken at short scales (between scale 2^0 and 2^4). Longer scales were not considered since the ground topography was found to play an increasingly important role in affecting the process. Future research which aims to link textural variations to forest parameters (e.g., crown dimensions, height and above-ground biomass) should take into account the influence of topography to avoid bias in the estimation of these parameters which could be caused by the underlying relief rather than structural parameters [73].

4.2. Canopy Structural Heterogeneity Based on 2D Wavelet Spectra

Airborne LiDAR CHM is optimal to gain understanding of the processes driving the wavelet signature due to the high resolution (1 m) and thus, the ability to resolve single crowns. Individual spectrum data points, one in each of the four land cover types (each corresponding to the local wavelet variance as a function of scale, i.e., a wavelet signature) were considered in order to help in the interpretation of wavelet spectra of a LiDAR CHM. Each spectrum sample corresponds to a local wavelet variance estimate at one point in space and for all scales (i.e., a wavelet signature). The interpretation of the wavelet signatures is based on two main considerations: (a) extent to which

the process presents self-similarity (correlation length); and (b) wavelet variance absolute values for a set of landscape heterogeneity cases is illustrated in Figure 6.

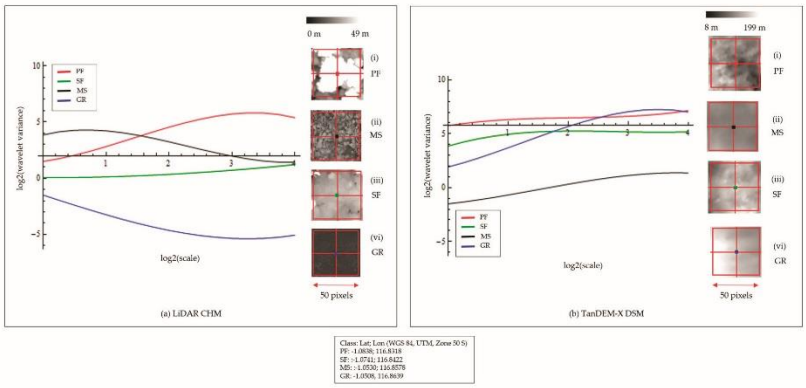

Figure 6. Wavelet signatures based on: (**a**) LiDAR CHM; and (**b**) TanDEM-X DSM based on one pixel taken in: PF (red), MS (black), SF (green) and GR (blue). Colored squares indicate the pixel selected for the analysis: 1 pixel (1 × 1 m^2 in LiDAR CHM and 4.6 × 4.6 m^2 in TanDEM-X DSM.

Wavelet signatures for a multi-layered, complex old-growth forest patch (PF) (red line) dominated by a large emergent crown (18 m) show the typical trend of stationary noise with an exponential autocorrelation function (increasing variance with scale, asymptotically converging to the process variance). Wavelet variance for PF ranges between 1.5 and 5.4 with a maxima (correlation length) around scale 2^3 (8 m). Of course, this figure must not be interpreted as a crown width measure, but as the neighborhood within the crown where the canopy height variations are still correlated. This can be verified by interpretation of inset (Figure 6a(i)) showing the presence of a large emergent crown surrounded by coalescing large crowns.

The flat wavelet signature for a pixel selected in SF (Figure 6a(iii)) composed of interlocking crowns of similar height (homogeneous structure) with a lack of emergent trees is markedly different from that of the heterogeneous PF. The signature is typical of a white noise process meaning that the process is scale invariant and also presents no correlation length meaning that the process is self-similar at all scales considered and this is due to the homogeneity of the forest patch, it does not present correlated features. The wavelet variance (in this case proportional to the scale variance) is lower compared to that of PF (range between 0.06 and 1.2).

The MS class signature (black line) reveals the presence of non-stationarity with full multi-scale correlation patterns (decreasing variance with increasing scale), and a first correlation length at short scale (2 m). This is because the size of crowns located in MS (as seen in Figure 6a(ii)) is much lower (1–2 m) compared to the size of emergent tree crowns in PF (Figure 6a(i)).

The GR class wavelet signature also presents a white noise process, with the lowest process variance. The corresponding LiDAR CHM pixel selected is shown in (Figure 6a(vi)) and is clearly dominated by a layer that is texturally homogeneous and featureless.

The corresponding TanDEM-X DSM analysis does not match with the LiDAR CHM analysis. This highlights the fact that the sensor resolution is of key importance in textural measures. The two forest classes (PF and SF) (red and green line) behave in a similar way, with the signatures revealing white noise processes. This is due to the fact that now single canopies cannot be resolved, and the correlated patterns appearing at 1 m resolution in the LiDAR CHM signatures are now not visible.

Appendix II

Nonetheless, the PF process features a higher process variance (Figure 6b(i)), meaning that still some discrimination between PF and SF is possible with the one-point statistic. The MS signature (Figure 6b(ii)) is again white noise and presents the lowest process variance. Again, this is due to the fact that smaller crowns cannot be resolved. Importantly, the GR signature (Figure 6b(vi)) reveals a stationary correlated process, with a still around 8 m (scale 2^3). This is ascribed to the influence of topography. Indeed, as these areas are dominated by surface scattering, from the spatial statistic (texture) point of view, the main dependence comes from the terrain height variations, whereas, in forested areas, volume scattering moves the PCH upwards towards the canopy upper layer and limits penetration capabilities.

4.3. Interpretation of Wavelet Measures of Structural Heterogeneity Based on Height Variance

4.3.1. Wavelet Signatures Polynomial Fit

Probability distributions (PD) for the first wavelet polynomial coefficient (P_0) derived from the 3rd order fitted polynomial are found in Figure 7. P_0 is the intercept with the y-axis in the log–log variance–scale plot, therefore it is a good approximation to the variance at short scale. From Section 4.1 we assume that most of the variation due to canopy structures occurs at short scale and thus, P_0 holds more information compared to the other polynomial coefficients (P_1, P_2 and P_3).

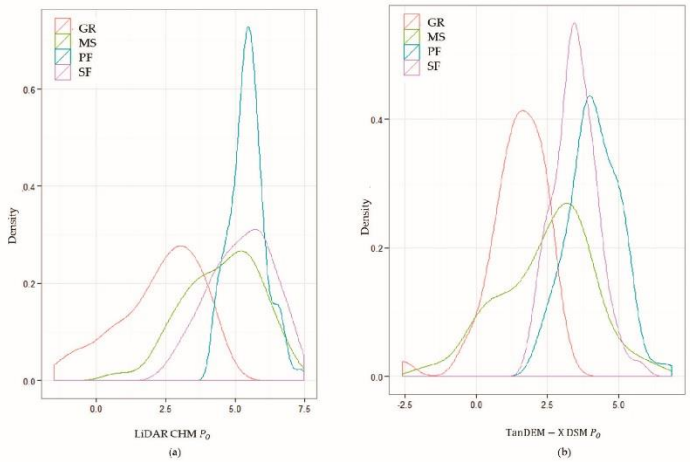

Figure 7. Probability distribution (PD) by class: (**a**) LiDAR CHM P_0 PD; and (**b**) TanDEM-X DSM P_0 PD. Greater information was observed using P_0 compared to P_1, P_2 and P_3.

4.3.2. Regression Analysis

In order to gain insight into the measures provided by the wavelet spectra and their mapping onto the physical characteristics of the observed random field (forest structural heterogeneity), a regression analysis was performed between the LiDAR CHM standard deviation and the LiDAR CHM P_0. P_0 is the constant term of the wavelet variance polynomial approximation. Therefore, it provides a figure of the overall variance (energy) carried by the wavelet representation. P_0 is also the intercept with the y-axis in the log–log variance–scale plot, therefore it is a good approximation to the variance at short scale.

We found that the LIDAR CHM P_0 is well correlated with the standard deviation of the LiDAR CHM (R^2 = 0.77, N = 315) (Figure 8a) and the TanDEM-X DSM P_0 is also well correlated with the

standard deviation of the TanDEM-X DSM (R^2 = 0.72, N = 315) (Figure 8b). This means that the two-point statistic (P_0) at short scale of the process carries the same information as the one-point statistic (standard deviation) of the same process. Moreover, the one-point statistic of the TanDEM-X DSM is also equivalent to the CHM two-point statistic. This point confirms that, at least at first order, the properties of the CHM process are reflected onto the TanDEM-X DSM process.

On the other hand, the LiDAR CHM standard deviation was weakly correlated with TanDEM-X P_0 (R^2 = 0.34, N = 315). This case indicates that the TanDEM-X DSM process is not related in a simple way to the CHM process, but it is the result of the superposition of several random processes, such as terrain topography and InSAR phase signal to noise ratio. Therefore, the textural dependency of the DSM cannot be measured only by a simple one-point statistic, or a one-scale two point statistic, but the full multi-scale measures (wavelet spectra) must be called into play.

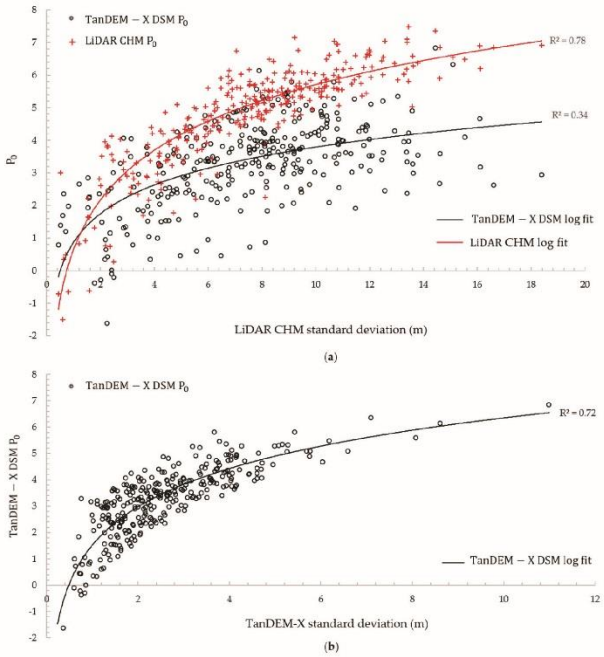

Figure 8. Logarithmic relationship between: (**a**) LiDAR CHM standard deviation (m) and LiDAR CHM P_0 (red cross) (R^2 = 0.77, N = 315), and LiDAR CHM standard deviation (m) and TanDEM-X DSM P_0 (black circle) (R^2 = 0.34, N = 315); and (**b**) TanDEM-X DSM standard deviation (m) and TanDEM-X P_0 (R^2 = 0.72, N = 315).

Finally, notice that the correlation between the two-point statistic P_0 and the one-point statistic (standard deviation) of the same process (Figure 8a) is in line with the claim that the wavelet variance is an asymptotic unbiased estimator of the process variance [74]. Indeed, given the wavelet frame of choice that acts a differential operator, the wavelet variance is tantamount to (Equation (6)):

$$\langle W(x,\tau)^2 \rangle = \langle (f(x) - f(x+\tau))^2 \rangle \, \tau \to \infty \xrightarrow{yields} 2(\langle f^2 \rangle - \langle f \rangle^2) = 2VAR(f) \quad (6)$$

Appendix II

Often in old-growth tropical forest height differences between individual trees is significant as a result of the presence of emergent trees [75]. The results are in line with findings based on optical sensors that indicate that texture is driven by the variation in vertical structure (presence of emergent trees) of the canopy and gives rise to canopy texture [76]. Stands with a high variance in tree height have a rougher upper canopy compared to those with lower variance [76]. However, in DEMs provided by ranging or interferometric sensors (e.g., from LiDAR or InSAR), texture is not related to shadowing effects but to the gradient of height information. The area covered by large emergent trees (>35 m) in SF (burned) plots is significantly different from PF ($p < 0.01$, N = 222). This is a good indicator to explain why SF presents a lower canopy roughness compared to PF.

4.3.3. LiDAR CHM and TanDEM-X Polynomial Coefficients and Standard Deviation Frequency Distributions

LiDAR CHM (height) frequency distribution (FD) in a 23 × 23 pixels (0.05 ha) area presenting low LiDAR CHM P_0 (0.12 ± 0.65) (mean± standard deviation) (SF) was compared with an area presenting high P_0 (5.6 ± 1.2) (PF) (Figure 9b). Indeed, the area with lowest P_0 (SF) presents a more homogeneous height distribution, ranging between 21.1 and 27.9 m (mean ± standard deviation) (25.9 ± 1.1) (Figure 9). Conversely, higher P_0 (black line) (Figure 9b) corresponds to a more heterogeneous structure comprising tree heights ranging between 11.8 m and 48.3 m (34.6 m ± 10.7 m) (Figure 9a).

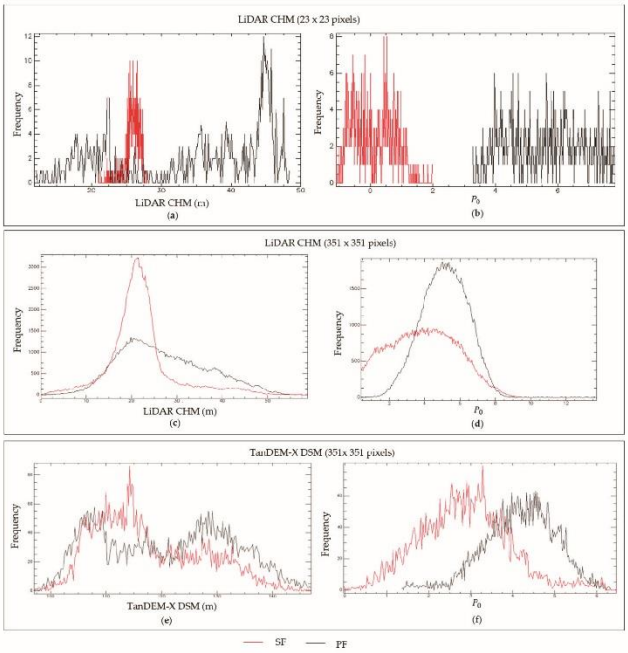

Figure 9. LiDAR CHM, TanDEM-X DSM and corresponding P_0 frequency distributions (FD) for primary forest (intact) (PF) (black line) and secondary forest (SF) (red line): (**a**) LiDAR CHM FD (23 × 23 pixels); (**b**) LiDAR CHM P_0 FD (23 × 23 pixels); (**c**) LiDAR CHM FD (351 × 351 pixels); (**d**) LiDAR CHM P_0 FD (351 × 351 pixels); (**e**) TanDEM-X DSM (m) FD (351 × 351 pixels); and (**f**) TanDEM-X DSM P_0 FD (351 × 351 pixels).

Appendix II

Lower tree height standard deviation (in this case provided by LiDAR CHM) observed in SF is often associated with young even aged stands of mono-dominant species [76]. Another independent dataset such as field data would be required to confirm this assumption. The forest successional gradient ranging from intact to burnt and ultimately regrowth and the variance of the CHM has been observed in other studies based on optical remote sensing, whereby the presence of emergent crowns caused a significant shadowing effect on the lower vegetation in PF influencing texture from spectral information [76].

Analysis taking into account 351 × 351 pixels plots of PF and SF was explored (Figure 9c–f). At this scale the LiDAR CHM FD indicates that the SF heights are no more restricted to the 21–27 m range like in the sub-hectare case (Figure 9a). However, there is a clear predominance around 22 m in the SF (Figure 9c). The SF also presents a long tail (not present in the sub-hectare case), which corresponds to patches that have not been burned within the burned matrix. Instead, homogeneous patches are areas where forest was affected by fire, and, after 17 years, a forest successional stage with a more uniform structure replaced heterogeneous old-growth formations. Because of the complex composition unburned small forest islands patches surrounded by burned forest, they will be more prone to fire disturbance since future fires will be facilitated by the more open canopy [15]. Instead the PF presents a distribution ranging from 0 to 59 m (mean ± standard deviation: 27 ± 9.5 m) (Figure 9c). At hectare scales the PF is still very heterogeneous and multi-layered, a characteristics observed in many tropical forests studies due to the high diversity of species [24].

Similar, effects can be noticed in the TanDEM-X DSM (Figure 9f) where SF P_0 ranges between −0.02 and 6.5 (mean ± standard deviation: 2.9 ± 1.0), while PF P_0 ranges between 1.3 and 6.3 (mean ± standard deviation: 4.2 ± 0.8). In this case, the one-point statistical separation between PF and SF is less evident due to two reasons: coarser resolution (4.6 m); approximation of the top canopy spatial variation provided by location of the coherence PCH, this in turn depending on the canopy volume density and the sensor's parameters [69]. However, notice that the distribution based on TanDEM-X DSM P_0 still bears information related to structural differences between PF and SF.

We can conclude that textural variation between SF and PF, as measured by one-point statistic (LiDAR CHM height FD) depends on the scale of observation and the disturbance conditions (e.g., presence of unburned forest patches within a burned forest matrix). This process has been observed in other tropical forest settings where, unburned forest patches were still present within the burned forest [77,78]. In this particular case, they formed connected ribbons of old-growth forest along streams [38] and they were not burned since the flammability in the presence of higher moisture is lower compared to those areas further away from water sources [15].

LiDAR CHM wavelet spectrum image (P_0) (Figure 10b) visual interpretation confirms the results from the FDs. Figure 10a shows a false color image of the LiDAR CHM, where the red line marks the boundary between PF and SF to illustrate how forest height varies across the LiDAR extent. Figure 10b shows the corresponding LiDAR CHM P_0. Lower LiDAR CHM P_0 (light green) indicates more homogeneous, even height forest patches while, high P_0 is represented in brown. The onset of the more homogeneous forest patches is clearly dominant in the region designated as the burned SF area of the SWPF to the North of the red line boundary. The TanDEM-X DSM (m) is shown in (Figure 10c) and the corresponding P_0 is illustrated in (Figure 10d) with low values in brown and high values in dark green. The results are further confirmed by class separability in the feature space of the wavelet spectra descriptors (Section 4.4).

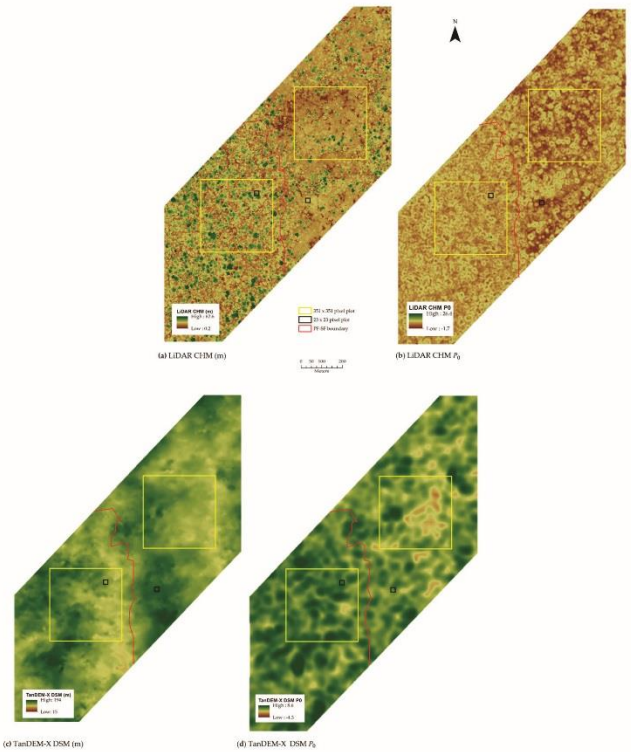

Figure 10. (**a**) LiDAR CHM; (**b**) LiDAR CHM wavelet spectrum image (P_0); (**c**) TanDEM-X DSM; and (**d**) TanDEM-X DSM wavelet spectrum image (P_0). The red line marks the boundary between SF and PF according to data supplied by the Indonesian Ministry of Forestry [66]. The onset of homogeneous (in terms of height distribution) forest patches, characteristics of the burnt SF, is clearly visible in the LIDAR CHM (**a**) to the North of the boundary line, and it is well detected by areas of lower LiDAR CHM P_0 in (**b**) and lower TanDEM-X P_0 corresponding toSF. Sample plots used in the FD analysis: 23 × 23 pixel plots (black) and 351 × 351 pixel plots (yellow).

4.4. LiDAR CHM and TanDEM-X DSM 2D Wavelet Spectra Class Separability

JM distance was performed based on the maximum number of common samples for each class pairs (GR/MS: 44, GR/SF: 44, GR/PF: 44, MS/SF: 49, MS/PF: 49, and SF/PF: 96).

4.4.1. Scale by Scale Class Separability

$LiDAR_{CHM}$ Wavelet Signature ($LiDAR_{CHM}WS$) separability (see Section 3.5 for WS definition) at different scales was performed on pairwise JM to assess the scale at which class separability was greater (Figure 11a). The JM distance ranges between 0 and $\sqrt{2}$ with highest values indicating greater class separability. Best separability between GR/MS ($JM_{GR/MS}$ = 0.82), GR/SF ($JM_{GR/SF}$ = 1.0) and GR/PF ($JM_{GR/PF}$ = 1.26) was achieved at 2.4 m (scale $2^{1.25}$), while the best separability between class pairs MS/SF ($JM_{MS/SF}$ = 0.49) and SF/PF ($JM_{SF/PF}$ = 0.81) was achieved at 2.8 m (scale $2^{1.5}$). Best separability between MS/PF occurred at 1.4 m (scale $2^{0.5}$) ($JM_{MS/PF}$ = 0.78).

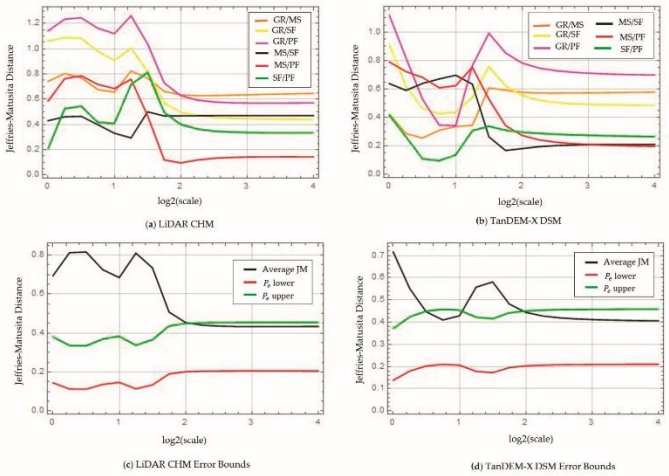

Figure 11. Scale by scale pairwise Jeffrries Matusita (JM) distance trend for primary forest (PF), secondary forest (SF), mixed scrub (MS) and GR (grassland) at four dyadic scales: (**a**) LiDAR$_{CHM}$WS; (**b**) TDX$_{DSM}$WS. ($n_{GR/MS}$ = 44; $n_{GR/SF}$ = 44; $n_{GR/PF}$ = 44, $n_{MS/SF}$ = 49, $n_{MS/PF}$ = 49 and $n_{SF/PF}$ = 96); (**c**) LiDAR$_{CHM}$WS average JM; and (**d**) TDX$_{DSM}$WS average JM with associated error bounds (P_e lower and P_e upper).

Separability results considering TDX$_{DSM}$WS scale by scale (Figure 11b) indicate that the highest separability between class pairs is achieved at 4.6 m (scale 2^0) for class pairs GR/SF (JM$_{GR/SF}$ = 0.91), GR/PF (JM$_{GR/PF}$ = 1.1), MS/PF (JM$_{MS/PF}$ = 0.80) and SF/PF (JM$_{SF/PF}$ = 0.41), while the highest separability between class pairs GR/MS (JM$_{GR/MS}$ = 0.61) is achieved at 13 m (scale $2^{1.5}$) and at 9.2 m (scale 2^1) for class pair MS/SF (JM$_{MS/SF}$ = 0.70).

LiDAR$_{CHM}$WS outperforms the TDX$_{DSM}$WS due to its higher resolution. Nonetheless, textural information derived from the TDX$_{DSM}$WS can still provide a certain degree of separability. Results also confirm that information at higher scales does not bear significant information on class separability and even the first few scales contain limited information when taken singularly. Analysis of the full WS is therefore essential to achieve improved separability.

4.4.2. Full Wavelet Signature (WS) Class Separability

Class separability results based on the full LiDAR$_{CHM}$WS and TDX$_{DSM}$WS using the JM distance are found in Table 2.

Table 2. JM distance separability between four classes considering full WS: TDX$_{DSM}$WS; and LiDAR$_{CHM}$WS. Range between 0 and $\sqrt{2}$ ($n_{GR/MS}$ = 44; $n_{GR/SF}$ = 44; $n_{GR/PF}$44, $n_{MS/SF}$ = 49, $n_{MS/PF}$ = 49 and $n_{SF/PF}$ = 96).

	Class	GR	MS	SF	PF
TDX$_{DSM}$WS	GR		1.29	1.35	1.39
	MS	1.29		1.23	1.26
	SF	1.35	1.23		1.18
	PF	1.39	1.26	1.18	
LiDAR$_{CHM}$WS	GR		1.29	1.35	1.39
	MS	1.29		1.31	1.32
	SF	1.35	1.31		1.36
	PF	1.39	1.32	1.36	

Appendix II

Class separability based on $LiDAR_{CHM}WS$ is high between all classes. Highest separability is achieved between GR and PF ($JM_{GR/PF}$ = 1.39) and lowest separability between GR and MS ($JM_{GR/MS}$ = 1.29). Results indicate that the separability between SF and PF ($JM_{SF/PF}$ = 1.36) is higher compared to the separability between MS and SF ($JM_{MS/SF}$ = 1.31). Instead the spatial configuration for GR is markedly separable from both SF and PF and this is reflected in the JM ($JM_{GR/SF}$ = 1.35 and $JM_{GR/PF}$ = 1.39).

$TDX_{DSM}WS$ achieves highest separation between GR and PF as well ($JM_{GR/PF}$ = 1.39) and lowest separation between SF and PF ($JM_{SF/PF}$ = 1.18). Compared to the $LiDAR_{CHM}WS$, the separability using $TDX_{DSM}WS$ is lower for the pairs MS/SF, MS/PF, SF/PF, and PF/MS, while identical separability was found between GR and all other classes. The analysis highlights the lower JM separability results considering a scale by scale analysis ($0.1 \leqslant JM \leqslant 1.26$ for LiDAR CHM; $0.1 \leqslant JM \leqslant 1.1$ for TanDEM-X DSM) (Section 4.4.1), compared to separability considering the full wavelet signature ($1.29 \leqslant JM \leqslant 1.39$ for LiDAR CHM; $1.18 \leqslant JM \leqslant 1.39$ for TanDEM-X DSM).

Statistical evaluation based on $TDX_{DSM}WS$ and $LiDAR_{CHM}WS$ is found in Table 3. The results for $TDX_{DSM}WS$ are reported as follows: P_e lower bound P_e upper bound (%), where P_e is the expected classification error. The lowest P_e is achieved between GR/PF and between MS/PF (0.06%–2.47%), while the highest P_e was found between GR/MS (2.13%–17.68%) followed by SF/PF (2.32%–15.22%). $LiDAR_{CHM}WS$ results achieved indicate the lowest P_e between classes GR/PF (0.02-1.23%), while highest P_e between MS/SF (1.31%–11.46%) followed by GR/MS (0.65%–8.07%).

Table 3. Class separability statistical evaluation based on pairwise JM distance: P_e lower bound; P_e upper bound (%) (N = 176, n = 44).

Metric	P_e (%)	Class Pair					
		GR/MS	**GR/SF**	**GR/PF**	**MS/SF**	**MS/PF**	**SF/PF**
$TDX_{DSM}WS$	Lower	3.13	0.18	0.06	0.18	0.06	2.32
	Upper	17.68	4.29	2.47	4.29	2.47	15.22
$LiDAR_{CHM}WS$	Lower	0.65	0.23	0.02	1.31	0.44	0.38
	Upper	8.07	4.77	1.23	11.46	6.60	6.18

Figure 12 highlights results using $LiDAR_{CHM}WS$ and $TDX_{DSM}WS$ representing wavelet signature (WS) averaged for 16 sample plots for each of the four classes considered. SF $LiDAR_{CHM}WS$ shows consistently lower wavelet variance (smoother spatial distribution), compared to PF with separation increasing at longer scales (>4 m). The increasing separation between the two classes at longer scales is an indication that the heterogeneity of PF is best detected when considering a larger area, since in this case the texture related patterns are the separate crowns. Correlation length is similar for both PF and SF (8 m) which indicates that the averaging of the signatures for 35×35 m^2 plots leads to the loss of information in terms of correlation length. This is possibly because the areas of SF within a 35×35 m^2 plot are composed of a mix of burned and unburned forest and, in particular, the unburned forest patches are similar in structure to the old growth PF.

GR, which is effectively a homogeneous layer of grass, exhibits the lowest wavelet variance among all classes and a longer correlation length (4 m). This is because GR is dominated by surface scattering (proven by high coherence values). While, MS, being a composite of surface and volume scattering, shows lower wavelet variance compared to SF but higher than GR. Both these low energy processes tend to a flat scale-independent functional relationship, which is indicative of a white noise process.

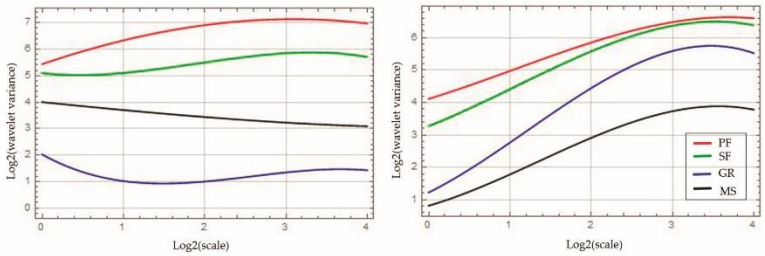

Figure 12. Average wavelet signatures for four classes (PF: red, SF: green, GR: blue and MS: black) (n = 16, N = 64): (**a**) $\overline{X}$LiDAR$_{CHM}$WS (scale: 2^0 = 1 m; 2^1 = 2 m; 2^2 = 4 m; 2^3 = 8 m; 2^4 = 16 m); and (**b**) $\overline{X}$TDX$_{DSM}$WS (scale: 2^0 = 4.6 m; 2^1 = 9.2 m; 2^2 = 18.4 m; 2^3 = 36.8 m; 2^4 = 73.6 m).

TDX$_{DSM}$WS (Figure 12b) indicates that wavelet variance is highest for PF followed by SF, GR and MS. This is in accordance with results derived from LIDAR$_{CHM}$WS aside for the wavelet variance between GR, which is higher than for MS (the opposite compared to the LIDAR CHM case). Therefore, it is the lack of volume (tree canopies) contributes to the higher penetration of TanDEM-X in grassland areas. Intuitively, the penetration of TanDEM-X to derive ground topography in lower vegetation or bare areas is greater because of lack of attenuation due the presence of volume. SF TDX$_{DSM}$WS is consistently lower compared to PF but the difference is reduced at longer scales, where SF and PF separation is reduce significantly.

Discrepancies are related to the difference in penetration depth of the two instruments and thus, the information that they provide. TanDEM-X DSM perceives the upper canopy roughness penetrating into the volume by several m (depending on the vegetation density and sensor configuration) but not reaching the ground surface in dense tropical forest. This assumption was confirmed in our context by estimating the fractional phase center height $fch = \frac{\varphi}{\beta h}$ (where β is the vertical wave number of the interferometer) from the vegetation height h provided by the LiDAR CHM along a 6.95 km transect in intact (PF) and disturbed secondary forest (SF) (see also Section 4.1). The PDF of the fch reveals the presence of two peaks, the first holding the majority of the population located at 0.8, and the second at 0.5. It has been found in some cases that a rather surprising penetration depth was achieved even in tropical forest due to clumpiness of canopy where gaps allow more penetration even at short wavelength (X-band) [61]. Higher penetration from LiDAR compared to TanDEM-X has been observed in dense tropical forest in the Amazon [61]. TanDEM-X phase conversion to a DSM is limited by the penetration depth at X-band, with the availability of future missions such as TanDEM-L [79], penetration depth into the canopy will be greater as this increases with wavelength [51]. This will provide a similar kind of information on ground topography similarly to a DTM generated from LiDAR returns and the possibility to generate CHMs using a combination of TanDEM-X/-L over a wide areal coverage [80].

5. Discussion

The understanding of forest canopy heterogeneity has impact on several ecological process including productivity and nutrient cycling [53]. Relationship between forest structure and textural properties is still not clearly understood [24,81]. This study provides increased understanding in canopy heterogeneity arising from fire disturbance and, in particular, the ability to detect areas of SF based on their structural arrangement.

Tropical forests structural heterogeneity is driven by a combination of processes: underlying topographic structure and canopy structure [54]. De-coupling the two processes to gain a better understanding of variations in canopy structure alone was considered by analysis of wavelet

variance and wavelet co-variance. This was achievable since the two processes are characterized by different dominant frequencies: high frequency components for canopy structure and low frequency components for topographic structure. Both the LiDAR CHM and the TanDEM-X DSM were affected by topographic features but only at longer scales (>2^3), while, at shorter scales (2^0–2^3), the dominant process was linked to canopy structure alone.

Secondly, height standard deviation (derived from high resolution LiDAR CHM) was found by regression analysis to be the main driver affecting wavelet based texture (P_0). Analysis reveals a logarithmic relationship between height standard deviation and P_0 for LiDAR CHM ($R^2 = 0.77$) and, with lower correlation ($R^2 = 0.34$), for TanDEM-X DSM. Results were visually confirmed from aerial photography showing areas with low LiDAR CHM P_0 corresponding to homogeneous patches with lack of tall (or limited) emergent trees, a condition stemming from the lower amount of shadowing cast by these.

LiDAR CHM standard deviation can be linked to successional stage, with more complex PF presenting higher height standard deviation compared to disturbed SF due to the presence of tall emergent trees. Results are in accordance with research indicating that height difference between individual trees can be significant, due to the presence of emergent trees, especially in old-growth tropical forests [75] and that disturbed secondary forests are less structurally complex compared to old-growth forest [82]. The addition of ground data information (e.g., fire history) on the forest condition could help the interpretation in term of the processes that generate such heterogeneity.

Potential of the wavelet signatures and wavelet spectra (WS) space-scale analysis was exemplified by selecting test cases on a high resolution dataset (airborne LiDAR CHM) to gain a better understanding as to the reasons behind wavelet variance values and their connection with statistical properties of the underlying process, such as correlation length. The interpretation of 1 m resolution LiDAR CHM was advantageous as the single crowns were resolvable thus increasing the level of detail compared to the lower resolution TanDEM-X DSM (approximately 4.6 m resolution). Visual interpretation indicates that wavelet variance is sensitive to target heterogeneity while correlation length is linked to the process self-similarity, with the limiting case of white noise with no correlation beyond zero lag.

$LiDAR_{CHM}WS$ and $TDX_{DSM}WS$ two-point statistic was successful to separate thematic classes. $LiDAR_{CHM}WS$ JM distance (with asymptotic value of $\sqrt{2}$) ranged within $1.29 \leqslant JM \leqslant 1.39$ (lowest between MS/GR) and generally (apart from separability between GR and all other classes) lower separability was achieved with $TDX_{DSM}WS$ ($1.18 \leqslant JM \leqslant 1.39$) (lowest between SF/PF).

Scale by scale separability analysis indicates that short scales (between scales 1.4 m and 2.8 m) are best for discriminating classes using $LiDAR_{CHM}WS$ with increasingly reduced separability at longer scales. In the case of $TDX_{DSM}WS$, scale by scale separability is highest between 4.6 m and 13 m. The reduced separability using $TDX_{DSM}WS$ is related to two main factors: lower spatial resolution of radar compared to LiDAR; difference in information provision of the vertical forest structure due to the lower penetration depth into the canopy (higher attenuation) of TanDEM-X compared to LiDAR in tropical forests [61]. TanDEM-X observations offer the major advantage of global coverage [57] as opposed to a restricted spatial coverage available from airborne LiDAR instruments. Therefore, despite the reduced resolution at the expenses of spatial coverage, 2D wavelet spectra derived from TanDEM-X DSM are still able (to a certain extent) to provide information on vegetation structure.

The method also provided evidence of the potential and limitation of 3D information provided by sensors with different characteristics. Moreover, regarding structural information extraction the improved performance of using two-point statistics as opposed to one-point statistics was proven. 3D information is more suitable for the characterization of areas that cannot be discriminated by two-dimensional datasets (e.g., backscatter). Requirement for 3D information is therefore suggested for the characterization of vegetation structure, in particular in view of the potential to discriminate between PF and SF. Furthermore, provision of a higher resolution DSM derived from InSAR (e.g., TanDEM-X in SpotLight mode at approximately 2 m resolution) could provide significant improvements in the characterization of canopy structure.

6. Conclusions

We found that two-point statistic applied to both TanDEM-X InSAR and LiDAR observations was effective for the discrimination of a range of thematic classes based on the Jeffries–Matusita (JM) distance. In particular, increased separability performance was found by employing the full wavelet signature (WS) compared to using each decomposition scale individually. This points to the importance of the use of multi-scale texture metrics such as these for extracting as much information from the data as possible. Of particular interest is the significant separability between PF and SF, even 17 years after the fire event.

Remote sensing instruments that provide 3D information such as TanDEM-X InSAR and LiDAR observations can be used to extract information on canopy structure. In particular, we highlight the potential of TanDEM-X DSM, which will be available globally (WorldDEM^{TM}) (but at a lower resolution of 12 m) [83] as opposed to airborne LiDAR acquisitions. These acquisitions, albeit they provide finer details, are limited in terms of area coverage, and currently less widely available and relatively costly [45].

Requirements to monitor the increase in areas of degraded forest at the expense of primary forests due to fires, a process that will be exacerbated by ENSO in the future, call for novel methods and datasets to characterize canopy structure. The test case undertaken in this work highlights the suitability of two-point spatial statistics, based on a wavelet space-scale analysis, using DEMs derived from LiDAR or InSAR observations as a tool for detecting and mapping landscape-level vegetation heterogeneity.

Acknowledgments: Elsa Carla De Grandi is supported by the Principal's Career Development Scholarship and the School of GeoSciences (University of Edinburgh). The authors would like to acknowledge the software providers Sarmap SA and EXELIS VIS (Sarscape 5.0). Data processing was undertaken in ENVI IDL and Wolfram Mathematica. Data providers: DLR (TanDEM-X AO VEGE6702), Indonesian Ministry of Forestry (land cover map), Dirk Hoekman (Wageningen University) for providing SAR expertise, the LiDAR data and aerial photography. The authors would also like to thank Lan Qie (University of Leeds) for providing information related to the study site.

Author Contributions: Elsa Carla De Grandi conceived and designed the experiments (assisted by Edward Mitchard). Elsa Carla De Grandi processed the TanDEM-X data, analyzed the data and wrote the paper. Edward Mitchard and Dirk Hoekman provided comments on the manuscript. Dirk Hoekman provided LiDAR and aerial photography datasets.

Conflicts of Interest: The authors declare no conflict of interest.

Abbreviations

The following abbreviations are used in this manuscript:

ENSO	El Niño Southern Oscillation
CHM	Canopy Height Model
DSM	Digital Surface Model
DTM	Digital Terrain Model
DEM	Digital Elevation Model
FOTO	Fourier Transform Textural Ordination
GR	Grassland
InSAR	Interferometric Synthetic Aperture Radar
JM	Jeffries–Matusita
LiDAR	Light Detection and Ranging
MS	Mixed scrub
PD	Probability Density
PF	Primary Forest
P_0	First wavelet Polynomial Coefficient
P_e	Probability Error
SAR	Synthetic Aperture Radar
SF	Secondary forest
TDX	TanDEM-X
VV	Vertical Send Vertical Receive
WS	Wavelet Spectra

Appendix II

References

1. Grace, J.; Mitchard, E.; Gloor, E. Perturbations in the carbon budget of the tropics. *Glob. Chang. Biol.* **2014**, *20*, 3238–3255. [PubMed]
2. Pan, Y.; Birdsey, R.A.; Fang, J.; Houghton, R.; Kauppi, P.E.; Kurz, W.A.; Phillips, O.L.; Shvidenko, A.; Lewis, S.L.; Canadell, J.G.; et al. A large and persistent carbon sink in the world's forests. *Science* **2011**, *333*, 988–993. [PubMed]
3. Mitchard, E.T.A.; Feldpausch, T.R.; Brienen, R.J.W.; Lopez-Gonzalez, G.; Monteagudo, A.; Baker, T.R.; Lewis, S.L.; Lloyd, J.; Quesada, C.A.; Gloor, M.; et al. Markedly divergent estimates of Amazon forest carbon density from ground plots and satellites. *Glob. Ecol. Biogeogr.* **2014**, *23*, 935–946. [CrossRef] [PubMed]
4. ITTO Guidelines for the Restoration, Management and Rehabilitation of Degraded and Secondary Tropical Forests. Available online: http://www.itto.int/direct/topics/topics_pdf_download/topics_id=1540000&no=1&disp=inline (accessed on 11 November 2015).
5. Harris, N.L.; Brown, S.; Hagen, S.C.; Saatchi, S.S.; Petrova, S.; Salas, W.; Hansen, M.C.; Popatov, P.V.; Lotsch, A. Baseline map of carbon emissions from deforestation in tropical regions. *Science* **2012**, *336*, 1573–1576. [CrossRef] [PubMed]
6. Kartawinata, K.; Abdullhadi, R.; Partomihardjo, T. Composition and structure of a lowland dipterocarp forest at Wanariset, East Kalimantan. *Malays. For.* **1981**, *44*, 397–406.
7. Potapov, P.; Yaroshenko, A.; Turubanova, S.; Dubinin, M.; Laestadius, L.; Thies, C.; Aksenov, D.; Egorov, A.; Yesipova, Y.; Glushkov, I.; et al. Mapping the world's intact forest landscapes by remote sensing. *Ecol. Soc.* **2008**, *13*, 1–16.
8. Mietten, J.; Stibig, H.J.; Achard, F. Remote sensing of forest degradation in Southeast Asia—Aiming for a regional view through 5–30 m satellite data. *Global Ecol. Conserv.* **2014**, *2*, 24–36. [CrossRef]
9. Giam, X.; Clements, G.R.; Aziz, S.A.; Chong, K.Y. Rethinking the 'back to wilderness' concept for Sundaland's forests. *Biol. Conserv.* **2011**, *144*, 3149–3152. [CrossRef]
10. Lewis, S.L.; Edwards, D.P.; Galbraith, D. Increasing human dominance of tropical forests. *Science* **2015**, *349*, 827–832. [CrossRef] [PubMed]
11. Berenguer, E.; Ferreira, J.; Gardner, T.; Oliveira Cruz Aragão, L.; Barbosa De Camargo, P.; Cerri, C.; Durigan, M.; De Oliveira, R.; Guimarães Vieira, I.; Barlow, J. A large-scale field assessment of carbon stocks in human-modified tropical forests. *Glob. Chang. Biol.* **2014**, *20*, 3713–3726. [CrossRef] [PubMed]
12. MacKinnon, K.; Hatta, G.; Halim, H.; Mangalik, A. *The Ecology of Kalimantan*, 1st ed.; Oxford University Press: Oxford, UK, 1997.
13. Goldammer, H.G. Fire management in tropical forests. In *Tropical Forestry Handbook*, 2nd ed.; Pancel, L., Köhl, M., Eds.; Springer-Verlag: Berlin, Germany, 2015; pp. 1–42.
14. Chisholm, R.A.; Wijedasa, L.S.; Swinfield, T. The need for long-term remedies for Indonesia's forest fires. *Conserv. Biol. Lett.* **2016**, *30*, 5–6. [CrossRef] [PubMed]
15. Cochrane, M. Fire science for rainforests. *Nature* **2003**, *421*, 913–919. [CrossRef] [PubMed]
16. Siegert, F.; Ruecker, G.; Hinrichs, A.; Hoffmann, A. Increased damage from fires in logged forests during droughts caused by El Nino. *Natl. Lett.* **2001**, *414*, 437–440. [CrossRef] [PubMed]
17. Gerwin, J. Degradation of forests through logging and fire in the eastern Brazilian Amazon. *For. Ecol. Manag.* **2002**, *157*, 131–141. [CrossRef]
18. Cai, W.; Borlace, S.; Lengaigne, M.; van Rensch, P.; Collins, M.; Vecchi, G.; Timmermann, A.; Santoso, A.; McPhaden, M.J.; Wu, L.; et al. Increasing frequency of extreme El Niño events due to greenhouse warming. *Nat. Clim. Chang.* **2014**, *4*, 111–116. [CrossRef]
19. Page, S.E.; Siegert, F.; Rieley, J.O.; Boehm, H.V.; Jaya, A.; Limin, S. The amount of carbon released from peat and forest fires in Indonesia during 1997. *Nature* **2002**, *420*, 61–65. [CrossRef] [PubMed]
20. Jordan, C.F.; Farnworth, E.G. Natural vs. plantation forests: A case study of land reclamation strategies for the humid tropics. *Environ. Manag.* **1982**, *6*, 485–492. [CrossRef]
21. Goldammer, J.G. Forests on fire. *Science* **1999**, *284*, 1782–1783. [CrossRef]
22. Toma, T.; Ishida, A.; Matius, P. Long-term monitoring of post-fire aboveground biomass recovery in a lowland dipterocarp forest in East Kalimantan, Indonesia. *Nutr. Cycl. Agroecosyst.* **2005**, *71*, 63–72. [CrossRef]

Appendix II

23. Kennel, P.; Tramon, M.; Barbier, N.; Vincent, G. Canopy height model characteristics derived from airborne laser scanning and its effectiveness in discriminating various tropical moist forest types. *Int. J. Remote Sens.* **2013**, *34*, 8917–8935. [CrossRef]
24. Mahli, Y.; Román-Cuesta, R.M. Analysis of lacunarity and scales of spatial homogeneity in IKONOS images of Amazonian tropical forest canopies. *Remote Sens. Environ.* **2008**, *112*, 2074–2087.
25. Weishampel, J.F.; Drake, J.B.; Cooper, A.; Blair, J.B.; Hofton, M. Forest canopy recovery from the 1938 hurricane and subsequent salvage damage measured with airborne LiDAR. *Remote Sens. Environ.* **2007**, *109*, 142–153. [CrossRef]
26. Frazer, G.W.; Wulder, M.A.; Niemann, K. Simulation and quantification of the fine-scale spatial pattern and heterogeneity of forest canopy structure: A lacunarity-based method designed for analysis of continuous canopy heights. *For. Ecol. Manag.* **2005**, *214*, 65–90. [CrossRef]
27. Bradshaw, G.A.; Spies, T.A. Characterizing canopy gap structure in forests using wavelet analysis. *J. Ecol.* **1992**, *80*, 205–215. [CrossRef]
28. Mallat, S. *A Wavelet Tour of Signal Processing*, 3rd ed.; Academic Press: New York, NY, USA, 2008.
29. Davis, A.; Marshak, A.; Wiscombe, W. Wavelet-based multifractal analysis of non-stationary and/or intermittent geophysical signals. In *Wavelets in Geophysics*, 1st ed.; Foufoula-Georghiou, E., Kumar, P., Eds.; Academic Press: New York, NY, USA, 1994; Volume 4, pp. 249–298.
30. Bongers, F. Methods to assess tropical rain forest canopy structure: An overview. *Plant Ecol.* **2001**, *153*, 263–277. [CrossRef]
31. Lertzman, K.; Fall, J. From forest stands to landscape: Spatial scales and the roles of disturbances. In *Ecological Scale: Theory and Applications*, 10th ed.; Peterson, D.L., Parker, V.T., Eds.; Columbia University Press: New York, NY, USA, 1998; pp. 339–368.
32. Barbier, N.; Couteron, P.; Proisy, C.; Malhi, Y.; Gastellu-Etchegorry, J-P. The variation of apparent crown size and canopy heterogeneity across lowland Amazonian forests. *Glob. Ecol. Biogeogr.* **2010**, *19*, 72–84. [CrossRef]
33. Palace, M.; Keller, M.; Asner, G.P.; Hagen, S.; Braswell, B. Amazon forest structure from IKONOS satellite data and the automated characterization of forest canopy properties. *Biotropica* **2008**, *40*, 141–150. [CrossRef]
34. Asner, G.P.; Palace, M.; Keller, M.; Pereira, R., Jr.; Silva, J.N.M.; Zweede, J.C. Estimating canopy structure in an Amazon forest from laser range finder and IKONOS satellite observations. *Biotropica* **2002**, *34*, 483–492. [CrossRef]
35. Wulder, M.; Franklin, S.E. *Remote Sensing of Forest Environments: Concepts and Case Studies*, 1st ed.; Springer: Dordrecht, The Netherlands, 2003.
36. Brearley, F.Q.; Prajadinata, S.; Kidda, P.S.; Proctor, J. Structure and floristics of an old secondary rain forest in Central Kalimantan, Indonesia, and a comparison with adjacent primary forest. *For. Ecol. Manag.* **2004**, *195*, 385–397. [CrossRef]
37. Delang, C.; Li, W.M. Forest structure. In *Ecological Succession on Fallowed Shifting Cultivation Fields: A Review of the Literature*, 1st ed.; Delang, C.O., Li, W.M., Eds.; Springer: Heidelberg, Germany, 2013; pp. 9–37.
38. Eichhorn, K.A.O. Plant Diversity after Rain-Forest Fires in Borneo. Ph.D. Thesis, University of Leiden, Leiden, The Netherlands, 17 May 2006.
39. Slik, J.W.; Verburg, R.W.; Keßler, P.J.A. Effects of fire and selective logging on the tree species composition of lowland dipterocarp forest in East Kalimantan, Indonesia. *Biodivers. Conserv.* **2002**, *11*, 85–98. [CrossRef]
40. Slik, J.W.; Bernard, C.S.; Van Beek, M.; Breman, F.C.; Eichhorn, K.A.O. Tree diversity, composition, forest structure and aboveground biomass dynamics after single and repeated fire in a Bornean rain forest. *Oecologia* **2008**, *158*, 579–588. [CrossRef] [PubMed]
41. Van Nieuwstadt, M.G. Trail by Fire. Postfire Development of a Tropical Dipterocarp Forest. Ph.D. Thesis, University of Utrecht, Utrecht, The Netherlands, 13 May 2002.
42. Yeager, C.P.; Marshall, A.J.; Stickler, C.M.; Chapman, C.A. Effects of fires on Peat Swamp and Lowland Dipterocarp Forests in Kalimantan, Indonesia. *Trop. Biodiver.* **2003**, *8*, 121–138.
43. Roughgarden, J.; Running, S.W.; Matson, P.A. What Does Remote Sensing Do For Ecology? *Ecology* **1991**, *72*, 1918–1922. [CrossRef]
44. Van der Sanden, J.J.; Hoekman, D.H. Potential of airborne radar to support the assessment of landcover in a tropical rainforest. *Remote Sens. Environ.* **1999**, *68*, 26–40. [CrossRef]

Appendix II

45. De Sy, V.; Herold, M.; Achard, F.; Asner, G.P.; Held, A.; Kellndorfer, J.; Verbesselt, J. Synergies of multiple remote sensing data sources for REDD + monitoring. *Curr. Opin. Environ. Sustain.* **2012**, *4*, 696–706. [CrossRef]
46. Gallardo-Cruz, J.A.; Meave, J.A.; González, E.J.; Lebrija-Trejos, E.E.; Romero-Romero, M.A.; Pérez-García, E.A.; Gallardo-Cruz, R.; Hernández-Stefanoni, J.L.; Martorell, C. Predicting tropical dry forest successional attributes from space: Is the key hidden in image texture? *PLoS ONE* **2012**, *7*, 1–12. [CrossRef] [PubMed]
47. Proisy, C.; Couteron, P.; Francois, F. Predicting and mapping mangrove biomass from canopy rain analysis using Fourier-based textural ordination of IKONOS images. *Remote Sens. Environ.* **2007**, *109*, 379–392. [CrossRef]
48. Kaasalainen, S.; Holopainen, M.; Karjalainen, M.; Vastaranta, M.; Kankare, V.; Karila, K.; Osmanoglu, B. Combining LiDAR and synthetic aperture radar data to estimate forest biomass: Status and prospects. *Forests* **2015**, *6*, 252–270. [CrossRef]
49. Couteron, P.; Pelissier, R.; Nicolini, E.A.; Paget, D. Predicting tropical forest stand structure parameters from Fourier transform of very high-resolution remotely sensed canopy images. *J. Appl. Ecol.* **2005**, *42*, 1121–1128. [CrossRef]
50. Lim, K.; Treitz, P.W.M.; St-Onge, B.; Flood, M. LiDAR remote sensing of forest structure. *Prog. Phys. Geogr.* **2003**, *27*, 88–106. [CrossRef]
51. Balzter, H. Forest mapping and monitoring with interferometric synthetic aperture radar (InSAR). *Prog. Phys. Geogr.* **2001**, *25*, 159–177. [CrossRef]
52. Kent, R.; Lindsell, J.A.; Vaglio Laurin, G.; Valentini, R.; Coomes, D.A. Airborne LiDAR detects selectively logged tropical forest even in an advanced stage of recovery. *Remote Sens.* **2015**, *7*, 8448–8367. [CrossRef]
53. Wedeux, B.; Coomes, D. Landscape-scale changes in forest canopy structure across a partially logged tropical peat swamp. *Biogeosci.* **2015**, *12*, 6707–6719. [CrossRef]
54. Véga, C.; Vepakomma, U.; Morel, J.; Bader, J-L.; Rajashekar, G.; Jha, C.S.; Ferêt, J.; Proisy, C.; Pélissier, R.; Dadhwal, V.K. Aboveground-biomass estimation of a complex tropical forest in Indian using LiDAR. *Remote Sens.* **2015**, *7*, 10607–10625. [CrossRef]
55. Garrity, S.R.; Meyer, K.; Maurer, K.D.; Hardiman, B.; Bohrer, G. Estimating plot-level tree structure in a deciduous forest by combining allometric equations, spatial wavelet analysis and airborne LiDAR. *Remote Sens. Lett.* **2012**, *3*, 443–451. [CrossRef]
56. Krieger, G.; Moreira, A.; Fiedler, H.; Hajnsek, I.; Wener, M.; Younis, M.; Zink, M. TanDEM-X: A satellite formation for high-resolution SAR interferometry. *IEEE Tran. Geosci. Remote Sens.* **2007**, *45*, 3317–3341. [CrossRef]
57. Bräutigam, B.; Martone, M.; Rizzoli, P.; Gonzalez, C.; Weclich, C.; Borla Tridon, D.; Bachmann, M.; Schulze, D.; Zink, M. Quality assessment for the first part of the TanDEM-X Global Digital Elevation Model. In Proceedings of the 36th International Symposium on Remote Sensing of Environment, Berlin, Germany, 11–15 May 2015; pp. 1137–1143.
58. Solberg, S.; Lohne, T.P.; Karyanto, O. Temporal stability of InSAR height in a tropical rainforest. *Remote Sens. Lett.* **2015**, *6*, 209–217. [CrossRef]
59. Kugler, F.; Hajnsek, I. Forest characterisation by means of TerraSAR-X and TanDEM-X (polarimetric and) interferometric data. In Proceedings of the IEEE International Geosciences and Remote Sensing Symposium, Vancouver, BC, Canada, 24–29 July 2011; pp. 2578–2581.
60. Praks, J.; Antropov, O.; Hallikainen, M. LiDAR-aided SAR interferometry studies in boreal forest: Scattering phase center and extinction coefficient at X- and L-Band. *IEEE Tran. Geosci. Remote Sens.* **2012**, *50*, 3831–3843. [CrossRef]
61. Treuhaft, R.; Gonçalves, F.; dos Santos, J.R.; Keller, M.; Palace, M.; Madsen, S.N.; Sullivan, F.; Graça, P.M.L.A. Tropical-forest biomass estimation at X-Band from. *IEEE Geosci. Remote Sens. Lett.* **2015**, *12*, 239–243. [CrossRef]
62. Hajnsek, I.; Kugler, F.; Lee, S.-K.; Papathanassiou, K. Tropical-forest-parameter estimation by means of Pol-InSAR: The INDREX-II campaign. *IEEE Tran. Geosci. Remote Sens.* **2009**, *42*, 481–493. [CrossRef]
63. Kugler, F.; Lee, S.-K.; Hajnsek, I.; Papathanassiou, K. Forest height estimation by means of Pol-InSAR data inversion: The role of the vertical wavenumber. *IEEE Trans. Geosci. Remote Sens.* **2015**, *53*, 5294–5311. [CrossRef]

Appendix II

64. Walsh, R.P.D. Drought frequency changes in Sabah and adjacent parts of northern Borneo since the late nineteenth century and possible implications for tropical rain forest dynamics. *J. Trop. Ecol.* **1996**, *12*, 385–407. [CrossRef]
65. Yassir, I.; van der Kamp, J.; Buurman, P. Secondary succession after fire in Imperata grasslands of East Kalimantan, Indonesia. *Agric. Ecosyst. Environ.* **2010**, *137*, 172–182. [CrossRef]
66. Indonesian Ministry of Forestry. Available online: http://webgis.dephut.go.id/ditplanjs/ (accessed on 20 September 2015).
67. Sarmap. 2012. Available online: http://www.sarmap.ch/pdf/SARscapeTechnical.pdf (accessed on 5 November 2015).
68. Goldstein, R.M.; Werner, C.L. Radar interferogram filtering for geophysical applications. *Geophys. Res. Lett.* **1998**, *25*, 4035–4038. [CrossRef]
69. Balzter, H.; Rowland, C.; Saich, P. Forest canopy and carbon estimation at Monks Wood National Nature Reserve, UK, using dual-wavelength SAR interferometry. *Remote Sens. Environ.* **2007**, *108*, 224–239. [CrossRef]
70. De Grandi, E.C.; Mitchard, E.; Woodhouse, I.; De Grandi, G.D. Spatial wavelet statistics of SAR backscatter for characterizing degraded forest: A case study from Cameroon. *IEEE J. Sel. Top. Appl. Earth Obs. Remote Sens.* **2015**, *8*, 3572–3584. [CrossRef]
71. Alexander, L.A.; Inggs, M.R. The investigation into the effects of speckle filters on classification. In Proceedings of the IEEE International Geosciences and Remote Sensing Symposium, Hamburg, Germany, 28 June–2 July 1999; pp. 1226–1228.
72. Kugler, F.; Sauer, S.; Lee, S.-K.; Papathanassiou, K.; Hajnsek, I. Potential of TanDEM-X for forest parameter estimation. In Proceedings of the 8th European Conference on Synthetic Aperture Radar (EUSAR), Aachen, Germany, 7–10 June 2010; pp. 178–181.
73. Proisy, C.; Barbier, N.; Guéroult, M.; Pélissier, R.; Gastellu-Etchegorry, J.-P.; Grau, E.; Couteron, P. Biomass prediction in tropical forests: The canopy grain approach. In *Remote Sensing of Biomass: Principles and Applications*; Fatoyinbo, L., Ed.; InTech: Rijeka, Croatia, 2012; pp. 1–18.
74. Percival, D.B.; Walden, A.T. *Wavelet Methods for Time Series Analysis*, 1st ed.; Cambridge University Press: Cambridge, UK, 2000.
75. Hoekman, D.H.; Varekamp, C. Observation of tropical rain forest trees by airborne high-resolution interferometric radar. *IEEE Tran. Geosci. Remote Sens.* **2001**, *39*, 584–594. [CrossRef]
76. Ouma, Y.O.; Tetuki, J.; Tateishi, R. Analysis of co-occurrence and discrete wavelet transform texture for differentiation in very high resolution optical-sensor imagery. *Int. J. Remote Sens.* **2008**, *29*, 3417–3456. [CrossRef]
77. Cochrane, M.A.; Schultze, M.D. Forest fires in the Brazilian Amazon. *Conserv. Biol.* **1998**, *12*, 948–950. [CrossRef]
78. Cochrane, M.A.; Schultze, M.D. Fires as a recurrent event in tropical forests of the Eastern Amazon. *Biotropica* **1999**, *31*, 2–16.
79. Krieger, G.; Hajnsek, I.; Papathanassiou, K.; Eineder, M.; Younis, M.; De Zan, F.; Prats, P.; Huber, S.; Werner, M.; Fiedler, H.; et al. The Tandem-L mission proposal: Monitoring earth's dynamics with high resolution SAR interferometry. In Proceeding of the IEEE Radar Conference, Pasadena, CA, USA, 4–8 May 2009; pp. 1–6.
80. Eineder, M.; Hajnsek, I.; Krieger, G.; Moreira, A.; Papathanassiou, K. TanDEM-L. In *Satellite Mission Proposal for Monitoring Dynamic Processes on the Earth's Surface*; German Aerospace Center: Cologne, Germany, 2014.
81. Sun, G.; Ranson, K.J. Radar modelling of forest spatial patterns. *Int. J. Remote Sens.* **1998**, *19*, 1769–1791. [CrossRef]
82. Brown, S.; Lugo, A.E. Tropical secondary forests. *J. Trop. Ecol.* **1990**, *6*, 1–32. [CrossRef]
83. WorldDEM™ Technical Product Specification. Version 1.0. Available online: http://www.engesat.com.br/wp-content/uploads/455--201404_worlddem_technicalspecs_i1.pdf (accessed on 11 November 2015).